DESIGN AND ANALYSIS OF ORBITAL DEBRIS PROTECTION FOR

SPACECRAFT COMPOSITE PRESSURE VESSELS

by

Aleksandr Cherniaev

A Thesis submitted to the Faculty of Graduate Studies of

The University of Manitoba

In partial fulfilment of the requirements of the degree of

DOCTOR OF PHILOSOPHY

Department of Mechanical Engineering

University of Manitoba

Winnipeg

ABSTRACT

Being parts of spacecraft systems, composite overwrapped pressure vessels (COPVs) are exposed to orbital debris environment. In the case of impact of orbital debris on a composite vessel, the vessel may fail non-catastrophically, possibly resulting in the loss of spacecraft, or catastrophically, producing numerous non-trackable fragments, which may result in the loss of spacecraft and also affect and destroy other active and future spacecraft in neighbor orbits. Consequences of orbital debris impacts, therefore, must be minimized with the use of an appropriate design strategy. For a weight-efficient design providing high level of protection for spacecraft composite pressure vessels, the following design strategy is suggested in this study:

- Exclude any involvement of the pressure wall in resisting orbital debris impacts by means of an <u>external shielding</u> designed for the same tolerable risk of penetration as the shielding of any other critical subsystem of the spacecraft (R_{1tol}; typically, 1-5%);

- Ensure that the <u>shielded</u> COPV will not fail catastrophically under conditions corresponding to even stricter tolerable risk of penetration (R_{2tol}), such that $R_{2tol} < R_{1tol}$, which can correspond to the tolerable risk of accidental explosion during mission operations in Orbit (typically, 0.1%).

Implementation of the proposed design paradigm required 1) weight-efficient shielding systems to be designed against highly probable impacts of small-size orbital debris; and 2) a procedure capable of predicting the behavior of a shielded COPV subjected to perforating orbital debris impacts to be developed. Correspondingly, this study focused on these two aspects. First, five different external shielding systems were analysed for their weight

efficiency when designed against small-size (1 mm) orbital debris impacts, including a novel orbital debris shield with ceramo-metallic bumper. Conducted evaluation made it possible to identify and recommend weight-efficient shielding designs in such categories as "Single purpose orbital debris shields" and "Multipurpose structural panels". In this part, the results are mainly applicable to the spacecraft in low Earth Orbit. Second, a two-step modeling procedure was proposed to simulate behavior of shielded composite overwrapped pressure vessels when subjected to perforating impacts by large-size hypervelocity projectiles. The procedure can be used to evaluate vulnerability of a shielded vessel to catastrophic failure. As a main part of this procedure, a novel meso-scale modeling approach suitable for simulating hypervelocity impact damage of filament-wound composite vessels was developed and verified against experimental data.

ACKNOWLEDGEMENTS

TABLE OF CONTENTS

NOMENCLATURE

List of Acronyms

AD	Areal Density
BLE	Ballistic Limit Equation
CFRP	Carbon Fiber Reinforced Plastic
CMWS	Ceramo-Metallic Whipple Shield
COPV	Composite Overwrapped Pressure Vessel
CSA	Canadian Space Agency
EOS	Equation of State
ESA	European Space Agency
FCSP	Foam-Core Sandwich Panel
FEM	Finite Element Method
HCSP	Honeycomb-Core Sandwich Panel
HDI	High Degree of Interweaving
HVI	Hypervelocity Impact
IADC	Inter-Agency Space Debris Coordination Committee
ISS	International Space Station
KFRP	Kevlar Fiber Reinforced Plastic
LDI	Low Degree of Interweaving
LEO	Low Earth Orbit
MLI	Multilayer Insulation
MMOD	Micro-Meteoroids and Orbital Debris
NASA	National Aeronautics and Space Administration
OD	Orbital Debris
ORDEM	Orbital Debris Engineering Model
PNP	Probability of No Penetration
PVD	Physical Vapor Deposition
RRR	Resin-Rich Region
S/C	Spacecraft
SPH	Smoothed-Particle Hydrodynamics
SWS	Stuffed Whipple Shield
WS	Whipple Shield

List of Common Symbols

A	Initial yield strength in the Johnson-Cook strength model
B	Hardening constant in Johnson-Cook strength model
C	Strain rate constant in the Johnson-Cook strength model
C_{ij}	Stiffness matrix coefficient
C_0	Speed of sound

c_w	Empirical coefficient in dual-wall shield ballistic limit equation
D_{cr}	Critical projectile diameter
D_{delam}	Equivalent diameter of delamination zone
D_{eff}	Equivalent diameter of perforation
D_i	Damage coefficient
d_p, D_p	Projectile diameter
d_w	Mesh wire diameter
e_H	Specific internal energy
G_f, G_{Ic}, G_{IIc}	Composite fracture toughness (critical strain energy release rate)
h	Gradient of linear softening
K'	Effective bulk modulus
L	Characteristic dimension in the meso-scale foam model
L_a	Size of mesh aperture
L_f	Thickness of aluminum foam
L_{FP}	Thickness of aluminum foam partially filled with paraffin
m	Thermal softening exponent in Johnson-Cook strength model
m_p	Mass of a projectile
n	Hardening exponent in Johnson-Cook strength model
p	Pressure
p_{MEOP}	Maximum expected operating pressure
PNP_{req}	Required probability of no penetration
R	Risk of penetration
R_{tol}	Tolerable risk of penetration
S	Standoff distance
S	Shear strength of unidirectional composite
Sfmax	Maximum failure strength in the Johnson-Holmquist model
S_{ILSS}	Interlaminar shear strength of composite
S1, S2	Strengths of the intact material in the Johnson-Holmquist model
$S^{\alpha\beta}$	Deviatoric stress tensor
t_b	Bumper thickness
t_f	Facesheet thickness
t_{HEL}	Thickness of helical layer
t_{HOOP}	Thickness of hoop layer
t_r, t_w	Rear wall thickness
T_H	Homologous temperature
U_s	Shock wave speed
U_p	Particle velocity
v_p	Initial velocity of a projectile
W	Plastic work
W_{ij}	Weighting kernel function (SPH)
X_T	Longitudinal strength of unidirectional composite
Y_T	Transverse strength of unidirectional composite
α	Relative density of aluminum foam
β	Filling coefficient for aluminum foam filled with paraffin
Γ	Gruneisen gamma
$\delta^{\alpha\beta}$	Kronecker delta

ε^f	Dynamic fracture strain
ε_p	Effective plastic strain
$\dot{\varepsilon}_p$	Effective plastic strain rate
$\dot{\varepsilon}^{\alpha\beta}$	Strain rate tensor
$\dot{\varepsilon}_p^*$	Dimensionless strain rate
ε_{ij}	Strain tensor component
ε^u	Ultimate strain
λ	Plastic factor
ρ	Density
σ^*	Dimensionless pressure-stress ratio
$\sigma^{\alpha\beta}$	Full stress tensor

LIST OF FIGURES

LIST OF TABLES

1. INTRODUCTION

1.1 Background

It has been almost six decades since the beginning of the space era when the first satellite "Sputnik I" entered Earth Orbit on October 4, 1957. At the moment, in 2016, there are over 22 hundred artificial satellites orbiting Earth, including military spacecraft (S/C), communications and navigational satellites, scientific research satellites, weather satellites, etc.

The increase of the human activity in space led over the years to the creation of a significant number of *unusable* man-made objects circling Earth. These objects are known as "space junk" or "orbital debris" and represent dysfunctional spacecraft, mission-related debris and fragmentation debris generated by collisions and explosions in Orbit. According to NASA [1], the current population of orbital debris consists of more than 21,000 unused objects with the size larger than 100 mm; about 500,000 objects between 10 and 100 mm; and over 100,000,000 debris particles smaller than 10 mm.

The engineering orbital debris model ORDEM 3.0, recently developed by NASA [2], breaks down the debris population into three categories according to the type of material, namely low- (plastics), medium- (aluminum) and high-density (steel and copper) classes. The medium-density fragments, having the average density of 2.8 g/cm^3 and corresponding to aluminum metal, dominate the overall population.

The average speed of orbital debris in low Earth orbit (LEO) is 7 km/s. Impact with such speed of even 1 mm medium-density particle on a functional spacecraft can result in significant amount of damage to the spacecraft hardware and can ultimately lead to the loss

of mission. Examples of damage that can be produced by 1 mm aluminum projectile accelerated to 7 km/s are given in Fig. 1.
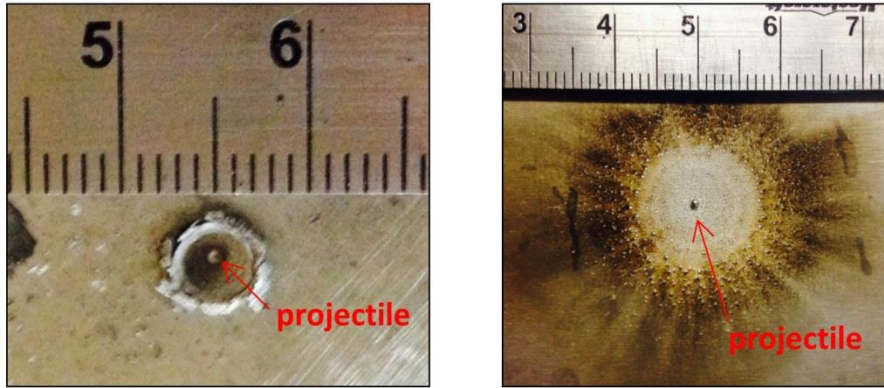
Figure 1 – Exemplary damage from 7 km/s impact of 1 mm aluminum projectile on monolithic (left) and spaced (right) aluminum targets (University of Manitoba data)

Collisions of functional spacecraft with large orbital debris can be catastrophic to both the satellite and LEO environment. Fortunately, debris fragments with the size over 100 mm are being tracked from Earth and in most cases collision avoidance maneuvers can be executed in order to prevent catastrophic consequences of such impacts.

Protection from collisions with non-trackable orbital debris smaller than 10 mm is typically implemented in terms of passive shielding, which has the main goal of fragmenting and decelerating an impacting particle. Guidelines and handbooks on designing orbital debris protection shields have been developed and published by national space agencies and Inter-Agency Space Debris Coordination Committee (IADC) [3 – 5].

A common design of an orbital debris shield is a system consisting of multiple walls, separated from one another by some standoff distance. The simplest of such systems, often referred to as a Whipple shield (WS) [6], is schematically represented in Fig. 2. It consists of two walls, a front bumper and a rear wall, which are usually made of aluminum. The

function of the bumper is to break up the projectile into a cloud of material that expands while moving across the standoff. The expansion results in a distribution of the impactor's energy and momentum over the rear wall, which has to be thick enough to withstand blast loading from the fragment cloud and be able to stop its further propagation [3].
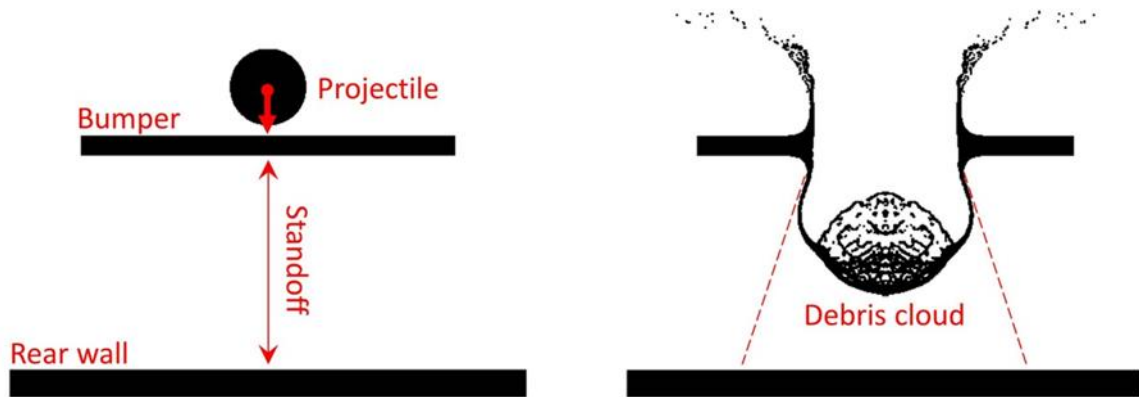
Figure 2 – Schematic of a Whipple shield: before impact (left) and after perforation of the bumper (right)

The probability of no penetration (PNP) is an important criterion in shield design, which ultimately determines the particle diameter to protect a spacecraft component against. The PNP can be calculated as

$$PNP = \exp\left[-\text{(orbital debris flux)} \times \text{(exposed area)} \times \text{(time of exposure)}\right],$$

where the flux is the number of particles of a given size passing through the square meter of space in the spacecraft orbit per year (# / m^2-year). It can be determined using the Micrometeoroids and orbital debris (MMOD) environment models, e.g. NASA's ORDEM 3.0 [7], ESA's MASTER [8] or Roskosmos's SDPA model [107]. The shield design must provide a PNP higher or equal than the minimal required (PNP_{req}).

The corresponding *tolerable* risk of perforation is

$$R_{tol} = 1 - PNP_{req}$$

The expressions above effectively mean that the critical projectile diameter depends on the spacecraft orbit (through MMOD flux), its area exposed to MMOD environment and time of exposure. Other factors, like spacecraft orientation and orbit inclination, are also of importance.

The particular value of R_{tol} for a spacecraft system or component is defined by the reliability and/or safety community [4]. For instance, NASA's standard [9] prescribes that the probability of MMOD impacts which can lead to loss of control over spacecraft and, therefore, "prevent compliance with the applicable postmission disposal requirements", must be less than 0.01 (i.e. the risk of impact must be less than 1%). Other sources indicate that the requirement may vary depending on the type of vehicle. For instance, lower PNP_{req} may be tolerable for unmanned spacecraft [10].

It should be emphasized that the structural weight sensitivity of spacecraft cannot permit an artificial understating of R_{tol}. This point can be illustrated by considering an example of a small satellite in 725 km orbit. Assuming parameters of the spacecraft as provided in Table 1 and using average flux – particle size graph generated using NASA ORDEM 3.0 program (Fig. 3), one can estimate that a decrease of tolerable risk of impact may result in the *substantial growth* of the required weight of MMOD shield[1].

---

[1] This simplified analysis is not specific to any particular spacecraft and provided for illustrative purposes only.

Figure 3 – MMOD cross-section flux vs. particle size for a spacecraft in 725 km orbit as

predicted by NASA's ORDEM 3.0 model

Table 1 – Estimation of required MMOD shield weight[2]

Area requiring shielding – 0.48 m^2; lifetime in orbit – 2 years; altitude – 725 km			
R_{tol}, %	PNP_{req}	Critical projectile diameter, mm	Required shielding weight, kg
5.0	0.950	1.8	1.847
1.0	0.990	2.5	2.850
0.5	0.995	3.0	3.609
0.1	0.999	4.5	6.220

---

[2] Estimated using Christensen Whipple shield BLE [3] with standoff between bumper and rear wall of 45 mm; and assuming that the non-ballistic weight is equal to 30% of the bumper weight

Figure 4 – Burst of a composite overwrapped pressure vessel (Image: NASA [11])

Another important factor that should be brought into consideration is the consequences of component failure in case of MMOD impact. This is especially the case for pressure vessels (used in spacecraft propulsion, attitude control systems, and life support applications), which can potentially fail violently if the pressure wall is damaged by orbital debris [4]. Such failure may be accompanied by fragmentation and not only result in loss of mission, but also can lead to a significant increase of orbital debris population due to the generation of non-trackable fragments and, through this, affect many other active satellites in neighbor orbits. Fig. 4 exemplifies possible consequences of bursting of a pressure vessel (image corresponds to pneumatic burst). In this regard, NASA's standard requirement is to keep the probability of accidental explosion during mission operations in Orbit less than 0.001 (i.e. order of magnitude lower than the "loss of mission" requirement when spacecraft remains intact) [9]. The requirement mainly addresses accidental explosions due to system malfunction and not explicitly related to MMOD impacts. It is clear, however, that catastrophic rupture of a pressure vessel due to perforation by orbital debris will have the same consequences as its explosion due to any other reason. The vessels, therefore, require

a higher level of protection from MMOD impacts as compared to other critical components.

The MMOD shield for a pressure vessel can be designed for lower tolerable risk of penetration, which effectively would mean that it will be able to protect against a larger projectile threat, as critical projectile diameter d_p = f {MMOD flux} (see Fig. 3) and

$$\text{MMOD flux} = - \ln [1 - R_{tol}] / [(\text{exposed area}) \times (\text{time of exposure})]$$

This approach, however, is conservative and, as in the numerical example above, will lead to a significant increase in the weight of the shielding.

Another approach can be proposed in order to reduce the risk of in-orbital explosions (due to vessel's catastrophic failure) while maintaining a reasonable weight efficiency of shielding for spacecraft pressure vessels. In this approach, different *tolerable risks* are associated with different modes of failure:

- Orbital debris (OD) shield for a pressure vessel can be designed with respect to the same tolerable risk of penetration (R_{1tol}) as it was used in the design of other non-explosive mission-critical components (e.g., 1%) Such shielding will be weight-efficient and provide protection from less hazardous (not leading to *immediate* catastrophic rupture of the vessel) but highly probable impacts of smaller particles.
- The possibility of catastrophic rupture of the vessel (can endanger active spacecraft in neighbor orbits) should be minimized by means of establishing stricter tolerable risk requirement (R_{2tol}), but only on this mode of failure (e.g., 0.1%).
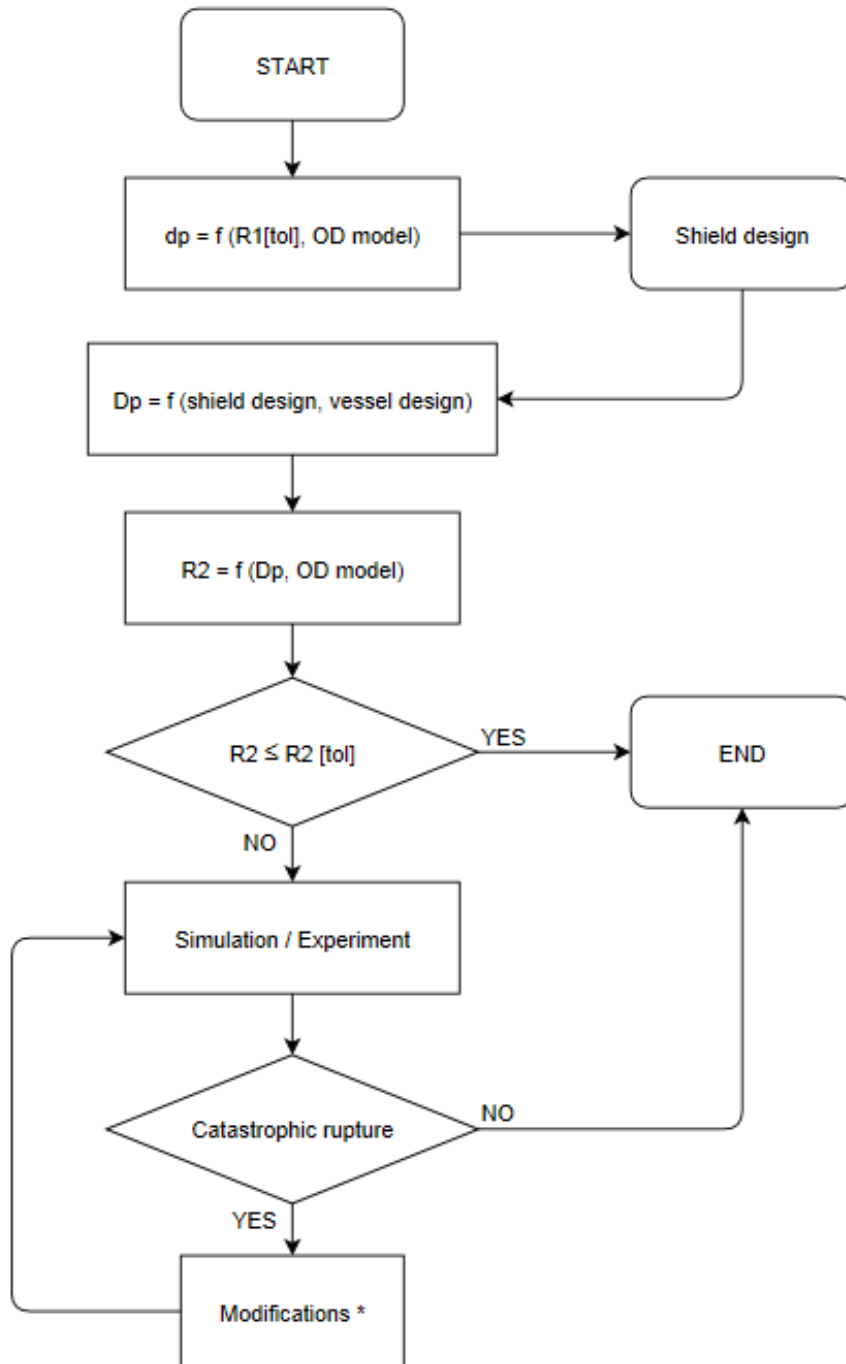
Figure 5 – Flowchart of the proposed design paradigm

The design procedure implementing this approach is schematically represented in Fig. 5 and can be described as follows:

1. The projectile diameter d_p to design a shield against is determined based on the tolerable risk of penetration R_{1tol}.

2. The shielding to defeat a projectile of this size is designed using ballistic limit equations (BLEs), hydrocode simulations and/or physical experiments. As a result, the shield prevents any damage to the vessel's surface by a particle of d_p and smaller.

3. Critical projectile diameter D_p ($D_p > d_p$) capable of perforating the system "external shield + pressure wall" is determined using BLEs (if available) or 2D hydrocode simulations.

4. The risk corresponding to such event (R_2) is determined using available orbital debris model (e.g., ORDEM 3.0).

5. If $R_2 \geq R_{2tol}$, the designer *must ensure* that perforation of the shielded pressure vessel by a fragment with a diameter equal to D_p will not lead to catastrophic failure and fragmentation, and rather result in non-violent pressure release via gas leaking through the perforated hole. This can be done using physical experiments or hydrocode simulations.

6. If simulation/experiment predicts that the vessel can fail catastrophically, modifications of the design or layout should be conducted in order to avoid such scenario.

It should be emphasized that up to certain extent, the modifications can be such that *no additional weight* is required. For example, it can be lowering of internal pressure in the vessel, which was recognized as one of the most efficient ways of preventing its catastrophic failure [12], or increasing standoff between the vessel and the rear wall of the shield.

Implementing this paradigm, one must assume that failure due to non-perforating impacts of particles with diameters larger than d_p but smaller than D_p (can perforate the shield but cannot perforate the pressure wall) will not lead to immediate fragmentation and can be handled through the use of damage monitoring systems (e.g., pressure release can be triggered by detection of vessel's damage).

Design according to the described paradigm implies that two subtasks must be completed:

1. A weight-efficient shielding system providing protection from small-size orbital debris impacts (with respect to the tolerable risk of impact of R_{1tol}) must be designed.
2. Simulations of the behavior of shielded pressure vessel upon perforation by a critical-size projectile (correspond to the tolerable risk of impact of R_{2tol}) must be performed.

As this study was conducted under a contract from Canadian Space Agency (CSA) on development of MMOD protection system for a satellite in an 800-km altitude Sun-synchronous orbit, the tolerable risk estimations for the shielding design (subtask #1) were carried out by CSA and resulted in the critical projectile diameter $d_p = 1$ mm [13]. The projectile was represented by aluminum sphere moving at a speed of 7 km/s.

As for the second subtask, the particular type of pressure tanks considered in this study are composite overwrapped pressure vessels (COPVs). Vessels of this kind are being used in spacecraft propulsion and attitude control systems, life support applications, etc. due to higher weight efficiency as compared to all-metallic containers. Common manufacturing technique for COPVs is filament winding, which is characterized by meso-scale inhomogeneity of the fabricated material in addition to microscopic inhomogeneity

inherent to all types of composites [14]. The former feature results from multiple interweaving of filament bands forming a filament-wound composite part (Fig. 6).
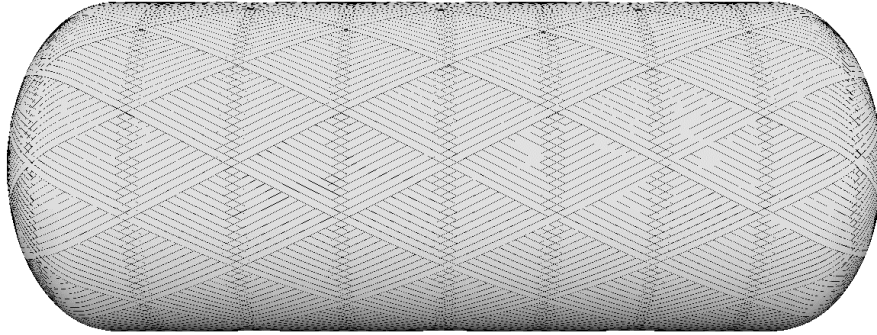
Figure 6 – An exemplary filament-wound composite part with noticeable multiple interweaving of filament bands (simulated using manufacturing software ComposiCAD)

To the best of our knowledge, there was no systematic experimental study specific to hypervelocity impact (HVI) on filament-wound COPVs in literature. Attempts to numerical modeling were also much more limited and rather simplified [15]. The simplifications, in particular, are associated with the common practice in HVI simulations to substitute real composite laminate by a homogeneous orthotropic material with similar effective properties (e.g., [16, 17]). However, the validity of this approach for filament-wound composites is questionable due to the presence of complex interweaving between filament bands.

Correspondingly, in order to complete the subtask #2, spacecraft engineers should be provided with a simulation approach capable of representing the behavior of COPVs subjected to HVI with a sufficient accuracy.

1.2 Objectives of Thesis

Following the rationale of minimizing the negative consequences of orbital debris impacts on composite pressure vessels, and based on the design paradigm described above, the objectives of this study are formulated as follows:

1. To design and evaluate the weight-efficiency of conventional and novel shielding systems capable of protecting spacecraft COPVs against small-size (up to 1 mm) orbital debris particles moving at a speed of 7 km/s.
2. To develop a simulation approach capable of predicting the behavior of shielded composite overwrapped pressure vessels subjected to perforating hypervelocity impacts by larger-size orbital debris.

1.3 Overview of Thesis

In *Chapter 2*, a review of relevant publications is presented. These publications focus on existing designs of orbital debris shields, the behavior of pressure vessels subjected to HVI, numerical techniques and material models for HVI simulations.

Chapter 3 presents design calculations for conventional shielding systems, including such concepts as Whipple shield, stuffed Whipple shield, honeycomb-core, and foam-core sandwich panels. A novel shield design with metallic bumper coated by the high-impedance ceramic material is also proposed in this chapter and studied both experimentally and theoretically. Finally, the conventional and novel shields designed against impacts of small-size orbital debris are compared in terms of their weight efficiency. This comparison allowed identifying the most efficient shielding systems in such categories as "Single purpose MMOD shields" and "Multi-purpose structural panels".

In *Chapter 4* a procedure for computationally efficient modeling of the behavior of shielded COPVs subjected to perforating impacts of larger-size orbital debris is proposed. As COPVs are typically fabricated by filament winding, which implies the presence of multiple interweaving of filament bands, the behavior of filament-wound composites subjected to HVI was experimentally studied and results of the study presented in *Chapter 4*. Based on this study, a meso-scale approach to modeling of HVI damage of filament-wound composites is proposed and validated. The chapter concludes with the example of the application of the proposed modeling procedure to investigating the behavior of a shielded COPV perforated by orbital debris.

Finally, *Chapter 5* presents key conclusions of the work undertaken, along with recommendations for future work.

1.4 Dissemination

The work presented in this thesis has been disseminated in the following way:

Journal papers:

1. Cherniaev A., Telichev I. Experimental and numerical study of hypervelocity impact damage in composite materials fabricated by filament winding. *International Journal of Impact Engineering* 98, 19-33 (2016)

2. Cherniaev A., Telichev I. Weight-efficiency of conventional shielding systems in protecting unmanned spacecraft from orbital debris. *Journal of Spacecraft and Rockets* [Article in Advance, DOI: 10.2514/1.A33596] (2016)

3. Cherniaev A., Telichev I. Meso-scale modeling of hypervelocity impact damage in composite laminates. *Composites Part B: Engineering* 74 (1), 95-103 (2015)

4. Cherniaev A., Telichev I. Numerical Simulation of Impact Damage Induced by Orbital Debris on Shielded Wall of Composite Overwrapped Pressure Vessel. *Applied Composite Materials* 21 (6), 861-884 (2014)

Conference papers:

1. Cherniaev A., Telichev I. Hypervelocity impact damage in composite materials fabricated by filament winding – *Proceedings of the 24th International Congress of Theoretical and Applied Mechanics (ICTAM), 21-26 August 2016, Montreal, Canada.*

2. Telichev I., Cherniaev A. Structural Integrity of Gas-Filled Composite Overwrapped Pressure Vessels Subjected to Orbital Debris Impact – *Proceedings of the 40th COSPAR Scientific Assembly, Moscow* (2014)

3. Cherniaev A., Telichev I. Modeling of damage formation on a front wall of shielded composite overwrapped pressure vessel subjected to space debris impact – *Proceedings of the 65th International Astronautical Congress, Toronto* (2014)

Conference presentations (without paper):

1. Cherniaev A.*, Telichev I. Hypervelocity impact damage to filament-wound composites – *15th Annual Canadian Space Society Summit*, Winnipeg, November 14-15, 2016.

2. Cherniaev A.*, Telichev I. Hypervelocity impact damage in composite materials fabricated by filament winding – *Consortium For Aerospace Research and Innovation in Canada (CARIC) Research Forum*, Winnipeg, MB, Canada, May 26, 2016 (poster presentation).

3. Cherniaev A.*, Telichev I. Weight-efficiency of conventional shielding systems for MMOD protection of unmanned spacecraft – *17th Astronautics Conference of the Canadian Astronautics and Space Institute (ASTRO 2016)*, Ottawa, ON, Canada, May 17-19, 2016.

4. Cherniaev A.*, Telichev I. Evaluation of efficiency of conventional shielding systems for spacecraft protection against small-size orbital debris impacts. *Canadian Space Summit, Vancouver*, November 2015.

2. LITERATURE REVIEW

2.1 MMOD Shields Design

A number of reports issued by NASA, ESA and IADC provide detailed descriptions of MMOD protection strategies, requirements for protection, and the means to meet these requirements [3 - 5]. This section describes the most widely used concepts of the MMOD protection systems.
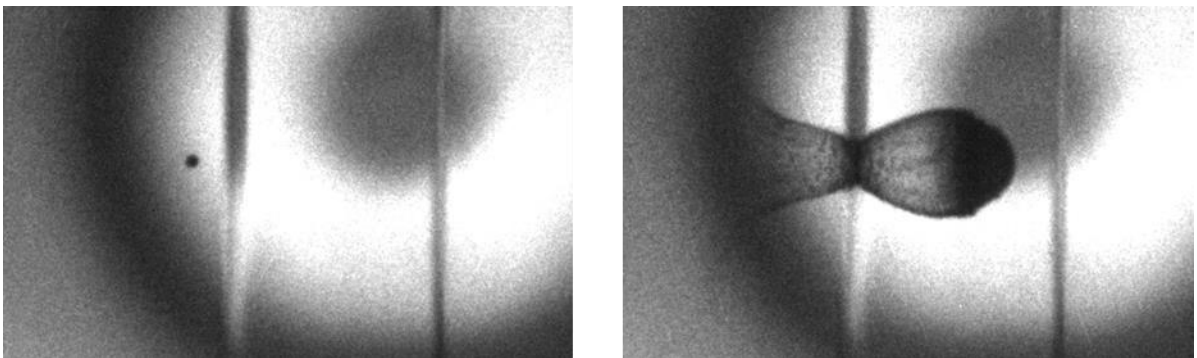
Figure 7 – Impact of a hypervelocity projectile on a Whipple shield (U of M data)

A standard design of a shield is based on the *Whipple shield* principle [6].The Whipple shield consists of a sacrificial outer bumper placed at a certain distance from the rear wall. It was the first spacecraft shield ever implemented and it is still in use today. The Whipple shield is particularly effective at high impact velocities, when the shock stresses generated by impact exceed the yield strengths of the impacting particle and the MMOD protection materials (by orders of magnitude) leading to particle fragmentation. For most conditions, a Whipple shield results in a significant weight reduction over a single monolithic plate. For the impact of aluminum debris on aluminum bumper shields, the fragmentation threshold is achieved at roughly 3 km/s [18]. The formed debris cloud (see Fig. 7) contains

the smaller and thus less lethal fragments, which distribute the momentum onto a larger area, with the rear wall being able to retain these fragments.

The *Stuffed Whipple Shield* (SWS) concept is an enhancement of a simple Whipple shield and incorporates a layer of fabric materials, called stuffing, in between a bumper and a rear wall. It is particularly effective for the requirement of short shield standoffs when the shield spacing to projectile diameter ratios is 15 or less. Stuffed Whipple shield was developed by NASA [19] for protecting US modules on the International Space Station (ISS). The protection performance was increased considerably using high-strength fabrics (e.g., Kevlar) in combination with ceramic fabrics (Nextel) as intermediate layers for "stuffing". Nextel is a flexible, ceramic fabric product manufactured by 3M Corporation which contains alumina, boron oxide and silica. Kevlar is a product of the E.I. DuPont Co. NASA has shown that alternative shields using aluminum, Nextel or Kevlar alone as the intermediate bumper did not provide the same level of protection performance for the equal areal weight as a combination of Nextel and Kevlar. Shield performance is improved (compared to aluminum) because Nextel ceramic fabric is better at shocking projectile fragments than aluminum, and Kevlar is better at slowing debris cloud expansion than aluminum. Also, in comparison with an aluminum bumper the Nextel/Kevlar layers contribute smaller fragments into the debris cloud resulting in less rear wall damage. In parallel to the development of the NASA Stuffed Whipple Shield, ESA developed a similar type of heavy protection shield [20]. The most notable principle difference between the shield configurations of NASA and ESA is the use of Kevlar–Epoxy composite plates for the ESA set-up whereas NASA relies on Kevlar fabrics. The Stuffed Whipple Shield

designed by NASA is slightly lighter and thinner; however the ESA shield has a better protection performance at low impact velocities (around 3 km/s).

Table 2 presents weight parameters for all-aluminum Whipple shields that are equivalent to stuffed shields in terms of ballistic performance, as designed using the Whipple shield ballistic limit equation provided in Ref. [3]. From this data, it can be deduced that, for the given projectile parameters, the SWS concept provides 21−26% lower ballistic weight as compared to the Whipple shield; however, the high additional non-ballistic weight of the standoff structure (e.g. fasteners, spacers) that is required for SWSs reduces their overall weight efficiency. Even with this restriction in place, though, significant mass savings (from 4 to 13% of the required WS mass) were achieved by using stuffed shields instead of the all-aluminum Whipple configuration.

Table 2 − Parameters of the MMOD shields used in ISS and of the equivalent Al6061-T6 Whipple shields

Parameters / Shield Type	NASA SWS	Equivalent WS	ESA SWS	Equivalent WS
Critical Al projectile diameter at $v_p = $ 7 km/s, mm	13	13	14.5	14.5
Overall standoff, mm	110	110	130	130
Bumper AD, g/cm^2	0.540	0.880	0.700	0.981
Stuffing AD, g/cm^2	0.800	—	1.100	—
Rear Wall AD, g/cm^2	1.400	2.830	1.400	3.062
Total Ballistic AD, g/cm^2	2.740	3.710	3.200	4.043
$\Delta_{ballistic}$, %	-26%		-21%	
Non-ballistic AD, g/cm^2	0.720	0.264	0.968	0.297
Total AD, g/cm^2	**3.460**	**3.974**	**4.168**	**4.337**
Δ, %	-13%		-4%	

Estimations of non-ballistic weight are based on data from Ref. [3, 67].

Other weight-efficient shielding concepts are continually being sought. In this regard, fragmentation capabilities of such elements as metallic meshes [21, 22] or different types of fabrics (e.g., Kevlar, Nextel or carbon) [23] have been studied.
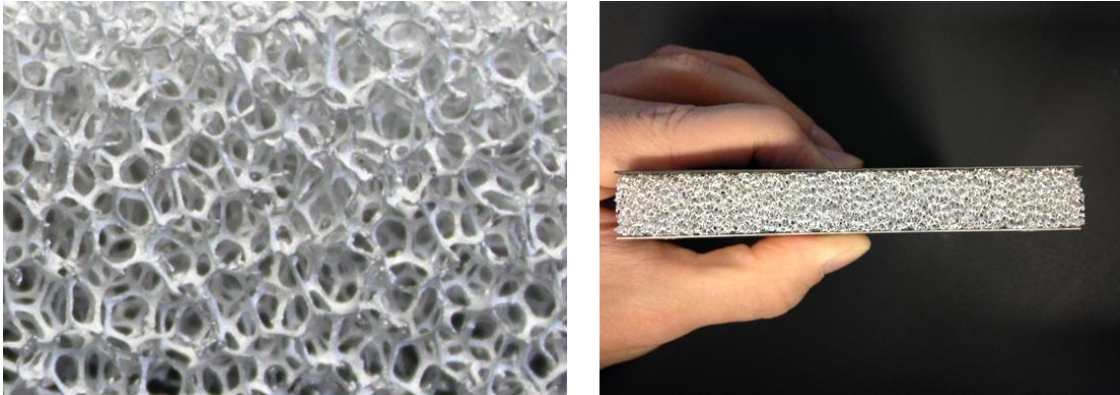
Figure 8 – Open-cell aluminum foam (left) and a foam-core sandwich panel (right)

The need to design weight-efficient spacecraft structures lead to the idea of employing already existing spacecraft structural parts for protection against orbital debris and, thus, avoiding installation of additional external shields [3]. One of the most common examples is the use of the *honeycomb-core sandwich panels* as protective elements. Panels of this kind are generic elements of many spacecraft structures. For instance, the bus structure of Canadian satellite CASSIOPE is made up of aluminum honeycomb panels with aluminum face sheets [24].

Experiments, however, have revealed that the honeycomb core restricts expansion of the debris cloud as it propagates through the interior of a panel (so called "channeling"), and this has an adverse effect on its ballistic performance. In Ref. [109], the ballistic performance of a honeycomb-core sandwich panel (HCSP) at normal incidence was found to be equivalent to the performance of a Whipple shield with 50% lower rear wall thickness than that of the sandwich panel.

As a promising alternative to the honeycomb design, open-cell aluminum foam (see Fig. 8) has been considered by a number of researchers. In an experimental study presented by NASA [110], foam-core sandwich panels (FCSPs) with 25–30% lower areal density than HCSPs demonstrated better ballistic performance. In [26], it was determined that, depending on impact conditions, double-layer foam shields provided from 3 to 15% improvement in critical projectile diameter as compared to double-layer honeycomb shields (which comprised two spaced honeycomb-core sandwich panels) of similar weight. The performance improvement in case of using the foams is not explained as a result of the simple absence of the channeling cells. Rather, the radial expansion of debris cloud and repeated impact of fragments on individual foam cell ligaments induced further fragmentation, melt, and vaporization of fragments [27]. In [111], an asymmetric FCSP combined with Kevlar stuffing was experimentally evaluated as an alternative to the existing stuffed Whipple shield of the ISS Columbus module. The configuration with aluminum foam revealed better ballistic performance than the SWS at velocities over 6.5 km/s.

Although all of these studies demonstrated the high potential of aluminum foam in MMOD shielding applications, they do not answer the important practical question of mass savings that can be achieved by replacing an HCSP with an FCSP, when ballistic performance of both panels is equivalent.

Another common feature of all studies mentioned above, is that they all focused on development of the shields for manned spacecraft. Another type of spacecraft, which prevails in orbit and often also requires MMOD protection, is unmanned spacecraft. For such vehicles, higher risk levels of collision with orbital debris are typically acceptable

[10]. The particle size to design a shield against, as it has been shown in the previous section, depends on the tolerable risk of penetration, area of a spacecraft and mission duration. Having higher tolerable risks and areas that are usually orders of magnitude lower than manned spacecraft (e.g., the shielded area of the U.S. Lab module is 129 m^2 [4], whereas a typical unmanned satellite has a total surface area of only a few square meters), robotic vehicles often only require protection against much smaller debris. No evidence, however, exists that the shielding systems efficient in protecting manned spacecraft against large-size debris will be as efficient in protecting an unmanned vehicle against small-size particles.

In addition to sandwich panels, other structural elements also have been studied for their HVI protection capabilities, including multilayer insulation blankets (MLI), thermal protection systems (ceramic tiles, reinforced carbon-carbon panels, ablators), etc [3].

2.2 HVI Behavior of Pressure Vessels

The gas-filled pressure vessels are recognized as the most critical spacecraft components due to high energies they contain during operation in the orbit. In the case of hypervelocity impact by orbital debris, they reveal high potential for catastrophic failure accompanied by fragmentation and, in turn, an increase of orbital debris population.

There are two general types of pressure vessels used in spacecraft structures: all-metallic (e.g., made of aluminum or titanium alloys) or composite overwrapped, consisting of thin metallic liner overwrapped by composite material. In the latter case, metal liner serves as a gas permeation barrier and may or may not carry substantive pressure loads. The composite overwrap carries pressure and environmental loads [28]. The high specific

strength of continuous fiber composite materials ensures higher weight efficiency of the composite overwrapped pressure vessels (COPVs) compared to standard all-metal containers.

The following literature review encompasses data on both composite and metallic pressure vessels in order to provide as complete as possible description of the physical phenomena revealing in the course of hypervelocity impact.

Numerous experimental programs were conducted by researchers to access hazards, which may be caused by space debris impact, investigate the behavior of pressure vessels under HVI and comprehend the physics involved. Historically, earliest studies in this area were conducted for *unshielded* pressure vessels.

Rucker [29] presented results of HVI tests performed on a number of pressurized vessels. He detected that, under some conditions, pressure vessels subjected to HVI demonstrate high potential for damaging surrounding objects. In his experiments, 1065 ml Kevlar® overwrapped pressure vessel with aluminum liner filled with oxygen at a pressure of 20.7 MPa (about 41% of static burst pressure) was ruptured into 5 pieces as a result of hypervelocity impact at 6.4 km/s by 3.18 mm aluminum projectile. The rupture was also accompanied by oxygen fire. On the other hand, 300 ml aluminum vessel filled with nitrogen at a 10 times lower pressure demonstrated significantly different response to HVI at similar conditions: a single 8.9 mm diameter circular entry hole was observed on the front side of the vessel and 8 full penetrations of up to 2.6 mm diameter with multiple "peppered" tracks of non-penetrating impacts were found on the rear side. The pressure was relieved without rupture.

Christiansen et al. [30] presented a systematic experimental study of HVI conducted mostly on pressurized aluminum soft drink cans to investigate the competitive effects of wall stress and ablation on vessels' response. The cans were 66 mm diameter and 123 mm long with a 50 mm-long 0.12 mm constant wall thickness region and subjected to a normal impact at velocities ~ 6 … 7 km/s by aluminum projectiles. In general, damage pattern reported by Christiansen et al. in most cases was similar to the one observed by *Rucker* on the gas-filled aluminum vessel and described above. Typical damage included single entry hole on the front wall and multiple rear wall perforations. Catastrophic failure might or might not occur, depending on the test conditions. Unpressurized specimens and specimens pressurized up to 0.1 MPa revealed no catastrophic failure, as the critical flaw size depending on vessel's wall stress was not reached. Further increase of pressure up to 0.15 and 0.2 MPa resulted in an increase of the wall stress and caused a rear-wall initiated rupture of the vessels. However, an additional increase of pressure up to 0.3 MPa did not lead to a catastrophic failure, revealing a significant change of the vessels' response. This result was explained by the intensification of the debris cloud ablation inside the vessels, which, in turn, resulted from the increase of gas density with the growth of the pressure.

Schaefer et al. [31, 32] also studied the propagation of HVI fragment clouds in pressure vessels. Their findings confirm that higher pressure inside a vessel results in more significant deceleration and ablation of the debris cloud. At constant pressure, they suggested the decrease of fragment cloud velocity in time as an exponential decay function. Shockwave in the gas generated by and traveling along with debris cloud, revealed as another consequence of gas – debris cloud interaction process. It resulted in a noticeable bulging of the rear wall, increasing with the increase of pressure.

More recently, *Schaefer et al.* [33] conducted HVI experiments on aluminum and titanium pressure vessels to establish loading conditions leading to catastrophic rupture. As a result, they stated the inverse correlation between hoop stresses in the pressure vessels and kinetic energy needed to produce failure. It was presented in the form of an experimental curve fitted through the tests results. Their experiments also revealed another failure mechanism – front wall initiated rupture resulting from the stress concentration around the impact hole. This new type of failure happened at high stresses and medium kinetic energies, whereas the rear wall failure normally required higher kinetic energy and could happen at both relatively low (about 20% of static burst pressure) and high hoop stresses (up to approximately 75% of static burst pressure in their experiments). Hence, the kinetic energy was recognized to be a driver from the front wall failure to the rear wall failure. The rear-wall failure was explained to be governed by two competitive phenomena. First, ablation reduces the damage of the rear wall with the increase of pressure, as it has been discussed above. It has been observed during experiments that the debris cloud was totally ablated if pressure exceeded a few atmospheres. On the other hand, at high pressures strong shock waves propagating in the gas bulged the rear wall that could result in failure. It may also be figured out from their results that impact energy needed to burst a pressure vessel is, at least, two orders of magnitude higher than the minimal perforation energy.

Lambert and Schneider [34] introduced into consideration another physical effect that may influence the rear wall bursting. They supposed that stress waves propagating from the impact hole through the vessel's wall may interfere on the rear side and trigger rear wall failure. To verify this idea they carried out the experiment in which a shield was placed inside the pressure vessel to prevent debris cloud from hitting the rear wall. Experimental

conditions were chosen to obtain the rear wall failure. In fact, the front side burst was obtained in the experiment. This allowed them to conclude that stress waves interference may not be a driving force causing the rear wall burst. Nevertheless, it seems to be obvious that one experiment cannot be sufficient to completely eliminate this effect from consideration.

Telitchev et al. [35] in their analytical study of pressure vessels fracture under HVI suggested that under some conditions front wall bursting may be governed by the combination of internal pressure and additional pressure pulse produced on the front wall by the shock wave generated by debris cloud and reflected from the vessel's rear wall. Estimations given by Telitchev for 150 mm-diameter vessel pressurized at 11.7 bar (1.17 MPa) and subjected to impact by 4.13 mm projectile at 6.8 km/s have shown that the additional shock pressure pulse might have an amplitude of 160 bar (16 MPa), which is almost 14 times higher than the static inflation pressure. Description of the procedure which enables to estimate pressure amplitude generated by the shock wave has been presented by *Telitchev and Eskin* [36]. It should be also noted also that this physical effect, probably, explains the behavior of the pressure vessel in the Lambert and Schneider experiment discussed in the previous paragraph. Front burst in that rear burst-configured specimen could happen as a result of shock wave reflection from the internal shield. The amplitude of pressure pulse should be quite high concerning that placement of the shield reduces wave propagation distance inside the vessel and, thus, impairs its damping.

In addition to the studies discussed above, some researchers reported results of experiments conducted on *shielded* pressure vessels. As it has been discussed in the previous sections,

the shielding consists of a barrier or a system of barriers placed at some distance from protected component.

Schaefer et al. [33] conducted two pairs of experiments that involved aluminum and titanium vessels shielded by, respectively, thin aluminum and titanium bumpers. Despite relatively high inflation pressures and wall stresses in all vessels, only one vessel responded to HVI by catastrophic failure. In all other cases shielding provided adequate protection from bursting by means of fragmentation of a projectile and formation of a large impact hole with subsequent fast pressure relieve.

In their follow-up work, *Schaefer et al.* [37] carried out a number of experiments at 7 km/s to find transition threshold between front wall cratering of shielded pressure vessels and their failure. Projectiles' kinetic energies were close to the ballistic limits of combined bumper and front wall systems. Thus, failure has been defined as a starting of gas leakage. As expected, no catastrophic rupture or "unzipping" has been detected at such impact energies. It has been shown that shielding effectiveness is a strong function of shield stand-off from the vessel's front wall.

Olsen and Nolen [38] systematically studied the effect of HVI (~ 7 km/s) on shielded aluminum vessels under low pressure of about 0.21 – 0.45 MPa (31 - 65 psi). The vessels considered as a scaled representation of habitable modules of the International Space Station. Different types of shielding have been used, including aluminum bumper, a combination of the aluminum bumper with multi-layer insulation (MLI) or bumper, MLI and Kevlar and Nextel fabrics at the same time. Only combination of the bumper (1.27 mm) at 101.6 mm (4 in) standoff and MLI placed directly on the vessel's front wall (~ 2

mm) led to the catastrophic failure at an inflation pressure of ~ 0.28 MPa (40 psi). Again, bursting was prevented by formation of large impact holes in all other experiments.

Telitchev [39], studying conditions at which shielded vessels under HVI switch their behavior from leakage to bursting, pointed out on the effect of fracture delay that precedes initiation of cracking. He suggested that depressurization of a shielded pressure vessel through the impact hole may prevent catastrophic bursting if the fracture delay exceeds some critical limit. Estimations he provided show that this limit has to be of the order of a millisecond. The level of vessel's depressurization during the period of fracture delay determines if bursting occurs after impact and obviously depends on the stored energy density.

Guan et al. [40] presented experimental results on 40 pressure vessels. The impact velocities were limited by $2.0 - 3.9$ km/s. In general, their experiments expand the database of results published in the open literature and confirm the findings of the earlier researchers.

2.3 Hydrocode Simulations

2.3.1 Numerical methods

Smoothed particles hydrodynamics (SPH) and finite element method (FEM) in the Lagrangian formulation are the two numerical techniques that have been generally used for HVI simulations (Fig. 9). As SPH is a relatively new technique, it will be discussed in this section in more details.

FEM typically provides a good balance between simulation accuracy and computational efficiency. However, it requires the utilization of non-physical erosion algorithm in order

to avoid excessive mesh distortions (i.e. degenerate cells) and tangling at high deformations, and depends on the critical geometric strain chosen, which is not known by default and should be calibrated by comparison with experimental data or set based on a user's experience [41].
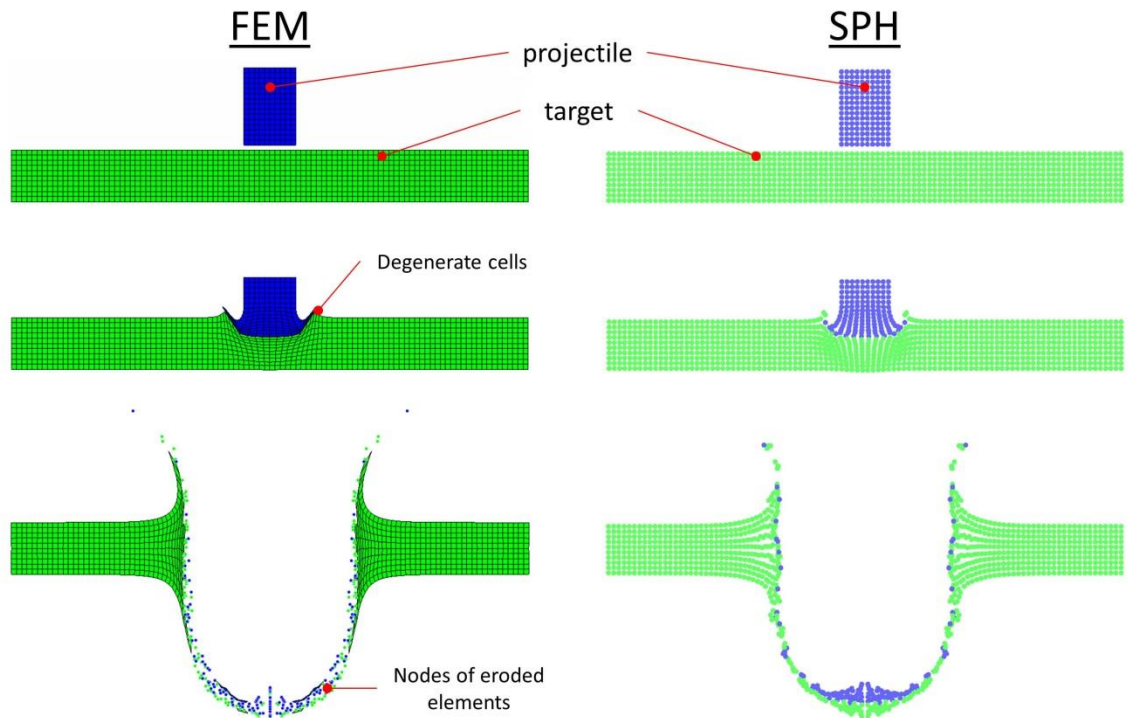
Figure 9 – Simulation of perforation using FEM and SPH

SPH is a mesh-free Lagrangian method for numerical solution of problems formulated in terms of partial differential equations of field variables (such as density, velocity, energy, etc.). The method uses "particles" to discretize continuum. The particles are not simple interacting mass points. Instead, they are used for interpolation in order to estimate values of the field variables and their derivatives in discrete points of continuum.
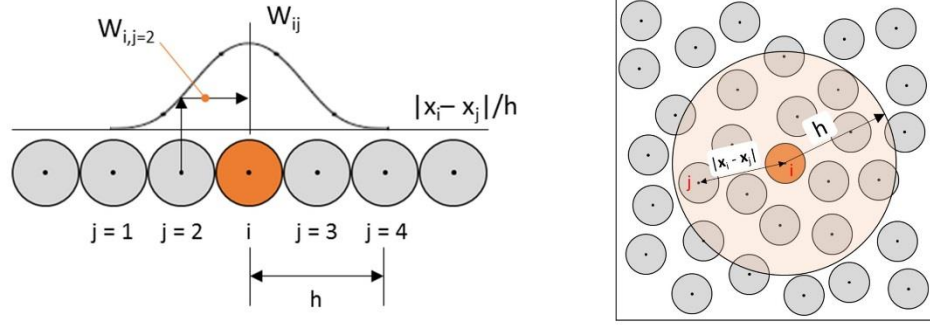
Figure 10 – Approximation of field variables at a point using SPH method (left – 1D; right – 2D)

The interpolation uses a weighting function (often referred to as "kernel") to approximate the field variables and their derivatives at any point of domain. For example, density at a point *i* with coordinates x_i can be estimated from the neighbouring particles as

$$\rho_i = \sum_j m_j \cdot W_{ij}\left(\left|x_i - x_j\right|, h\right),$$

where m_j is the mass of j-th particle, W_{ij} is a weighting kernel function (typically a cubic B-spline) and *h* is so called smoothing length, which determines a support domain for approximation, as it is exemplified in Fig. 10 for a one-dimensional and a two-dimensional case.

Another example can be given for the strain rate tensor $\dot{\varepsilon}^{\alpha\beta} = \frac{1}{2}\left(\frac{\partial v^\alpha}{\partial x^\beta} - \frac{\partial v^\beta}{\partial x^\alpha}\right)$, for which the SPH approximation can be written as follows [112]:

$$\dot{\varepsilon}^{\alpha\beta} = \frac{1}{2}\sum_j \frac{m_j}{\rho_j}\left(\left(v_j^\alpha - v_i^\alpha\right)\frac{\partial W_{ij}}{\partial x_i^\beta} + \left(v_j^\beta - v_i^\beta\right)\frac{\partial W_{ij}}{\partial x_i^\alpha}\right).$$

The conservation equations of continuum mechanics and their SPH approximations are represented in Fig. 11. The derivation of these approximations can be found elsewhere, e.g. [113].

	Continuum mechanics	SPH approximation
Conservation of mass	$\dfrac{d\rho}{dt} = -\rho \cdot \dfrac{\partial v^\beta}{\partial x^\beta}$	$\dfrac{d\rho_i}{dt} = -\rho_i \sum_j \dfrac{m_j}{\rho_i}\left(v_i^\beta - v_j^\beta\right)\cdot W_{ij,\beta}$
Conservation of momentum	$\dfrac{dv^\alpha}{dt} = -\dfrac{1}{\rho} \cdot \dfrac{\partial \sigma^{\alpha\beta}}{\partial x^\beta}$	$\dfrac{dv_i^\varepsilon}{dt} = -\sum_j m_j\left(\dfrac{\sigma_i^{\alpha\beta}}{\rho_i^2} - \dfrac{\sigma_i^{\alpha\beta}}{\rho_j^2}\right)\cdot W_{ij,\beta}$
Conservation of energy	$\dfrac{de}{dt} = -\dfrac{\sigma^{\alpha\beta}}{\rho} \cdot \dfrac{\partial v^\alpha}{\partial x^\beta}$	$\dfrac{de_i}{dt} = -\dfrac{\sigma_i^{\alpha\beta}}{\rho_i^2} \sum_j m_j\left(v_i^\alpha - v_j^\alpha\right)\cdot W_{ij,\beta}$

Figure 11 – Conservation equations

In these equations, $\sigma^{\alpha\beta}$ is the full stress tensor, which can be represented in terms of hydrostatic pressure p and deviatoric stress tensor $S^{\alpha\beta}$, as $\sigma^{\alpha\beta} = p\delta^{\alpha\beta} + S^{\alpha\beta}$. The hydrostatic pressure can be determined using an equation of state (EOS), such as, for example, Mie-Gruneisen EOS (see Section 2.3.2.1).

The constitutive equations, determining components of the deviatoric stress tensor, can be formulated in different ways, depending on materials being in consideration and assumptions of physical behavior for a particular problem. For example, in case of small displacements, it can be written [113]:

$$\dot{S}^{\alpha\beta} = G\left(\dot{\varepsilon}^{\alpha\beta} - \frac{1}{3}\delta^{\alpha\beta}\varepsilon^{\gamma\gamma}\right),$$

where G is the shear modulus. For finite displacements, an expression for the frame independent stress rate can also be stated and will include the rotation rate tensor, as can be found elsewhere (e.g. [112, 113]).

The plastic flow regime may be determined by Von-Mises criterion. In this case, when the second invariant (J) of the deviatoric stress tensor exceeds the flow stress (Y), the individual deviators will be brought back to the flow surface through the following modification:

$$S^{\alpha\beta} = S^{\alpha\beta} \sqrt{\frac{Y^2/3}{J^2}}.$$

The yield stress can be either constant (e.g., in the case elasto-plastic material model), or be a function of different parameters. For example, the Johnson-Cook strength model used in this study for modeling of all metallic materials, takes into account effects of strain rate, strain hardening and thermal softening on the flow stress (see Section 2.3.2.1).

In addition to the strength model, a failure model can also be incorporated into the computation. Such model determines the conditions when the material "comes apart". A number of failure models, including ones for metals, ceramics and composites, will be discussed in Section 2.3.2.

Finally, the overall computational cycle of SPH solver (at each timestep) is represented in Fig. 12. Here, for explicit time integration, the leapfrog technique is typically used.

SPH is often advantageous over FEM in modeling physical processes involving extreme deformations, high strain rates, perforation and fragmentation due to the absence of the mesh tangling problems (no mesh = no tangling) and the lack of need to use the artificial erosion mechanism. The SPH-particles "naturally" form discontinuities in the continuum such as cracking, penetration, and fragmentation as particles are forced to separate during the penetration event. The main disadvantage of SPH is tensile instability, i.e. a possibility

of numerical fracture in the regions of high tensile stresses due to loss of interaction between initially neighboring particles [43, 44].
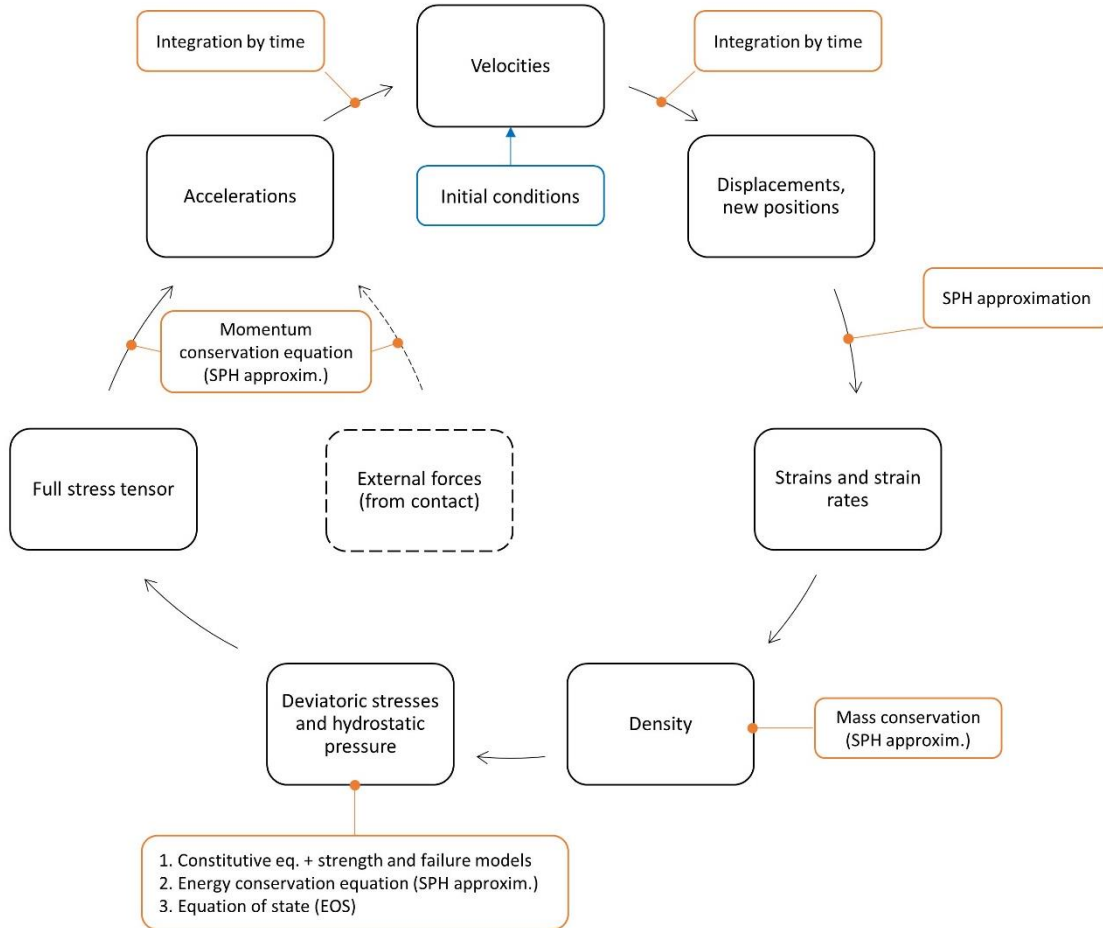
Figure 12 – Computational cycle of SPH solver

Applications of these numerical techniques to HVI modeling are as follows. *Pezzica et al.* [45] modeled hypervelocity impact of an aluminum sphere on a 3-walled aluminum structure with all components represented by Lagrangian finite elements. Debris cloud in the simulation was formed by the nodes of eroded elements. For particular values of critical geometric strain, the results were found to be in a good agreement with experimental data. SPH was successfully used in the simulations of hypervelocity impacts on different targets,

including thin plates [46], stuffed Whipple shields [47], brittle targets [48] and laminated composite materials [49].

Palmeri et al. [50] explored the applicability of numerical modeling (AUTODYN-2D) to simulate the damage of impacted but not perforated front wall of shielded pressure vessels. Bumper and projectile were represented by SPH particles; the vessel shell was represented by Lagrangian FE mesh. After appropriate mesh refinement, a 2% correlation between experimental and simulation results in terms of impact-induced front wall crater depth has been obtained.

Maveyraud et al. [15] and also *Salome et al.* [51] simulated behavior of composite pressure vessels (titanium liner wrapped by carbon fibers) subjected to HVI at $5-20$ km/s. Potential damage scenarios have been explored for Xenon and Helium-filled vessels. Model sensitivity analysis to composite properties has been conducted to allow for the lack of experimental data on the dynamic material characteristics. In simulations, the real composite laminate was substituted by a homogeneous orthotropic material with analogous effective properties.

2.3.2 Material modeling

Constitutive material models for hypervelocity impact simulations typically consist of three general parts: equation of state (EOS), strength model and failure/damage model. The equation of state represents relationship between the hydrostatic pressure, the local density and the local specific energy; strength model is required to relate deviatoric stresses and strains; and failure model is used to simulate a continuous degradation of material

properties (e.g., due to microcracking), which ultimately results in its inability to withstand tensile stresses exceeding its local tensile strength [52, 53].

Numerous material models have been developed in the recent decades in order to represent the macroscopic behavior of different structural materials under dynamic loading, including metals and alloys, brittle (e.g., concrete and ceramics) and granular materials, porous materials, fibrous composites, etc. The following subsections will describe only the material models relevant to the hydrocode simulations conducted in this study.

2.3.2.1 Modeling of dynamic behavior of metallic materials

Equation of state. Mie-Gruneisen equation of state [54] is one of the most common choices for metallic materials due to its simplicity and relatively good correlation with experimental data for this class of materials [53]. It establishes relationship between pressure, density and specific energy of a solid material subjected to shock loading in the following form:

$$p = p_H + \Gamma \rho \cdot (e - e_H),$$ (1)

where p, e, ρ are pressure, specific energy and density of the material correspondingly; Γ is Gruneisen gamma (constant); p_H and e_H are the reference pressure and specific energy determined from material's shock Hugoniot. In turn, to define the shock Hugoniot, linear relationship between shock velocity (U_s) and particle velocity (U_p) was used:

$$U_s = C_0 + S \cdot U_p,$$ (2)

34

where C_0 is the bulk acoustic sound speed and S is the slope of the $U_s - U_p$ relationship. Given C_0 and S provided as material properties and using conservation of mass, momentum and energy equations (e.g. in the form of the Rankine-Hugoniot conservation equations [52]), p_H and e_H in equation (1) can be represented as functions of material density:

$$p_H = \frac{\rho_0 C_0^2 \mu (1 + \mu)}{[1 - (S-1)\mu]^2},$$ (3)

where $\mu = (\rho / \rho_0) - 1$, ρ is current density, ρ_0 is the initial density, and

$$e_H = \frac{1}{2} \left(\frac{p_H}{\rho_0} \right) \left(\frac{\mu}{1 + \mu} \right),$$ (4)

Strength model. Although equation of state effectively describes the behavior of materials subjected to shock loading in the course of hypervelocity impact, strength effects may also be important or even dominating in so-called "far-field" and "late-time" regimes. Strength behavior of all metallic materials considered in this study has been represented in terms of Johnson-Cook model [55], which is a typical choice for metals subjected to high strains, high strain rates and high temperatures. In this model, the yield stress of material is represented as

$$Y = \left[A + B \cdot \varepsilon_p^n \right] \cdot \left[1 + C \cdot \ln \dot{\varepsilon}_p^* \right] \cdot \left[1 - T_H^m \right],$$ (5)

where ε_p, $\dot{\varepsilon}_p^*$ and T_H are effective plastic strain, normalized effective plastic strain rate and homologous temperature $\left(T_H = \frac{T - T_{room}}{T_{melt} - T_{room}} \right)$, correspondingly; A, B, C, n and m are material constants, namely initial yield strength, hardening constant, strain rate

35

constant, hardening exponent and thermal softening exponent. In Johnson-Cook plasticity model, calculation of plastic strain is based on the von Mises yield surface and the associated flow rule. Expression in the first brackets of the equation (5) gives the yield stress as a function of plastic strain; the second set of brackets represents the effects of strain rate on stress; and the third set of brackets determines thermal softening of a material. It should be noted that as the temperature reaches melting temperature of the material (T_{melt}), its yield strength drops to zero. As at high strain rates the deformation process is mainly adiabatic, the temperature in equation (5) is calculated by means of converting 90% of plastic work into heat.

Failure model. In this study Johnson-Cook failure model [55] has been used for all metallic materials. This model defines dynamic fracture strain as a function of pressure, strain rate and temperature in the following manner:

$$\varepsilon^f = \left[D_1 + D_2 \cdot \exp(D_3 \cdot \sigma^*)\right] \cdot \left[1 + D_4 \cdot \ln\left|\dot{\varepsilon}_p^*\right|\right] \cdot \left[1 + D_5 \cdot T_H\right], \qquad (6)$$

where σ^* and $\dot{\varepsilon}_p^*$ are dimensionless pressure-stress ratio and dimensionless strain rate, correspondingly; D_i are damage parameters of the material ($D_1 - D_3$ - failure strain parameters, D_4 and D_5 are the strain rate and temperature parameters, correspondingly). The dimensionless pressure-stress ratio is defined as $\sigma^* = \sigma_m / \overline{\sigma}$, where σ_m is the average of the three normal stresses and $\overline{\sigma}$ is the von Mises equivalent stress. Damage is then defined as the ratio of the incremental effective plastic strain in an integration cycle and equivalent strain-to-fracture under the current conditions of strain rate, temperature,

pressure and equivalent stress: $D = \sum \frac{\Delta \varepsilon}{\varepsilon^f}$. Fracture of material occurs instantaneously when $D = 1.0$.

2.3.2.2 Modeling of dynamic behavior of ceramic materials

The ceramics are known for their brittle nature and the influence of hydrostatic pressure on the strength of the material. Correspondingly, their response to dynamic loading is quite different as compared to metals and its macro-scale description requires different material models.

Equation of state. The general form of Mie-Gruneisen equation of state – Polynomial EOS – can be used to represent the behavior of ceramic materials, such as silicon carbide. This EOS defines the pressure in the following form:

$$p = A_1\mu + A_2\mu^2 + A_3\mu^3 + (B_0 + B_1\mu)p_0 e, \tag{7}$$

for compression (i.e. when $\mu. > 0$), and

$$p = T_1\mu + T_2\mu^2 + A_3\mu^3 + B_0 p_0 e, \tag{8}$$

for tension (i.e. when $\mu. < 0$). Here A_i, B_i and T_i are material constants. The Gruneisen gamma is defined by this EOS as $\Gamma = \frac{B_0 + B_1\mu}{1+\mu}$.

Strength and Failure model. A typical choice of a strength and failure model for ceramic materials is the Johnson-Holmquist model. Two forms of this model – continuous (JH-2) and segmented (JH-1) – are presented in the literature. Recent studies indicate that segmented form may be more accurate [56]. In this model, material strength is

approximated by linear segments and the damage is always applied instantaneously. The behavior of the intact (in a sense that it has not yet experienced damage) and the damaged material at a reference strain rate $\dot{\varepsilon}^{*} = \dot{\varepsilon}/\dot{\varepsilon}_0$ (for $\dot{\varepsilon}_0 = 1.0\ s^{-1}$) is described by two different curves (Fig. 13). The curves are determined by such parameters as "strengths" (von Mises equivalent stresses) of the intact material S1 and S2 at compressive pressures P1 and P2, corresponding to the slope changes on the experimental strength-pressure relationship (see e.g. [56]); maximum tensile hydrostatic pressure (T); the maximum failure strength of damaged material (Sf$_{max}$); and the slope of the strength curve of the failed material (alpha).
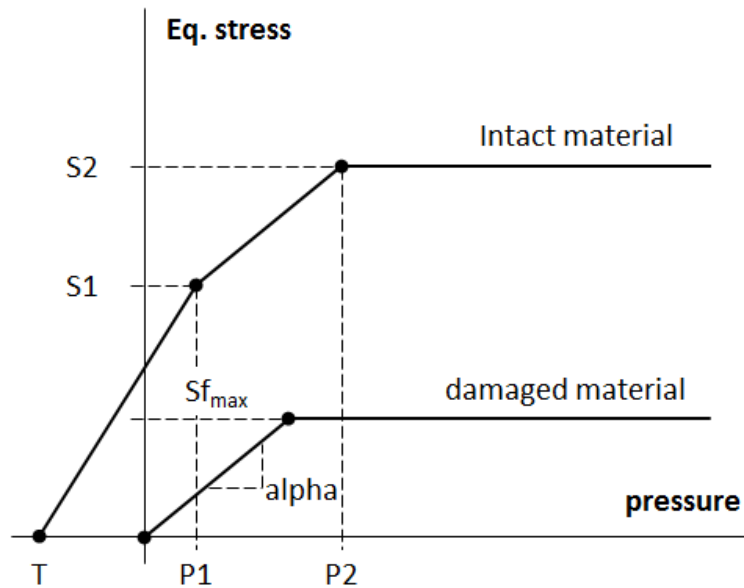
Figure 13 – Strength-pressure dependency in JH-1 model

Failure strain

εf_{max}

$\phi = \varepsilon f_{max} / (P_3 + T)$

pressure

T   P3
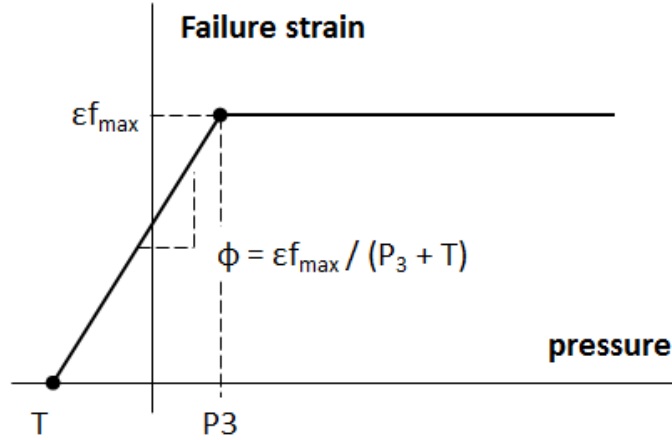
Figure 14 – Failure strain-pressure dependency in JH-1 model

For a strain rate different than the reference one, strength can be determined as

$$\sigma = \sigma_0 \left(1.0 + C \cdot \ln \dot{\varepsilon} *\right), \tag{9}$$

where σ_0 is available strength at the reference strain rate; and C is the strain rate constant.

The accumulated damage for failure is $D = \sum \dfrac{\Delta \varepsilon_p}{\varepsilon_p^{\,f}}$, where $\varepsilon_p^{\,f}$ is the equivalent plastic

strain at failure, such as $\varepsilon_p^{\,f} = \varphi(P + T)$ (see Fig. 14).

2.3.2.3 Modeling of dynamic behavior of ceramic fabric Nextel

Up-to-date and most comprehensive material models representing the behavior of Nextel under HVI loading has been developed and described in Ref. [57] (AMMHIS project). These models reflect such experimentally observed phenomena as compaction of Nextel, associated with subsequent fragmenting into macroscopically homogeneous substance consisting of fractured filaments.

For Nextel, models of two types are described in Ref. [57]: an orthotropic model with compaction and porous isotropic model. It has been shown that simulations with the simpler porous isotropic Nextel model produce very similar results as compared with the complex orthotropic model, which makes the former model a preferred choice for the numerical simulations. In this model, Nextel is simply represented using the porous EOS defined via density – pressure data points (i.e. tabulated data).

2.3.2.4 Modeling of dynamic behavior of Kevlar-epoxy composite

Kevlar/Epoxy model was specifically designed for HVI simulations in Ref. [57] (AMMHIS project). The multidirectional composite laminate in this model is represented as a homogeneous orthotropic material. The incremental stress-incremental strain relations for an orthotropic material as follows:

$$
\begin{bmatrix} \Delta\sigma_{11} \\ \Delta\sigma_{22} \\ \Delta\sigma_{33} \\ \Delta\sigma_{23} \\ \Delta\sigma_{31} \\ \Delta\sigma_{12} \end{bmatrix} = \begin{bmatrix} C_{11} & C_{12} & C_{13} & 0 & 0 & 0 \\ C_{21} & C_{22} & C_{23} & 0 & 0 & 0 \\ C_{31} & C_{32} & C_{33} & 0 & 0 & 0 \\ 0 & 0 & 0 & C_{44} & 0 & 0 \\ 0 & 0 & 0 & 0 & C_{55} & 0 \\ 0 & 0 & 0 & 0 & 0 & C_{66} \end{bmatrix} \cdot \begin{bmatrix} \Delta\varepsilon_{11} \\ \Delta\varepsilon_{22} \\ \Delta\varepsilon_{33} \\ \Delta\varepsilon_{23} \\ \Delta\varepsilon_{31} \\ \Delta\varepsilon_{12} \end{bmatrix} \tag{10}
$$

As, in general, the response of composites to shock loading is nonlinear, incremental stress-incremental strain relationships described by equation (10) require modification. The aim of such modification is to separate volumetric response of the composite from its ability to carry shear stresses and to describe the former in terms of the nonlinear equation of state (EOS). According to AMMHIS model, strain increments ($\Delta\varepsilon_{ij}$) in equations (10) can be split into their average ($\Delta\varepsilon_{ave}$) and deviatoric ($\Delta\varepsilon_{ij}^{d}$) components in the following manner:

$$\Delta\varepsilon_{ij} = \Delta\varepsilon_{ij}^{d} + \Delta\varepsilon_{ave} \tag{11}$$

Defining the average strain increment as a third of the trace of the strain tensor

$$\Delta\varepsilon_{ave} = \frac{1}{3}\left(\Delta\varepsilon_{11} + \Delta\varepsilon_{22} + \Delta\varepsilon_{33}\right), \tag{12}$$

and approximating, for small strain increments, the volumetric strain increment as

$$\Delta\varepsilon_{vol} \approx \Delta\varepsilon_{11} + \Delta\varepsilon_{22} + \Delta\varepsilon_{33}, \tag{13}$$

the total strain increments can be expressed in terms of the volumetric and deviatoric strain increments, which results in the following orthotropic constitutive relation:

$$\begin{bmatrix} \Delta\sigma_{11} \\ \Delta\sigma_{22} \\ \Delta\sigma_{33} \\ \Delta\sigma_{23} \\ \Delta\sigma_{31} \\ \Delta\sigma_{12} \end{bmatrix} = \begin{bmatrix} C_{11} & C_{12} & C_{13} & 0 & 0 & 0 \\ C_{21} & C_{22} & C_{23} & 0 & 0 & 0 \\ C_{31} & C_{32} & C_{33} & 0 & 0 & 0 \\ 0 & 0 & 0 & C_{44} & 0 & 0 \\ 0 & 0 & 0 & 0 & C_{55} & 0 \\ 0 & 0 & 0 & 0 & 0 & C_{66} \end{bmatrix} \cdot \begin{bmatrix} \Delta\varepsilon_{11}^{d} + \dfrac{1}{3}\Delta\varepsilon_{vol} \\ \Delta\varepsilon_{22}^{d} + \dfrac{1}{3}\Delta\varepsilon_{vol} \\ \Delta\varepsilon_{33}^{d} + \dfrac{1}{3}\Delta\varepsilon_{vol} \\ \Delta\varepsilon_{23} \\ \Delta\varepsilon_{31} \\ \Delta\varepsilon_{12} \end{bmatrix}, \tag{14}$$

Defining pressure increment as one-third of the trace of the stress increment tensor

$$\Delta p = -\frac{1}{3}\left(\Delta\sigma_{11} + \Delta\sigma_{22} + \Delta\sigma_{33}\right), \tag{15}$$

and substituting $\Delta\sigma_{ii}$ in (15) from (14), yields:

41

$$\Delta p = -\frac{1}{9}\left[(C_{11} + C_{22} + C_{33} + 2(C_{12} + C_{23} + C_{31}))\right]\Delta\varepsilon_{vol} -$$
$$-\frac{1}{3}\left[C_{11} + C_{21} + C_{31}\right]\Delta\varepsilon_{11}^d - \frac{1}{3}\left[C_{12} + C_{22} + C_{32}\right]\Delta\varepsilon_{22}^d - \quad , \tag{16}$$
$$-\frac{1}{3}\left[C_{13} + C_{23} + C_{33}\right]\Delta\varepsilon_{33}^d$$

Here multiplier of volumetric strain increment can be recognized as "effective" bulk modulus (K') of orthotropic material (following the analogy with isotropic bulk modulus):

$$K' = -\frac{1}{9}\left[(C_{11} + C_{22} + C_{33} + 2(C_{12} + C_{23} + C_{31}))\right] \tag{17}$$

Finally, equation (16) can be modified to take into account nonlinear dependence of pressure on volumetric strain:

$$\Delta p = \Delta p(\Delta\varepsilon_{vol}) -$$
$$-\frac{1}{3}\left[C_{11} + C_{21} + C_{31}\right]\Delta\varepsilon_{11}^d - \frac{1}{3}\left[C_{12} + C_{22} + C_{32}\right]\Delta\varepsilon_{22}^d -, \tag{18}$$
$$-\frac{1}{3}\left[C_{13} + C_{23} + C_{33}\right]\Delta\varepsilon_{33}^d$$

where the pressure contribution from volumetric strain $p(\varepsilon_{vol})$ can be expressed in the polynomial form:

$$p = K'\varepsilon_{vol} + A_2(\varepsilon_{vol})^2 + A_3(\varepsilon_{vol})^3 + (B_0 + B_1\varepsilon_{vol})\rho_0 e, \tag{19}$$

where A_2, A_3, B_0, B_1 are material constants, ρ_0 is the initial density, e is internal energy per unit mass.

Failure of Kevlar/Epoxy in the AMMHIS model is represented in terms of Material stress/strain model with the orthotropic post-failure option. Here failure is initiated if any of the principal material strains exceed their respective failure levels. Orthotropic post-failure implies that failure of the material in one direction may affect its strength in other directions. Such experimentally observed feature as decomposition of Kevlar subjected to high uniaxial strain loading is implemented in the model using the decomposition temperature parameter (it was experimentally found in [57] that Kevlar undergoes a phase change of thermal decomposition at velocities above 1 km/s).

2.3.2.5 Modeling of dynamic behavior of carbon fiber reinforced plastics

A material model for multidirectional carbon-fiber reinforced plastics (CFRP) has been presented by *Wicklein et al.* [75]. Similar to Kevlar/epoxy laminates, the CFRP laminate in this model is considered as a homogeneous orthotropic material. Its EOS, therefore, and can be expressed by means of equations (18) – (19).

Unlike Kevlar/epoxy in the AMMHIS model, the model for carbon-fiber composite takes into account the *non-linear hardening* of the material (more details can be found in [75]), which can be attributed to the cumulative effect of matrix plasticity, fiber reorientation and matrix/fiber damage under impact loading. Hardening is represented phenomenologically by means of the generalized yield function proposed by *Chen* [58] for anisotropic materials:

$$
\begin{aligned}
f\left(\sigma_{ij}\right) &= a_{11}\sigma_{11}^2 + a_{22}\sigma_{22}^2 + a_{33}\sigma_{33}^2 + 2a_{12}\sigma_{11}\sigma_{22} + 2a_{23}\sigma_{22}\sigma_{33} + 2a_{13}\sigma_{11}\sigma_{33} + \\
&+ 2a_{44}\sigma_{23}^2 + 2a_{55}\sigma_{31}^2 + 2a_{66}\sigma_{12}^2 = k
\end{aligned}
\tag{20}
$$

Here a_{ij} are the plasticity parameters and k is the hardening parameter depending on plastic

deformation and defined as $k = \dfrac{2}{3}\bar{\sigma}^2$, where $\bar{\sigma}$ is the effective stress.

Following [58] and [59], relationship between plastic strain increments $d\varepsilon_{ij}^p$ and stress

increments in this plasticity model is defined in terms of associated flow rule, and can be

written out explicitly as

$$
\begin{bmatrix} d\varepsilon_{11}^p \\ d\varepsilon_{22}^p \\ d\varepsilon_{33}^p \\ d\varepsilon_{23}^p \\ d\varepsilon_{31}^p \\ d\varepsilon_{12}^p \end{bmatrix} = \begin{bmatrix} 2a_{11}\sigma_{11} + 2a_{12}\sigma_{22} + 2a_{13}\sigma_{33} \\ 2a_{12}\sigma_{11} + 2a_{22}\sigma_{22} + 2a_{23}\sigma_{33} \\ 2a_{13}\sigma_{11} + 2a_{23}\sigma_{22} + 2a_{33}\sigma_{33} \\ 4a_{44}\sigma_{23} \\ 4a_{55}\sigma_{31} \\ 4a_{66}\sigma_{12} \end{bmatrix} \cdot d\lambda
\tag{21}
$$

where $d\lambda$ is the proportionality factor, which can be determined from a simple tensile test

stress-strain curve. Effective plastic strain increment $d\bar{\varepsilon}^p$ (scalar parameter) can be

introduced using concept of plastic work:

$$
dW^p = \sigma_{ij} \cdot d\varepsilon_{ij}^p = \bar{\sigma} \cdot d\bar{\varepsilon}^p ,
\tag{22}
$$

Using (20), (21) and (22) it can be shown that at any timestep effective plastic strain can

be found from

$$
\left(d\bar{\varepsilon}^p\right)^2 = \frac{8}{3} f(\sigma_{ij}) \cdot (d\lambda)^2
\tag{23}
$$

If stresses at any timestep are found to lie outside the yield surface defined by equation

(20), the backward-Euler algorithm gets activated to return the stress state back to the yield

surface (details of its implementation can be found in [60]). Once the yield function is satisfied, the plastic portion of the strain increment can be determined from equation (23).

Unlike Kevlar/epoxy in the AMMHIS model, the *nonlinear softening* (i.e. damage) of carbon-fiber composite is represented in terms of the modified Hashin failure criterion [49] and the orthotropic damage model.

The failure initiation criteria are represented for each failure plane (*ii*) in the following form:

$$e^2_{ii} = \left(\frac{\sigma_{ii}}{\sigma_{ii,fail}} \right)^2 + \left(\frac{\sigma_{ij}}{\sigma_{ij,fail}} \right)^2 + \left(\frac{\sigma_{ik}}{\sigma_{ik,fail}} \right)^2 \geq 1 \tag{24}$$

If in any of the planes the criterion is satisfied at equality, the damage model gets activated. It assumes the linear softening of the material, so that its behavior schematically can be represented as it is shown in Fig. 15. Here the area A under the softening portion of the stress-strain curve is related to the fracture energy G_f, as $A = G_f / L$, where L is a characteristic cell dimension in the direction of failure and is included to reduce the mesh dependency of the solution.
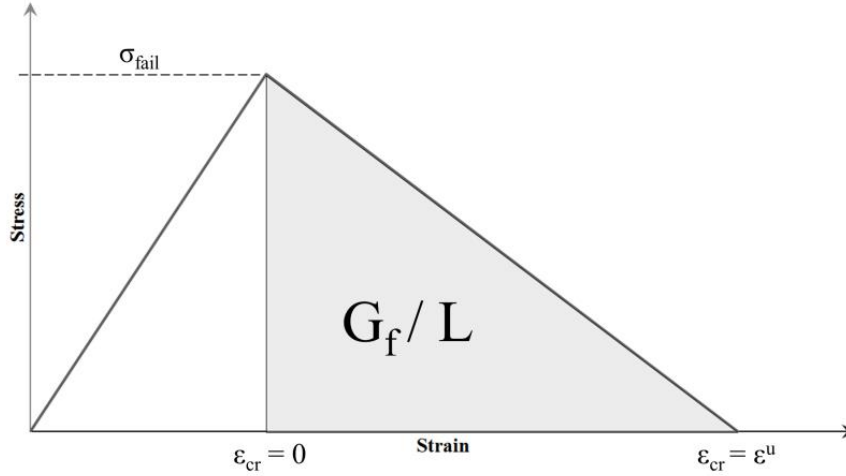
Figure 15 – Crack softening

The ultimate strain in this case can be calculated as

$$\varepsilon^u = \frac{2G_f}{\sigma_{fail}L} \tag{25}$$

and gradient of linear softening can be found as

$$h = \frac{\sigma_{fail}L}{2G_f} \tag{26}$$

If at any timestep after failure initiation the state of stress is found to lie outside of failure surface defined by criterion (24), a backward-Euler algorithm is used to return the stress back to the surface. In this part, the procedure is analogous to the handling of material plastic behavior. The resulting inelastic increment of strain is then accumulated as crack strain ε_{cr}. Softening in this case may be expressed in terms of damage parameter D:

$$D = \frac{\varepsilon_{cr} \cdot h}{\sigma_{fail}} \tag{27}$$

Just before the failure initiation, when $\varepsilon_{cr} = 0$, the damage parameter $D = 0$; when $\varepsilon_{cr} = \varepsilon^u$, the damage parameter takes the value of unity $(D = 1)$. Here crack strain and, correspondingly, damage are tensors with each component of the crack strain tensor associated with corresponding damage variable. Maximum tensile stress at any time after failure initiation can be calculated as

$$\sigma_{max} = \sigma_{fail}(1 - D) \tag{28}$$

Failure surface for the plane ii in the course of failure progression is updated according to the following criterion:

$$e_{ii}^2 = \left(\frac{\sigma_{ii}}{\sigma_{ii,fali}(1 - D_{ii})}\right)^2 + \left(\frac{\sigma_{ij}}{\sigma_{ij,fail}(1 - D_{ij})}\right)^2 + \left(\frac{\sigma_{ik}}{\sigma_{ik,fail}(1 - D_{ik})}\right)^2 \geq 1 \tag{29}$$

The damage variable D_{ii} at any calculation time-step n+1 can be defined as

$$D_{ii}^{n+1} = D_{ii}^n + \frac{\varepsilon_{ii}^{cr} \cdot h_{ii}}{\sigma_{ii,fail}} + C \cdot \frac{\varepsilon_{ij}^{cr} \cdot h_{ij}}{\sigma_{ij,fail}} + C \cdot \frac{\varepsilon_{ik}^{cr} \cdot h_{ik}}{\sigma_{ik,fail}} \tag{30}$$

Analogous expressions can be written for other failure planes. Here C is the damage coupling coefficient, which represents the possibility that damage due to tensile loading may reduce material capability to resist shearing, and vice-versa.

2.4 Summary

1. A number of orbital debris shielding concepts is presented in the literature and new concepts are continually being sought. Weight efficiency of the existing shields has

been mainly studied relative to the application for protection of different modules of International Space Station or other manned spacecraft. This implies that that the shields were designed to protect large spacecraft against relatively large-size projectiles (e.g. ESA stuffed Whipple shield was designed against a hypervelocity projectile of 14.5 mm in diameter [20]). There is however not enough data to make definitive conclusions about the efficiency of the same shielding concepts for protecting unmanned spacecraft. Investigation of a novel shielding concept and analysis of the weight efficiency of existing ones for the case of the small-size (1 mm) hypervelocity projectile are the subjects of *chapter 3*.

2. In the case of the small-size projectiles, it may be beneficial to adapt already existing spacecraft structural elements (e.g. sandwich panels) for HVI shielding. The design of such shields must take into account existence of design constraints other than ballistic performance (e.g., minimal bending stiffness for sandwich panels). The shields, therefore, must be compared in two separate categories, namely *Single-purpose MMOD shields* and *Multi-purpose structural panels*. The corresponding approach is employed in the following section.

3. Smoothed particles hydrodynamics and finite element method in the Lagrangian formulation are the main techniques used for the hypervelocity impact simulations. Both methods, however, have some limitations with regard to this class of problems (due to the tensile instability of SPH and problems with modeling of fragmentation using FEM). It would be beneficial therefore to use their combination in each numerical analysis in order to compensate the disadvantages while efficiently exploiting their

capabilities. The corresponding approach is proposed and employed in the subsequent chapters.

4. As it has been shown in this chapter, macroscopic material models for different structural materials, including metals, ceramics, ceramic fabrics and polymer composites, are readily available for hydrocode simulations. However, it should be noted that macroscopic modeling *might not be suitable* for the composite materials fabricated by filament winding (such as those used in COPVs). This problem will be addressed experimentally and numerically in *chapter 4*.

5. At least 5 types of interactions have to be considered when analyzing behavior of COPVs under HVI, including:

- interaction of orbital debris with an external shield;

- interaction of the secondary debris with the pressure wall;

- interaction of the tertiary debris (generated upon perforation of the vessel) with the gas or liquid within the vessel;

- propagation and interaction of the shock wave generated in the gas or liquid with the perforated pressure wall;

- interaction of tertiary debris cloud with the rear side of the vessel.

Simultaneous representation of all of these interactions within a single numerical model (i.e. full "coupling") may be inefficient in terms of computational expensiveness and complexity. A multistep modeling procedure is proposed in chapter 4, which allows to "decouple" modeling of some of these physical processes from the others and, through this, reduce the complexity of the problem.

3. DESIGN AND EVALUATION OF EXTERNAL SHIELDING SYSTEMS

3.1 Introduction

Orbital debris impacts represent a serious threat to any space mission. Protection from collisions with non-trackable orbital debris is typically implemented in terms of passive shielding which has the main goal of fragmenting and decelerating an impacting particle.

Non-trackable orbital debris in Earth Orbit is represented by particles of 10 mm in diameter and below. Due to the higher risk level acceptable for unmanned spacecraft (in comparison with the manned missions' safety requirements) and their relatively low area, unmanned missions do not require heavy-weight MMOD protection.

Consequently, the study presented in this chapter aims to quantify and compare the weight efficiency of a novel shield, as well as "conventional" MMOD shields—i.e., those that were previously studied for manned spacecraft—when used to protect an unmanned vehicle against small debris. All shields in this study were designed according to the requirements of the Canadian Space Agency to provide protection against 1 mm orbital debris at an impact velocity of 7 km/s [13]. Impactors were represented by aluminum spheres, which according to NASA's engineering model (ORDEM) correspond to the medium-density class of orbital debris that prevails in the overall orbital debris population [2].

As a result of the different sets of constraints used in their design (as described in the next section), shielding systems were compared within two separate categories:

I. *Single-purpose MMOD shields*, including such design concepts as

- Whipple shield (WS),

- Stuffed Whipple shield (SWS), and

- Whipple shield with ceramo-metallic bumper (CMWS, a novel concept);

II. *Multi-purpose structural panels*, including

- Honeycomb-core sandwich panels (HCSP), and

- Foam-core sandwich panels (FCSP).

Set of parameters providing the minimal weight for each of the design concepts is determined via numerical simulations. Their weight efficiencies are compared in terms of areal densities. The novel concept of the shield with the ceramo-metallic bumper is studied by means of both experimental and numerical analyses.

3.2 Numerical Modeling

3.2.1 Overall approach

The modeling approach employed in this study is based on simultaneous utilization of both SPH and FEM in each numerical simulation. The SPH method was used to represent the behavior of parts exhibiting fragmentation, namely, bumpers, front facesheets, aluminum foam, and stuffing. At the same time, rear walls experience significantly lower strain rates and no fragmentation. Here, regions of high tensile stresses may be created either immediately after impact by reflection of the initial compression wave from the free surface or in the late-time regime by the momentum of the debris cloud distributed over the rear wall. In the former case, the numerical fracture may produce unphysical spallation of material from the rear surface; in the latter case, it may result in "pressing-out" of a large

fragment from the rear wall. In both cases, the preliminary numerical fracture may cause underprediction of the ballistic performance of a shielding system. It was, therefore, beneficial to use finite elements for discretization of rear walls/rear facesheets, instead of SPH particles. FEM was also used to represent the honeycomb core design in simulations. The reason for this choice is that, in the case of normal collisions, honeycomb walls are parallel to the direction of impact, and no significant fragmentation of the honeycomb cells is expected. All simulations were preformed using ANSYS Autodyn v15.0.7.

3.2.2 Material modeling

Table 3 provides the nomenclature of material models employed in numerical analyses to represent the behavior of the aluminum parts (projectile, front and rear walls/facesheets and foam), Nextel fabric, Kevlar/Epoxy and silicon carbide (used in the design of the novel shield). The description of the models was provided in the previous chapter. All corresponding material properties are based on experimental data from the literature and presented in Appendix B, where corresponding reference documents are also listed.

Table 3 – Material models employed in numerical simulations

#	Material	Equation of State	Strength Model	Failure Model
1	Aluminum alloys (Al 6061-T6, Al 1100-H12, Al2024-T4)	Mie-Gruneisen [103-104, 106]	Johnson-Cook [103-104, 106]	Johnson-Cook [103-104, 106]
2	Nextel	Porous Isotropic [57]	–	–
3	Kevlar-Epoxy	Orthotropic (polynomial volumetric response) [57]	Elastic	Material stress/strain (orthotropic) [57]
4	Silicon Carbide	Mie-Gruneisen (polynomial formulation) [56]	Johnson-Holmquist [56]	

3.2.3 Identification of erosion strain

As the numerical modeling scheme described above employs finite elements to represent the aluminum (Al6061-T6) rear walls/rear facesheets of the shields, it should be used in conjunction with an erosion mechanism in order to prevent excessive mesh distortions and tangling at high deformations. The erosion mechanism works by removing finite elements in the regions where geometric strain has reached a user-specified value. The default value of the erosion strain in AUTODYN is 1.50. However, it was expected to be somewhat lower for Al6061-T6 because of the relatively low deformability of this alloy. In order to identify the erosion that would provide the best match between a physical test and the simulation, a calibration experiment was conducted.

Table 4 – Experimental data for erosion strain calibration [61]

Test #	D_p, mm	Projectile material	v_p, km/s	t_b, mm	Bumper material	S, mm	t_w, mm	Wall material	Wall perforation
A1076	2.0	Al2017-T4[3]	6.37	0.64	Al1100	60	0.41	Al6061-T6	Yes
A1077	2.0	Al2017-T4	6.77	0.41	Al1100	60	0.64	Al6061-T6	No

In the calibration experiment, conditions of two physical HVI tests reported in [61] were simulated. The tests' parameters are presented in Table 4 (source notation of the tests has been retained). These particular experiments were chosen because they represent borderline cases in terms of rear wall perforation, as well as because of the fact that they

---

[3] As a result of the lack of the full set of material data required for HVI simulations for Al2017-T4 (in particular, coefficients for Johnson-Cook failure model were not available), this was substituted in simulations by data for Al2024-T4, assuming a high level of similarity in their behavior..

are quite close to the design conditions considered in this study in terms of projectile speed and diameter and rear wall material.
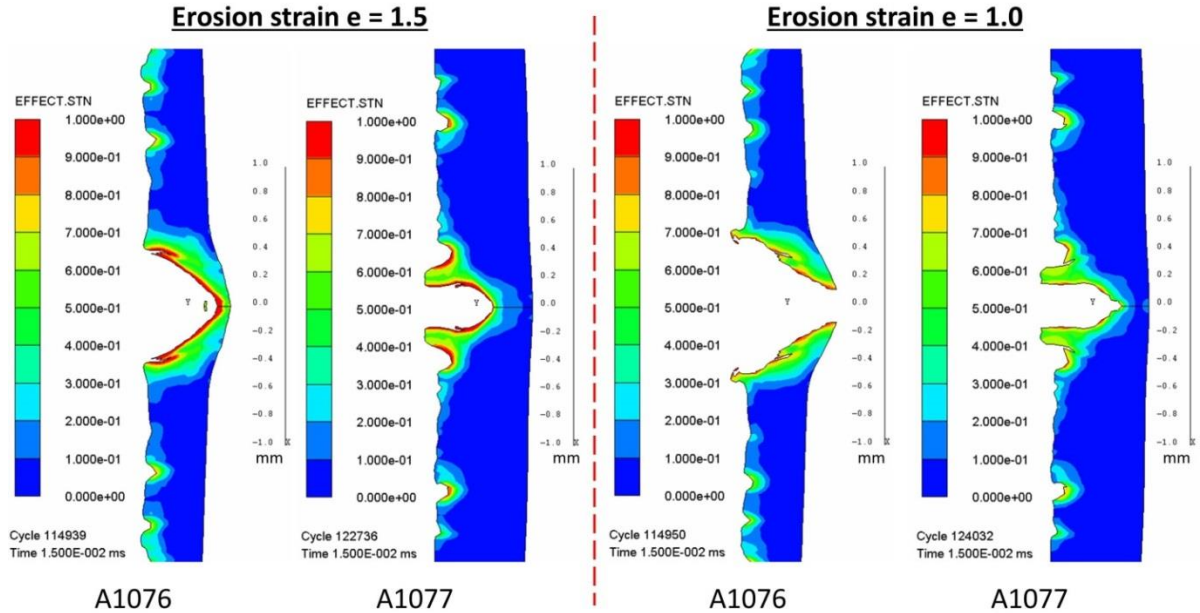
Figure 16 – Calibration of erosion strain (for impact conditions – see Table 4)

Simulations were carried out with back wall material erosion strains of 1.50, 1.25 and 1.00. Results in terms of rear wall damage corresponding to the former and the latter cases are exemplified in Fig. 16 (for the most damaged central regions of the plates only). As can be deduced from the figure, an erosion strain of 1.00 provides a good match between experimental and numerical results predicting perforation for the configuration #A1076 and no perforation for the configuration #A1077. With all other considered erosion strains, perforation of the rear wall, as observed in test #A1076, was not obtained. On the other hand, further reduction of erosion strain below 1.0 would result in perforation of both targets.

3.3 Conventional Shielding Configurations

The four conventional configurations considered in this study are schematically shown in Fig. 17. The first two – the Whipple Shield and Stuffed Whipple Shield – represent the class of *Single-purpose MMOD shields*. The only purpose of these systems is to protect spacecraft hardware from orbital debris impacts, with no additional requirements imposed.
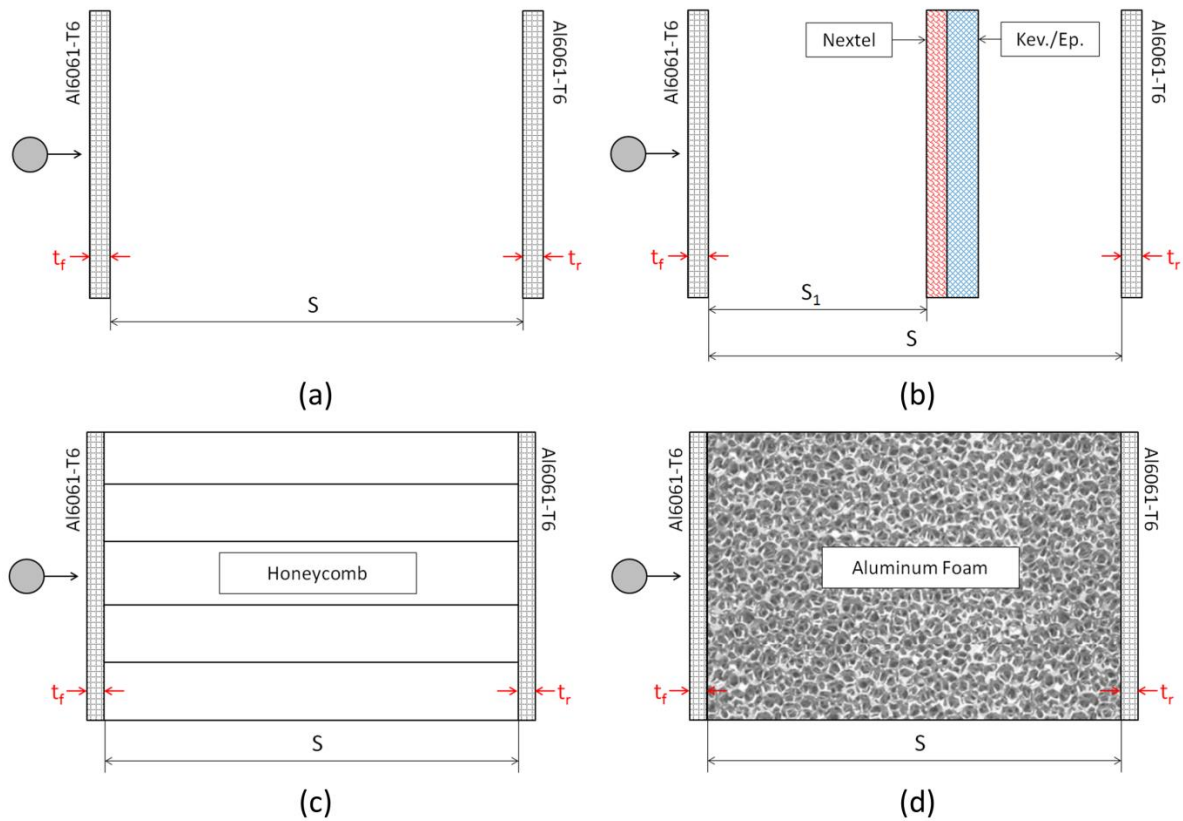
Figure 17 – Considered conventional shields: a) Whipple shield; b) Stuffed Whipple shield; c) Honeycomb-core sandwich panel; and d) Foam-core sandwich panel

The Whipple shield consists of two aluminum sheets separated by a standoff S [Fig. 17 (a)]. In this configuration, the first wall breaks up a projectile into a cloud of material ("debris cloud") that expands while moving across the standoff. This results in a distribution of impactor energy and momentum over a wide arear of the rear wall.

55

The stuffed Whipple shield [Fig. 17 (b)] is an enhancement of the Whipple shield concept that incorporates a layer of fabric-based materials ("stuffing") in between the front bumper and the rear wall. There exist two configurations of Stuffed Whipple Shields: one developed by NASA [19] for protecting US modules on the International Space Station (ISS) and another developed by ESA for the protection of the European Columbus module of the ISS [20]. Both shields demonstrate similar protection capabilities (see Table 2), but have slightly different stuffing configurations; the stuffing of the NASA shield consists of layers of Nextel cloth followed by layers of Kevlar fabric, while in the ESA shield, layers of Nextel are followed by a Kevlar-Epoxy composite plate. In this study, we considered shields with a stuffing analogous to the ESA system.

Configurations shown in Fig 17 (c) - (d)—honeycomb-core and foam-core sandwich panels—represent the class of multi-purpose structural panels. Panels of this kind are generic elements of spacecraft load-bearing structures and may also perform as shielding systems at no extra cost for the mounting/fastening elements typically needed to attach an external shield. This can be advantageous in terms of weight savings, as well as savings in space, materials, and manufacturing costs. The structural functionality of these panels is ensured by their flexural stiffness, which has to be no lower than some minimum specified value.

In this work, the minimal required level of flexural stiffness was determined by a *reference honeycomb sandwich panel* with 0.5-mm-thick aluminum facesheets and a 16-mm-thick core. These parameters of the reference sandwich panel are close to the lower boundary of the typical range for unmanned spacecraft structures, which is 0.25–2.00 mm for the facesheet thickness and 5–50 mm for the overall panel thickness [4].

56

In addition, these panels often have equal-thickness facesheets in order to avoid unwanted bending-stretching coupling when subjected to structural loads. Correspondingly, the sandwich panels considered in this study were symmetrical relative to their midsurface.

Honeycomb core sandwich panels [Fig. 17 (c)] are well-known for their superior structural properties. However, compared with Whipple shields, honeycomb panels are more easily penetrated in the case of normal impacts, because of channeling of the debris cloud after perforation of the first facesheet [1]. This channeling results from the interaction of the debris cloud with the walls of the honeycomb cells.

Metallic foam-core sandwich panels have been recognized as prospective substitutes for honeycomb core panels, because of the lack of such a tunneling effect and the multi-shock action on the debris cloud propagating within the space filled with foam. In this work, we considered a shield configuration utilizing open-cell aluminum foam as an intermediate layer between the aluminum facesheets [Fig. 17 (d)].

The standoff between the bumper and the rear wall (or front and rear facesheet for sandwich panels) was the same for all configurations and chosen from the typical range of $15D_p < S < 30D_p$ (see Ref. [62]) as $S = 16$ mm.

It must be emphasized that, as WS and SWS on the one hand and HCSP and FCSP on the other are designed with different sets of constraints ("no perforation" only for the shields and "no perforation" + structural requirements for the sandwich panels), they were only compared within their own categories; intercategorial comparisons were not considered.

3.4 Preliminary Sizing of Conventional Shields Using BLEs

Ballistic limit equations (BLE) are empirical design equations, developed by NASA and ESA, which can be used to size a shield so as to provide protection against a specific particle threat. Preliminary sizing of the four conventional shielding configurations has been conducted using the BLEs described in Ref. [3, 62 and 63] and briefly introduced below.

1. According *to Christiansen et al.* [3], to defeat a particle moving with velocity of $v_p \geq 7$ km/s, a dual-wall system with the front wall ("bumper") of $t_f \geq 0.25 \cdot D_p \dfrac{\rho_p}{\rho_f}$ should have a rear with a thickness equal to

$$t_r = c_w \cdot D_p^{0.5} \cdot \left(\frac{\rho_p}{\rho_f}\right)^{1/6} \cdot m_p^{1/3} \cdot \frac{v_p \cdot \cos\theta}{\sqrt{S}} \cdot \sqrt{\frac{70}{\sigma_y}} \tag{31}$$

where $c_w = 0.16 \, cm^2 \cdot \sec/ g^{2/3} \cdot km$; D_p, m_p and ρ_p are projectile diameter (cm), mass (g) and density (g/cm^3), correspondingly; ρ_f is the density of the front wall material (g/cm^3); σ_y is rear wall yield stress (ksi); θ is impact angle.

2. For sizing of the stuffed Whipple shield, Ref. [3] defines the following equations:

$$t_b = 0.15 \cdot D_p \cdot \left(\frac{\rho_p}{\rho_f}\right) \tag{32}$$

$$AD_{stuffing} = 0.23 \cdot D_p \cdot \rho_p \tag{33}$$

$$t_r = c_w \cdot \left(\frac{t_b \rho_b + AD_{stuffing}}{c_0 \cdot D_p \cdot \rho_p} \right)^{-1.1} \cdot m_p \cdot \frac{v_p \cdot \cos^{\frac{3}{2}} \theta}{\rho_w S^2} \cdot \sqrt{\frac{40}{\sigma_y}} \tag{34}$$

Here $c_w = 8.8 \, s/km$ and $c_0 = 0.38$. If the projectile and the bumper and rear wall of the SWS are made of material with the same density (ρ), then equations (2)–(4) express the areal density of the SWS as $AD_{SWS} = D_p \cdot \rho \left[c_b + c_{st} + K_{SWS} \cdot \frac{v_p}{\bar{S}^2} \right]$, where $K_{SWS} = 4.611 \, s/km$ and $\bar{S} = \frac{S}{D_p}$. Therefore, the SWS BLE implies the existence of a linear correlation between the weight of the shield and the projectile diameter.

3. Two different BLEs have been described in the literature for sizing the HCSP. First, according to Ref. [3], the ballistic limit for honeycomb-core sandwich panels can be estimated using the Whipple shield equation (31) where the parameter S, representing the standoff distance in the original WS equation, is replaced by either the product of twice the honeycomb cell diameter (D_{cell}), or by the core thickness, whichever is less:

$$S' = \min(2 \cdot D_{cell} \, ; S) \tag{35}$$

This constraint reflects the fact that honeycomb panels are more easily penetrated as compared to the dual walls, because of channeling of the debris cloud after perforation of the first facesheet [3]. This channeling results from the interaction of the debris cloud with the cells of the honeycomb.

Second, the equation described in [62] estimates required facesheets thickness (in the case of normal impacts) as

$$t_f = t_r = 0.8056 \cdot D_p^{3/2} \cdot K_{3D} \cdot \rho_p^{1/2} \cdot \rho_f^{1/6} \cdot \frac{v_p \cos^{\frac{3\delta}{2}} \theta}{\sqrt{S}} \cdot \sqrt{\frac{70}{\sigma_y}} \,, \tag{36}$$

where $K_{3D} = 0.4$ for the case of aluminum outer bumper; $\delta = 4/3$ if $45º \geq \theta \leq 65º$ or 5/4 if $45º < \theta > 65º$.

4. The BLE for sizing of the FCSP used in this study was adopted from Ref. [63]. It defines the critical projectile diameter capable of perforating a foam-core panel:

$$D_{cr} = \frac{t_{fs}^{2/3} \cdot t_{foam}^{1/3} \cdot \left(\sigma_y / 70\right)^{1/3}}{0.866 \cdot C_2 \cdot \rho_{fs}^{1/9} \cdot \rho_p^{1/2} \cdot v_p^{\frac{2}{3}} \left(\cos\theta\right)^{0.85}} \,, \tag{37}$$

where $C_2 = 0.15 \cdot t_{foam}^{-0.6}$; t_{foam} is the core thickness and t_{fs} is the facesheet thickness; ρ_{fs} is the facesheet density. Using equation (37), t_{fs} was calculated for $D_{cr} = 1$ mm and $v_p = 7$ km/s.

The following important comments on the applicability of equations (31) – (37) must be emphasized.

1. It was found in Ref. [64] that equation (31) was capable of correctly predicting results for only 71% of 750 Al-Al HVI experiments.

2. Equations (32) – (34) are only partially applicable for sizing SWS with a stuffing containing KFRP plates, as they were designed for the NASA configuration of an SWS with Kevlar cloth. Analysis of the ESA configuration described in Ref. [57] shows that its front bumper maintains the same correlation between t_b and D_p, as suggested by

equation (32), namely $\dfrac{t_b}{D_p}\left(\dfrac{\rho_f}{\rho_p}\right) = 0.15$. Moreover, the areal density of the stuffing as

determined via equation (33) exactly corresponds to the total areal density of Nextel

and Kevlar fabric used in the original ESA shield (though this does not include the areal

density of the epoxy resin, which adds an additional 40% to the weight of the KFRP

plates in the ESA configuration). However, the ratio of the Kevlar to Nextel areal

weight is significantly different between the two configurations and corresponds to

$\dfrac{AD_{KEV}}{AD_{NEX}} = 0.33$ for the NASA shield and $\dfrac{AD_{KEV}}{AD_{NEX}} = 1.48$ for the ESA shield (or

$\dfrac{AD_{KFRP}}{AD_{NEX}} = 2.50$ if the weight of epoxy is also considered). It also should be noted that

equations (32) – (34) have been verified for projectile sizes in the range from 7 to 16

mm only.

3. According to Ref. [3], the approach described by equation (35) provides only a *rough* estimate of the ballistic limit for honeycomb sandwich structures. Equation (36) is independent of the honeycomb cell diameter, which according to equation (35) may be a significant factor limiting the performance of a honeycomb-core panel. It should also be noted that equations (35) and (36) predict significantly different facesheet thicknesses for the same impact conditions (see Table 5).

4. Equation (37) was derived based on data from HVI experiments on sandwich panels with the foam core having reference density 6 – 8% of the base material (Al 6061-T6), which is 2.0 – 2.7 times higher than the foam density considered in this study (3%). Equation (36) is, therefore, *a priori* overestimates the ballistic performance of the low-density FCSPs.

Table 5 – Parameters of the shields as predicted by BLEs (1 mm, 7 km/s Al projectile)

	Shielding System	t_b, mm	t_{NEX}, mm	t_{KFRP}, mm	S_1, mm	S, mm	t_w, mm	AD, g/cm²
Type I	Whipple Shield	0.25	–	–	–	16.00	0.60	0.230
	Stuffed Whipple Shield	0.15	0.33[4]	0.38[5]	9.00	16.00	0.17	0.173
Type II	Honeycomb-core Sandwich Panel[3]	0.95[6]	–	–	–	16.00	0.95	0.669
		1.45[7]					1.45	0.939
	Foam-core Sandwich Panel	0.50[8]	–	–	–	16.00	0.50	0.400

In the presence of the major assumptions and limitations listed above, sizing with equations (31) – (36) can only be used for a very first-order estimate of the parameters of the shielding systems considered in this study. These preliminary estimates are represented in Table 5. Further optimization of the shield designs was conducted using hydrocode simulations, as described in the following sections. It should also be noted that, in the case of oblique impacts, equations (31) and (34) – (37) predict lower required wall/facesheet thicknesses for all shielding configurations considered in this study, as compared to impacts at normal incidence ($t_w \sim (\cos\theta)^{\alpha}$, where $\alpha > 0$). For instance, in the case of oblique impact at 45 degrees, BLE (36) predicts minimal required facesheets thickness for the HCSP panel of 0.76 mm, which is almost twice as low as that predicted for the normal impact. However, it is a standard practice to design against the worst case scenario. As a result, *only normal impacts* are considered in the following calculations.

---

[4] corresponds to 1 layer of Nextel 312 AF-12 fabric with the areal density $AD_{NEX} = 0.025$ g/cm² [65];

[5] corresponds to 1 layer of Kevlar-Epoxy with the areal density $AD_{KFRP} = 0.062$ g/cm²;

[6] as predicted by equation (35) for HCSP with 1/8 - .0015 hexagonal aluminum honeycomb core by Hexcel

[7] as predicted by equation (36);

[8] BLE prediction is 0.25 mm; increased to 0.5 mm due to the flexural stiffness constraint

3.5 Sizing of Conventional Shields Using Hydrocode Simulations

3.5.1 Single-purpose MMOD shields

3.5.1.1 Whipple shield

Results of the numerical simulation of HVI on a Whipple shield with parameters as predicted by BLE (see Table 5) are represented in terms of rear wall damage in Fig. 18 (a). No perforation of the rear wall was observed in this case. Attempts to further reduce the rear wall thickness ($t_w = 0.5$ mm) led to perforation, as it is shown in Fig. 18 (b). Therefore, the optimal parameters of the Whipple shield as determined via numerical simulations are in exact agreement with the prediction of BLE.
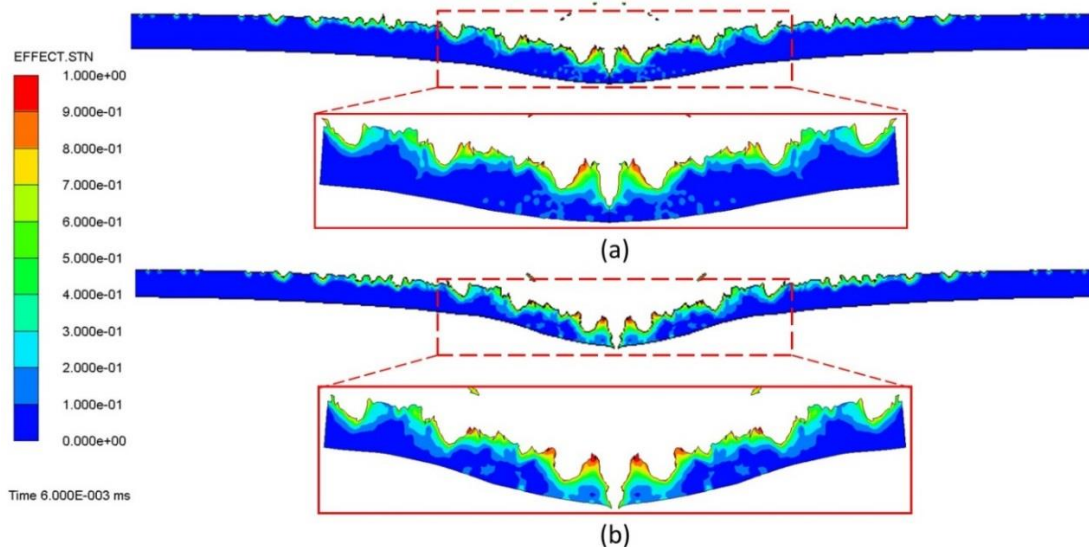
Figure 18 – Damage of the rear wall of Whipple Shield: a) $t_w = 0.6$ mm; b) $t_w = 0.5$ mm

(impact of 1 mm, 7 km/s projectile)

3.5.1.2 Stuffed Whipple shield

The validity of simulations with stuffed Whipple shields was preliminarily tested by repeating HVI simulations with large-size projectiles described in Ref. [57] and confirming

their correlation with experimental data presented in the same report. Mesh parameters from successful preliminary simulations were scaled down to have similar projectile diameter-to-SPH smoothing length ratios.

As opposed to WS, which failed because fragment penetration, Stuffed Whipple shields with bumper and stuffing parameters as given in Table 5 mainly exhibited momentum failure caused by fragments of decomposed Kevlar-Epoxy (controlled by the temperature of decomposition, see Section 2.3.2.4), Nextel and decelerated fragments of aluminum (see Fig. 19). This failure mechanism is quite characteristic for SWS shields, as is also reported in the experimental study [61]. The momentum failure happens at a "late time" (i.e. much later than impact of the most energetic leading fragments on the rear wall) because of inability of the rear wall to absorb momentum of the whole debris cloud. Such failure typically leads to large petalled holes on the rear wall [61].

Results of HVI simulations on SWS with the rear wall thickness as predicted by the BLE (0.17 mm) and higher are presented in Fig. 20 in terms of rear wall damage. As can be deduced from the figure, these simulations suggest a slight perforation of the shield with $t_w = 0.35$ mm and no perforation when $t_w = 0.45$ mm. Total kinetic energies for all moving fragments of SWSs with rear walls of 0.35 and 0.45 mm at $t = 30$ µs were estimated using Autodyn tools, and these equaled 1.783 and 1.757 J, respectively. The total kinetic energy was non-zero in the second case (no perforation of the rear wall), as many of the fragments moved in the direction opposite to the direction of impact (so-called "ejecta"). Assuming that the kinetic energies of ejecta clouds are the same for both shields (only rear walls of the shields are different, whereas most ejecta are produced during fragmentation of the projectile on the front bumper and the stuffing), the remaining kinetic energy of the

fragments after perforation of the 0.35 mm rear wall can be estimated as the difference

Ek [tw = 0.35 mm] – Ek [tw = 0.45 mm] = 0.026 J. For the sake of comparison, an energy

of 0.026 J is equivalent to the kinetic energy of a 1 mm aluminum projectile with a speed

of 190 m/s or, alternatively, to the energy of a 0.1 mm aluminum particle with a speed of

6 km/s. This energy corresponds to ~0.075% of the initial kinetic energy of the projectile

(34.79 J), which means that the shield with a 0.35 mm rear wall is quite close to its ballistic

limit. Considering that some scatter is possible because of the nature of numerical

simulations, weight estimates for both rear wall thicknesses are provided in the Discussion

section in the end of this chapter.
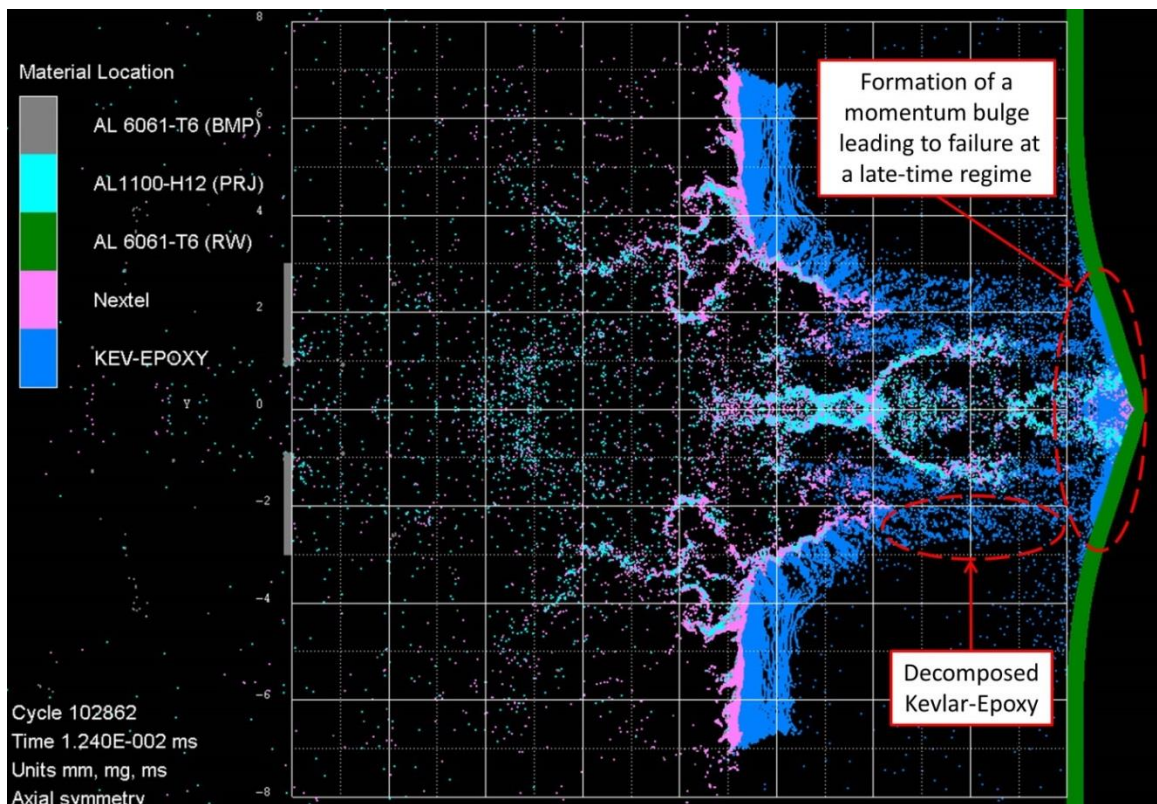
Figure 19 – HVI on Stuffed Whipple shield (T = 12.4 μs)

(impact of 1 mm, 7 km/s projectile)
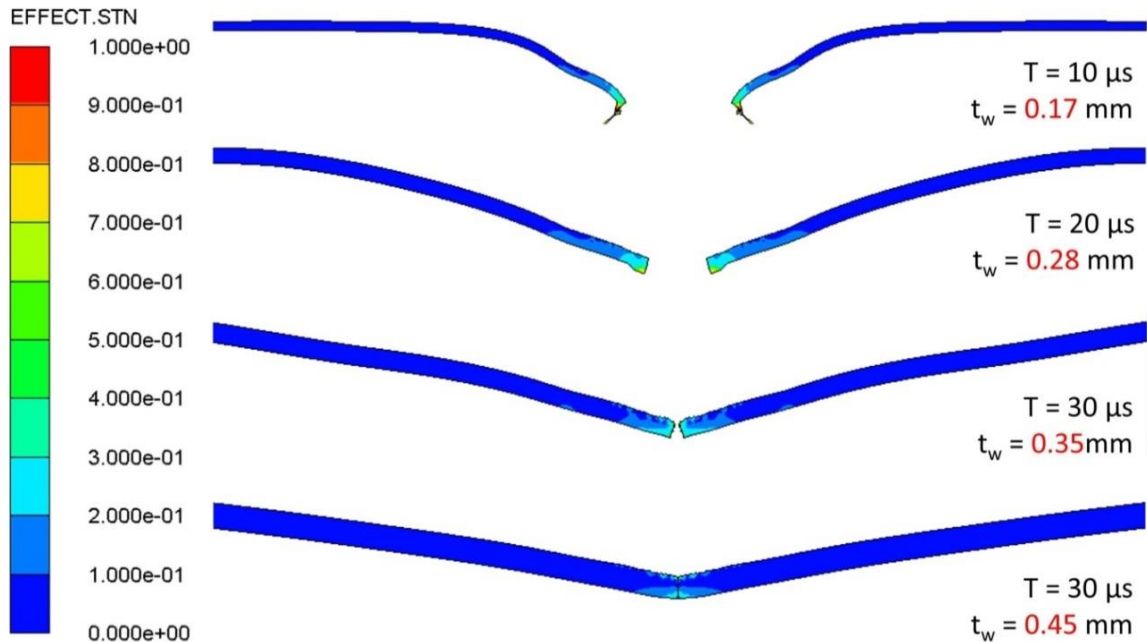
Figure 20 – Damage of the rear wall of Stuffed Whipple shield

(impact of 1 mm, 7 km/s projectile)

An additional simulation carried out with $\frac{AD_{KEV}}{AD_{NEX}} = 0.33$ (as for the NASA configuration,

see Section 3.4), demonstrated perforation of the rear wall due to penetration of aluminum

fragments even when $t_w = 0.45$ mm was used.

3.5.2 Multi-purpose structural panels

Parameters of the HCSP and FCSP cores considered in this study are presented in Table 6.

The cores have similar values of reference density. The cell size of the aluminum foam was

chosen so as to be less than the diameter of the projectile, in order to maximize the intensity

of the interaction between the foam layer and the debris cloud. This consideration led to

the minimal commercially available size of 40 pores per inch (ppi).

Table 6 – Parameters of the cores for sandwich panels

#	Core type	Core thickness, mm	Reference density, % of base material
1	1/8 – 0.0015[1] aluminum honeycomb by Hexcel	16.0	3.60
2	40 ppi aluminum foam by ERG Aerospace	16.0	3.00

[1] Hexcel honeycomb designation: Cell size (in.) – Wall thickness (in.)

3.5.2.1 Honeycomb-core sandwich panel

Uncertainty in the design of the honeycomb panels (two existing BLEs for HCSP predict significantly different facesheet thicknesses, as reported in Section 3.4) was resolved in this study using numerical analysis. This analysis was carried out for the configuration suggested by equation (35), which predicted $t_f = t_r = 0.95$ mm. The representative element of this honeycomb panel is shown in Fig. 21.
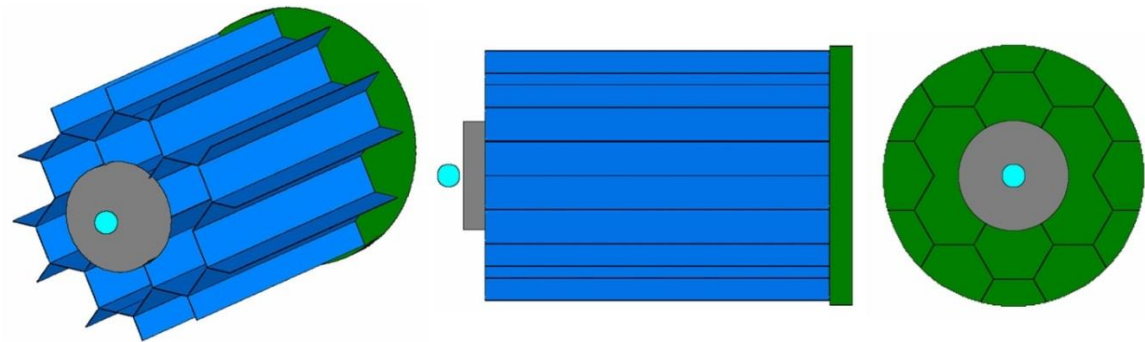
Figure 21 – Representative element of honeycomb core sandwich panel
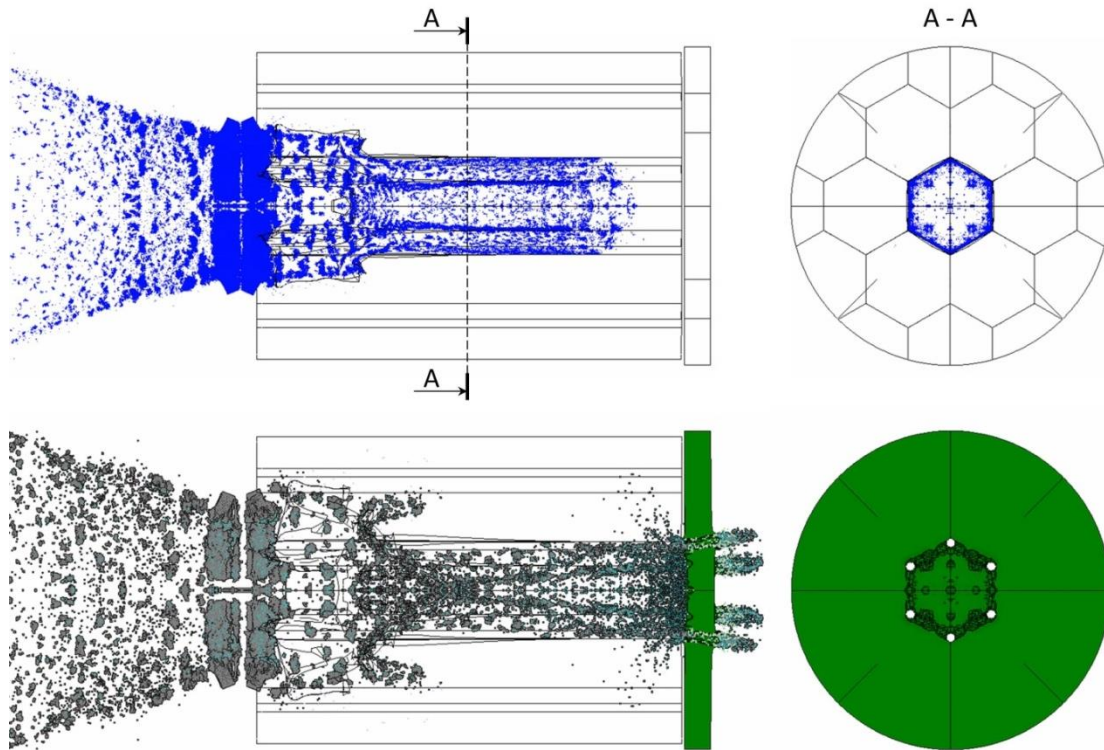
Figure 22 – Simulation of HVI on honeycomb-core sandwich panel (top – before impact on the rear wall; bottom – after perforation of the rear wall; 1 mm, 7 km/s projectile)

Results of the simulation (see Fig. 22) indicate that the panel will be easily perforated by a 1 mm aluminum projectile with an initial speed of 7 km/s. It can be noted that, because of the shape of the honeycomb cell, not all locations are equipotential and material in the debris cloud (in the course of radial expansion) tends to concentrate in the corners of the hexagon rather than being uniformly distributed over its circumference. This effect reveals itself in the resulting perforation pattern, as it is shown in Fig. 22. Taken together with the well-known channeling effect (i.e., constraining of expansion of the debris cloud by the honeycomb cells), the honeycomb at normal impact thus produces "double-focusing" of the debris cloud (the debris cloud is focused/channeled by a cell and, within the cell, it is focused in its corners).

As the numerical simulation predicted perforation of the HCSP with the parameters suggested by equation (35), all weight comparisons were conducted with facesheet thicknesses of 1.45 mm (see Table 5) given by the more conservative estimate, i.e. the one suggested by equation (36).

3.5.2.2 Foam-core sandwich panel

As a result of the complex three-dimensional structure of open-cell aluminum foam, a meso-scale approach to the representation of its geometry has been employed in our numerical modeling. The original structure that forms metallic foam is a three-dimensional array of bubbles having a maximum volume for the minimal surface area and surface energy. In the course of the fabrication process, membranes of the bubbles are removed, leaving an interconnected network of solid struts.
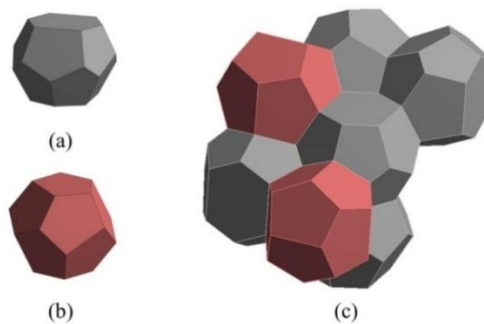
Figure 23 – Geometric modeling of aluminum foam: (a) – Tetrakaidecahedron; (b) – Dodecahedron; (c) – Translation unit of Wearie-Phelan packing

A common approach to geometric modeling of open-cell foams is based on Wearie-Phelan idealization [108]. It represents a structure consisting of equal-volume bubbles of two different shapes, namely, the 14-sided tetrakaidecahedron [Fig. 23 (a)] and the 12-sided dodecahedron [Fig. 23 (b)]. It is believed that Wearie-Phelan packing provides a minimal

surface area for a given volume of cells/bubbles [108]. The periodic domain (translation unit) of Wearie-Phelan tessellation is shown in Fig. 23 (c).

It should be noted that the use of Wearie-Phelan idealization suggests a regular array of bubbles; however, real foams are random structures. In order to increase the realism of the modeling, therefore, a foam randomization mechanism was implemented. The idea of foam randomization can be explained as follows. If each point where foam ligaments connect to each other is thought of as a "node" with coordinates $\{x_i\} = \{x_1, x_2, x_3\}$, then the foam structure can be randomized by performing node perturbation according to the following rule: $\tilde{x}_i = x_i + \delta_i \cdot L$, where $\delta_i = rand[-1;1]$ and L is a characteristic dimension controlling severity of the perturbation.
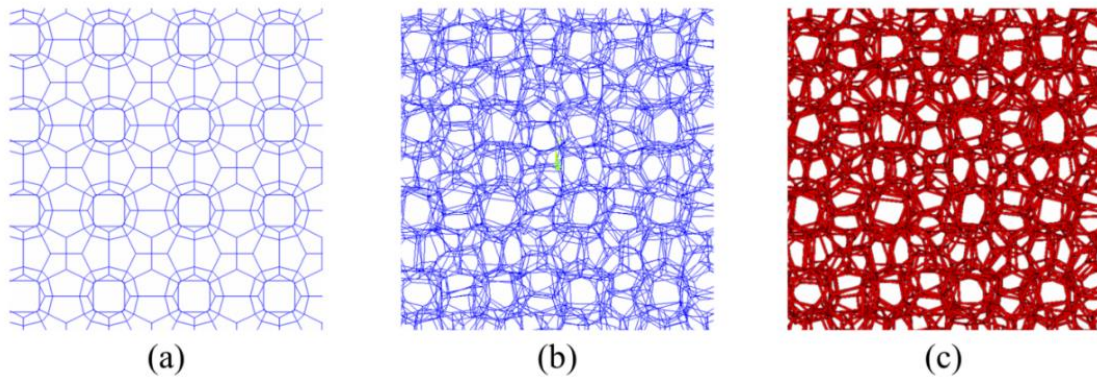
Figure 24 – Meso-scale geometric modeling of aluminum foam: from structured frame to randomized solid model: a) idealized line-based geometry; b) randomized line-based geometry; c) randomized solid geometric model
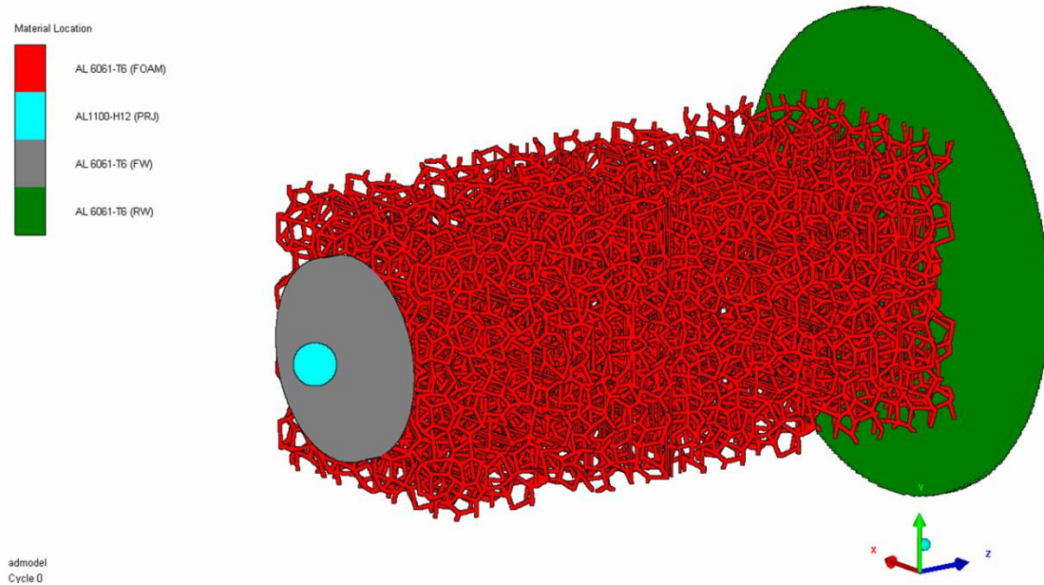
Figure 25 – Numerical model of the foam-core sandwich panel

The overall algorithm for the geometric modeling can thus be described as follows:

1. Generation of the representative volume element (RVE) of aluminum foam with specified dimensions, providing the required ppi index, based on Wearie-Phelan idealization; at this stage, the geometric model consists of multiple lines connected with each other in nodal points [see Fig. 24 (a)];

2. Randomization of the foam using the node perturbation idea described above [see Fig. 24 (b)];

3. Development of a solid geometric model using the randomized line-based geometry [see Fig. 24 (c)]. The required reference density of the foam (3% in this study) is achieved by the choice of the ligaments' thickness.

The foam modeling algorithm has been implemented in the form of a script written in ANSYS Parametric Design Language (APDL) and provided in Appendix C.
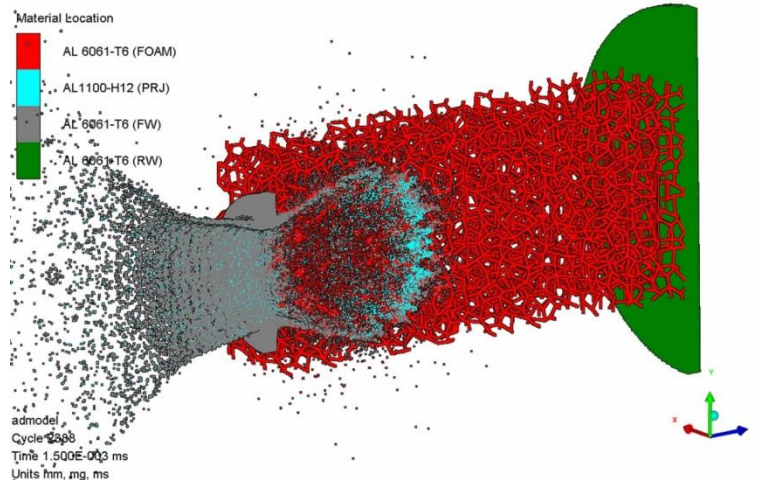
(a)
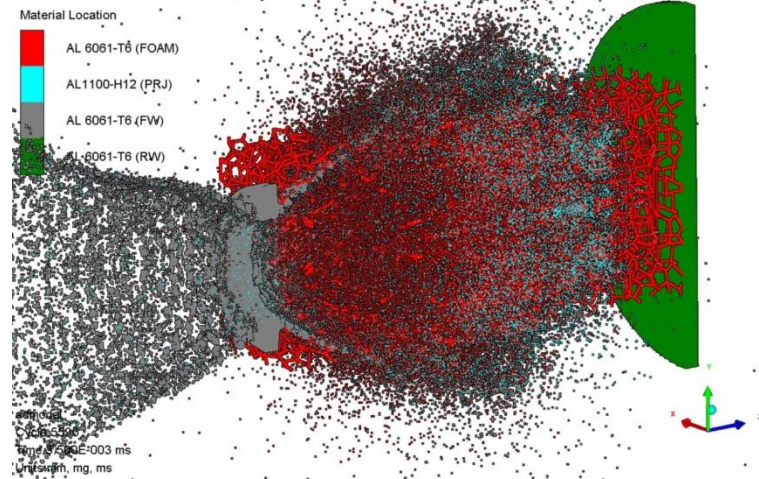
(b)
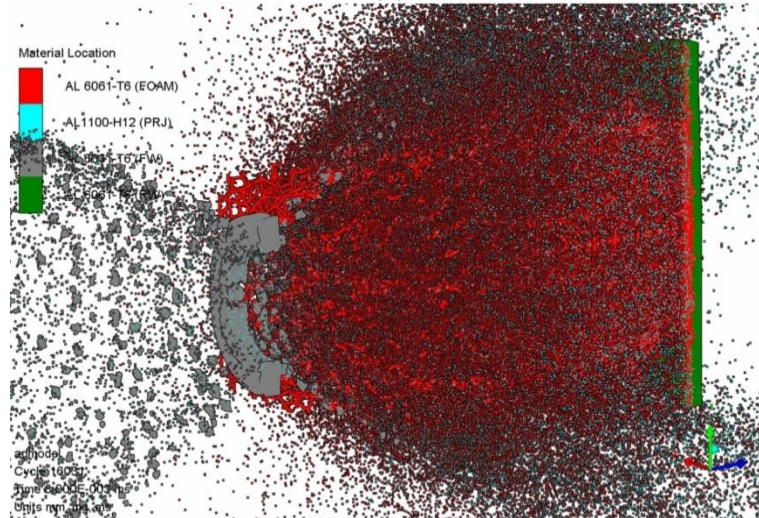
(c)

Figure 26 – Results for the foam-core sandwich panel: a) t = 1.5 µs; b) t = 3.5 µs; c) t =

8.5 µs (impact of 1 mm, 7 km/s projectile)

72

The SPH model of the foam core sandwich panel is depicted in Fig. 25. It consists of approximately 2 million SPH particles. In order to represent thin ligaments of aluminum foam with a satisfactory accuracy, a smoothing length of 0.015 mm has been used. The model exploited the idea of quarter-symmetry. Although aluminum foam has a random structure and is not exactly symmetrical relative to any cutting plane, isotropy of its effective properties allows for such an assumption. The foam in the model is present only in the central region of the panel, where the most energetic fragments with the greatest damage potential will propagate. Additional lateral extension of the foam model was found to be impractical, as it is associated with high computational expenses. Some "peripheral" fragments (usually have much lower energy than the central ones) were allowed to escape the interaction with the rear wall, assuming that their damaging potential was negligible.

Results of the conducted simulation are presented in Fig. 26, which demonstrates three consequent moments of time, when debris cloud propagates through the aluminum foam. It can be seen in the figure that multi-shock action of the foam effectively breaks up fragments of the projectile and the front bumper, converting them into a cloud of small disperse particles. No perforation of the rear wall has been detected in the course of the numerical experiment.

In view of the novelty of the foam modeling approach (i.e., its meso-scale representation in HVI analysis), the numerical prediction was verified by means of a physical experiment, so as to ensure satisfaction of the no-perforation constraint for the designed foam-core sandwich panel. The experiment was carried out using a two-stage light gas gun at the HIT Dynamics Ltd. impact testing facility (NB, Canada).

The tested panel consisted of two Al6061-T6 facesheets and 16-mm-thick 3% 40 ppi aluminum foam from ERG Aerospace. As the requirement of minimal bending stiffness had been anticipated as the active constraint, the tested panel had a slightly lower facesheet thickness (0.4 mm instead of 0.5 mm as dictated by the stiffness requirement) in order to probe the proximity of the FCSP design to its ballistic limit (i.e. to see if the panel with facesheets thinner than those needed to satisfy the flexural stiffness constraint, will still be able to resist the impact of 1 mm, 7 km/s projectile).
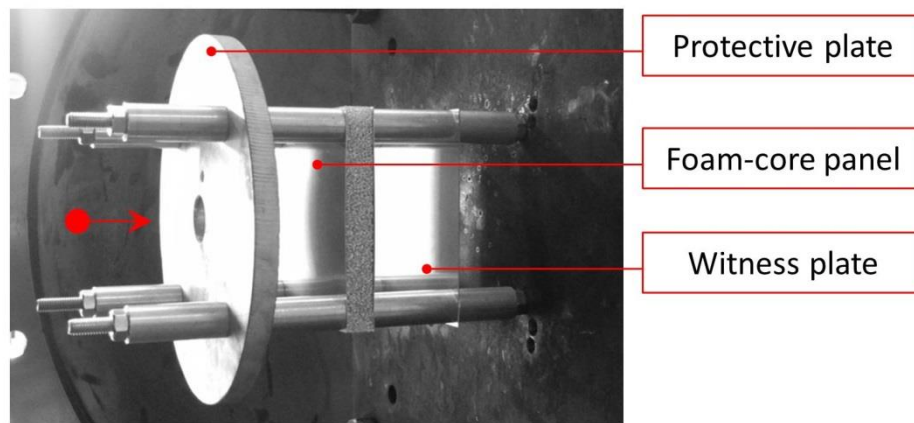
Figure 27 – Experimental setup
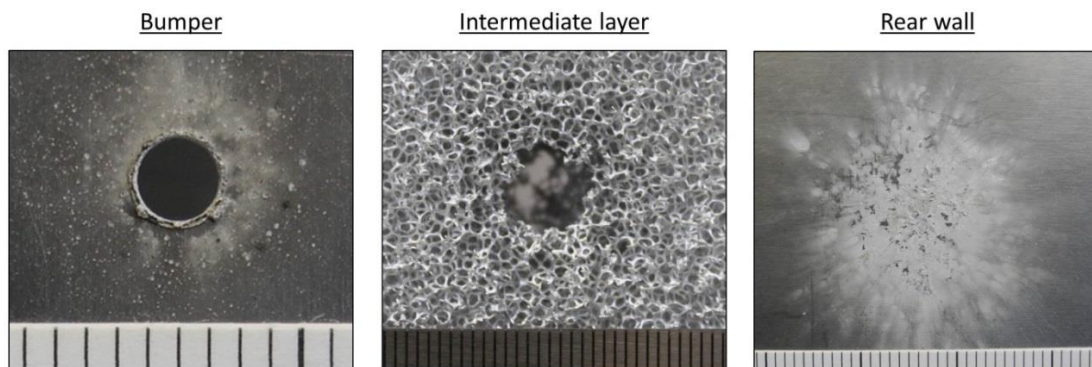
Figure 28 – Results of experiment for FCSP (impact of 1 mm, 6.965 km/s projectile)

74

The panel was impacted by a 1 mm aluminum projectile at 6.965 km/s (measured by laser intervalometers), and the resulting damage to the panel is shown in Fig. 28. Rear wall damage was represented by discoloration and barely noticeable bulging. No perforation of the rear wall was detected, which supports the results of the numerical simulation. The configuration of FCSP considered in this study therefore provides the minimal required bending stiffness (see Section 3.3) and can be used to protect a spacecraft from 7 km/s impacts of 1 mm debris particles.

3.6 A Novel Shield with Ceramo-metallic Bumper

In its "conventional" design, the bumper of a Whipple shield is monolithic and made of an isotropic material, typically aluminum, known for its ability to efficiently break up medium-density (~2.8 kg/m^3) projectiles. Other possible designs of the shielding systems are continuously being sought with the ultimate purpose of increasing their structural weight efficiency. In this regard, a stuffed Whipple shield [66] concept has been found beneficial. While utilizing advanced flexible materials in its design, this shield still has its outer bumper made of aluminum. Recent studies aimed to evaluate the efficiency of other types of outer layers for orbital debris shields, e.g. flexible fabrics [23], established the superiority of monolithic all-aluminum bumpers over the considered substitutes.

 In this work, instead of looking for a complete substitute for aluminum front bumper, we investigate a possibility for further enhancement of its performance by combining it with thin layers of *high-impedance ceramic material* (silicon carbide). The obtained laminated bumper is tailored based on the principle of matching shock impedance of ceramic and metallic layers. This part of the study uses both theoretical hydrocode-based analysis and

physical experiments in order to investigate and quantify possible benefits from using the ceramo-metallic plates as outer bumpers of orbital debris shields.
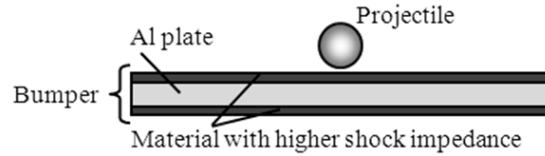
Figure 29 – Laminated bumper with outer layers of high shock impedance
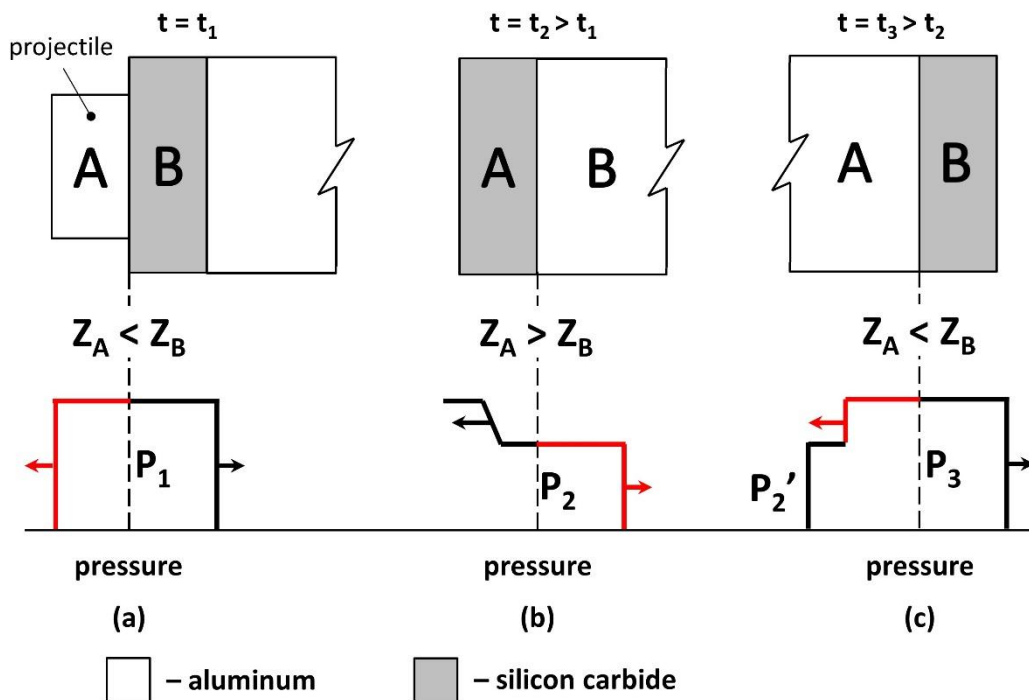
Figure 30 – Interaction of shock wave with impedance boundaries in the laminated

bumper configuration (Z – acoustic impedance)

Let us consider a composite bumper consisting of three layers: intermediate aluminum layer and two outer layers made of a material with shock impedance higher than that of aluminum, as it is shown in Fig. 29. The shock impedance can be defined as a product of material initial density and shock wave velocity and represents a measure of material's

ability to generate pressure under impact loading. For the sake of simplicity, in the further considerations we use the acoustic approximation of shock impedance, i.e. reduce it to acoustic impedance $Z = \rho_0 C_0$, where ρ_0 and C_0 are material density and bulk sound velocity respectively.

Upon impact of an aluminum projectile on the front layer ($t = t_1$), a pair of compressive shock waves of the same initial amplitude of pressure will originate on the impedance boundary and propagate in the opposite directions: one towards the projectile and another towards the bumper. This process is schematically illustrated in Fig. 30 (a). Due to higher impedance of the outer layer, the generated pressure will be higher than it would be in the case of the impact of an aluminum projectile on the aluminum bumper, thus resulting in more significant damage and better fragmentation of the projectile.

When at $t = t_2$ shock wave in the front layer reaches interface with the intermediate aluminum layer [see Fig. 30 (b)], the release pulse (decompression wave) will be sent through the front layer while compression pulse (P_2) enters aluminum. Due to impedance difference, this compressive pulse will have a lower amplitude as compared with the incident pulse impacting front layer/aluminum interface ($P_2 < P_1$). At $t = t_3$, the shock wave will reach the aluminum/back layer interface [see Fig. 30 (c)], where pressure will rise due to impedance difference up to $P = P_3$. Being reflected from the boundary, this pulse will interact with the release portion of the incident shock wave, which will result in the drop of pressure to $P = P_3 - P_2'$. This compressive wave will propagate in the intermediate layer towards approaching projectile increasing the degree of its fragmentation and suppressing spall.

77

Table 7 – Properties of various materials

No.	Material	Density, g/cm³	Bulk modulus, GPa	Speed of sound, m/s	Impedance, [kg/(s*m²)]x10⁶
1	Aluminum[9]	2.703	70	5092	13.76
2	Steel	7.810	163	5185	40.49
3	Titanium	4.506	110	5090	22.93
4	SiC	3.210	203	11300	36.27

The described effects are favorable when exploited for the spacecraft orbital debris shielding while the key factor in their implementation is the right choice of material for external layers. After considering of a number of perspective materials, ceramics and, more precisely, silicon carbide was chosen for this application. The reasons for such choice can be illustrated by comparing properties of ceramics and typical metallic materials (see Table 7). It can be seen from Table 7 that metals provide either high impedance for the price of high structural weight (e.g. steel) or low structural weight for the price of low impedance (e.g. titanium). Unlike metals, silicon carbide is known for its low density (and, correspondingly, structural weight) and very high bulk modulus. The latter provides an impedance of silicon carbide 2.6 times higher than the one of aluminum and equivalent to that of steel while having density only slightly higher than aluminum and 2.4 times lower than steel.

Finally, it should be noted that a concept of a protective plate containing layers of materials with different impedance has been proposed by *Musante and Morrow* [114] for military applications. It is, however, quite different from the idea of the laminated bumper proposed in this study, in terms of both application and implementation. The differences are contrasted in Table 8.

---

[9] the reference material

Table 8 – Comparison of the proposed laminated bumper with the concept of armor plate proposed by *Musante and Morrow* [114]

	Proposed MMOD shield bumper	Armor plate proposed by Musante and Morrow [114]
Application	MMOD shielding	Armored vehicle protection
Projectile speeds	Hypervelocity impact	High velocity impact
Outer non-metallic layer	Ultrathin (tens of microns) layer of silicone carbide	N/A
Impedance of the outer layer material, as compared to the impedance of the intermediate layer	Higher	N/A
Purpose of the outer layer	Increased shock pressure in the projectile enhancing its disruption	N/A
Intermediate layer	Aluminum	Aluminum
Backing non-metallic layer	Ultrathin (tens of microns) layer of silicone carbide	3 - 38 mm-thick polymer composite reinforced with ceramic or metallic powder
Impedance of the backing layer material, as compared to the impedance of the intermediate layer	Higher (reflects incident compressive wave as compressive wave)	Lower (reflects incident compressive wave as tensile wave of low amplitude)
Purpose of the backing layer	Additional shocking of the approaching projectile; suppression of spall	Suppression of spall
Attachment of non-metallic layers to the intermediate layer	Physical vapor deposition	With adhesive or application of the composite in uncured state with subsequent polymerization

3.7 Local Response of Ceramo-metallic Bumper to HVI

This section presents results of numerical investigations of the response of ceramo-metallic bumper to hypervelocity impact of the 1 mm medium-density (aluminum) projectile. The response is compared with the corresponding behavior of all-aluminum bumper. The aluminum bumper considered in the computations had the thickness of 0.4 mm; while the ceramo-metallic bumper consisted of 0.4 mm-thick aluminum substrate coated from both sides with 0.05 mm-thick silicone-carbide layers (see Fig. 31). According to the manufacturer (Entegris Specialty Coatings), this corresponds to the upper boundary of the range of thicknesses that can be fabricated using PVD equipment.
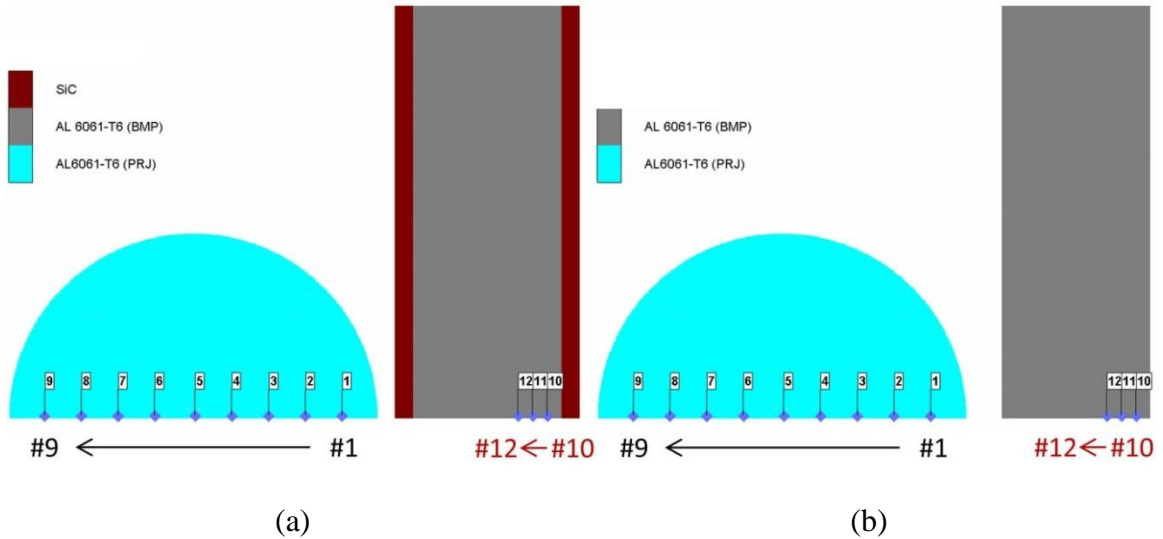
Figure 31 – Location of gauges: a) projectile and ceramo-metallic bumper; b) projectile and all-aluminum bumper

As described in Section 2, at the initial moment of impact two pressure pulses initiate and propagate within the projectile and the bumper. Those pulses are shown in Fig. 32 for ceramo-metallic and all-aluminum bumpers at the moment of time when they reach the rear impedance boundary of the bumper (note: in the case of the all-aluminum bumper, the impedance boundary is simply represented by the free surface on the back of the bumper). Directions of those pulses are shown by the white arrows in the figure.

In order to estimate their amplitudes and to study their evolution, a set of virtual gauges was placed in the projectile and the front bumper (Fig. 31). For each configuration, 9 gauges were distributed along the diameter of the projectile (gauges No.1–9) and 3 gauges (No.10–12) were placed close to the back-side impedance boundary of each bumper. The gauges stored values of the main field variables (e.g. pressure, density, velocity) at each integration step during the numerical analyses.

(a)   (b)
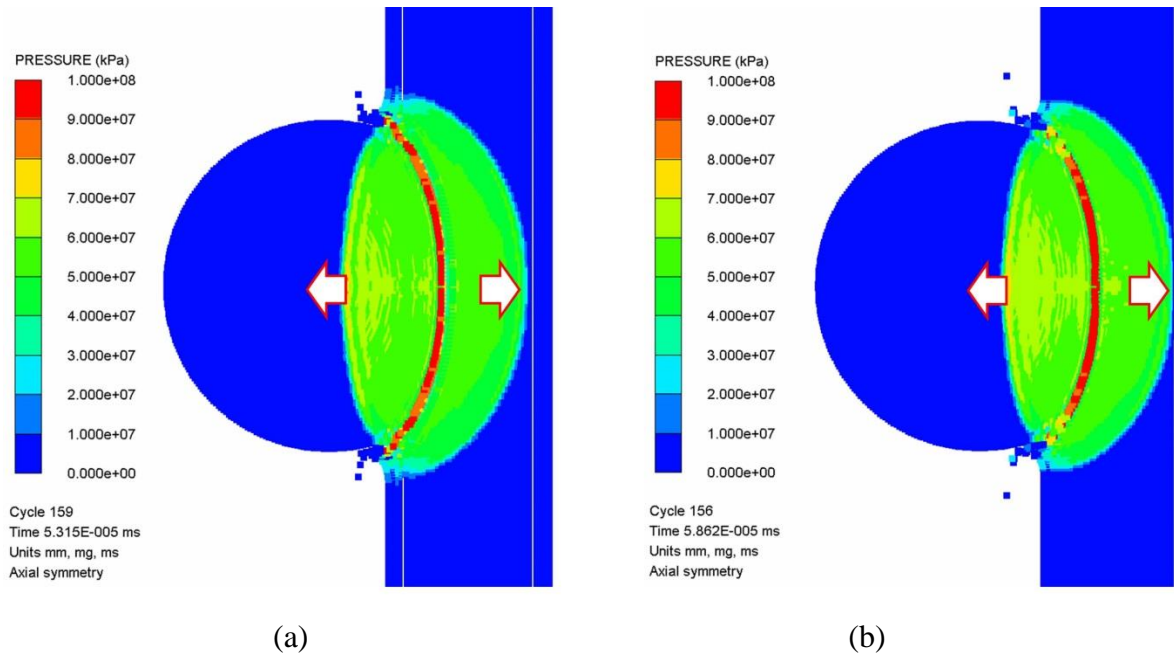
Figure 32 – Shock waves in projectile and bumper at the time of arrival to the impedance

boundary: a) ceramo-metallic bumper; b) all-aluminum bumper

Fig. 33 illustrates decay of the shock wave amplitude in the course of its propagation within

the projectile. Each data point in the figure corresponds to the maximum pressure passing

through the corresponding gauge during propagation of the shock wave from the impact

interface to the back side of the projectile. According to the figure, at the initial moment of

time after impact, the interaction of the projectile with the high impedance SiC layer

generates a shock wave with the amplitude about 18 GPa higher than in the case of the

impact of an aluminum projectile on the all-aluminum bumper. In both cases, shock wave

amplitudes are subject to decay due to the energy dissipation. At the time when the shock

waves pass through gauges #9, this difference reduces to 1.2 GPa, according to the

numerical analyses. It is expected that higher initial pressure in the projectile, in case of

laminated bumper, can assist in its better fragmentation.

81
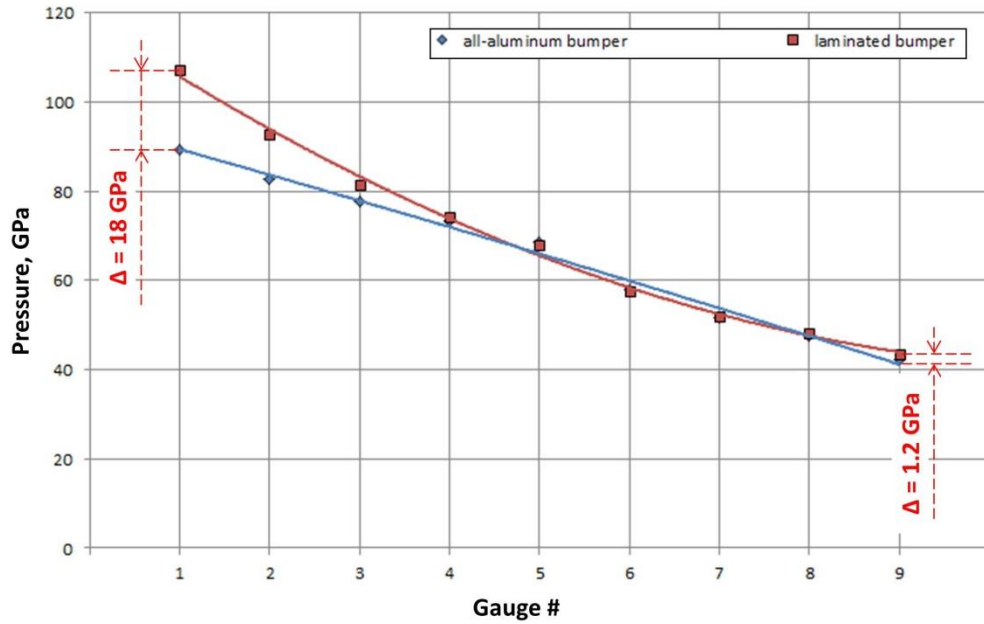
Figure 33 – Shockwave amplitude in aluminum projectile

(a)   (b)
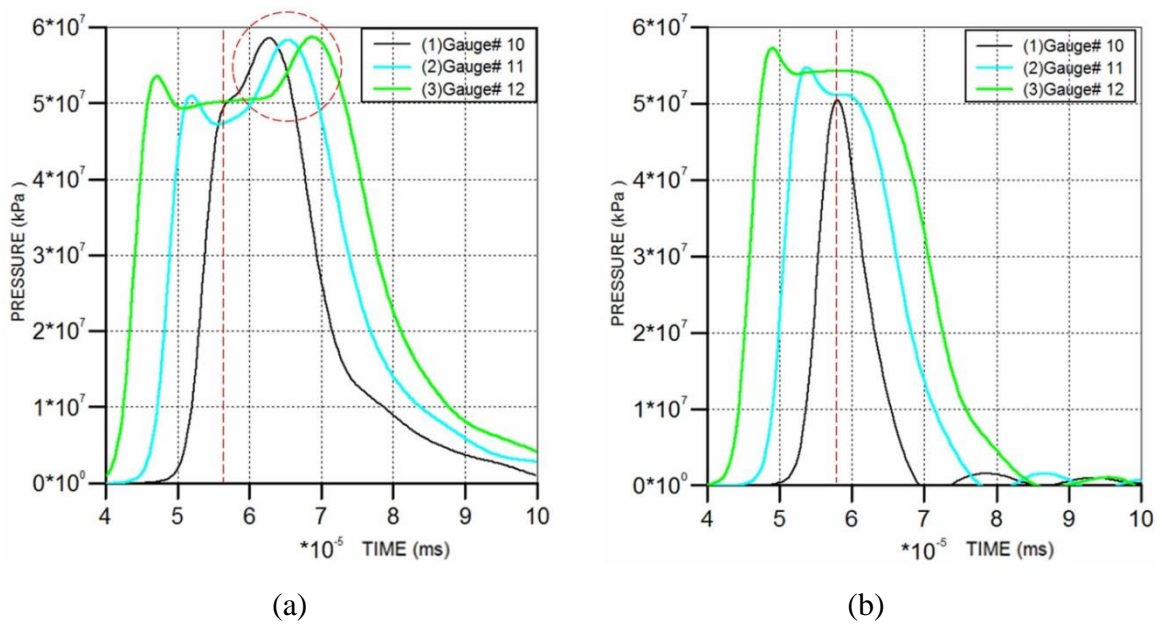
Figure 34 – Pressure pulses passing through the gauges No.10 – 12 in ceramo-metallic

bumper (a) and all-aluminum bumper (b)

Pressure pulses passing through the gauges No.10–12 in the laminated bumper and all-

aluminum bumper are shown in Fig. 34 (a) and (b), respectively. The moments of time

when the shock waves arrive at the corresponding back side impedance boundaries are shown by the red vertical lines in Fig. 34 (a), (b). In the case of the all-aluminum bumper, the shock wave expectedly reflects from the free surface as a rarefaction wave (note a pressure drop on all gauges in Fig. 34 (b) after reflection from the impedance boundary).

On the contrary, when the shock wave in ceramo-metallic bumper reaches the second high impedance layer, the pressure will rise due to impedance difference. The pressure peaks detected on gauges No. 10–12 in Fig. 34 (a) (encircled) correspond to the pressure jump that was schematically shown in Fig. 30 (c) in Section 3.6. According to data acquired from these gauges, the pressure rise has the order of 8 GPa. The reflected compressive wave of this amplitude will propagate in the compressed core material (aluminum) towards the approaching projectile, suppressing spall and increasing the overall shock pressure.

3.8 Whipple Shields with Ceramo-metallic Bumpers

This section presents results of the physical and numerical HVI experiments on Whipple shields with ceramo-metallic bumpers. As the reference designs to compare with, Whipple shields with all-aluminum bumpers were also considered.

Two types of bumpers, namely "optimal" and "non-optimal", were studied in this section. The optimal bumpers (both all-aluminum and laminated) had bumper thickness-to-projectile diameter ratio, which provides the minimal weight for all-aluminum Whipple shield, while satisfying the no-perforation constraint. According to Ref. [3], this ratio is $t_b/D_p = 0.25$. Both optimal and non-optimal laminated bumpers have been designed to contain approx.75% of aluminum by weight. Parameters of all bumpers considered in this section are provided in Table 9.

Table 9 – Parameters of the non-optimal and optimal bumpers

Type of bumper	Bumper thickness to projectile diameter ratio	Thickness of SiC layer, mm	Thickness of aluminum layer, mm	Areal density, g/cm²
Non-optimal bumpers				
All-aluminum	0.40	–	0.40	0.108
Laminated	0.50	0.05 x 2	0.40	0.140
All-aluminum	0.52	–	0.52	0.140
Optimal bumpers				
All-aluminum	0.25	–	0.25	0.068
Laminated	0.24	0.03 x 2	0.18	0.068

Calculations with the optimal bumpers of the same weight were conducted in order to determine how the use of ceramo-metallic bumpers can improve weight-efficiency of the Whipple shield. The non-optimal bumpers were considered in this study for two reasons. First, experiments with the non-optimal bumpers were used for validation of the numerical models. Also, the non-optimal bumpers can have a practical application as face sheets of multifunctional sandwich panels, where "additional" thickness may be needed due to structural requirements (e.g., minimal bending stiffness of a sandwich panel), or can be parts of single-purpose MMOD shields in case when using the optimal thickness might result in undesired buckling and permanent deformation of the bumper under launch loads or in installation/manufacturing, etc.

Nominal parameters of the projectile for all physical and numerical experiments described in this section are provided in Table 10.

Table 10 - Initial nominal parameters of the projectiles in the physical and numerical experiments

Diameter, mm	Mass, mg	Speed, m/s	Kinetic energy, J	Momentum, mg*m/s
1.0	1.4	7000	34.4	9820

Rear walls of the Whipple shields in all cases were made of aluminum. The standoff between the bumper and the rear wall was the same for all configurations and chosen from the typical range of $15Dp < S < 30Dp$ (see Ref. [62]) as $S = 16$ mm.

3.8.1 Whipple shields with the non-optimal bumpers

Whipple shields with the non-optimal bumpers were studied both experimentally and theoretically. The physical HVI experiments were conducted using a two-stage light gas gun at HIT Dynamics Ltd. impact testing facility (NB, Canada). The 0.05 mm silicon-carbide layers were deposited on aluminum substrates in a customized Balzer's chamber using the physical vapor deposition technique (PVD) by Entegris Specialty Coatings. Parameters of the fabricated specimens and the experimental setup are exemplified in Fig. 35 and Fig. 36, correspondingly. Thickness of the coating was measured by the manufacturer using both profilometery, and using an eddy current meter on the actual part.

In the physical tests, all projectiles came from the same lot and had a diameter tolerance of ±0.03 mm. All tests were performed in an evacuated chamber with a pressure of approximately 31 Torr. The targets were aligned such that the angle of incidence was within ±1degree. The imagery was recorded using the high-speed framing camera. Initiation of the image sequence was triggered from laser trap output and timed according

to the expected projectile speed. The camera settings were the same for all tests, which resulted in a total time between frames of 0.381 μs. Speed measurements were performed using laser intervalometers as the primary means, with high-speed video imagery being a secondary means. Measured projectile speeds for the case of 0.4 mm all-aluminum and 0.5 mm ceramo-metallic Whipple shields were 7.102 km/s and 7.063 km/s, correspondingly.

Comparison of the high-speed photographs and results of hydrocode simulations conducted for the same impact conditions are shown in Fig. 37. The following features of the debris clouds can be distinguished in the figure:

- the debris cloud produced by the impact on the ceramo-metallic bumper is visually "darker". This may be an indication of more uniform distribution of individual fragments over the surface of debris cloud and finer fragmentation of the projectile;

- the speed of the debris cloud in the case of the all-aluminum bumper is noticeably higher;

- the radial expansion of the debris cloud is higher for the case of the all-aluminum bumper.

It can be deduced from Fig. 37 that the numerical simulations are capable of predicting all of the features listed above, and the predictions, including the overall shapes of the debris clouds, are very similar to those observed in the physical experiments.
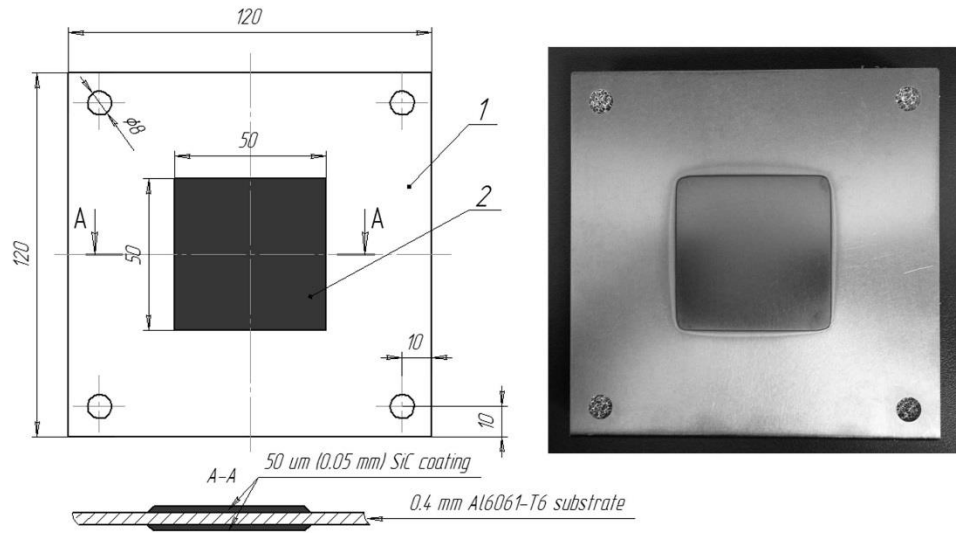
Figure 35 – Ceramo-metallic bumper with SiC coating (note: thickness of the coating was intentionally exaggerated in the drawing)
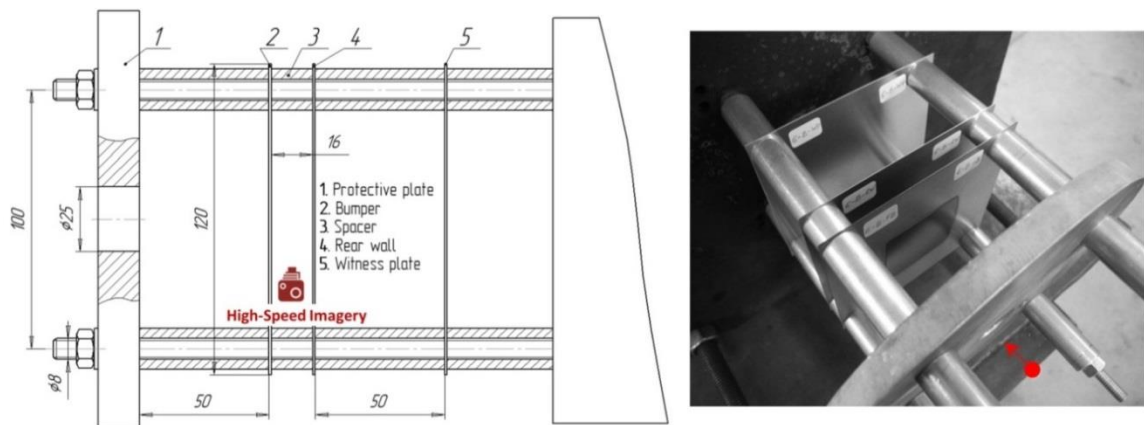
Figure 36 – Test setup for HVI experiments
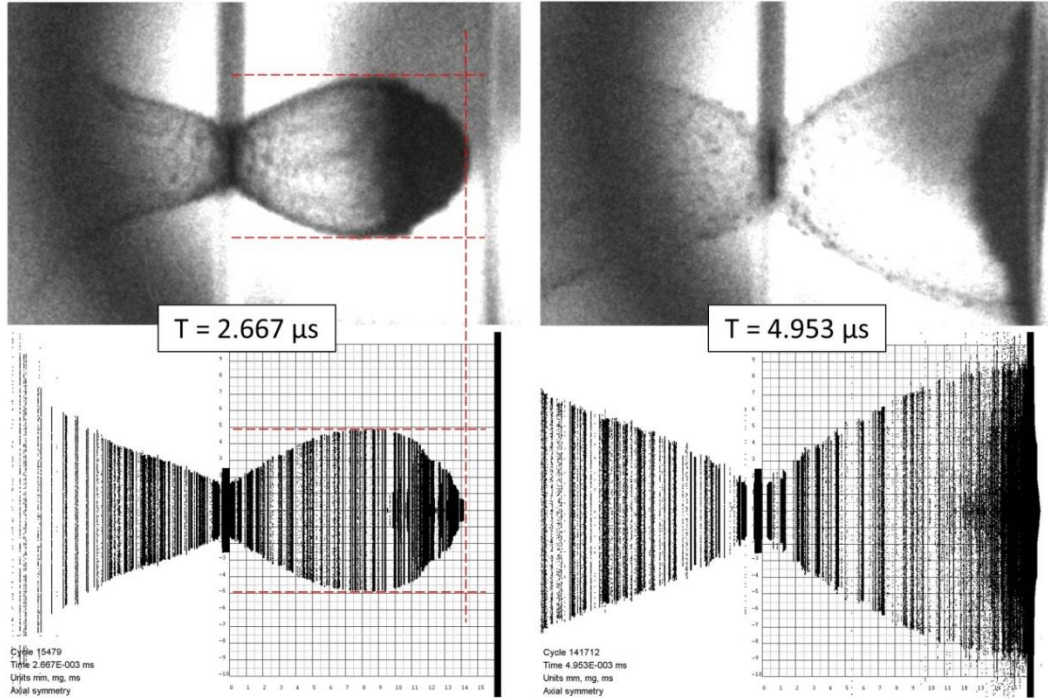
(a)
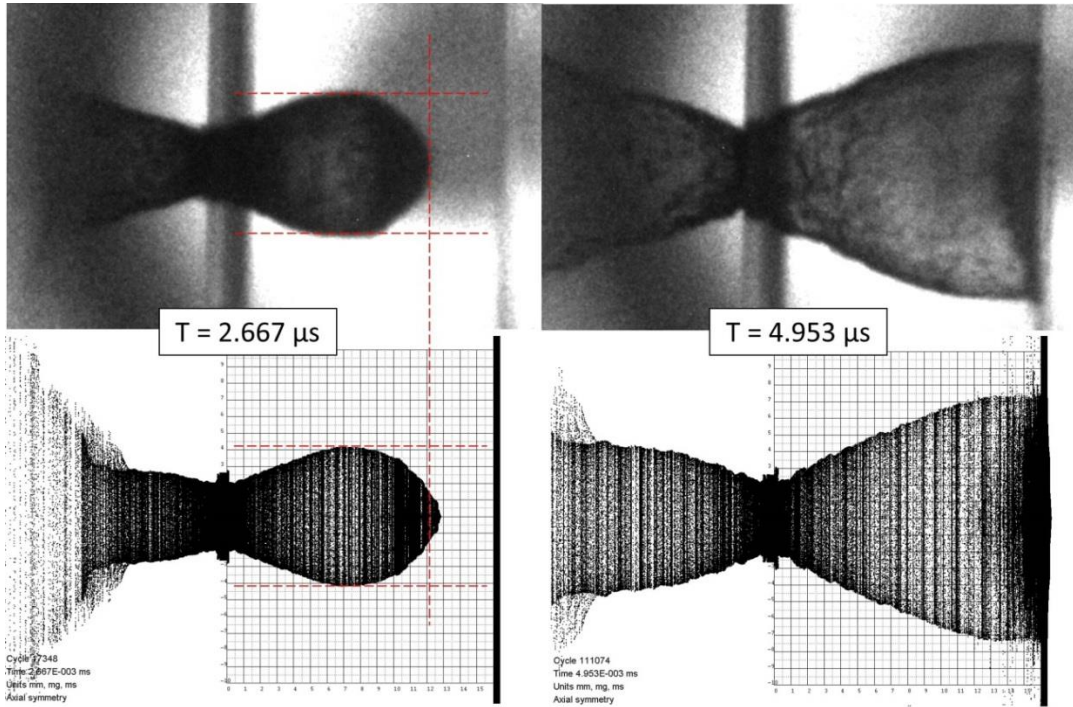
(b)

Figure 37 – Comparison of debris cloud shapes (experiment vs. simulation) for <u>0.4 mm</u>

all-aluminum (a) and ceramo-metallic (b) bumpers
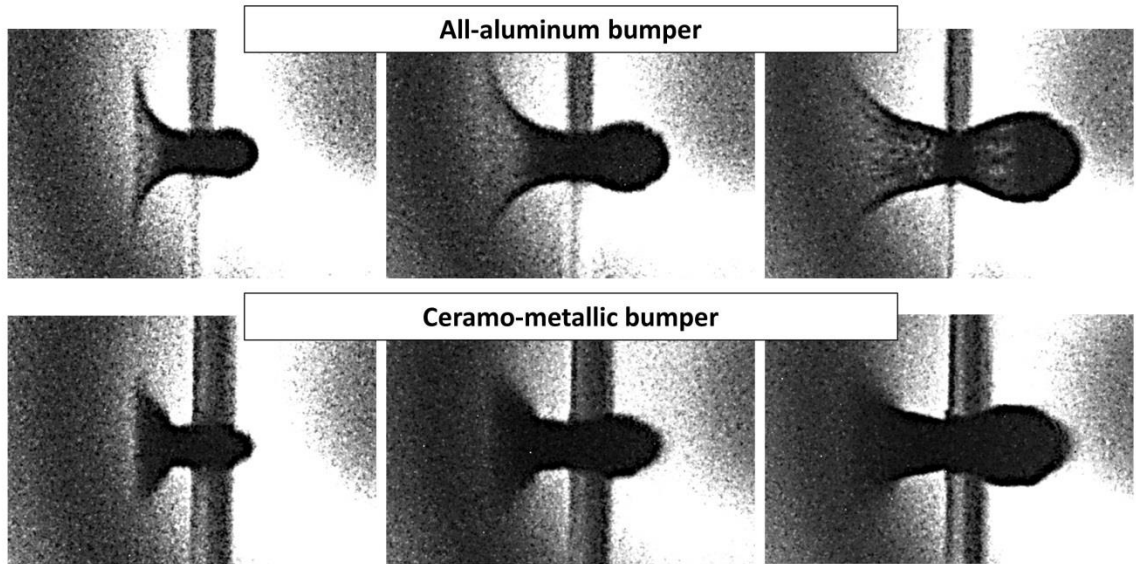
Figure 38 – Shapes of debris clouds

Shapes of debris clouds at initial moments after perforation of the bumpers are shown in Fig. 38. As it can be deduced from the figure, the presence of the SiC layers affects the initial shape of the debris cloud.

Additional statistical information on the fragments size and distribution was gained through the use of «Output Fragment Analysis» option in AUTODYN, which provides the fragmentation information summary. All statistical estimates hereafter consider only fragments between the bumper and the rear wall and having positive velocity vector components coincident with the direction of impact, which excludes all ejecta from consideration.

In addition to the shield configurations tested experimentally, the statistical data was also obtained for a configuration with the all-aluminum bumper of the same weight as the tested ceramo metallic bumper, which corresponded to the thickness of all-aluminum bumper of 0.52 mm. The statistical parameters are provided in Table 11. Fig. 39 – 42 provide

information on the distribution in debris clouds of the fragments with high weight and momentum.

Table 11 – Statistical data on the fragments moving towards the rear wall at t = 2.667μs after projectile-bumper collision (non-optimal bumpers)

Parameter	All-aluminum bumper (0.40 mm)	All-aluminum bumper (0.52 mm)	Ceramo-metallic bumper (0.50 mm)
Total number of fragments	185	205	172
Total mass of fragments / Projectile mass	1.56	1.83	1.60
Average mass per fragment, mg	0.0118	0.0125	0.0131
Mass standard deviation, mg	0.0221	0.0255	0.0228
Total kinetic energy of fragments / Initial projectile energy	0.61	0.48	0.46
Total X-wise momentum of fragments/ Initial X-wise momentum of projectile[10]	0.88	0.80	0.76
Weight of the most massive fragment, mg	0.187	0.163	0.110
Speed of the most massive fragment, m/s	4780	4440	4340
Kinetic energy of the most massive fragment, J	2.23	1.66	1.09
X momentum of the most massive fragment, mg*m/s	892	723	476

The statistics show that although fragments in average are slightly less massive in the case of 0.4 mm all-aluminum bumper, the largest fragment in the debris cloud is in this case almost twice as massive and energetic as compared with the largest fragment in the case of the ceramo-metallic bumper. For the case of equivalent-weight all-aluminum bumper (t_b =

---

[10] X is the impact direction

90

0.52 mm), both average fragment weight and the largest fragment weight are significantly higher than in the case of the ceramo-metallic bumper. The bumper with the high impedance coating, therefore, outperforms both of the considered all-aluminum bumpers.
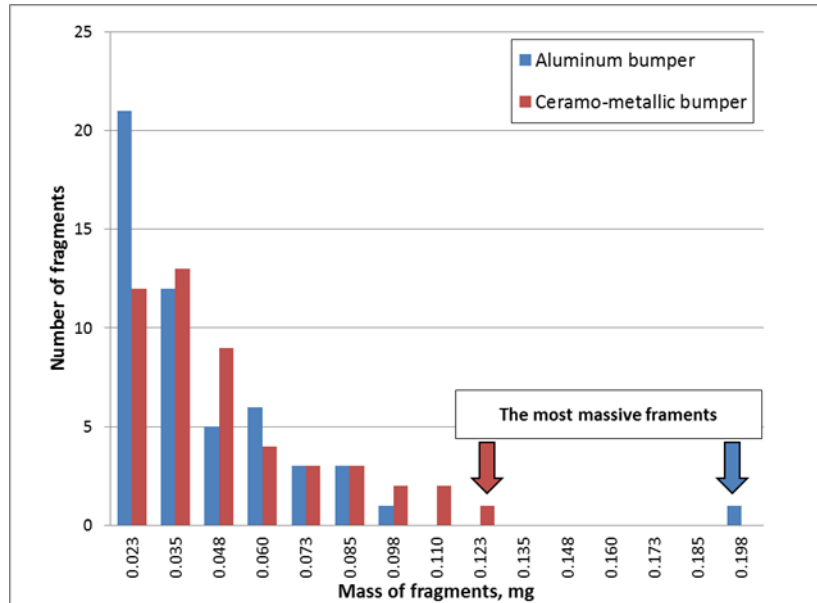
Figure 39 – Fragments with the weight over 0.01 mg
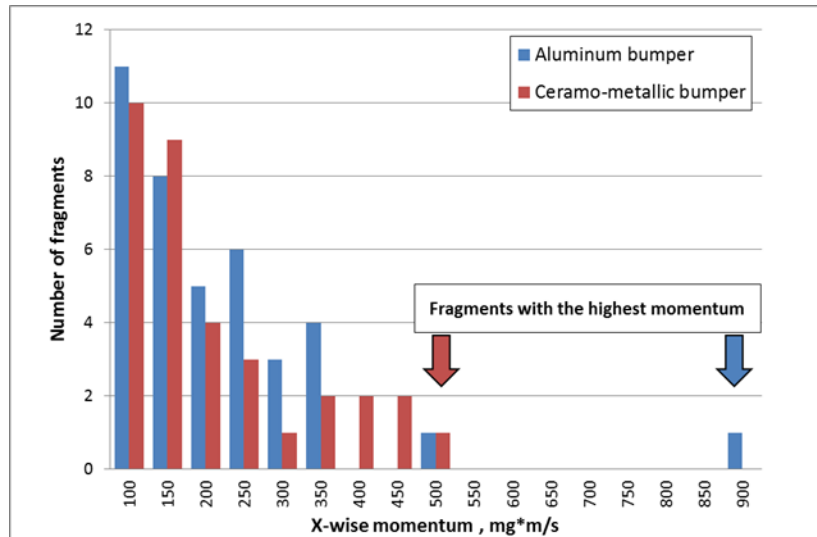
Figure 40 – Fragments with momentum in the rear-wall direction over 50 mg*m/s
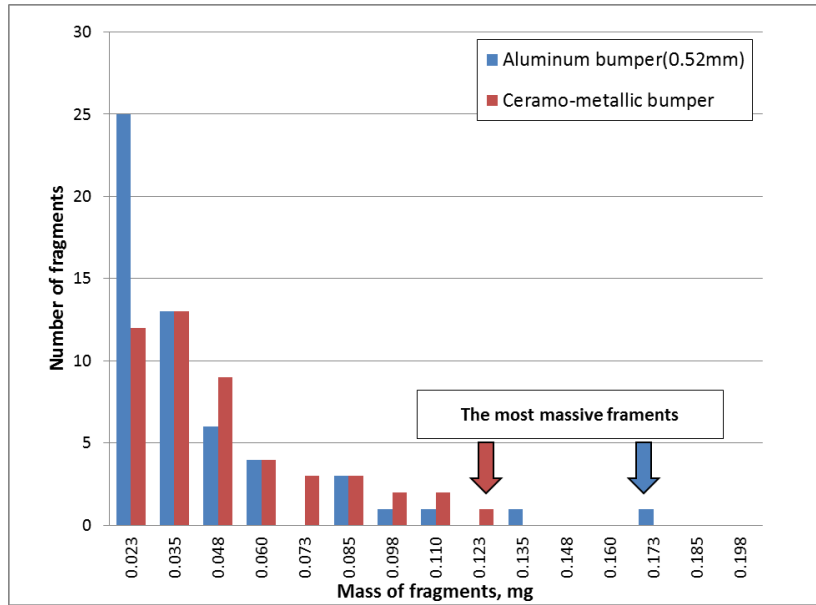
Figure 41 – Fragments with the weight over 0.01 mg (comparison with the equivalent-weight aluminum bumper)
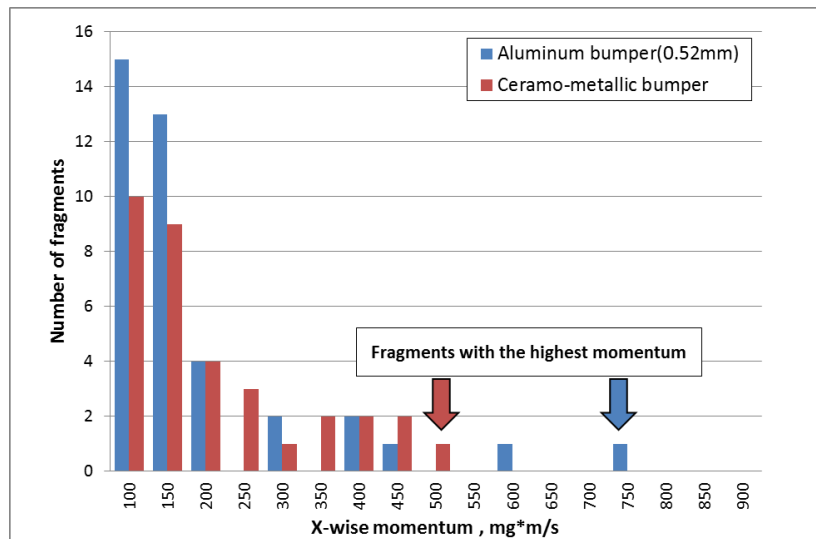
Figure 42 – Fragments with momentum in the rear-wall direction over 50 mg*m/s (comparison with the equivalent-weight aluminum bumper)

Experimental HVI damage of the bumpers and rear walls is exemplified in Fig. 43. The following observations can be made:

- the diameter of the perforation hole was slightly smaller in the case of 0.4 mm all-aluminum bumper;

- only small amount of SiC coating was removed by the impact in the region around the perforated hole; no "major" disruption of the coating occurred.

- rear wall damage of the all-aluminum specimens was surrounded by «burned» regions, whereas no such effect was observed with the ceramo-metallic specimens.

- relatively large momentum bulges were observed on the rear walls; measurements conducted using micrometer indicated that momentum bulge in the ceramo-metallic configuration was ~12.5% smaller than in the case when the 0.4 mm all-aluminum bumper was used.

- individual fragments form craters on the rear walls, which can be seen as tiny bumps from the back side; performed optical microscopy identified that none of them are perforations.

Numerical predictions for the bumper and rear wall damage are exemplified in Fig. 44 – 45. Comparison of the corresponding experimental and numerical results is given in Table 12. The numerical predictions are in good agreement with experimental data. It can also be noted that although slightly smaller rear wall deflection was obtained for the case of the equivalent-weight all-aluminum bumper (0.60 mm), than for ceramo-metallic bumper (0.64 mm), in the former case much larger individual craters were formed on the rear wall (encircled in Fig. 45), which indicates the presence of large individual fragments in debris

cloud generated after impact on the 0.52 mm all-aluminum bumper. Such fragments do not form if the ceramo-metallic bumper is used.
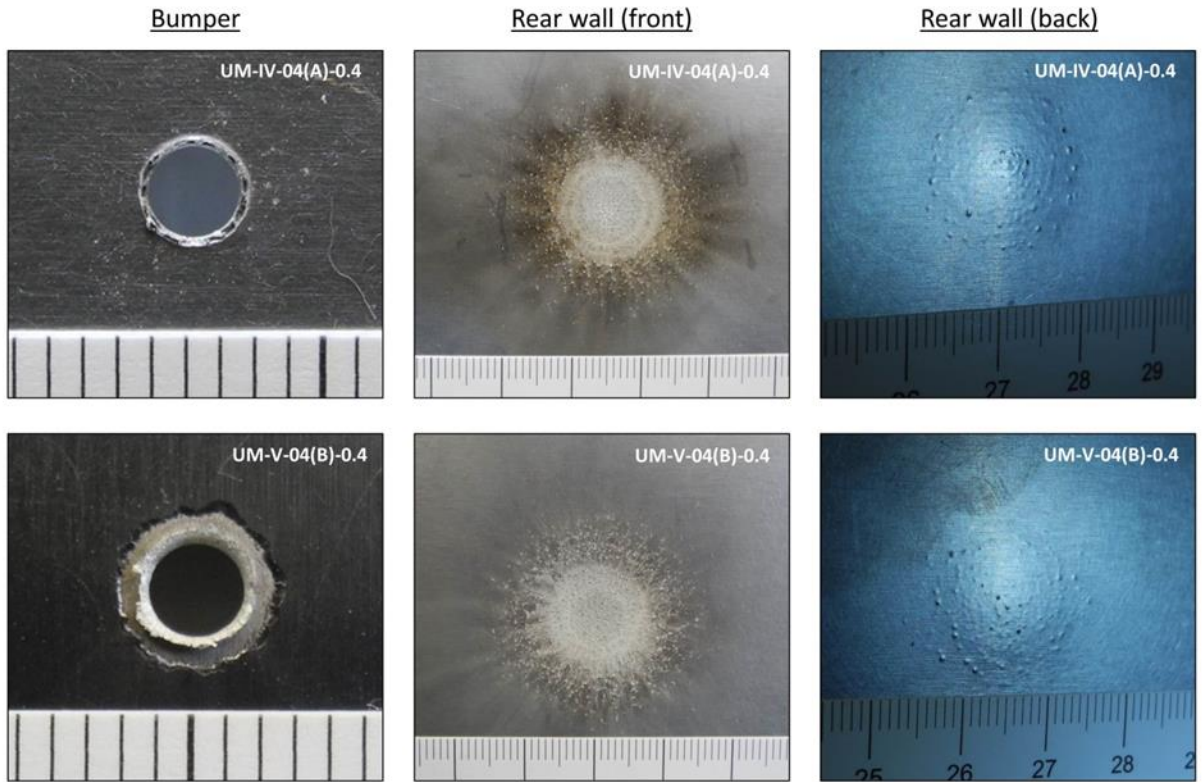
Figure 43 – Damage of the Whipple shields with 0.4 mm all-aluminum (top) and 0.5 mm ceramo-metallic (bottom) bumpers
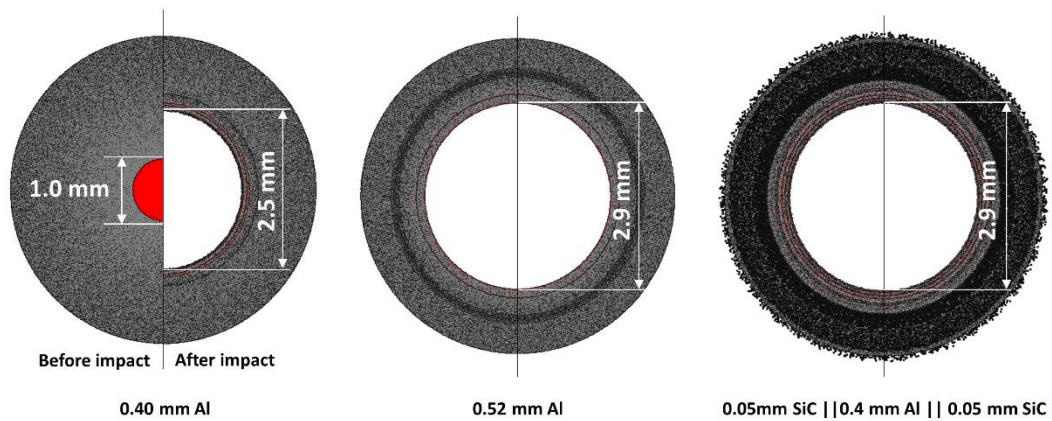
Figure 44 – Bumper holes predicted by the numerical experiments
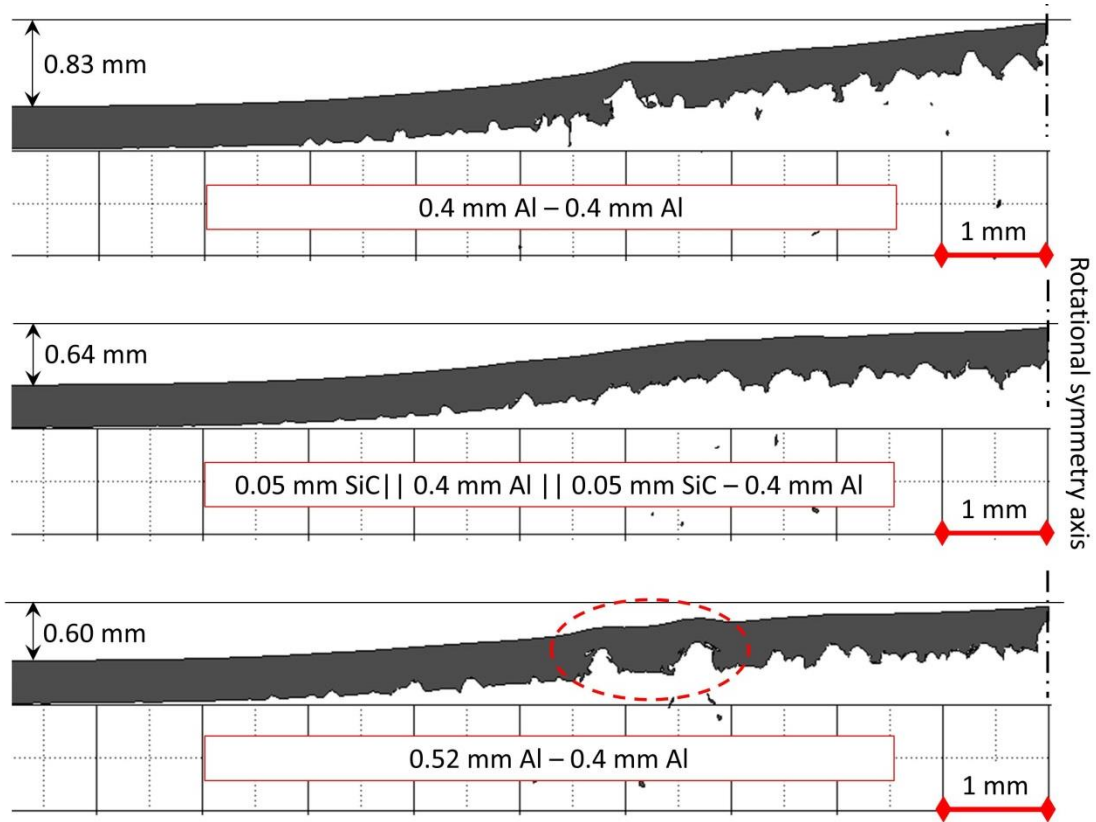
Figure 45 – Measuring the rear wall bulge height as predicted by numerical experiments

for the Whipple shield with 0.4 mm all-aluminum bumper (top), 0.5 mm ceramo-metallic

bumper (middle) and 0.52 mm all-aluminum bumper (bottom)

Table 12 – Comparison of the experimental measurements and simulation predictions

	Shield with 0.40 mm all-aluminum bumper	Shield with 0.52 mm all-aluminum bumper	Shield with ceramo-metallic bumper
Bumper hole diameter from physical experiment, mm	2.60	N/A	2.80
Bumper hole diameter from simulation, mm	2.50	2.90	2.90
Rear wall bulge height from physical experiment, mm (in)	0.813 (0.032)	N/A	0.711 (0.028)
Rear wall bulge height from simulation, mm	0.830	0.600	0.640

Consequently, the results provided in this section allow considering the simulations as sufficiently validated. In addition, the obtained results indicate that the ceramo-metallic shield provides better protection as compared to both of the considered all-aluminum configurations, including the all-aluminum configuration with the bumper weight equivalent to that of the ceramo-metallic bumper.

Additional series of computations was carried out with the equal weight all-aluminum and ceramo-metallic bumpers of the "optimal thickness" (i.e. when bumper thickness – projectile diameter ratio $t_b/d_p = 0.25$). These computations are described in the following section.

3.8.2 Whipple shields with the optimal bumpers

The debris clouds generated as a result of HVI on optimal bumpers with parameters presented in Table 9 are exemplified in Fig. 46. It can be deduced from the figure that the speed of the debris clouds and their radial expansion are similar in the case of equivalent-weight all-aluminum and ceramo-metallic bumpers.

The statistical data regarding parameters and distribution of fragments in the debris clouds is provided in Table 13 and Fig. 47 – 48. Analysis of this data confirms that the use of ceramo-metallic bumpers results in better fragmentation of the projectile, less massive and less energetic fragments as compared with the all-aluminum bumper of the same weight.
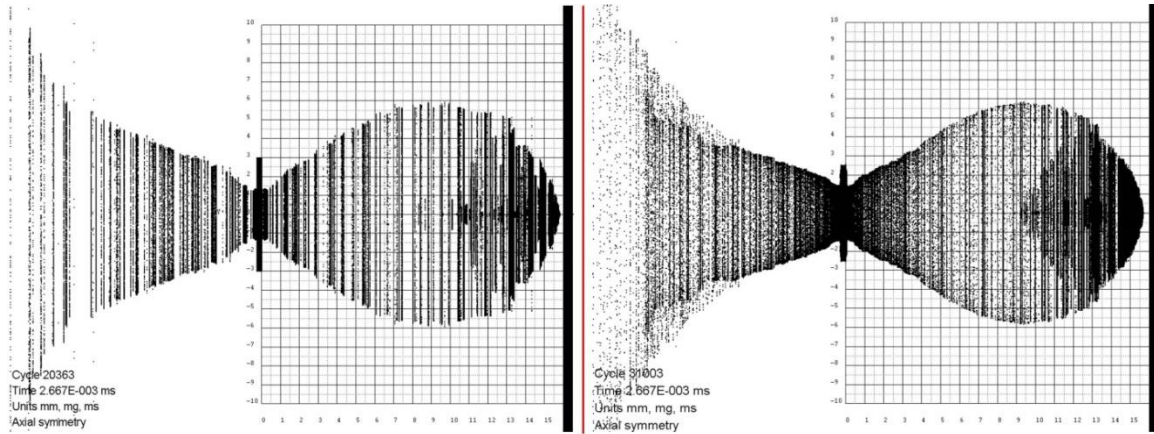
Figure 46 – Shapes of the debris clouds after impact on all-aluminum bumper (left) and ceramo-metallic bumper (right) at t = 2.667 μs

At the next stage, Whipple shields with the both types of bumpers were designed to have the minimal possible weight while satisfying the no-perforation criterion, by varying rear wall thicknesses. As a starting point in the design process, all-aluminum Whipple shield with parameters as predicted by the Christiansen ballistic limit equation [3, 62] was considered. The BLE predicts the rear wall thickness of $t_w = 0.60$ mm for the given impact conditions. No perforation of the rear wall was observed in this case in numerical simulation [see Fig. 49 (a)]. Attempts to further reduction of the rear wall thickness ($t_w = 0.50$ mm) led to its perforation [Fig. 49 (b)]. Therefore, optimal parameters of the all-aluminum Whipple shield determined via hydrocode simulations are in exact agreement with the prediction of BLE. As can be deduced from Fig. 49 (c) - (d), at the same impact conditions the ballistic limit of the Whipple shield with the ceramo-metallic bumper corresponds to the rear wall thickness of 0.5 mm. This makes the Whipple shield with the ceramo-metallic bumper 11.7% lighter than the optimal all-aluminum Whipple shield. Parameters of the optimal Whipple shields satisfying the no-perforation criterion are given in Table 14.
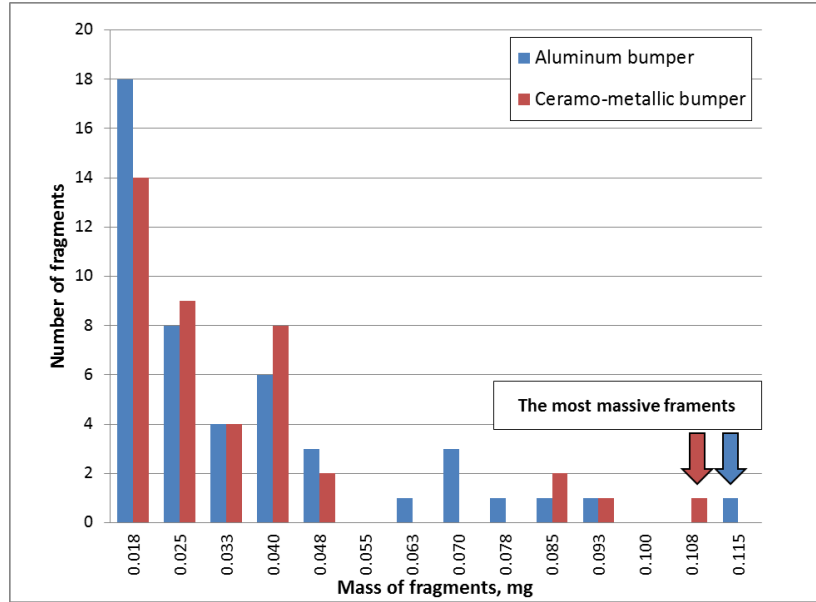
Figure 47 – Fragments with the weight over 0.01 mg
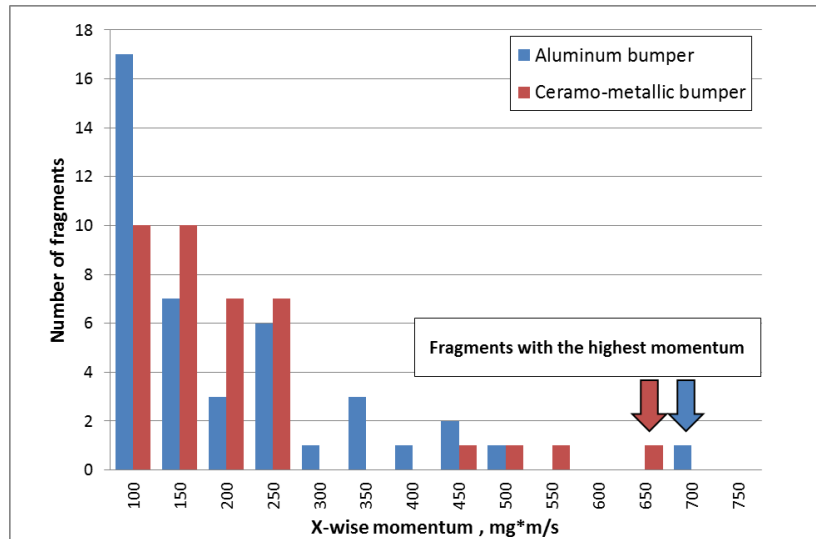
Figure 48 – Fragments with momentum in the rear-wall direction over 50 mg*m/s

98

Table 13 – Statistical data on the fragments moving towards the rear wall at t = 2.667μs after projectile-bumper collision (optimal bumpers)

Parameter	All-aluminum bumper	Ceramo-metallic bumper
Total number of fragments	239	259
Total mass of fragments / Projectile mass	1.26	1.19
Average mass per fragment, mg	0.0074	0.0064
Mass standard deviation, mg	0.0158	0.0136
Total kinetic energy of fragments / Initial projectile energy	0.74	0.69
Total X-wise momentum of fragments/ Initial X-wise momentum of projectile[1]	0.91	0.86
Weight of the most massive fragment, mg	0.111	0.103
Speed of the most massive fragment, m/s	6030	6060
Kinetic energy of the most massive fragment, J	2.03	1.90
X momentum of the most massive fragment, mg*m/s	670	623

Table 14 – Parameters of the optimal Whipple shields

Type of shield	Bumper	Standoff	Rear wall	Areal density
Whipple shield with *all-aluminum* bumper	0.25 mm Al6061	16 mm	0.6 mm Al6061	0.230 g/cm^2
Whipple shield with *ceramo-metallic* bumper	0.03 mm SiC ‖ 0.18 mm Al6061 ‖ 0.03 mm SiC	16 mm	0.5 mm Al6061	0.203 g/cm^2
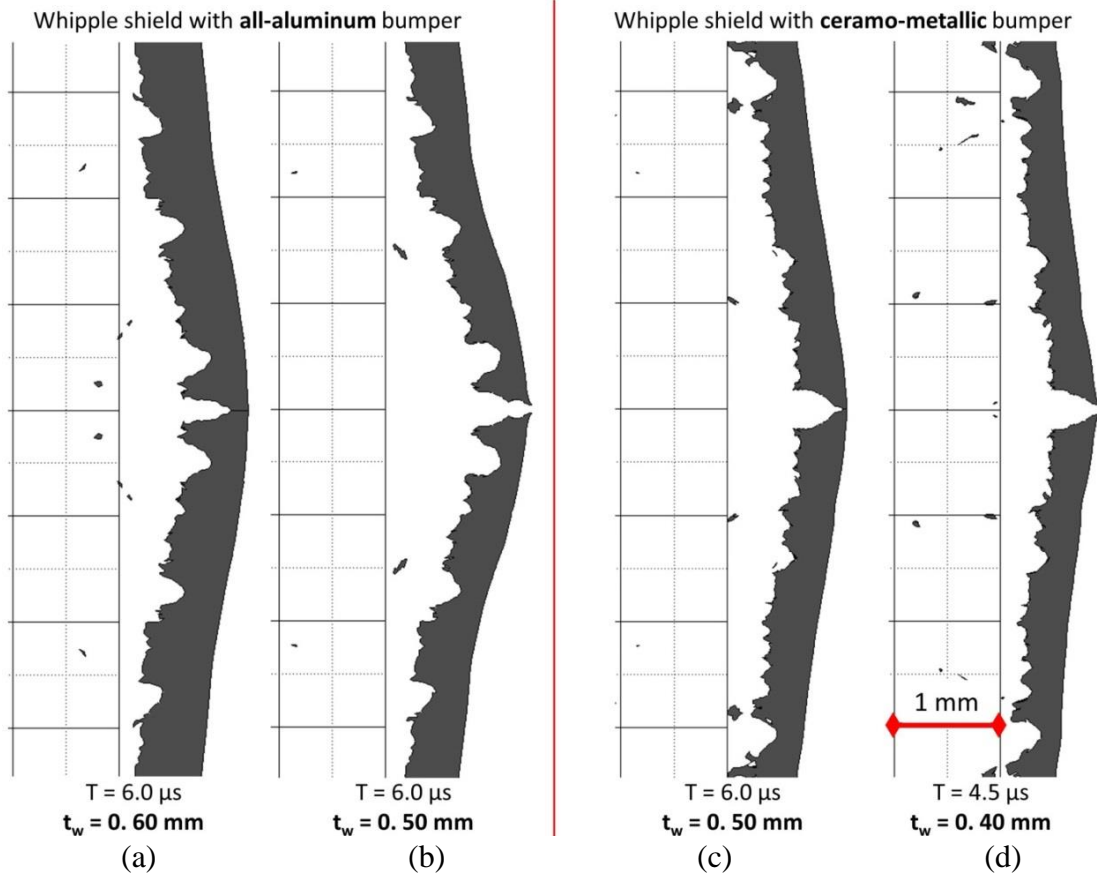
Figure 49 – Rear wall damage for the Whipple shields with the optimal bumpers

3.9 Discussion

According to the numerical simulations, the parameters of the shielding configurations that satisfied the imposed constraints ("no-perforation" for single-purpose shields and "no-perforation" + bending stiffness and equal facesheet thickness for multi-purpose structural panels) and had the minimal weight in their class are as follows:

1. Single-purpose MMOD shields:

    *   WS: 0.25 mm Al6061 + 0.6 mm Al6061;

    *   SWS: 0.15 mm Al6061 + 1 ply Nextel 312 AF-12 || 1 ply KFRP + 0.45 mm Al6061;

    *   CMWS: 0.03 mm SiC || 0.18 mm Al6061 || 0.03 SiC + 0.5 mm Al6061;

2. Multi-purpose structural panels:

- HCSP: 1.45 mm A6061 + [1/8 – 0.0015] aluminum honeycomb (16 mm-thick) + 1.45 mm Al6061;

- FCSP: 0.5 mm Al6061 + 3% 40 ppi aluminum foam (16 mm-thick) + 0.5 mm Al6061.

	WS	CMWS	SWS		HCSP	FCSP
☐ Non-ballist. weight	0.069	0.061	0.134		0.000	0.000
▨ Rear wall	0.162	0.135	0.122		0.392	0.135
⊠ Core or stuffing	0.000	0.000	0.087		0.156	0.130
■ Front wall	0.068	0.068	0.041		0.392	0.135
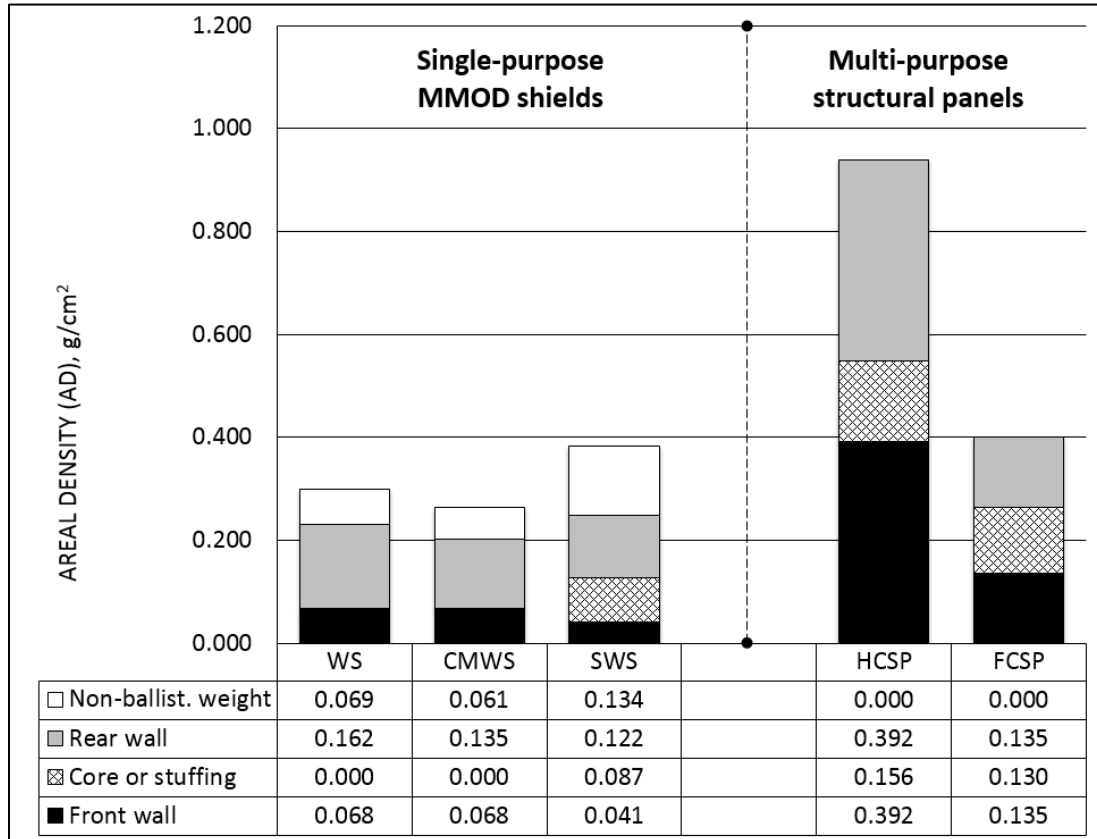
Figure 50 – Areal densities of the shielding configurations

(Total areal densities of the shields, g/cm^2: 0.299 [WS], 0.264 [CMWS], 0.384 [SWS],

0.940 [HCSP], and 0.400 [FCSP])

It should be noted that, in addition to ballistic weight, the single-purpose shields also have

some non-ballistic mass associated with the standoff structure, which, according to Ref.

[3] and [67], can be estimated as 30% of the ballistic weight for Whipple shields (the same

was assumed for the ceramo-metalic Whipple shield) and 35% of the total (i.e., both non-ballistic and ballistic weights included) weight for stuffed Whipple shields.

Areal densities of the shields are compared in Fig. 50. Analysis of this data for the conventional shields (i.e. WS and SWS only) shows that, in terms of ballistic weight, neither of them has a significant advantage over the other when designed against small-size orbital debris impacts. Indeed, the ballistic weight of WS is 0.230 g/cm^2 and the ballistic weigh of SWS with 0.45 mm rear wall is 0.250 g/cm^2. However, when the non-ballistic weights are added, the total weight of the SWS (0.384 g/cm^2) appears to be significantly higher than the total weight of the Whipple shield (0.299 g/cm^2).

This trend remains even if the slightly perforated SWS configuration with a 0.35 mm-thick rear wall is considered (ballistic areal density is 0.226 g/cm^2; total AD = 0.342 g/cm^2). Quantitatively, the total area density of the SWS is 14–28% higher (lower and upper estimates are for SWSs with 0.35 and 0.45 mm rear walls, respectively) than that of WS.

This result is unexpected, as the stuffed shield concept is typically thought of as more weight-efficient (as confirmed for ISS shields designed against centimeter-size projectiles; see Table 2). A possible reason for this is that the linear dependence between SWS weight and projectile diameter, which exists for the large hypervelocity projectiles (see Section 3.4), may not hold for millimeter-size particles that are orders of magnitude less energetic.

The total areal density of the ceramo-metallic shield (0.264 g/cm^2) is 11.7% lower than the Whipple shield because of the thinner rear wall, and $23 - 31\%$ lower than that of the stuffed Whipple shield. The higher weight efficiency of the ceramo-metallic shield can be explained by the combined action of a) stronger shock loading of the projectile, potentially

resulting in its better fragmentation; and b) compressive stress wave reflected from the rear impedance boundary and propagating towards the approaching projectile, which increases the overall shock pressure.

It can therefore be suggested to consider the ceramo-metallic Whipple shield or, as a second choice, simpler Whipple shield configuration for protecting critical components of unmanned spacecraft, when the baseline spacecraft structure does not provide the means of protection against orbital debris.

As can be seen in Fig. 50, the absolute winner in the "multi-purpose structural panels" category is the foam-core sandwich panel. The areal density of FCSP is more than twice as low in comparison with HCSP having a similar ballistic performance, even in the presence of the minimal bending stiffness constraint (see Section 3.3), which limits further reduction of the FCSP facesheets' thickness. The physical experiment conducted revealed a positive margin of safety for the foam-core panel against perforation by a 1 mm, 7 km/s aluminum projectile. Conversely, the reference structural sandwich panel (0.5 mm facesheets and a 16-mm-thick core; see Section 3.3), if made with a honeycomb core in the baseline design, will not provide the required level of protection against orbital debris for the critical spacecraft components located behind it. It follows from Fig. 50, then, that modification of this panel by thickening its facesheets is weight inefficient as compared to replacement of the honeycomb by the open-cell aluminum foam design. In the latter case, there will be zero weight impact for the spacecraft structure, as the weight of the FCSP is similar to the weight of the reference HCSP (both have 0.5-mm-thick facesheets, and core density is also similar; see Table 6).

The absolute winner in the "Multi-purpose structural panels" category is the foam-core sandwich panel. The FCSP is *more than twice as light* as the honeycomb-core panel having similar ballistic performance, even in the presence of the minimal bending stiffness constraint limiting the further reduction of facesheets' thickness of the FCSP. Conducted physical experiment revealed positive margin of safety for the foam-core panel against perforation by a 1 mm 7 km/s aluminum projectile. This demonstrates potential for even higher weight savings when using FCSPs in case if design considerations allow for relaxing the stiffness constraint.

Also, it can be noted in Fig. 50 that the areal density of FCSP, even in the presence of the structural constraint, is comparable to the values provided by the single-purpose shields. This makes it possible to consider FCSP as a prospective alternative to WS and SWS in their category for protection against small-size projectiles. If the structural constraint is relaxed, then the required facesheet thickness of FCSP will be in the range from 0.25 mm (as predicted by BLE in Section 3.4; this may be a non-conservative prediction) to 0.4 mm (the panel with such facesheet thickness was found in our experiment to be safely below its ballistic limit, as described in Section 3.5.2.2). The ballistic areal density of such panels then will be in the range of 0.265–0.346 g/cm^2. Even at the lower end of this range, this is higher than the ballistic areal densities of WS and SWS. However, the non-ballistic weight of the foam panel may be significantly less than that of the WS and SWS, as no additional stiffeners or other supporting elements may be required because of the inherently high stiffness of the sandwich panel. Moreover, the non-ballistic weight estimates provided in this study for WS and SWS relied on statistics for the shields designed against large-size projectiles. It may be expected, however, that for shields designed against small-size

debris, the percentage of non-ballistic weight in the total weight of WS and SWS may be somewhat higher. For example, additional or thicker stiffeners may be required to avoid buckling or irreversible deformations of the thin bumpers at launch, etc. However, because of the lack of dedicated statistical or other estimates, it is not possible to make a definitive conclusion on the efficiency of FCSP as a single-purpose MMOD shield at this time.

3.10 Summary

In this chapter, four *conventiona*l shielding systems and one *novel* shielding concept were evaluated for their weight efficiency when designed to protect a spacecraft against small-size (1 mm) orbital debris impacts at 7 km/s. The shielding systems were compared within two categories, namely "Single-purpose MMOD shields" represented by Whipple shield, stuffed Whipple shield and a novel shield with the ceramo-metallic bumper, and "Multi-purpose structural panels" category represented by honeycomb-core and foam-core sandwich panels.

Sizing of the shields was carried out using ballistic limit equations and numerical analyses employing a combination of Ansys AUTODYN finite element (FE) and smooth particle hydrodynamics (SPH) solvers. Experimental results-based procedure for identification of erosion strain for FE-discretized parts was described.

Prediction of performance of the foam-core panel was based on the meso-scale representation of the open-cell foam geometry and was verified by means of the physical experiment. Physical experiments were also used for verification of the numerical models used in the simulations of the ceramo-metallic shields (the case of non-optimal bumpers).

The following conclusions can be made based on the results presented in this chapter:

1. If the baseline spacecraft structure does not provide the means for protecting a critical component against orbital debris, installation of an all-aluminum Whipple shield may be a better option than the stuffed Whipple shield, when protection against millimeter-size particles is required. Additional weight savings can be achieved if the ceramo-metallic shield is used.

2. If the critical component is located behind a honeycomb-core sandwich panel, which must be in place for structural reasons, and the structural panel in the baseline design does not provide the required level of orbital debris protection, then its modification through the replacement of the honeycomb core by aluminum foam will be more weight efficient than thickening the facesheets of the baseline honeycomb core panel. The calculations provided in this study show that HCSP will require almost 2.5 times more weight as compared with the FCSP, when both are designed against the same set of ballistic and structural constraints.

4. ANALYSIS OF HVI DAMAGE IN SHIELDED COPVs

4.1 Introduction

Following the design and evaluation of the shielding systems protecting a spacecraft pressure vessel against small-size orbital debris, it is important to develop a simulation approach capable of representing the behavior of shielded COPVs when perforated by larger-size hypervelocity projectiles. The simulation approach then can be used according to the design paradigm proposed in *Section 1.1* in order to predict whether the vessel will fail catastrophically or via non-violent gas leakage through the perforated hole.

In this chapter, a two-step procedure for computationally efficient modeling of HVI behavior of COPVs is proposed. The HVI behavior of the composite materials fabricated by means of the same manufacturing process as COPVs (filament winding) is then experimentally studied. Based on this study, the meso-scale technique suitable for modeling of the filament-wound composites is proposed and verified. The overall modeling procedure is then illustrated by an example of simulation of HVI on a shielded composite overwrapped pressure vessel.

4.2 Two-step Modeling Procedure

As it has been mentioned in *chapter 2*, at least 5 types of interactions have to be considered when analyzing behavior of shielded COPVs under HVI, including:

- interaction of orbital debris with the external shield;
- interaction of the secondary debris with the pressure wall;
- interaction of the tertiary debris (generated upon perforation of the vessel) with the gas or liquid within the vessel;

- propagation and interaction of the shock wave generated in the gas or liquid with the perforated pressure wall;

- interaction of tertiary debris cloud with the rear side of the vessel.

Simultaneous *explicit* representation of all of these interactions within a single numerical model (i.e. full "coupling") may be inefficient in terms of computational expensiveness and complexity. Review of the experimental observations presented in *chapter 2* provides the means of simplifying the numerical calculations. In particular, it has been observed experimentally that the tertiary debris cloud was totally ablated and decelerated if the pressure within the vessels exceeded a few atmospheres [33]. As in the most of the practical cases the internal pressure corresponds to hundreds of atmospheres (typically in the range of $100 - 800$ atm.), modeling of the interaction of the tertiary debris cloud with the gas and with the rear wall of the vessel can be omitted without affecting the adequacy of analysis. The presence of the gas, therefore, is required only for the modeling of the loading of the shell through internal pressure and the interaction of the shock wave with the perforated pressure wall. The latter effects, however, can be represented by the boundary conditions and do not require the explicit modeling of the gas in the three-dimensional calculations.

The effect of such simplification can be illustrated using an example of a cubical shell of thickness δ encompassing an internal volume of a^3. One can show that the ratio between the number of elements required to represent the internal volume $N_{el}^{<\text{int}>}$ and the number of elements required to represent the shell $N_{el}^{<shell>}$ is equal to $\dfrac{N_{el}^{<\text{int}>}}{N_{el}^{<shell>}} \approx \dfrac{a}{6\delta}$ (the case of structured mesh and equal-size cubical elements). In case when $a = 120$ mm and $\delta = 1$

mm, this ratio is equal to 20, which means that 95% of all elements representing the cubical tank will be the elements required to represent its internal volume and only 5% are the elements required to represent the shell. It is obvious then that the use of an *implicit representation* of the gas in the numerical model can dramatically increase the computational efficiency.
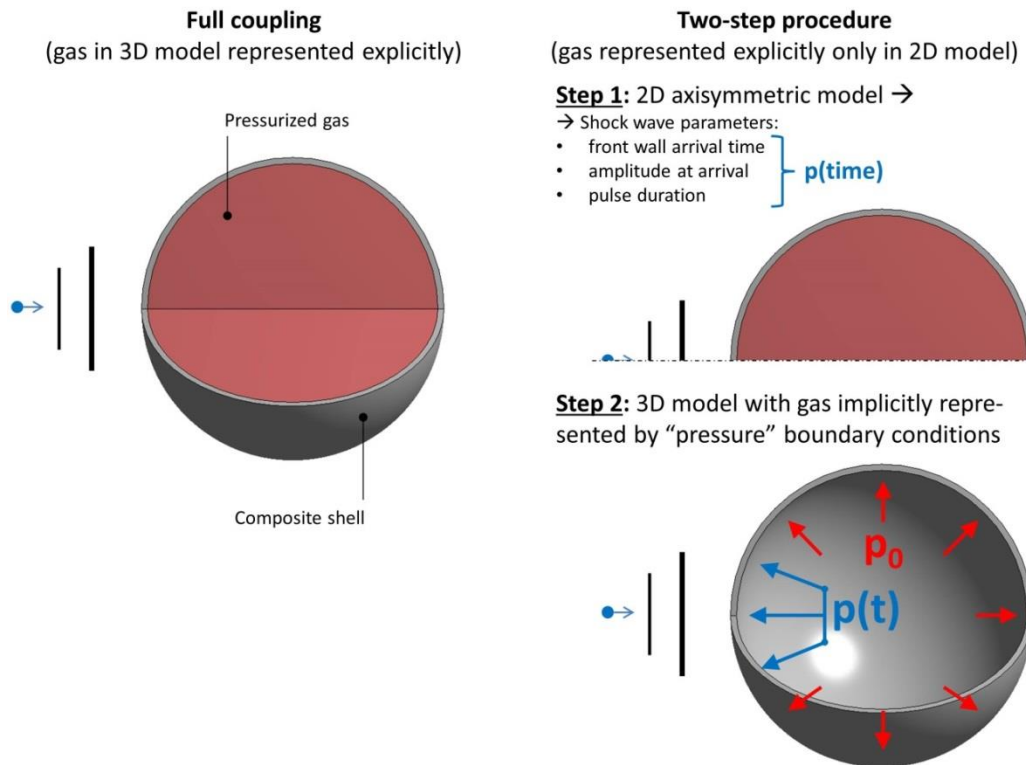
Figure 51 – Modeling of HVI on a shielded pressure vessel

This can be achieved through the use of a two-step modeling procedure, as it is illustrated in Fig. 51. At the first step, a two-dimensional axisymmetric analysis must be performed with the main goal of determining *parameters of the shock wave* generated in the pressurized gas. More precisely, the time of the wave arrival to the front wall (after reflection from the rear wall), pressure pulse amplitude and duration are of interest. At this

stage, composite shell representation can be simplified and described by the properties of a homogeneous material, as only through-the-thickness parameters are important.
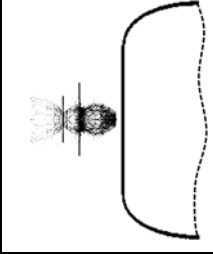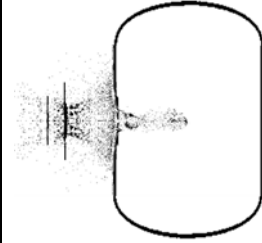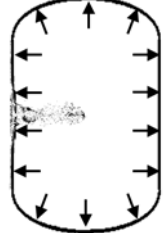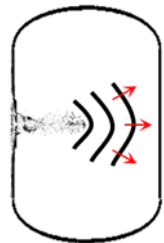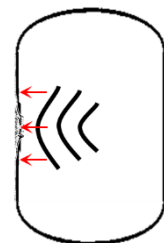
At the second step, a three-dimensional analysis of HVI on the shielded pressurized shell must be performed. In this analysis, the action of the gas can be implicitly represented by two sets of boundary conditions applied to the interior surface of the pressure shell. First of them imitates the static pressure exerted by the gas. The second set represents the action of the pressure pulse arriving on the front wall after reflection of the shock wave from the rear wall of the vessel, with parameters of the pulse as determined in the previous step via a 2D axisymmetric analysis.

It should be noted that the gradual decrease of internal pressure due to venting of the gas through the perforated hole can be easily incorporated into the proposed modeling procedure. It was however estimated in [68] that the venting time is typically many orders of magnitude higher than the time needed for the traveling of the stress wave around the circumference of a pressure vessel. The internal pressure can, therefore, be considered constant during the time of HVI analysis.

The interaction of orbital debris with the external shield can be represented in the numerical analysis by the similar means as it has been done in *chapter 3*, i.e. using SPH method or its combination with FEM. Adequate numerical modeling of the remaining type of interactions, i.e. the interaction of the secondary debris with the composite pressure wall, requires an additional investigation to be conducted, as the filament-wound composites are expected to exhibit complex behavior under HVI loading. Such investigation is the subject of the following sections.

The physical interactions and their suggested representation in the numerical modeling are summarized in Table 15.

Table 15 – Modeling of the HVI on shielded COPV

#	Interaction type	Schematic	Consequences	Implementation in numerical model
1	Projectile – External shield		• Fragmentation of the projectile; • Perforation of the external shield; • Formation of the secondary debris cloud (DC)	• SPH method and the mAcro-scale material models for the projectile and external shield
2	Secondary DC – Composite pressure wall		• Damaging and perforation of the pressure wall; • Formation of the tertiary DC	• SPH – FEM coupling; • MEso-scale modeling of the composite pressure wall (*see the following sections*)
3	Pressurized gas (static) – Composite shell		• Loading of the composite shell and, through this, supplying energy for the cracks around the perforation	• Boundary conditions
4	Tertiary DC – Pressurized gas		• Complete ablation of the DC; • Formation of the shock wave in the gas	• Deactivation of the DC before impact on the rear pressure wall (ablation); • Determination of the shock wave parameters using 2D axisymmetric analysis
5	Shock wave – Perforated pressure wall		• Impulsive loading of the composite shell and, through this, supplying additional energy for the cracks around the perforation	• Boundary conditions with parameters of the pressure impulse determined in the 2D axisymmetric analysis

4.3 Experimental Study of HVI Damage in Composites Fabricated by Filament Winding

Common manufacturing technique for COPVs is filament winding, which is characterized by *meso-scale inhomogeneity* of the fabricated material in addition to microscopic inhomogeneity inherent to all types of composites [14]. The former feature results from multiple interweaving of filament bands forming a filament-wound composite part, as described later in this chapter (see Section 4.3.2).

(a)   (b)

Figure 52 – Examples of helical winding with different densities of interweaving of filament bands: a) "low" density (LDI); b) "high" density (HDI)

As parts of spacecraft systems, COPVs are exposed to orbital debris (OD) environment and, therefore, may be subjected to hypervelocity impacts (HVI) by orbital debris particles. The behavior of composites under HVI has been studied experimentally and numerically by many researchers, e.g. [17, 69 - 75]. However, most of the reported work was confined to the class of standard laminated composites, whereas no attention has been paid to the filament-wound materials.

Preliminary numerical studies conducted by *Cherniaev and Telichev* [76] indicated that HVI damage of filament-wound materials may significantly depend on the degree (or "density") of the interweaving of the elementary filament bands. The degree of interweaving, in turn, is a manufacturing parameter; and its value may vary over a relatively wide range due to the flexibility of filament winding equipment. An example of winds with different degrees of interweaving is given in Fig. 52.

This section presents results of experimental studies that assess the effect of the following parameters on HVI damage of filament-wound composite:

- impactor energy (in terms of projectile diameter);

- pre-loading; and

- the degree of interweaving («low» vs. «high»).

4.3.1 Experimental model

Experimental model is an experimental representation of attributes of a real physical system that is being studied. As composite overwrapped pressure vessels represent the main type of spacecraft parts that can be fabricated by filament winding, the employed experimental model incorporates some specific features relevant to these components, e.g. presence of external orbital debris shielding. However, findings of the study may also be useful for the design of other spacecraft parts that will be found rational to be fabricated by filament winding, e.g. composite truss tubes.

The experimental model represents the following constituents of the physical system:

- *Environment:* all tests were conducted in a vacuum chamber in order to represent conditions encountered in space. However, some pressure (~30 Torr of nitrogen) was retained to assist in sabot separation during HVI tests.

- *Orbital debris*: orbital debris was represented by aluminum (Al6061-T6) spheres of two different diameters, namely 3.175mm (1/8 inch) and 4.7625mm (3/16 inch) with a nominal speed of 7.0 km/s. Aluminum projectiles represent the medium-density class prevailing in the space debris population [2].

- *Composite pressure vessel:*

    a) Front (relative to impact) wall of a pressure vessel was represented by 3 mm-thick composite panels manufactured via filament winding, as described in the following section.

    b) Wall stresses created in a COPV by inflation pressure were represented via pre-loading of the composite panels. In order to simplify the pre-loading apparatus, control and interpretation of measurements, the loading of the composite panels was uniaxial, as compared to biaxial stress state generated by inflation pressure in a shell of a real COPV.

- *External OD shielding*: pressure vessels pertain to the critical spacecraft systems of highest vulnerability with respect to orbital debris impacts, and therefore typically have to be protected from highly probable impacts of submillimeter debris particles. The presence of such protection was modeled by placing a 0.8 mm-thick aluminum (Al6061-T6) bumper at a standoff of 23 mm from the composite panels.

4.3.2 Fabrication of composite specimens

In filament winding, the carriage unit of a winding machine moves back and forth relative to the rotating mandrel and lays down on it the resin-impregnated fibers (towpreg) at a specific angle. Fibers are placed onto a mandrel in the form of filament bands, each containing few thousands of fibers. Bands containing 24,000 of fibers were used in this study.
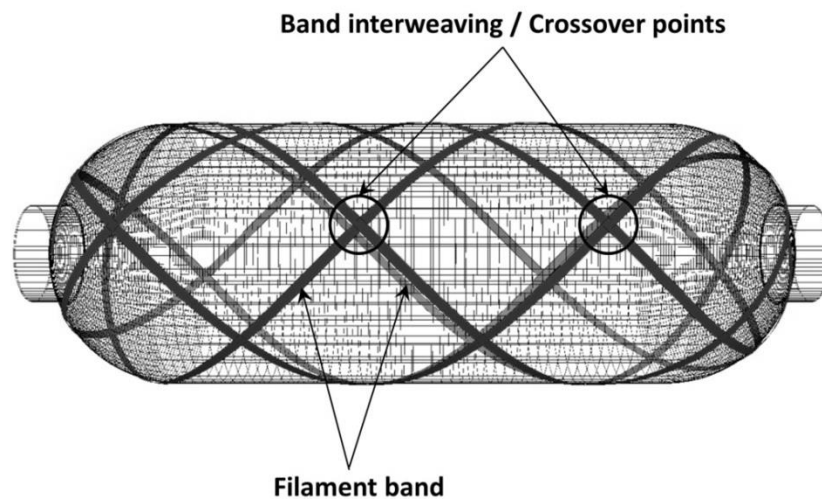
Figure 53 – Architecture of a filament-wound composite.

At each circuit (one back and forth pass of the carriage unit along a mandrel), filament bands are laid on a mandrel at "+" (forward motion) and "−" (back motion) angle. Normally, many circuits are needed to completely cover the mandrel. Each circuit results in crossovers between filament bands of "+" and "−" angle. The presence of crossovers is intrinsic to filament winding and forms its well recognizable patterns. Typically, it is possible to fabricate a vessel of a given capacity and configuration using different winding patterns, as they are easily programmable using software supplied with the filament winding equipment.

All composite specimens in this study were manufactured using towpreg consisted of Toray T700SC-24K-50C carbon fibers pre-impregnated with UF3376-100 epoxy resin, in cooperation with Lawrie Technology, Inc.

<div align="center">(a)   (b)</div>
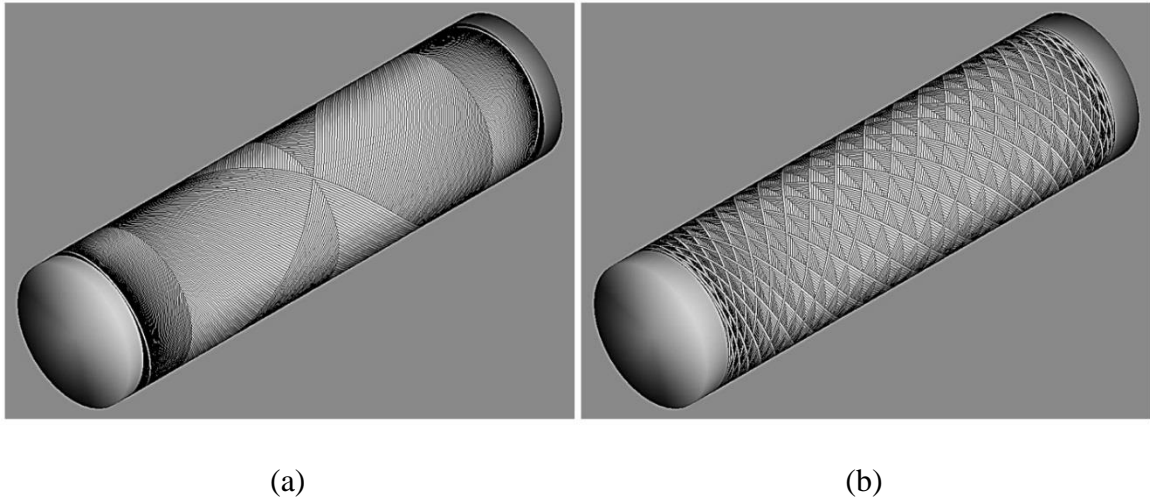
Figure 54 – Filament winding patterns: a) LDI (1/1); b) HDI (13/11)

Two types of filament-wound specimens, different in terms of degree (or "density") of filament bands interweaving, were considered. The types were designated as "low" and "high" degree of interweaving specimens (LDI and HDI, correspondingly). More specifically, pattern names can be defined as N/M, where N is the number of winding passes before a new pass is adjacent to the first and M describes the relative position of the intermediate passes. In this notation and with mandrel diameter of 8 inch, generated LDI pattern corresponds to 1/1 and HDI pattern corresponds to 13/11. The wind patterns generated using commercial software are shown in Fig. 54. The 45 degree wind angle was controlled within the area of interest.
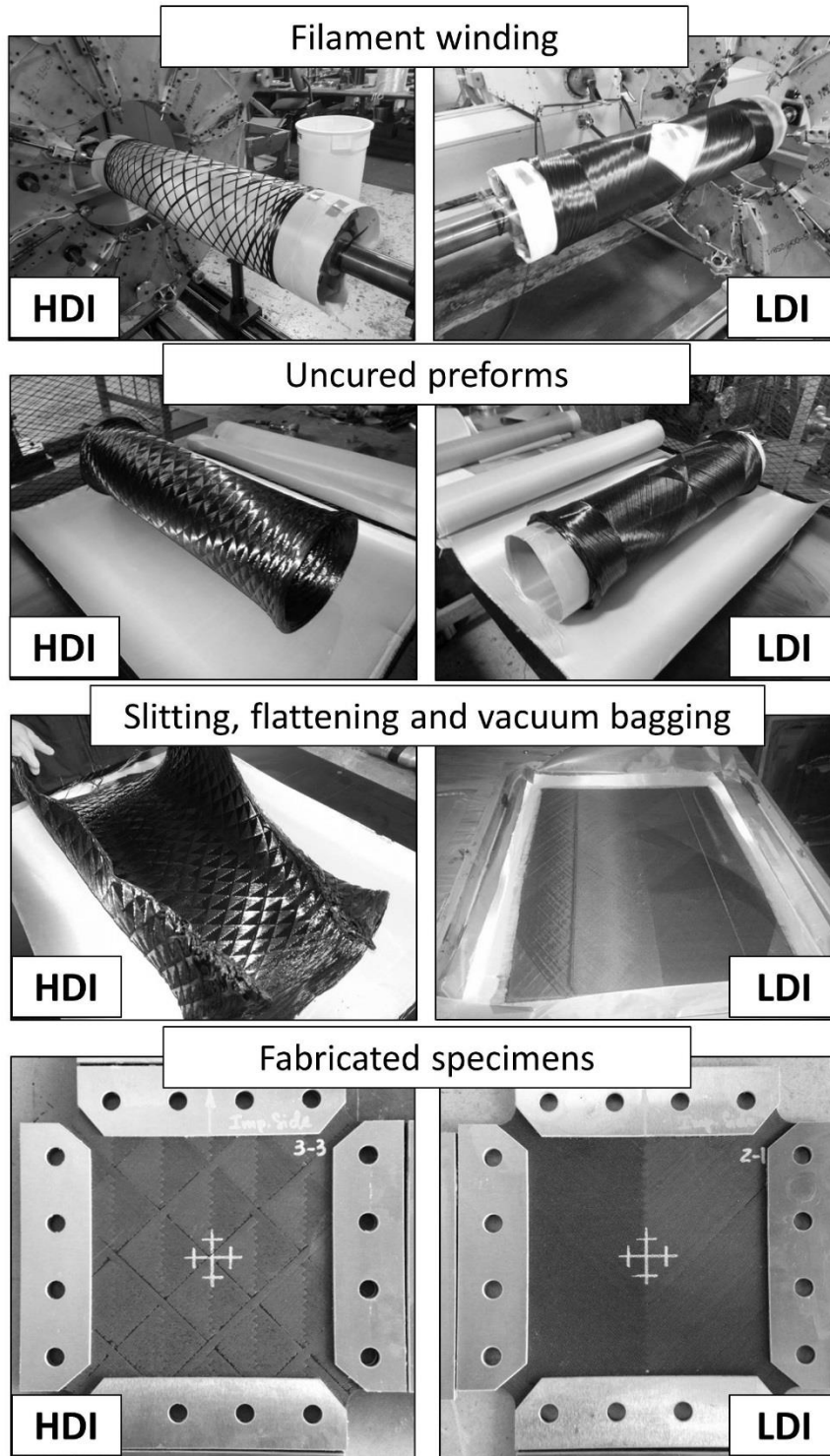
Figure 55 – Manufacturing of composite specimens

The overall manufacturing process, schematically illustrated in Fig. 55, included the following steps:

1. Filament winding with ±45º fiber angles in the area of interest;

2. Sliding the uncured preforms off the mandrel;

3. Slitting the uncured preforms along the length and flattening them;

4. Curing the flattened winds in the vacuum bag apparatus;

5. Cutting specimens out of the cured panels using waterjet cutting machine;

6. Bonding metallic strips to the regions of fixation/load application.

As a result, flat 200x200 mm specimens with filleted corners and metallic reinforcing tabs were fabricated. LDI specimens had a single row of filament band crossover points in the center; whereas HDI specimens had multiple rows of crossovers in the test area (see Fig. 55).

Vacuum bagging was used for curing the flattened winds in order to replicate the consolidation pressure generated during filament winding, which was estimated to have an order of magnitude of 0.1 MPa (i.e. the same pressure as created by vacuum bag apparatus). Flat-shaped specimens were used in order to simplify their pre-loading in the impact experiments.

4.3.3 Experimental setup and procedure

A test fixture was designed and manufactured in order to provide the following functionality:

1. Hold the bumper (external shielding), composite specimen and witness plate during the HVI tests;

118

2. Pre-load the composite specimens, when required.

The fixture consisted of a steel frame and a set of turnbuckles used to fix and load composite specimens (see Fig. 56).

(a)   (b)   (c)
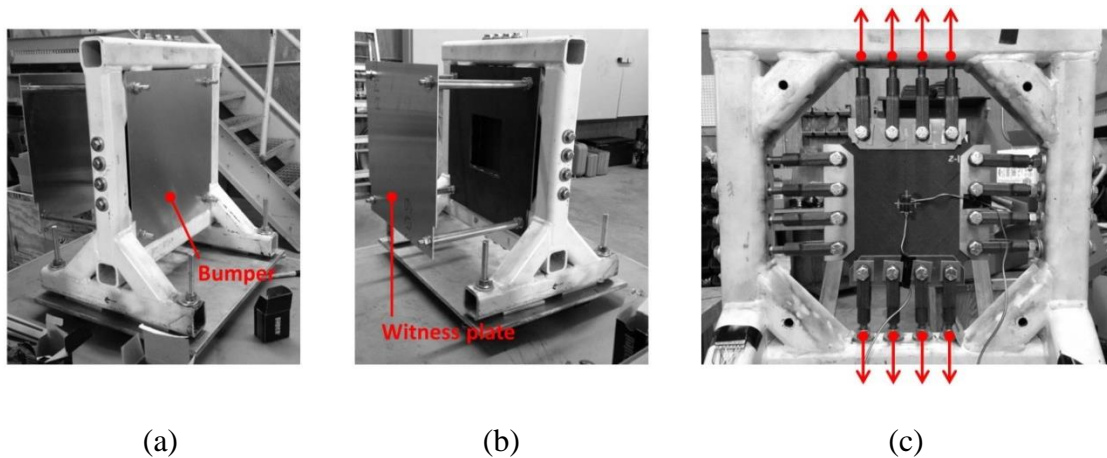
Figure 56 – Test fixture: a) front; b) back; c) specimen pre-loading

Pre-loading was controlled by a strain gauge that was aligned with the direction of loading [see Fig. 56 (c)]. It was created by tightening the turnbuckles using an adjustable torque wrench, starting from small torque and gradually increasing it until the strain detected by the strain gauge achieved the desired value, which was always in the elastic region. An additional strain gauge, installed in the direction perpendicular to loading, was used to control the value of Poisson ratio. The latter is constant in the elastic region, whereas changes of the Poisson ratio from its initial value would indicate an undesirable inelastic deformation of the composite due to plasticity and damage. During pre-loading, the specimen was fixed only in the direction of external forces [shown by red arrows in Fig. 56 (c)]. Turnbuckles were attached to the specimen, in the perpendicular direction, only when pre-loading was completed. This allowed the specimen to contract in the direction that was perpendicular to loading, due to the Poisson effect.

119

The following steps were performed in the course of HVI experiments:

1. Insertion of a composite specimen into the loading frame.

2. Alignment of the composite specimen relative to the fixture frame using a level gauge.

3. *(Optional)* Pre-loading of the composite specimen.

4. Installation of the front 0.8 mm Al6061-T6 bumper at a standoff of 23 mm from the composite specimen.

5. Installation of the 1 mm Al6061-T6 witness plate at a standoff of 275 mm from the composite specimen.

6. Installation of the assembled fixture into the testing chamber.

7. Performing a hypervelocity shot with 3.125 or 4.763 mm projectile at (nominally) 7 km/s according to the test matrix (see Section 4.3.4).

8. Disassembling the target.

9. Performing an ultrasound inspection (C-Scan) of the specimen, in order to detect internal damage that was induced in the composite panel by the hypervelocity impact.

The HVI shots were conducted using a two-stage light gas gun at HIT Dynamics Ltd. impact testing facility (NB, Canada).

The ultrasonic examination was performed using the Immersion Automated Ultrasonic Testing (Immersion-AUT) technique, which can detect such defects as delaminations, large internal voids, and large subsurface cracks, by measuring the time-of-flight of the ultrasound signal that was sent through a composite panel. The data was collected on a 1 mm x 1 mm grid and presented in the form of C-Scan images. In C-Scan, the features that reflect the sound within and on the surfaces of a test piece are displayed on its planar view.

4.3.4 Experimental results

Table 16 summarizes the test sequence, panel configuration and as-tested projectile impact speeds for each test. In total, eight successful hypervelocity impact experiments were conducted with specimens of two different winding patterns (LDI and HDI), subjected to two different loading conditions (pre-loaded and not pre-loaded) and using two different projectile diameters (3.125 and 4.763 mm). The unidirectional pre-load stresses corresponding to the measured pre-load strains given in Table 16 were estimated using the classical lamination theory. They were found to be equal to 63 and 70 MPa for the LDI and HDI panels, respectively.

Fig. 57 exemplifies the typical damage patterns for the aluminum bumper and the aluminum witness plate when impacted by 3.125 and 4.763 mm projectiles. In all cases, the witness plates were not perforated.

Table 16– Test parameters

Test #	Specimen #	Type	Pre-loading	Measured strain	Projectile diameter (mm)	Projectile mass (g)	Projectile velocity (km/s)
1	1-2	LDI	No	–	3.125	0.046	6.822
2	2-1	LDI	Yes	0.00483	3.125	0.046	6.828
3	3-2	HDI	No	–	3.125	0.047	6.847
4	4-2	HDI	Yes	0.00483	3.125	0.045	6.878
5	1-3	LDI	No	–	4.763	0.153	6.786
6	2-3	LDI	Yes	0.00540	4.763	0.156	6.786
7	4-3	HDI	No	–	4.763	0.154	6.922
8	3-3	HDI	Yes	0.00548	4.763	0.154	6.781

Damage in the composite specimens produced by 3.125 and 4.763 mm projectiles is shown in Fig. 58 and Fig. 59, correspondingly. Here, each row (from left to right) illustrates a specimen from the front side, from the rear side and the C-Scan image overlaid onto the specimen picture.
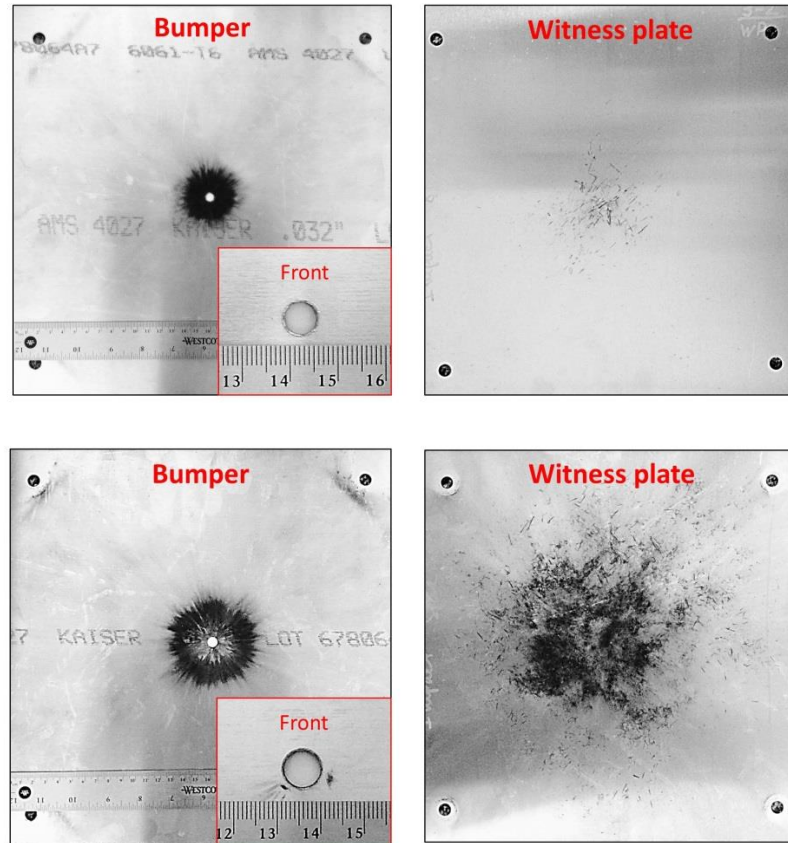
Figure 57 – Exemplary damage of bumper and witness plate, top: $d_p = 3.125$ mm; bottom: $d_p = 4.763$ mm

During ultrasonic examination, the top surface was the side that was struck by the hypervelocity projectiles. The C-Scan images that were obtained were then "mirrored" and overlaid onto the rear surface of the specimens, in order to superimpose the resulting visual damage with the damage detected by ultrasonic inspection.
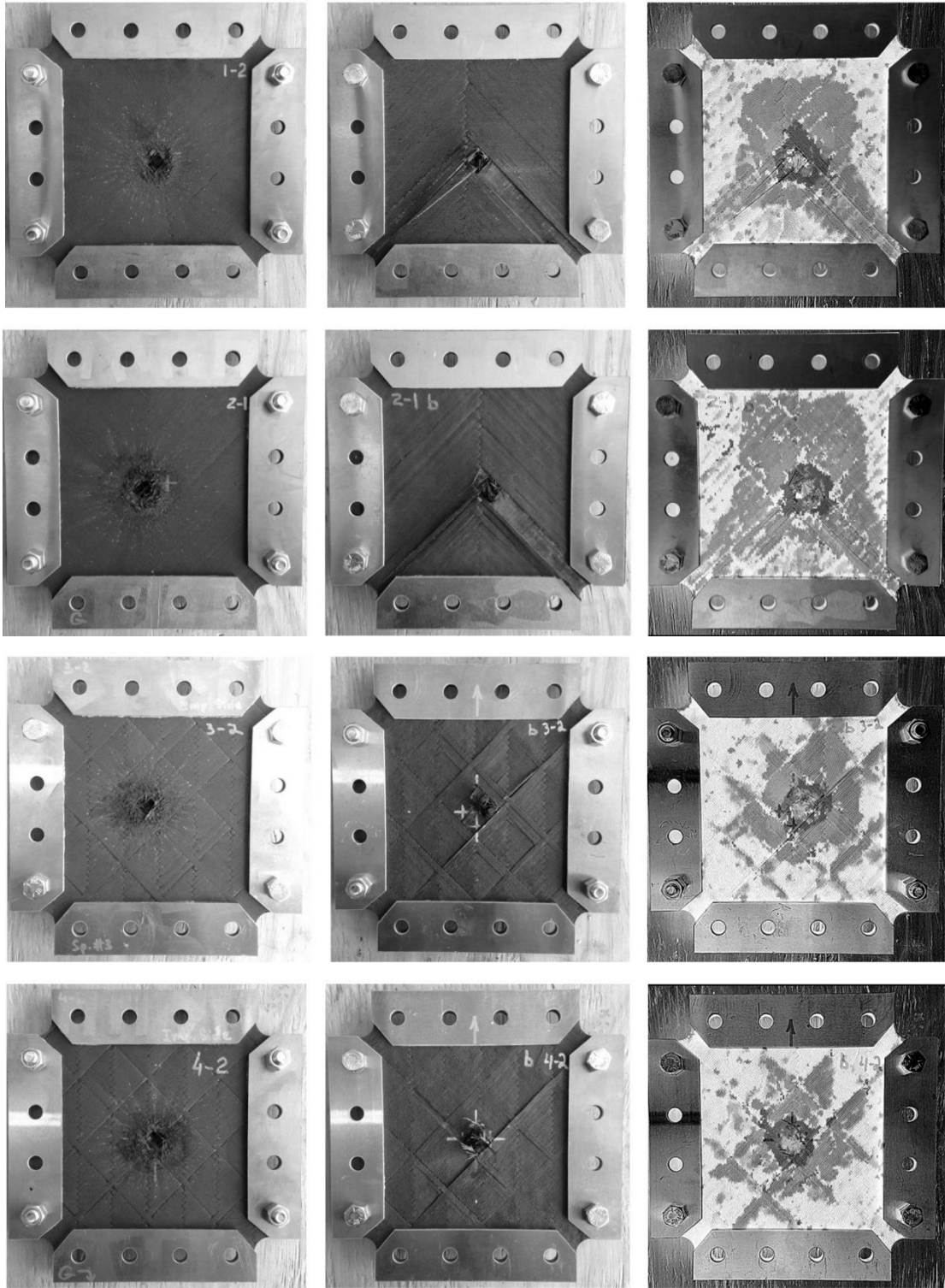
Figure 58 – Damage in specimens impacted by 3.125 mm projectile

(left – front wall, middle – rear wall, right – C-Scan)
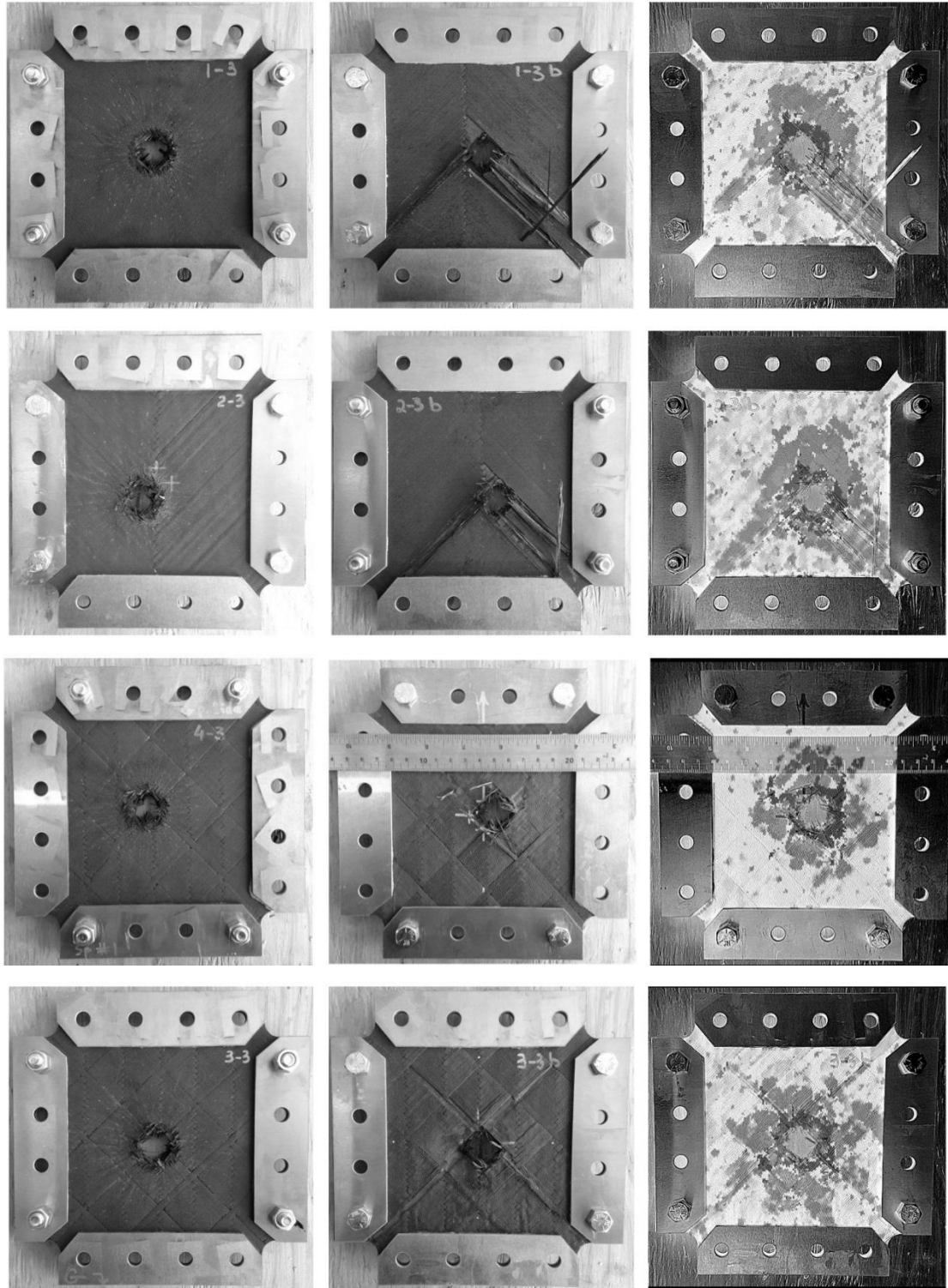
Figure 59 – Damage in specimens impacted by 4.763 mm projectile

(left – front wall, middle – rear wall, right – C-Scan)

The diameters of the perforated holes were determined using a visual inspection of the post-impact specimens (D_{h_vis}), as well as the C-Scan images (D_{h_c-sc}). In the latter case, the "effective diameter" of the perforated hole was calculated as a diameter of a circle enclosing the same area as the non-uniform perforation area (A_{h_c-sc} – determined using Adobe Photoshop tools) on the C-Scan image, specifically $D_{h\_c-sc} = \sqrt{\dfrac{4 \cdot A_{h\_c-sc}}{\pi}}$ (Fig. 60). Results of these measurements are summarized in Table 17.
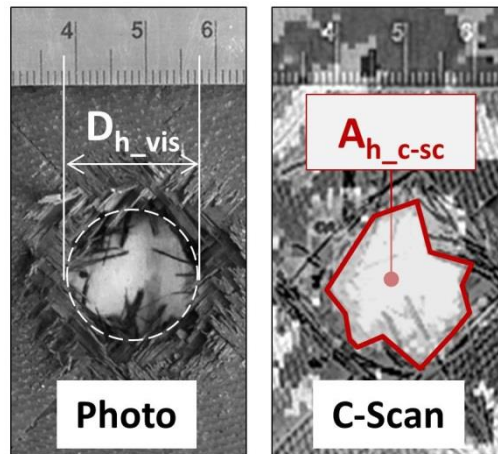
Figure 60 – Measurement of the size of perforation

Table 17 – Diameters of perforated hole in the composite specimens

Specimen #	Type	Projectile diameter (mm)	D_{h_vis}, mm	D_{h_c-sc}, mm
1-2	LDI	3.125	11.0	10.63
2-1	LDI	3.125	11.0	10.80
3-2	HDI	3.125	11.0	13.34
4-2	HDI	3.125	11.0	10.78
1-3	LDI	4.763	21.0	21.43
2-3	LDI	4.763	21.0	21.61
4-3	HDI	4.763	20.0	21.89
3-3	HDI	4.763	21.0	21.46

The total damage zone areas (include delamination, surface damage and perforation, as shown in Fig. 58 – 59) were measured from the C-Scan images using Adobe Photoshop tools. The measurement procedure included the following steps: 1) manually selecting all damaged regions on a C-Scan image and placing them in a separate "layer" in Adobe Photoshop; 2) calculating the number of pixels in such layer (N_{dam}) and the total number of pixels (N_{tot}) in the whole image (automated functions in Adobe Photoshop); and 3) determining the total damaged area as being equal to (N_{dam} / N_{tot}) × A_g, where A_g is the gross area of the specimen (mm2). Results of these measurements are compared in Fig. 61.
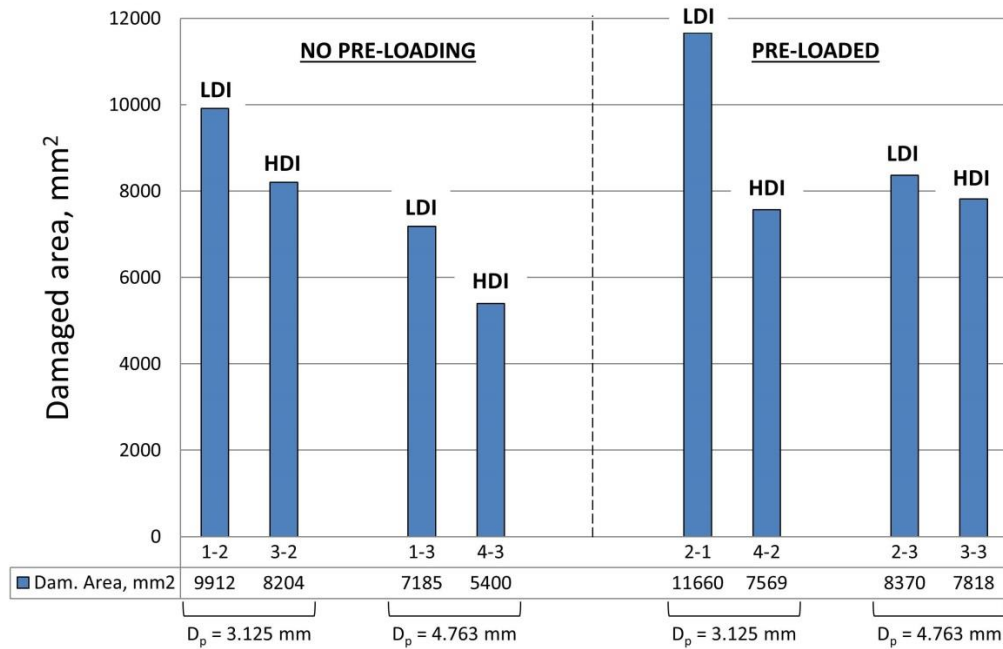
Figure 61 – Damaged area of the specimens determined from the C-Scan images

4.3.5 Discussion of the experimental results

An inspection of the visible and subsurface damage of the specimens in Fig. 58 – 59 reveals the following *qualitative* features:

126

1. In all cases, visible damage on the front side was represented by the entry crater only. The specimens did not demonstrate any surface ply-peeling phenomenon, as observed by many experimentalists in the case of HVI on standard laminated composites (e.g. [69, 71]).

2. At the same time, peeling of a significant amount of material was observed on the rear surface of all LDI specimens. HDI specimens revealed almost no rear surface material peeling at all (specimens tested without pre-loading) or very limited amount of it (pre-loaded specimens).

3. Both photographs and C-scan images reveal qualitatively different damage patterns for LDI and HDI specimens.

Analysis of Fig. 61 and the data from Table 17 allows a number of general trends in HVI damage behavior of the filament-wound composites to be identified, as well as some *quantitative* observations to be made:

1. In all cases, the damage zone area in the HDI specimens is smaller as compared with the LDI specimens. The difference varies from 7 to 35%, depending on impact conditions.

2. In most cases, pre-loading leads to formation of a larger damage zone. This is especially the case for LDI specimens, where damage zone area drastically increases (~15%, almost independent on impactor's energy) with the introduction of pre-loading. Primarily, it is associated with an increase of the subsurface delamination area, whereas visible surface damage remains almost the same for both pre-loaded and non pre-loaded LDI specimens. This trend remains for the HDI specimens impacted with higher energy ($d_p = 4.763$ mm), where the damage zone area demonstrates ~30% increase with pre-loading applied.

However, in this case, its growth is associated with both delamination and an increase of the surface damage. To the contrary, HDI specimens impacted with the lower energy (d_p = 3.125 mm) did not reveal a noticeable sensitivity to pre-loading.

3. In most of the cases, impacts of smaller projectiles result in larger delamination area. This can be explained by different energy absorption mechanisms dominating at different impact conditions. With smaller projectiles (d_p = 3.125 mm), the system "Al bumper – composite specimen" is close to its ballistic limit (lower energy of impact; and $t_b/D_p = 0.25$, which according to Ref. [3, 62] provides the most efficient fragmentation of projectile). The dominating energy absorption mechanism in this case is delamination. Contrarily, the dominating energy absorption mechanism for a larger projectile is fiber breakage (larger energy of impact and, in general, larger individual fragments of the projectile as t_b/d_p = 0.17 only).

4. The size of the perforated holes does not show dependence on the filament-winding pattern. This result is expected, as properties of all panels are almost identical in the through-the-thickness direction.

4.4 Meso-scale Approach to Modeling of HVI Damage in Composites

Numerical techniques for the modeling of composite behavior under hypervelocity impact loading have been described in the literature [17, 75] and implemented in commercial software packages, e.g. ANSYS Autodyn [60]. These techniques are designed for the standard laminated composites and based on the *homogenization* of a composite laminate, which is represented in the modeling as a macroscopically homogeneous orthotropic media with effective properties equivalent to those of the real material (Fig. 62).

HVI damage of filament-wound composites, as found in the previous section, depends on the particular winding pattern used in fabrication. Correspondingly, the homogenization-based techniques are inapplicable to this class of materials. Instead, in this study, we introduce and verify a more general approach based on meso-scale representation of composite laminates, including modeling of individual plies (or filament bands) and resin-rich regions between them. Due to its generality, this approach can be applied to both standard laminated composites and to materials fabricated by filament winding.
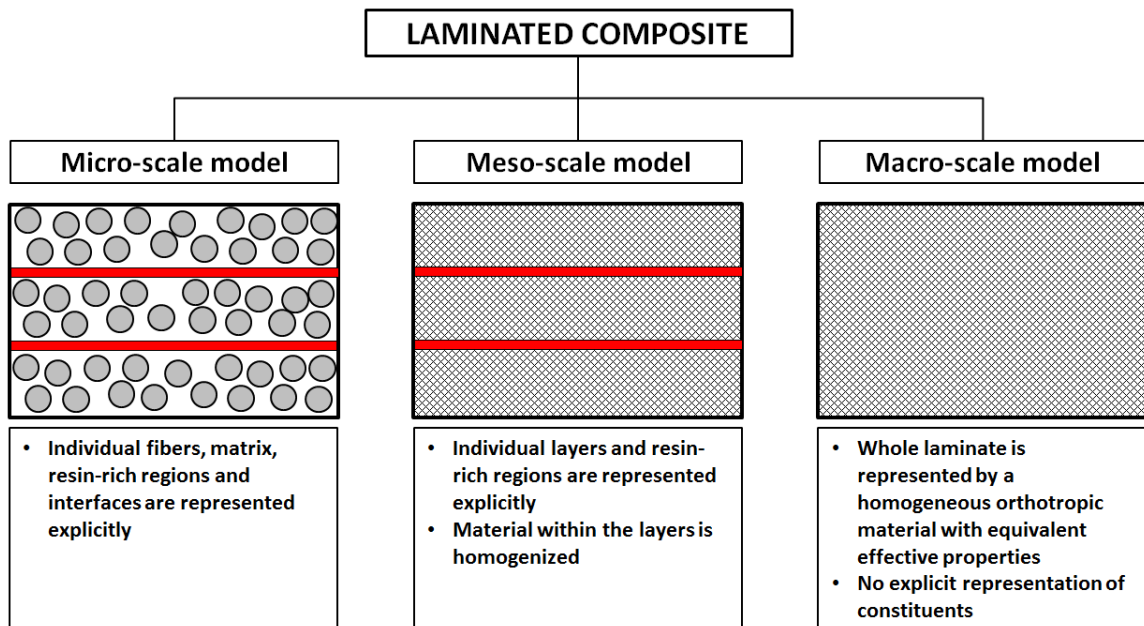
Figure 62 – Modeling of composite material

4.4.1 General considerations

Fracture of a composite includes both *intralaminar* and *interlaminar* damage mechanisms. In the former case, it is confined to anisotropic linearly elastic fiber-reinforced layers of a laminate and is brittle in nature for the most of existing CFRP systems. Mechanisms of intra-ply damage include fiber breakage and matrix cracking along fibers. Interlaminar

fracture or delamination is attributed to relatively tough isotropic polymer matrix concentrated in the resin-rich regions (RRR) between each pair of fiber-reinforced layers. Deformation in these regions prior to failure initiation is determined by the properties of the polymer resin. Subsequent damage and fracture may be either due to deformation of the matrix within RRR (cohesive fracture), or due to debonding at the interface between the resin-rich region and fibers adjacent to it (adhesive fracture) [77]. To reproduce the above-mentioned fracture mechanisms more precisely, each composite laminate can be represented as a structure consisting of alternating fiber-reinforced and finite-thickness resin-rich layers. By doing that, we uncouple the description of the behavior of the two physically different components of a laminate and employ more suitable material models for each of them. This introduces a higher level of realism in modeling compared to the case of macro-scale representation.

It has been shown in *chapter 2* that in order to be suitable for hypervelocity impact simulations, materials being modeled have to be characterized in terms of the equation of state (EOS), strength model and failure/damage model. Two following sub-sections describe material models employed in our study to simulate the behavior of fiber-reinforced layers/filament bands (Section 4.4.2) and interlaminar regions (Section 4.4.3).

4.4.2 Modeling of fiber-reinforced layers

According to the meso-scale approach, each layer was considered as a homogeneous orthotropic material. Its EOS, therefore, and can be expressed by means of equations (18) – (19) presented in *chapter 2*, i.e.

$$\Delta p = \Delta p(\Delta \varepsilon_{vol}) -$$

$$-\frac{1}{3}[C_{11} + C_{21} + C_{31}]\Delta \varepsilon_{11}^d - \frac{1}{3}[C_{12} + C_{22} + C_{32}]\Delta \varepsilon_{22}^d - \tag{38}$$

$$-\frac{1}{3}[C_{13} + C_{23} + C_{33}]\Delta \varepsilon_{33}^d$$

where the pressure contribution from volumetric strain $p(\varepsilon_{vol})$ is given as:

$$p = K'\varepsilon_{vol} + A_2(\varepsilon_{vol})^2 + A_3(\varepsilon_{vol})^3 + (B_0 + B_1\varepsilon_{vol})\rho_0 e, \tag{39}$$

and

$$K' = -\frac{1}{9}[(C_{11} + C_{22} + C_{33} + 2(C_{12} + C_{23} + C_{31}))] \tag{40}$$

It should be emphasized, however, that the stiffness matrix coefficients in these equations in the case of meso-scale model must correspond to the properties of a *unidirectional ply* rather than the whole laminate (as it would have been had the macro-scale representation been employed).

The intralaminar failure is brittle for most of CFRP systems. Thus, it can be considered as instantaneous for the corresponding direction once one of the following criteria has been satisfied:

$$e^2 = \left(\frac{\sigma_{11}}{X_T}\right)^2 + \left(\frac{\sigma_{12}}{S}\right)^2 + \left(\frac{\sigma_{13}}{S}\right)^2 \geq 1 \tag{41}$$

for the fiber failure, and

$$e^2 = \left(\frac{\sigma_{22}}{Y_T}\right)^2 + \left(\frac{\sigma_{12}}{S}\right)^2 \geq 1 \tag{42}$$

for the transverse matrix cracking. Here X_T and Y_T are the longitudinal and in-plane transverse strength of a composite, correspondingly; S is the in-plane shear strength.

Failure due to through-the-thickness loading was attributed to the interlaminar region and is described in the following subsection.

4.4.3 Modeling of interlaminar regions

The EOS of the RRR material can be represented either using the linear pressure-volumetric strain dependence (assuming that the EOS of thin resin-rich regions will not have significant effect on overall volumetric response of the composite under HVI loading), or using the Mie-Gruneisen EOS with shock Hugoniot, describing linear relationship between shock velocity (U_s) and particle velocity (U_p) in the polymeric resin as:

$$U_s = C_0 + S \cdot U_p,$$

(43)

where C_0 is the bulk acoustic sound speed in the resin and S is the slope of the $U_s - U_p$ relationship. For better representation of the resin response under HVI loading, the latter option is recommended.

The material of the resin-rich regions is homogeneous and isotropic. However, its behavior prior to failure initiation may depend on the type of the polymer resin:

- in the case of *thermoset-resin* composites, it can be approximated as linearly elastic, as thermosets typically do not undergo a significant amount of plastic deformation prior to initiation of failure.

132

- in the case of *thermoplastic-resin* composites, material plasticity cannot be ignored, and it should be modeled as elastoplastic, with the von Mises J₂ function determining the yield surface.

Due to software limitations, however, it is not possible in AUTODYN to combine directly von Mises strength model and the Crack Softening algorithm (used to simulate interlaminar failure) within a single material model. This problem was solved by employing the general-case anisotropic yield model (see *chapter 2*) and reducing it to the von Mises yield function by careful selection of plasticity parameters (a_{ij}). In this model, the yield surface is given as

$$f(\sigma_{ij}) = a_{11}\sigma_{11}^2 + a_{22}\sigma_{22}^2 + a_{33}\sigma_{33}^2 + 2a_{12}\sigma_{11}\sigma_{22} + 2a_{23}\sigma_{22}\sigma_{33} + 2a_{13}\sigma_{11}\sigma_{33} + $$
$$+ 2a_{44}\sigma_{23}^2 + 2a_{55}\sigma_{31}^2 + 2a_{66}\sigma_{12}^2 = k \qquad (44)$$

Here k is the hardening parameter depending on plastic deformation and is defined as $k = \frac{2}{3}\bar{\sigma}^2$ [see 58, 59], where $\bar{\sigma}$ is the effective stress. The above function reduces to the von Mises yield criterion if the following values of plasticity parameters are used:

$$a_{11} = a_{22} = a_{33} = \frac{2}{3}; \quad a_{12} = a_{23} = a_{13} = -\frac{1}{3}; \quad a_{44} = a_{55} = a_{66} = 1 \qquad (45)$$

Substituting definition of k and plasticity parameters given by (45) into (44), one can obtain:

$$\bar{\sigma}^2 = \frac{1}{2} \cdot \left[(\sigma_{11} - \sigma_{22})^2 + (\sigma_{22} - \sigma_{33})^2 + (\sigma_{33} - \sigma_{11})^2 + 6 \cdot (\sigma_{23}^2 + \sigma_{31}^2 + \sigma_{12}^2) \right], \qquad (46)$$

which represents the general form of the von Mises yield criterion.

To predict failure initiation in the interlaminar region, the following interactive quadratic criterion can be used:

$$e^2 = \left(\frac{\sigma_{33}}{Z_T}\right)^2 + \left(\frac{\sigma_{23}}{S_{ILSS}}\right)^2 + \left(\frac{\sigma_{13}}{S_{ILSS}}\right)^2 \geq 1 \qquad (47)$$

As, in general, failure may initiate within the matrix, as well as at the fiber-matrix interface, the strength constants in (20) correspond to the through-the-thickness tensile Z_T and interlaminar shear S_{ILSS} properties of the composite, rather than the properties of the bulk polymer resin.

Formation of the discontinuities in the interlaminar region following the failure initiation was modeled implicitly, according to the principles of damage mechanics. The technique employed here is analogous to the crack softening algorithm from the CFRP model described in *chapter 2* (section 2.3.2.5), *but in the case when it is applied to the 33-plane only*. The algorithm assumes linear softening of the RRR material due to microcracking. Correspondingly, the failure surface in the course of failure progression will be updated according to the following criterion:

$$e_{33}^2 = \left(\frac{\sigma_{33}}{Z_T(1-D_{33})}\right)^2 + \left(\frac{\sigma_{23}}{S_{ILSS}(1-D_{23})}\right)^2 + \left(\frac{\sigma_{31}}{S_{ILSS}(1-D_{31})}\right)^2 \geq 1 \qquad (48)$$

The damage variable D_{33} for any time-step n+1 can be defined as

$$D_{33}^{n+1} = D_{33}^n + \frac{\varepsilon_{33}^{cr} \cdot h_{33}}{\sigma_{33\,fail}} + C \cdot \frac{\varepsilon_{23}^{cr} \cdot h_{23}}{\sigma_{23\,fail}} + C \cdot \frac{\varepsilon_{31}^{cr} \cdot h_{31}}{\sigma_{31\,fail}}, \qquad (49)$$

where h_{ij} is the gradient of linear softening (see Section 2.3.2.5). Analogous expressions can be written for other damage variables (D_{23}, D_{31}). Here C is the damage coupling coefficient, which represents the possibility that damage due to tensile loading may reduce

material capability to resist shearing, and vice-versa. Its value may vary between 0 and 1. The value of $C = 0.2$, recommended in AUTODYN [60], was employed in this study.

As there is no direct translation of the fracture toughness of a bulk resin into the interlaminar fracture toughness of composite (see e.g. Ref. [77] for discussion on this topic), values of G_{Ic} and G_{IIc} of composite should be used with the above damage model, rather than strain energy release rates corresponding to the pure matrix.
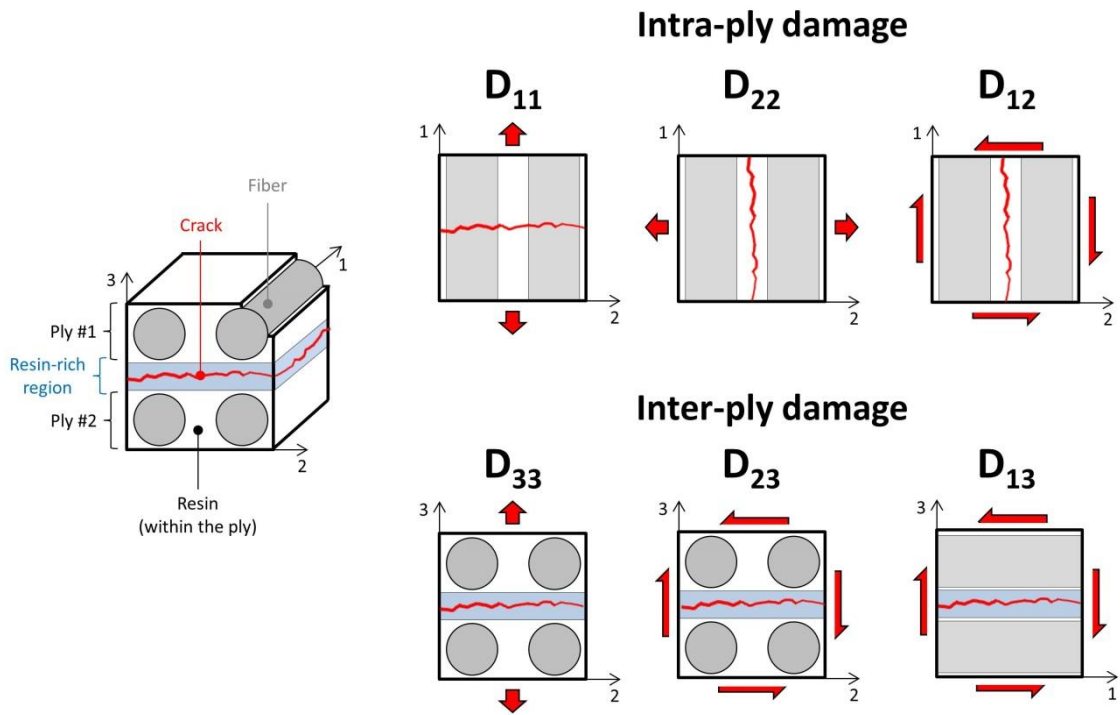
Figure 63 – Physical meaning of the damage coefficients

It should be noted that although the intralaminar failure is assumed to be brittle (see the previous section), the damage parameters are still calculated for this type of failure and represented by the coefficients D_{11}, D_{22} and D_{12}. Unlike damage parameters of the interlaminar region which can change continuously from 0 to 1, the intralaminar damage coefficients in an element can only take on values of 0 ("no damage") or 1 ("complete

fracture" – upon satisfaction of criteria given by eq. (41) or (42)). As a result, damage of the composite can be represented by a tensor containing 6 damage coefficients, including 3 coefficients for intralaminar damage (damage within a fiber-reinforced ply/band) and 3 coefficients for interlaminar damage (damage within a resin-rich region):

- D_{11} for the fiber breakage;
- D_{22} for the in-plane matrix cracking due to normal stresses;
- D_{12} for the in-plane matrix cracking due to shear stress;
- D_{33} for the delamination due to normal stress
- D_{23} and D_{13} for the delamination due to shear stresses.

The physical meaning of all of these damage coefficients is schematically illustrated in Fig. 63.

4.5 Validation of the Meso-scale Approach for Laminated Composites

4.5.1 Experimental data

A number of experimental programs have been conducted over the last 25 years to study the behavior of composites under HVI. Many experimental results from different sources were gathered and statistically analyzed by *Tennyson and Lamontagne* [74]. Their statistical analysis, carried out specifically for carbon fiber reinforced plastics, resulted in establishment of empirical correlations between projectile kinetic energy, target and projectile material properties, and resulting hypervelocity impact damage. The correlations determine diameter of a perforation hole/crater (D_{cr}) and "equivalent" diameter of damaged zone obtained by ultrasonic C-scan inspection (D_{c-scan}), as follows:

$$D_{cr} = 1.06 \cdot \sqrt[3]{E_k \frac{t \cdot \rho_t}{D_p \rho_p}} \, , \tag{50}$$

$$D_{c-scan} = 4.04 \cdot \sqrt[3]{E_k \frac{t}{D_p}} \, , \tag{51}$$

where E_k – projectile kinetic energy, t – thickness of the target, D_p – diameter of the projectile, ρ_t and ρ_p are target and projectile densities. The D_{c-scan} parameter should be understood as the diameter of a circle encapsulating the area equivalent to irregular-shaped delamination area measured by c-scan, including the area of perforation hole. Correlations (50) and (51) have been made through a wide range of CFRP thicknesses and impact energies.

Two validation cases from those analyzed by *Tennyson and Lamontagne* have been selected. They correspond to experiments conducted at the University of Kent at Canterbury (UKC) and Johnson Space Center (JSC). The cases were chosen in such a manner to represent different impact energies. Test parameters and experimental results for both cases are shown in Table 18.

Table 18 – Experimental data

Shot ID from [74]	Target parameters			Projectile parameters			Results	
	No of plies	Thickn., mm	Lay-up	Diameter, mm	Velocity, km/s	Energy, J	D_{cr}, mm	D_{c-scan}, mm
UKC #4	16	1.83	[0, ±45, 90]s	2	4.66	123	4.3	19.5
JSC #2	16	1.96	[0, ±45, 90]s	2	6.75	258	5.6	25.0

4.5.2 Material properties

In both cases targets were made of AS4/PEEK (APC-2) composite, whereas projectiles were of aluminum. The original source presenting results of UKC experiments [78] gives mechanical properties of the composite exactly the same as those provided by the APC-2 resin manufacturer [79]. They are listed in Table B.6 (Appendix B). Table B.7 provides properties of the bulk APC-2 resin.

Due to lack of data on fracture toughness of composites at loading rates corresponding to HVI, the values obtained experimentally by *Smiley and Pipes* [80, 81] for AS4/APC-2 composite under dynamic loading at $\sim 10^2$ mm/s were employed in our study. They correspond to $G_{Ic} = 350$ J/m^2 and to $G_{IIc} = 400$ J/m^2, and reflect a dramatic reduction of the fracture toughness for both first and second opening modes, as compared with the static values provided by the manufacturer (1700 J/m^2 and 2000 J/m^2, correspondingly [79]).

A few assumptions regarding composite properties have been made to complete its characterization in terms of established material models. First, interlaminar shear strength, which value is not provided by the manufacturer, was determined using the following correlation, given in [82] specifically for carbon fiber/PEEK composites: $S_{ILSS} = Flexural\ Strength / 15$. This gives the value of $S_{ILSS} = 135$ MPa. Second, Ryan et al. [83] have shown that different types of CFRP systems reveal a high level of similarity in their response to shock loading. Having this in mind, we adopted for the equation of state (see equation (19)) the values of $A_2 = A_3 = 0$ and $B_0 = B_1 = 2.5$ obtained experimentally in [83] for UMS2526/Krempel carbon fiber reinforced plastic.

The behavior of projectiles has been modeled using a combination of the shock equation of state, Johnson-Cook strength and failure models with material properties of Al6061-T6 as provided in Appendix B.

4.5.3. Numerical models

The Smooth Particles Hydrodynamics method (SPH) has been used to model adequately deformation and fragmentation of aluminum projectile in the course of impact event. The 2 mm-diameter projectile was represented by 8063 SPH nodes (corresponds to "Particle size" of 0.08 mm).

Targets represented by 100×60 mm laminated plates have been modeled using Finite Element method in the Lagrangian formulation. Each layer, as well as each resin-rich region, had been modeled as individual solid bodies with adjacent faces tied among themselves using simple "Bonded Contact with NO separation" feature in AUTODYN (see Fig. 64).
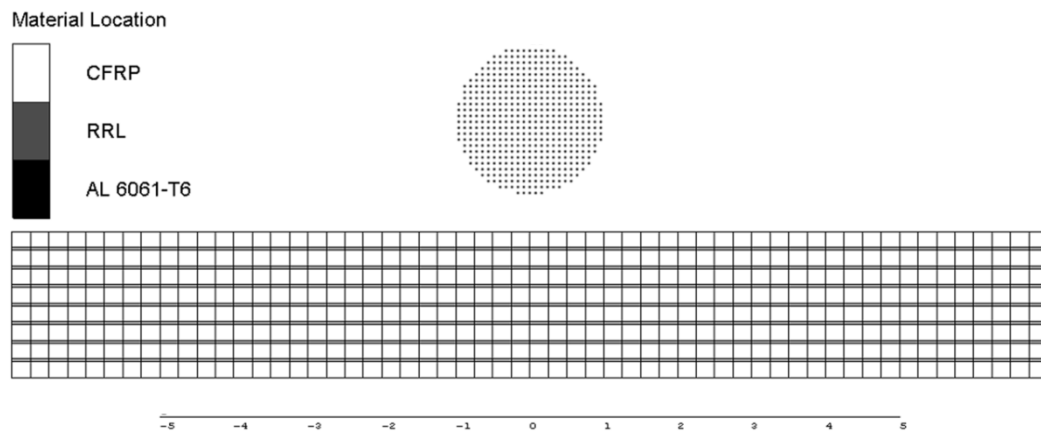
Figure 64 – Discretization of the composite plate and 2 mm aluminum projectile

139

As no separation was allowed on the interfaces, all of the through-the-thickness damage in the model, characterized by such macromechanical properties as interlaminar strength and fracture toughness, was confined to the RRR elements.

In total, laminates consisted of 8 unidirectional plies and 7 resin-rich layers. RRL thickness was assumed to be equal to 0.035 mm for all simulations, which is within the typical range of 0.01 – 0.1 mm.

Uniform meshing of the composite plates resulted in 1440000 0.25x0.25 mm hexahedral finite elements (96000 per ply, including resin-rich layers) with one element through the thickness of each layer. Preliminary studies showed that solution became almost mesh-independent if aforementioned element size was employed.

To allow modeling of target perforation, numerical mechanism of erosion has been utilized. It automatically removed heavily distorted finite elements from the model when effective strain had reached a user-specified value. The threshold values of effective strain were determined by calibration of simulation results (the size of perforated hole) against experimental data from [74]. In case of lack of direct experimental data for particular CFRP material system, the empirical relation (50) can be recommended to conduct such calibration. It was found in the preliminary studies that erosion strain of 0.55 for brittle UD plies used along with the ultimate effective strain of 3.0 for ductile RRR material provided an acceptable level of correlation between numerical and experimental results in terms of perforated hole diameter.

4.5.4 Results and discussion

Impact holes predicted for UKC #4 and JSC #2 data sets along with surrounding delamination are exemplified in Fig 65. Here red-colored elements indicate complete damage in the interlaminar region (material cannot resist tension or shear). Fig. 65 also shows secondary debris clouds resulting from fragmentation of the target and the projectile. It should be noted that fragments of the projectile are modeled with SPH particles, whereas fragments of the composite plate are represented in the numerical model by nodes of eroded elements. Therefore, the debris cloud is a mixture of both. This technique allows to retain inertia in the simulation upon erosion of finite elements and to use their nodes for modeling of subsequent impact events.

(a)

(b)
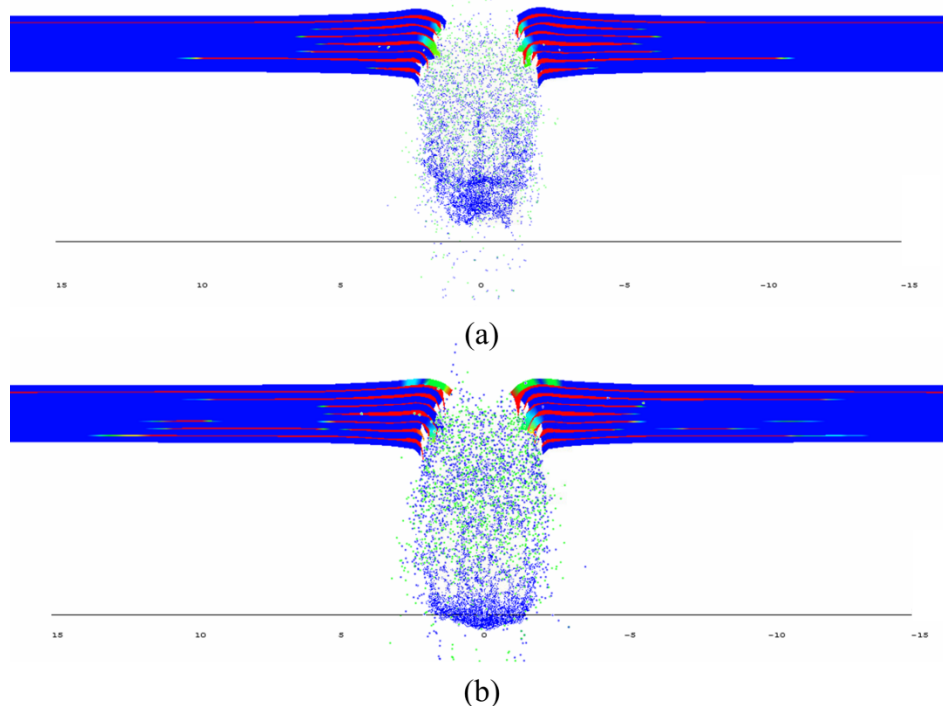
Figure 65 – Predicted impact hole and surrounding interlaminar damage for a) UKC #4 and b) JSC #2 input data

Fig. 66 exemplifies predicted intra- and interlaminar damage for the UKC #4 simulation (only damage tensor components of main influence are presented, including D_{22} and D_{12} for intralaminar failure, and D_{33} for delamination). The contour plots for damage variables D_{22}, D_{12} and D_{33} show the elements which are not capable of resisting transverse tension, in-plane shearing and through-the-thickness tensile loading, correspondingly. JSC #2 calculations are not shown for the sake of brevity, as results are qualitatively the same due to the similarity of the layup. It should be noted that intralaminar failure has been modeled as a brittle phenomenon. As a result, variables D_{22} and D_{12} for an element were set to unity immediately after corresponding stress limit had been reached in it.
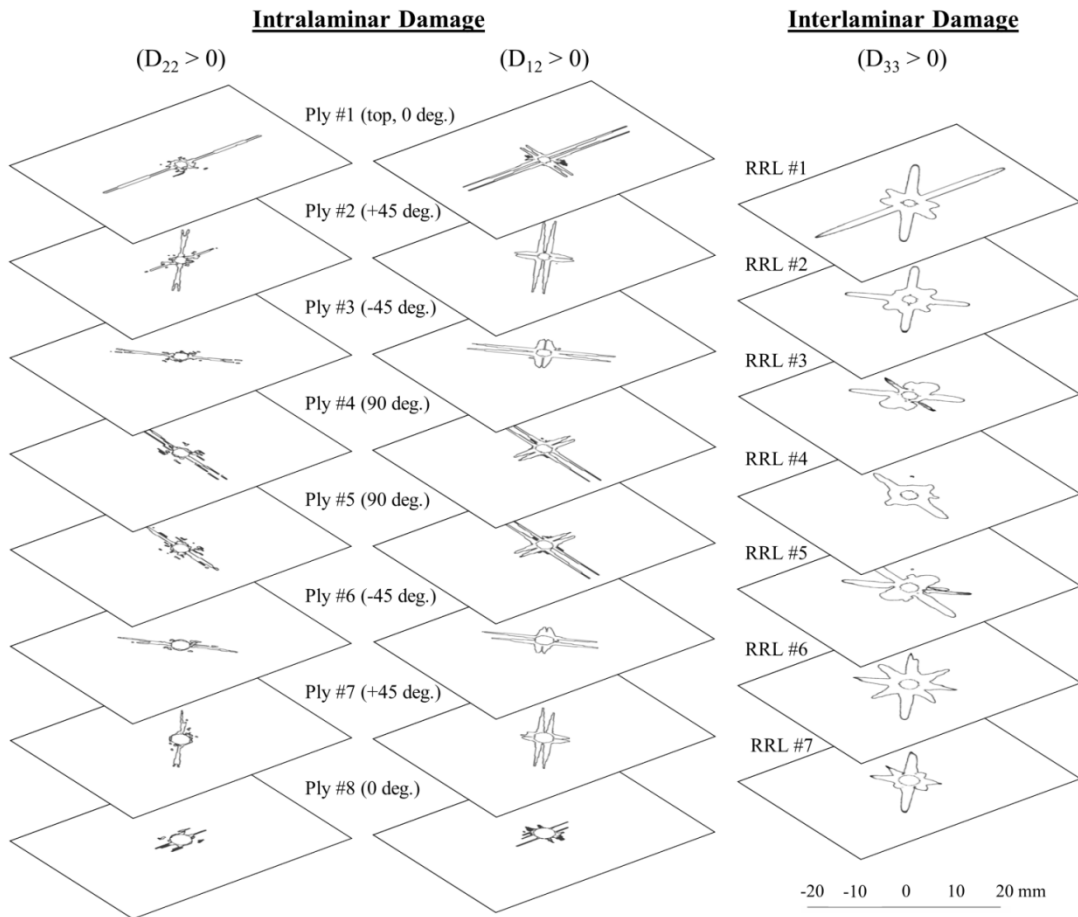
Figure 66 – Intralaminar and interlaminar damage predicted for UKC #4 data set

Many experimentalists reported that in unidirectional composites exposed to hypervelocity impacts, perforation was accompanied by the front surface delamination and peeling (see e.g. original paper describing UKC experiments [78], as well as [69], [71] and [84]). This surface damage always had a form of elongated strips emanating from the impact crater in the direction of reinforcing fibers' axis in external layer. Mechanism of such type of damage was also discussed in [76]. It was explained by shearing along the interface of adjacent plies with dissimilar orientation, produced by longitudinal waves traveling away from the area of impact. Damage pattern presented for the upper layer in Fig. 66 coincides with the description given above. It is characterized by a zone of intralaminar damage and delamination elongated in the direction of fibers in the outer ply. This evidences that the model is capable of representing experimentally observed phenomenon in a qualitative manner.
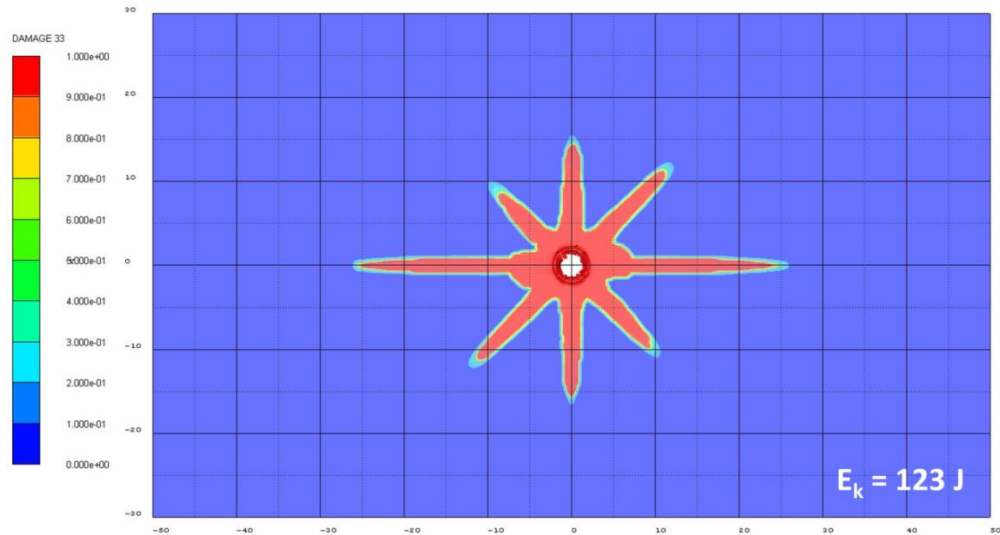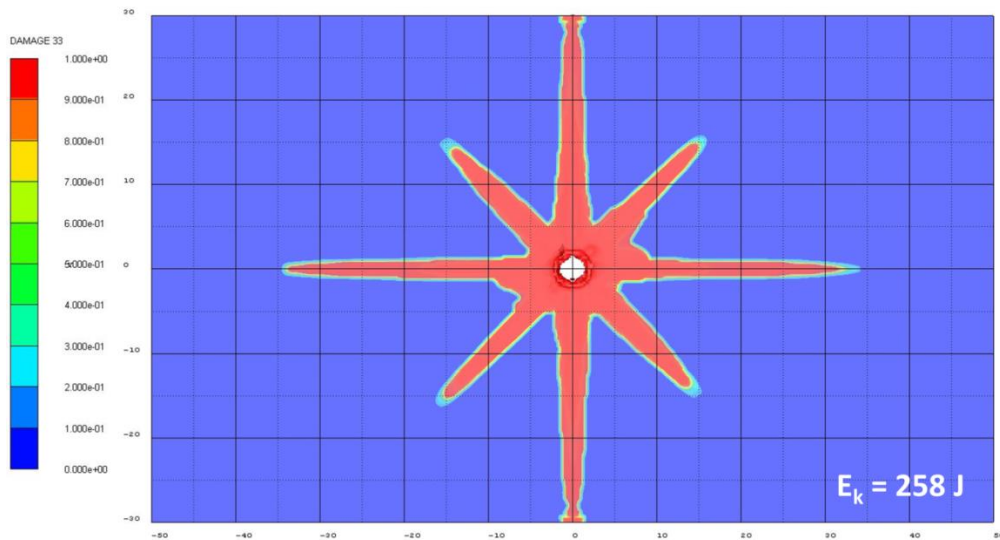
Figure 67 - Delamination patterns obtained from simulations with dynamic fracture

toughness: a) UKC #4 and b) JSC #2 (All damaged surfaces projected on a single plane)

The quantitative assessment of the model's accuracy has been done by comparison of

predicted and experimentally determined (by means of c-scan) delamination area. In order

to make numerical results comparable to c-scan measurements obtained in UKC and JSC

experiments, damage contours from all resin-rich layers were projected on a single plane.

It was accomplished by setting up 50% opacity for the resin-rich layers while contours of D_{33} damage variable were being displayed. Resulting images are shown in Fig. 67.

Damaged areas A_{delam} in Fig. 67 were carefully measured and used to calculate the "equivalent diameter of delaminated zone" as $D_{delam} = \sqrt{\frac{4A_{delam}}{\pi}}$. Only completely damaged elements with $D_{33} = 1$ were taken into account when calculating the delamination area, as there is no absolute certainty that partly damaged areas could be detected by c-scan equipment. Results of calculations and their comparison with experimental c-scan measurements are presented in Table 19. A good correlation (within ~12%) between numerical and experimental results was found.

Table 19 – Comparison of numerical and experimental results

UKC #4		Δ, %	JSC #2		Δ, %
D_{delam}, mm			D_{delam}, mm		
simulation	17.2	-11.8	simulation	24.1	-5.5
experiment	19.5		experiment	25.5	

The sensitivity of the solution to fracture toughness was explored by carrying out an additional pair of computations with the static values of G_{Ic} and to G_{IIc}. Although overall damage pattern remained unchanged, the delamination area in this case was significantly underpredicted as compared with experimental data, resulting in an equivalent diameter of delamination of 8.9 and 11.8 mm for UKC #4 and JSC #2 experiments, correspondingly. Thus, availability of dynamic fracture toughness data for the thermoplastic composite system of interest is important for accurate predictions of delamination.

4.6 Validation of the Meso-scale Approach for Composites Fabricated by Filament Winding

4.6.1 Experimental data

Conditions of two experimental shots, namely 1-3 (LDI) and 4-3 (HDI), were chosen for numerical modeling, as they result in significantly different damage patterns, as determined both by C-Scan and visual inspection (see Fig. 59). In the case of HDI, specimen inspection revealed "containment" of impact damage within the region restricted by 2x2 HDI units adjacent to the perforated hole, whereas in LDI specimen damage propagates outwards this region along directions of fibers, especially in the bottom left and bottom right directions. The simulation approach, therefore, was tested for its capability to represent those features.

4.6.2 Material properties

Composite parts fabricated by filament winding contain higher volume fraction of voids (typically from 5 to 10% of voids [14]) as compared to pressure-cured parts (usually contain 1-2% of voids). The high volume fraction of voids can affect mechanical properties of the composite. Moreover, the mechanical properties provided by manufacturers are typically corresponding to pressure-cured composites with high fiber volume fractions. Therefore, the volume fractions in the filament-wound material must be determined and its properties must be updated based on the actual content of fibers, voids and matrix.

In order to do that, specimens for microscopy were cut-off from the filament-wound material using waterjet cutting machine. Next, specimens were subjected to grinding and polishing using the technique described in [85]. After polishing, specimens were subjected to optical microscopy. Micrographs with different magnifications are shown in Fig. 68.

| ×5 magnification | ×20 magnification | ×100 magnification |
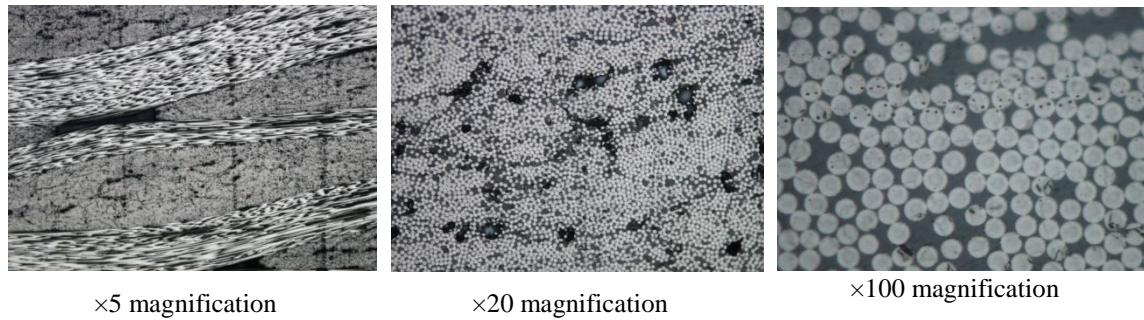
Figure 68 – Microscopy of the filament-wound composite

Two types of voids were identified. The first type is the voids formed at crossover regions (noticeable at the micrograph made at ×5 magnification). These voids are believed to be an artifact of filament winding. Their presence may result in stress concentration at crossovers leading to the formation of cracks and preliminary disintegration of filament wound composite under in-plane tensile and shear loading. It is obvious that higher degree of interweaving leads to a higher density of such voids. Voids of this type will be explicitly modeled in the frame of the meso-scale approach, as described in the next section.

Another type of voids represented by the pores formed within the filament bands. As in meso-scale approach material of the filament bands must be substituted by equivalent homogeneous orthotropic material, the content of these voids must be measured and this data must be used for the update of the filament band properties.

The volume fraction of the type-two voids was determined using image processing method. Voids in a number of micrographs with ×20 magnification were carefully selected and placed in separate "layers" in Adobe Photoshop (see Fig. 69). Number of pixels in such layer divided by a number of pixels in the corresponding image gives volume fraction of voids. It averaged 8.5% of voids within a filament band.

147

(a) HDI pattern, k_v = 9.5 %

(b) HDI pattern, k_v = 7.5 %
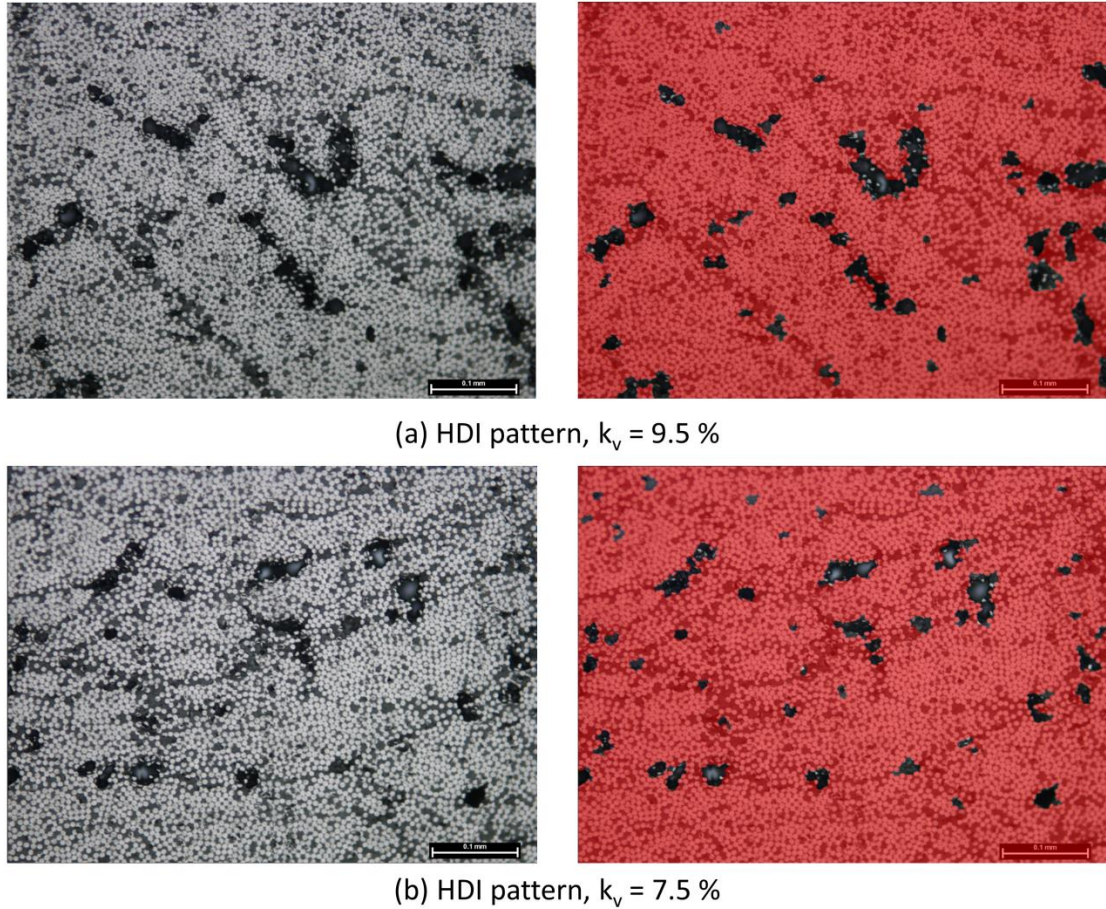
Figure 69 – Determination of void content in composite specimens (k_v is the volume

fraction of voids)

Based on this analysis, the actual composition of the material of filament bands was found

to be as follows: fibers – 54.4% by volume, voids – 8.5%, matrix – 37.1%.

As a result of relatively high void content in filament band its mechanical properties may

deviate from the values specified by the manufacturer [86]. The method proposed by

Chamis [87] was used to reduce transverse and shear properties as a function of volume

fraction of voids. Elastic properties of the composite were also updated based on the actual

volume fractions of fibers and matrix (see Table 20) using micromechanical formulae (see

Appendix B for more details). Properties of constituents for micromechanical calculations were provided by the manufacturer [86, 88].

Table 20 – Properties of manufactured composite

Property	Manufacturer [86] for 60% fiber volume fraction	Calculations for 54% of fibers and 8.5% of voids	
		Updated value	Micromechanical model
Modulus of elasticity along fibers, GPa	135	122	Rule of mixtures
Modulus of elasticity in transverse direction, MPa	N/A	8172	Modified rule of mixtures
Shear Modulus, MPa	N/A	3676	Hashin-Rosen self-similar model
Longitudinal tensile strength, MPa	2550	2312	Rule of mixtures
Transverse tensile strength, MPa	69	42	Chamis [87]
In-plane shear strength, MPa	N/A	22	Chamis [87]

Another important property of the filament-wound composite that has to be determined is its fracture toughness. According to the results of several investigations by previous researchers, the fracture toughness of thermoset-resin composites does not reveal strain-rate dependence [89, 90]. Correspondingly, in this study mode I and mode II fracture toughness of the composite were determined at quasi-static conditions.

In both cases, electromechanical testing machine (MTS) with a maximal loading capacity of 30 kN was used. Load-displacement data was acquired in both types of experiments and then used to calculate corresponding strain energy release rates. Mode I fracture toughness was determined in accordance with the method described in ASTM D 5528-01 standard [91]. This method uses double cantilevered beam (DCB) specimens. For mode II fracture

toughness experiments, a method described in [92] was used. In this method, end notched flexure (ENF) specimens are being subjected to 3-point bending. Averaging of experimental data resulted in 95 J/m^2 for G_{Ic} and 140 J/m^2 for G_{IIc}. The mode III fracture toughness was assumed to be the same as the mode II (i.e. $G_{II} = G_{III}$).

The behavior of aluminum parts (projectile and front bumper) was represented in the modeling by a combination of Mie-Gruneisen equation of state and Johnson-Cook strength and failure models. The full set of material properties employed in the numerical simulations is provided in Appendix B.

4.6.3 Numerical model

Generally, two numerical techniques have been widely accepted and used for HVI simulations, such as Finite Element Method (FEM) and Smooth Particle Hydrodynamics (SPH). FEM typically provides a good balance between simulation accuracy and computational efficiency, and is well-suited for tracking materials' interfaces. However, SPH is often advantageous over FEM in modeling physical processes involving extreme deformations and fragmentation.

The modeling approach employed in this study is based on simultaneous utilization of both SPH and FEM in each numerical simulation. The SPH method was used to represent the behavior of parts that exhibited fragmentation, namely projectiles and bumpers. At the same time, composite panels with a meso-scale representation of filament winding patterns, which contained multiple interfaces between filament bands and resin-rich regions, were modeled using FEM in the Lagrangian formulation combined with erosion mechanism.

150

The use of erosion helped to avoid excessive mesh distortions and tangling at high deformations. All simulations were conducted in ANSYS Autodyn hydrocode [93].

<center>(a)   (b)</center>
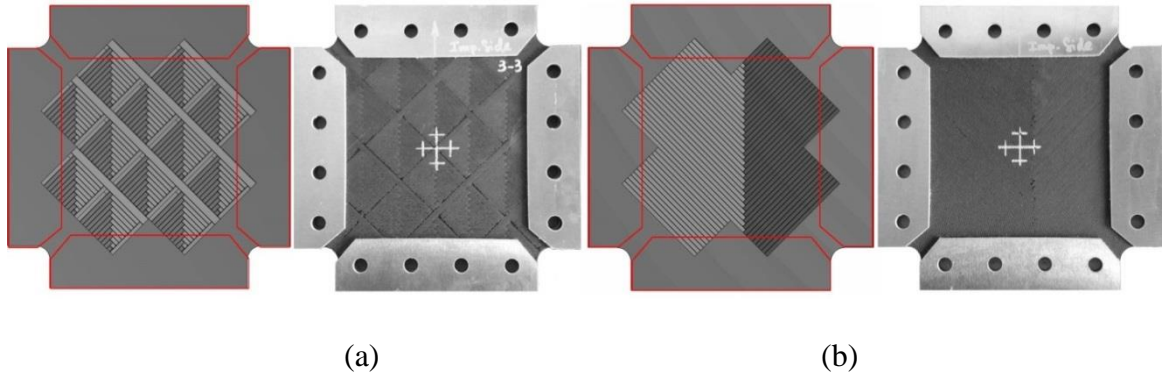
Figure 70 – Geometrical models and the real filament-wound specimens: a) HDI; b) LDI
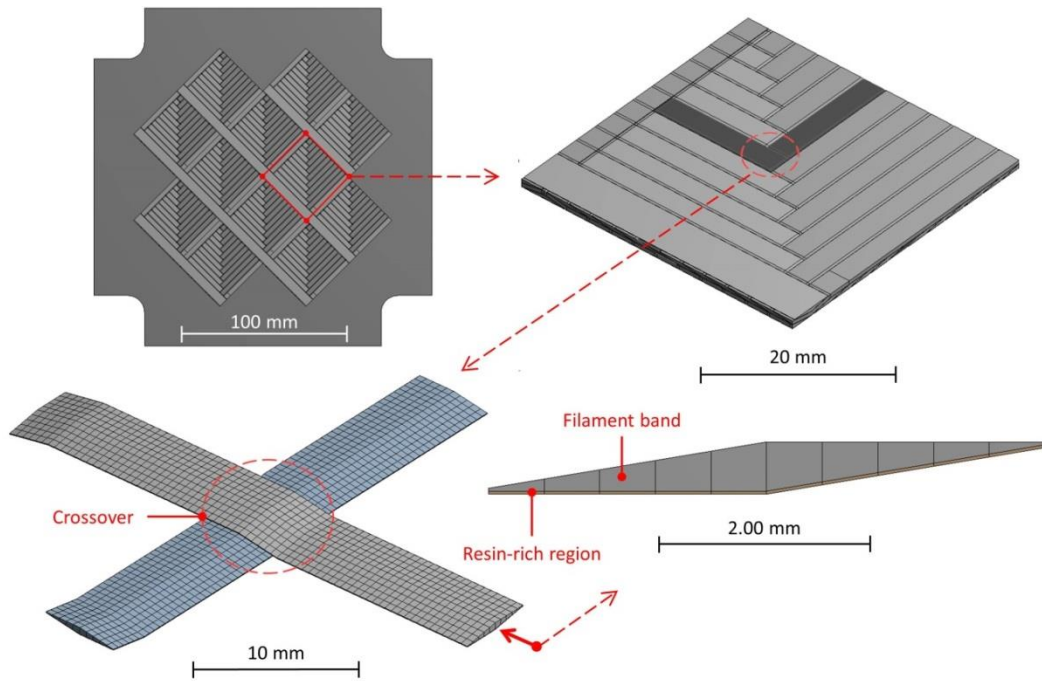
Figure 71 – Meso-scale modeling of the filament-wound specimen

The detailed meso-scale representation of filament winding was used only in the region of interest in order to minimize the computational cost. Around that region, the composite was represented by a homogeneous orthotropic material with effective properties

<center>151</center>

equivalent to those of the real material. The geometrical models of the HDI and LDI panels compared with the real specimens are represented in Fig. 70.

Fig. 71 represents the main features of the numerical models, including: a macro-scale appearance of the specimen model; a translational unit of the filament winding pattern model; a pair of interweaving filament bands; and a cross-section of a filament band (the shape determined by microscopy) with an adjacent resin-rich region.

The thickness of the resin-rich regions in the modeling was 0.025 mm, which is within the range of 0.01 mm – 0.1 mm that is typical for carbon-fiber reinforced plastics. The maximum thickness of the filament bands was 0.47 mm. The total thicknesses of the composite panels, each consisting of 3 layers of the filament-wound material, were 3.0 mm.

A cross-section of the modeled HDI panel is shown in Fig. 72 (a) and exemplifies multiple crossover regions. Optical microscopy (see Fig. 72 (b)) revealed the existence of voids in these regions, which are encircled by red lines. As it was mentioned in the previous section, these voids are believed to be an artifact of filament winding and may result in stress concentration at crossovers leading to the formation of cracks and preliminary disintegration of the filament-wound composite when subjected to static or impact loading. A higher density of crossovers leads to a higher density of such voids, which may be a limiting factor for the application of composites with high degrees of interweaving. On the geometrical level, this feature was represented in the model as shown in Fig. 72 (c).

Based on a preliminary mesh dependency study, the modeled parts were discretized using a smoothing length of 0.1 mm and an in-plane finite element size of 0.5 mm. This resulted

in 419,808 SPH particles in the model. Among them the 4.763 mm projectile was represented by 57,856 particles. Approx. 2,000,000 finite elements represented the composite specimens. Discretization of the filament bands is shown in Fig. 71.
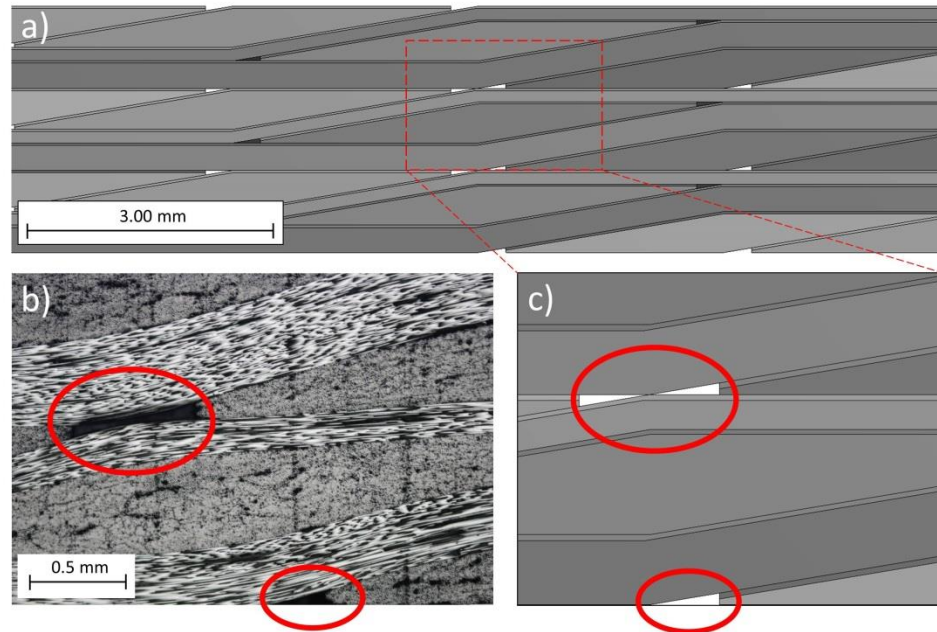
Figure 72 – Voids in crossover regions: microphotograph and numerical model

The interaction between SPH and FE-discretized parts was modeled using the "Trajectory contact" feature in Autodyn with "Penalty" option, and by retaining the inertia of eroded nodes [93]. Within the composite part, elements representing resin-rich regions were attached to the filament bands along adjacent surfaces using "Bonded Contact" feature with the option of "NO separation". As no separation was allowed on the interfaces, all of the inter-band damage in the model, characterized by such macromechanical properties as interlaminar strength and fracture toughness, was confined to the resin-rich region elements.

Clamping of the composite specimens was represented in the model by applying the "General 3D velocity" boundary condition with all nodal velocities equal to zero in the

corresponding regions, as exemplified in Fig. 77, where the constrained nodes labeled with diamond-shaped marks. The constraints are applied in the regions represented by the homogeneous material only.

4.6.4 Results of hydrocode modeling

Both simulations with HDI and LDI specimens were terminated at t = 18 μs after initiation of impact on the front aluminum bumper. Beyond approx. 17 μs, no further growth of the damaged areas in the composite panels was observed. Two moments of time – just before impact on a composite plate and after its perforation – are shown in Fig. 73. It should be noted that as fragments of the projectile were modeled with SPH particles and fragments of the composite plate were represented by nodes of eroded elements, the debris cloud that was generated after perforation of the composite panel is a mixture of both. The resulting hole in the composite panel is compared with the experimentally obtained perforation, as represented in Fig. 74.

Before perforation

After perforation

SPH-particles +
Nodes of eroded FE
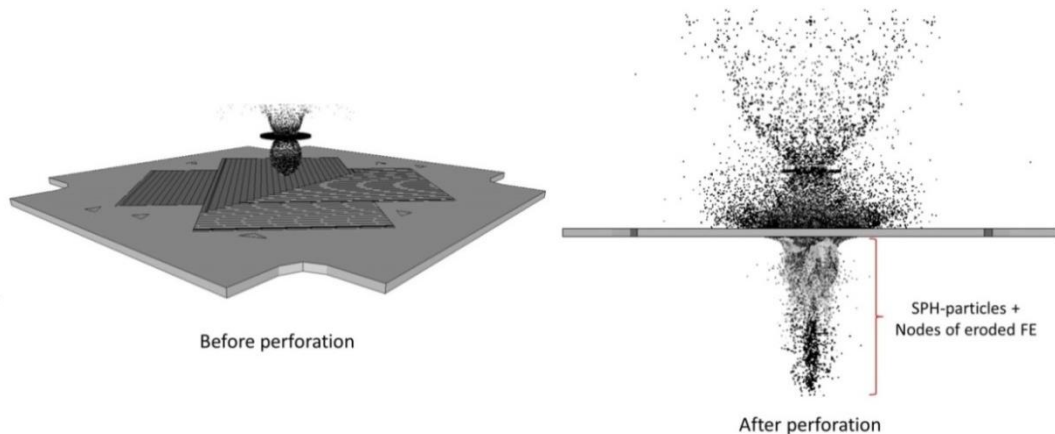
Figure 73 – Perforation of the composite plate

According to the material model described in Section 4.4, damage of the composite can be represented in terms of damage tensor with its coefficients corresponding to different

internal loads. Here *intra-band* damage is determined by coefficients D_{11}, D_{22} and D_{12}, representing correspondingly fiber breakage, matrix cracking due to stresses perpendicular to fibers and matrix cracking due to in-plane shear stresses. Contrastingly, *inter-band* damage (delamination between filament bands) is determined by coefficients D_{33} (mode I fracture in the resin-rich region due to through-the-thickness tensile stresses), D_{23} and D_{31} (mode II and mode III fracture due to through-the-thickness shear).
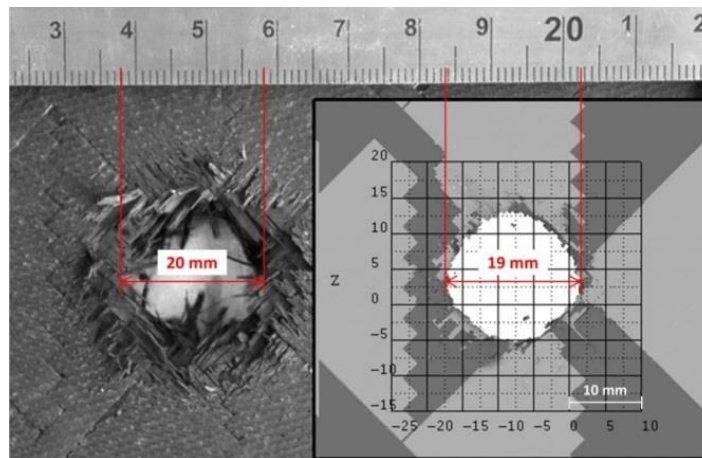
Figure 74 – Size of perforated hole: experiment vs. simulation

The damage contours for each of these modes, as detected by simulations, are represented in Fig. 75 and Fig. 76 for the LDI and HDI specimens, respectively. It should be noted that in these figures, the damage contours are only shown for those finite elements where corresponding damage tensor coefficients reached their maximum value, such as $D_{ij} = 1$, which physically corresponds to a local coalescence of microcracks into a macrocrack. The damage contours are shown in a semi-transparent regime, which makes it possible to project all of the areas affected by the damage on a single surface, independently on their through-the-thickness location.
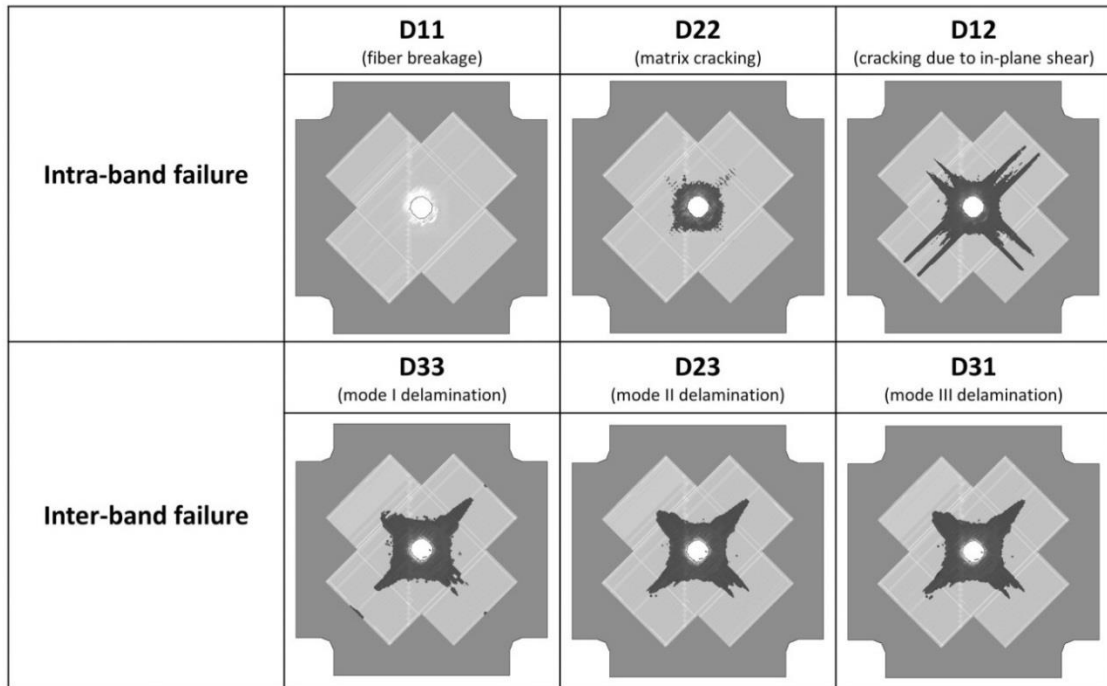
Figure 75 – Damage tensor components for the LDI specimen
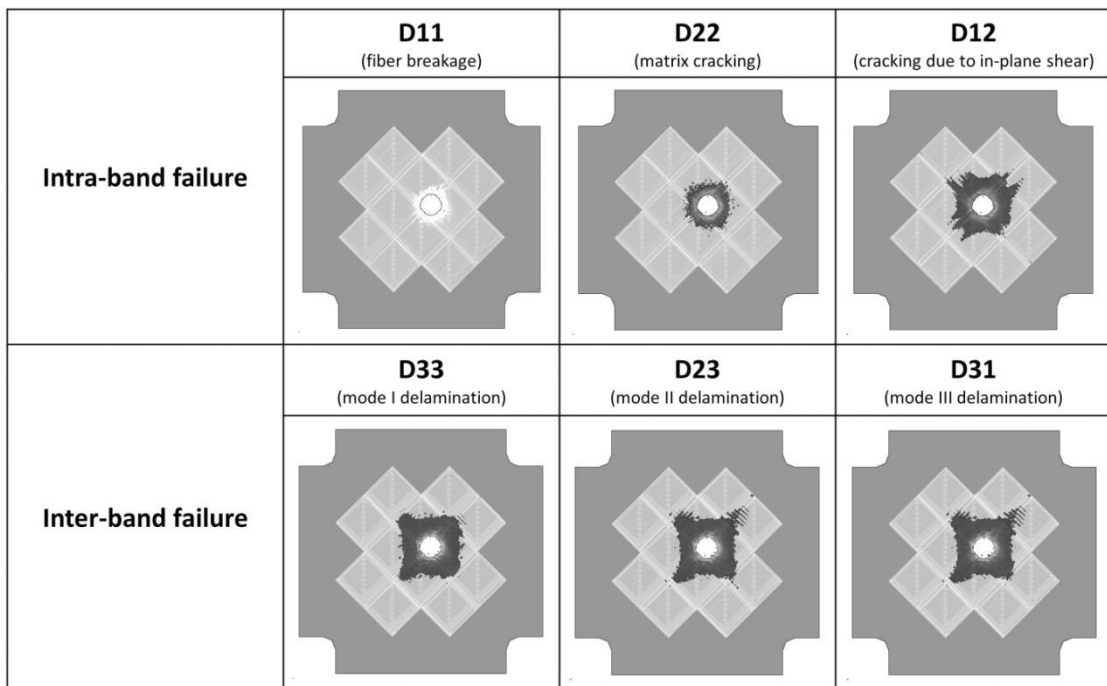
Figure 76 – Damage tensor components for the HDI specimen

Fig. 77 (a) and (c) represent a comparison of the *superposition* of all damage contours from Fig. 75 and 76, respectively, as well as the corresponding damage profiles that were obtained via ultrasound inspection of the real specimens. Fig. 77 (b) and (d) represent a comparison of the visually observed damage on the specimens' rear surfaces and the corresponding rear surface damage predicted by numerical modeling.

HDI: superposition of all damaged surfaces

(a)

HDI: rear surface damage only

(b)

LDI: superposition of all damaged surfaces

(c)

LDI: rear surface damage only

(d)
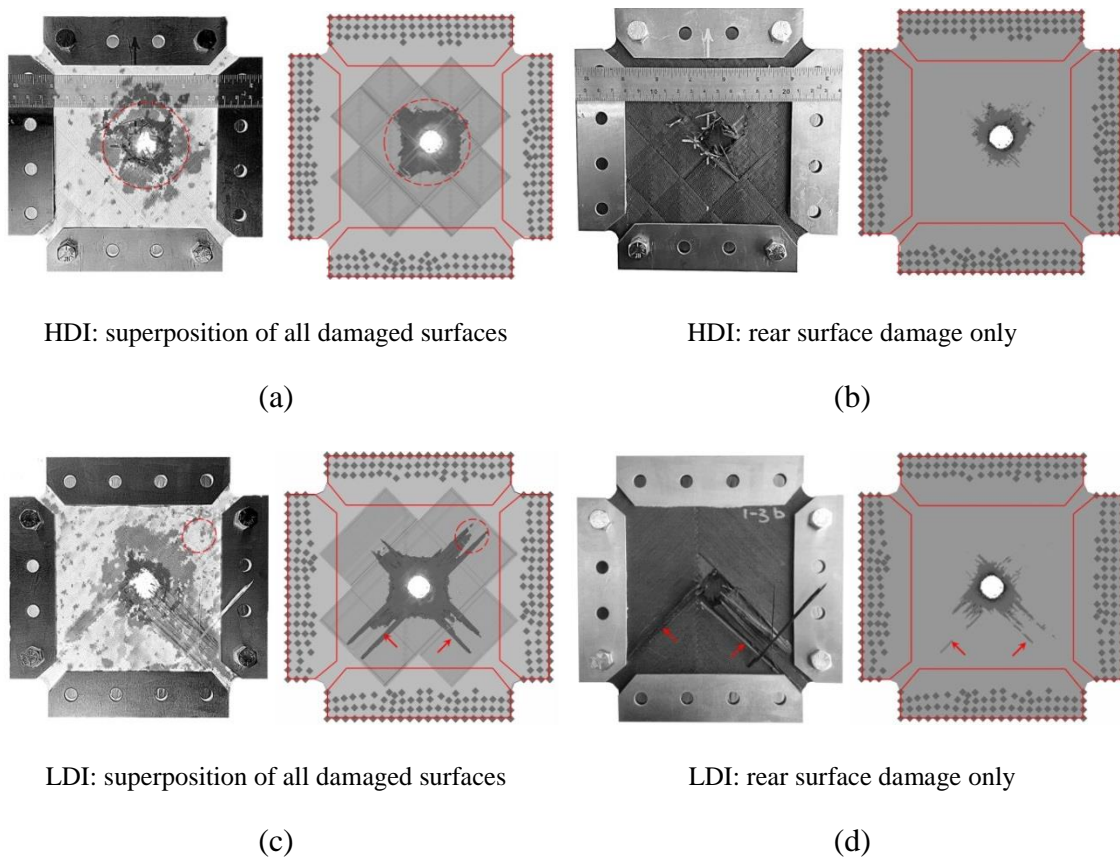
Figure 77 – Composite damage: comparison of experimental results and numerical predictions: top – HDI panel; bottom – LDI panel

4.6.5 Discussion of modeling results

On the *quantitative* level, a comparison of experimental results and numerical predictions reveals the following:

- The predicted diameters of the perforated holes agree within 5% with the experimentally obtained values, as shown in Fig. 74 for the HDI specimen.

- Simulations tend to somewhat underpredict the damaged area as compared to the damage detected by C-Scan. The exact reason for the underprediction is unknown, but may be attributed to the presence of a strain-rate dependence of the composite fracture toughness that was ignored in the modeling.

On the *qualitative* level, the introduced meso-scale modeling approach is capable of representing the main features of HVI damage of the composites with the different filament winding patterns:

- For the HDI specimen, the simulation predicts "containment" of the HVI damage within the region restricted by 2x2 HDI units adjacent to the perforated hole, which is the same damage pattern observed in the experiment.

- For the LDI specimen, the simulation predicts further propagation of damage outwards this region along fiber directions, which is also consistent with the experimental results. Moreover, modeling allows the identification of the damage mode (damage due to in-plane shear stresses; represented by D_{12} coefficient in Fig. 75), governing such response of the composite to HVI loading. This information can be used for identification of critical material properties and proper material selection. It should be noted however

that the simulation also predicts the propagation of damage in the right-top corner of the specimen (encircled in Fig. 77 (c)) that was not observed on the C-Scan image.

- Damage patterns on the rear surface predicted by simulations for both HDI and LDI specimens are qualitatively in very good agreement with the experiment, as shown in Fig. 77 (b) and (d).

It also can be noted in Fig. 75 – 76 that all predicted damage modes, from matrix cracking to delamination, affect noticeably smaller areas in HDI panel as compared with the LDI panel, mostly being bounded by crossovers.

4.7 Case Study of HVI on a Shielded COPV

Having the meso-scale approach suitable for modeling of the interaction between the secondary debris cloud and the composite pressure wall formulated and verified against experimental data, the two-step simulation procedure (*section 4.2*) can now be used to investigate the behavior of shielded COPVs subjected to HVI. This section presents a case study illustrating the use of the two-step modeling procedure.

Parameters of the vessel considered in this section are represented in Fig.78. The vessel is a cylindrical carbon-fiber composite overwrapped pressure tank with the diameter of 150 mm and the length of the cylindrical part of 300 mm. The carbon fiber layers are wrapped around the titanium liner.
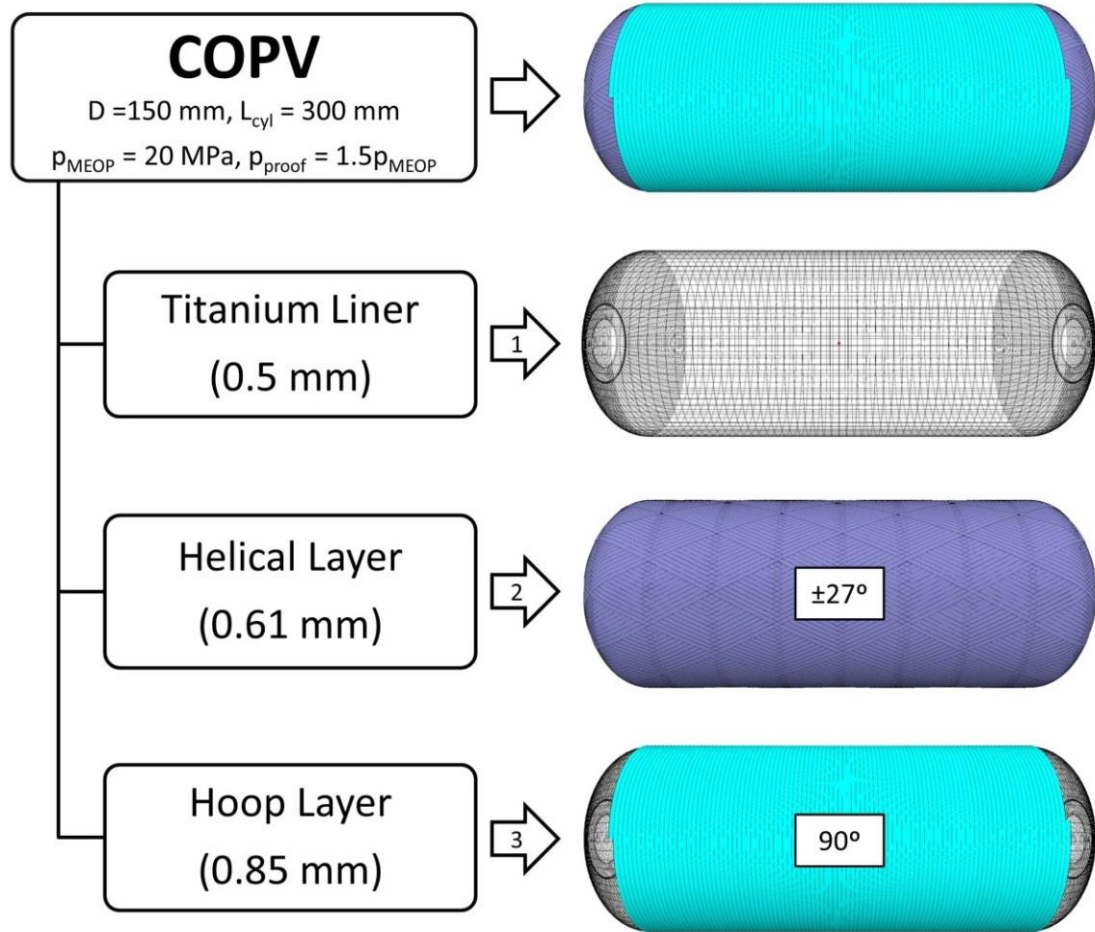
Figure 78– Layout and parameters of the pressure vessel with carbon-fiber overwrap

The carbon-fiber overwrap consists of a helical layer with the fiber orientation $\pm\varphi$ and a hoop layer (fibers are oriented at 90 degrees relative to the axis of the vessel). The width of the filament bands is 4 mm, which corresponds to the typical range of $2 - 4\%$ of the vessel's diameter [14]. Winding angle for the helical layer and the winding pattern were predicted using ComposiCAD[TM] manufacturing software. The software uses geometry of the vessel (including size of its openings) and parameters of the filament band as input data and estimates parameters of the wind in a way to guarantee no slippage of the filament bands during the winding process. The obtained value of the winding angle is ±27 degrees. The winding pattern for the helical layer is shown in Fig. 78 and Fig. 83.

The maximum expected operating pressure (MEOP) for the vessel is 20 MPa. Correspondingly, the vessel was designed in order to withstand a proof pressure of 1.5 times the MEOP, i.e. 30 MPa. Thicknesses of the layers were determined using the *netting analysis* [14], which provides the following design equations:

$$t_{HEL} = \frac{p_{proof} \cdot R}{2 \cdot \sigma_{1\,max} \cdot \cos^2 \varphi_{HEL}} \text{ for the helical layer; and} \qquad (52)$$

$$t_{HOOP} = \frac{p_{proof} \cdot R}{2 \cdot \sigma_{1\,max}} \left(2 - \tan^2 \varphi_{HEL}\right), \text{ for the hoop layer} \qquad (53)$$

According to these equations and using the strength of the composite along fibers $\sigma_{1\,max} = 2312$ MPa, the required thicknesses were found to be equal to 0.61 mm and 0.85 mm for the helical and the hoop layers, correspondingly.

The thickness of the titanium liner was equal to 0.5 mm, which corresponds to a typical value used to ensure that the liner will not buckle during the filament winding. It should be noted that the sizing of the composite layers does not take into account the load-sharing function of the liner. The liner, therefore, considered only as a gas permeation barrier and a mandrel for filament winding. As a result, the vessel's margin of safety against the static bursting is somewhat higher than the one determined by the safety factor of 1.5 used in the calculations.

Given the design of the vessel (quite typical for cylindrical COPVs) and understanding loading of the composite shell (dominated by the hoop stresses), it is possible to establish a simple engineering criterion for fragmentation:

161

- COPV fragmentation is only possible when its hoop layer fails across its whole length (measured along the axis of the vessel) by means of **fiber breakage**.

One can also affirm the opposite: unless fibers across the hoop layer (the outer layer) are broken, the vessel will not be fragmented.

The vessel was shielded by a simple aluminum Whipple shield consisting of the 0.8 mm front bumper placed at the standoff of 16 mm from the 0.8 mm rear wall. According to the Whipple shield BLE, such combination can provide protection from a small-size hypervelocity projectile with a diameter up to 1.2 mm. The shield is placed at a distance of 50 mm from the pressure wall. The projectile diameter $D_p = 7$ mm capable of perforating the system "external shield + pressure wall" was used in the analysis of the COPV's fragmentation hazard.

It should be emphasized that the COPV was sized using equations (52) – (53) to withstand a static proof pressure, whereas all of the calculations related to the orbital debris impacts must be conducted for the pressure corresponding to the maximum pressure expected in the vessel's operational life, i.e. p_{MEOP}, which is 1.5 times lower than the p_{proof}.

4.7.2 Step one: determination of the shock wave parameters

As the first step of the two-step modeling procedure formulated in *section 4.2*, a two-dimensional analysis must be performed in order to determine the parameters of the shock wave generated in the pressurized gas.

Potentially, the shock wave can reach the rear side of the vessel, reflect, travel back to the front wall and produce a pressure pulse there. If the pressure pulse is strong enough, it may

be able to make a significant contribution into further damaging of the perforated front wall and triggering catastrophic rupture of the vessel had it not started earlier due to the action of the wall stresses around the perforation.

The purpose of the numerical experiment described in this section, therefore, was estimating the amplitude of the pressure pulse resulted from its perforation by the secondary debris cloud. In order to broaden the scope of this numerical experiment, the shock wave parameters were estimated for the case of 10 mm aluminum projectile, which corresponds to the upper limit of the projectile size for which the passive shielding is being designed.

The following assumptions were made in the numerical analysis:

1. The problem was considered in the two-dimensional axisymmetric formulation, which dramatically reduced the number of degrees of freedom in the simulation (and therefore the computational time), but implied that the curvature of the shell had to be neglected in order to comply with the axial symmetry requirements;

2. The vessel's rear wall was considered as rigid, which resulted in a rather conservative estimate of the shock wave amplitude after its reflection from the rear side of the vessel;

3. The behavior of nitrogen was represented by the simple ideal gas equation of state.
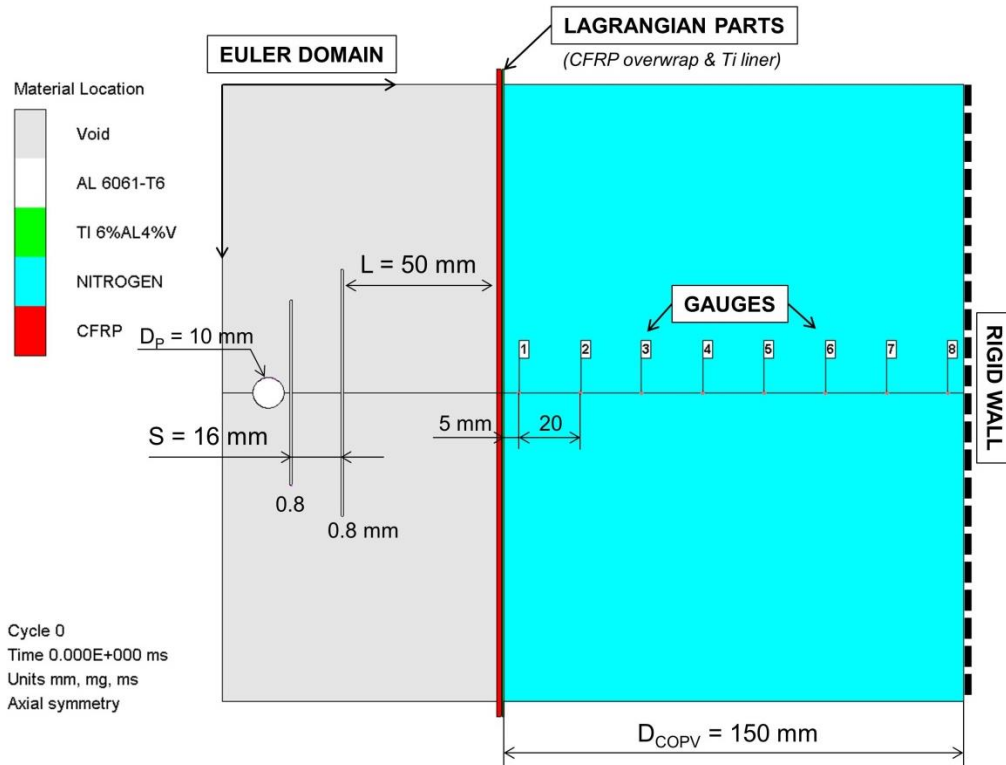
Figure 79 – Initial setup for numerical experiment

The initial setup for the numerical experiment is shown in Fig. 79. The projectile, the shield and the gas inside the vessel were modeled using multi-material Euler solver of Autodyn, whereas composite shell (overwrap and liner) were represented by Lagrangian solver in order to enable advanced material models for CFRP and apply appropriate boundary conditions (no displacements at the end). Rigid rear wall of COPV was represented in the simulation implicitly by a boundary of the Euler domain.

164
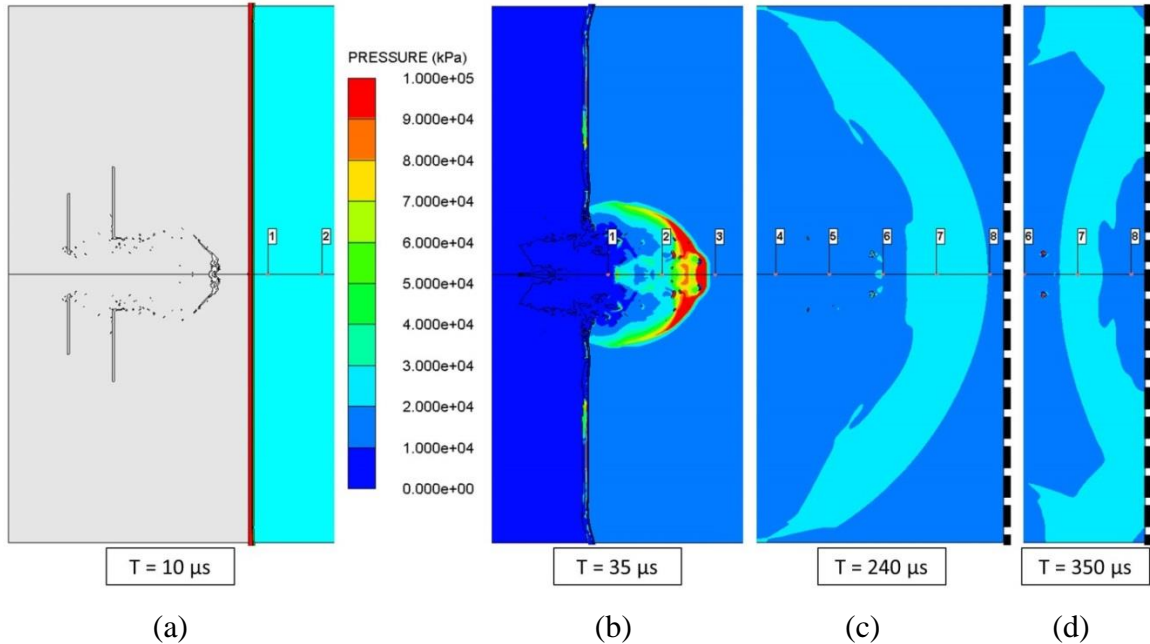
Figure 80 – (a) fragments cloud just before impact on the front wall; (b) shock wave after perforation of the front wall; (c) shock wave just before impact on the rear wall; (d) pressure pulse after reflection from the rear wall

Virtual pressure gauges were set within the vessel along the symmetry axis, as indicated in Fig. 79. Debris cloud just before impact on the front wall and shock wave at three different stages after perforation of the COPV, as predicted by simulation, are exemplified in Fig. 80.

Results of conducted numerical experiment are represented in Fig. 81. Here Fig. 81 (a) illustrates the rapid decrease of shock wave amplitude while it moves from the front to the rear wall of COPV and on its way back to the front side upon reflection. Fig. 81 (b) illustrates amplitudes of the incident and reflected pressure pulses as detected at the gauge #7, which was placed at a distance of 25 mm from the rear wall. It can be deduced from the figure that the difference between the reflected pulse and the static inflation pressure in the vessel is only 3 MPa. This means that the wave will be *completely damped out* in the

165

close vicinity from the rear wall, and will not be able to reach the front side of the vessel upon reflection.
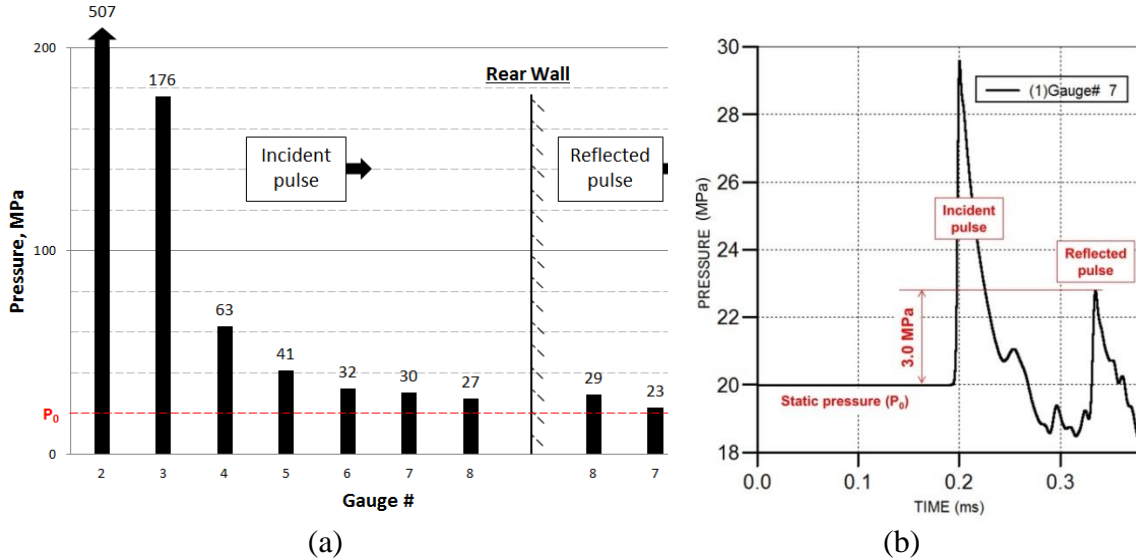
Figure 81 – (a) Shockwave amplitude, as detected at the virtual gauges; (b) pressure pulses detected at gauge #7

This analysis demonstrates that influence of the shock wave on the overall damage of even lightly shielded COPV can be considered as negligible. The damage, therefore, is determined by parameters of the impactor, shielding, composite shell and static pressure within the vessel.

4.7.3 Step two: analysis of the pressure wall damage

According to the two-step modeling procedure (see *Section 4.2*), at this step the three-dimensional analysis of HVI on the shielded pressurized shell must be performed with the goal of evaluating its fragmentation hazard.

As the onset and propagation of the cracks, which potentially may lead to the catastrophic rupture of the vessel, is believed to occur on the perforated front wall, only this part of the COPV required the detailed meso-scale modeling and a fine discretization (see Fig. 82). The rest of the vessel was represented by the rougher mesh, homogenized helical layer and without the resin-rich regions between the hoop, helical and titanium layers.
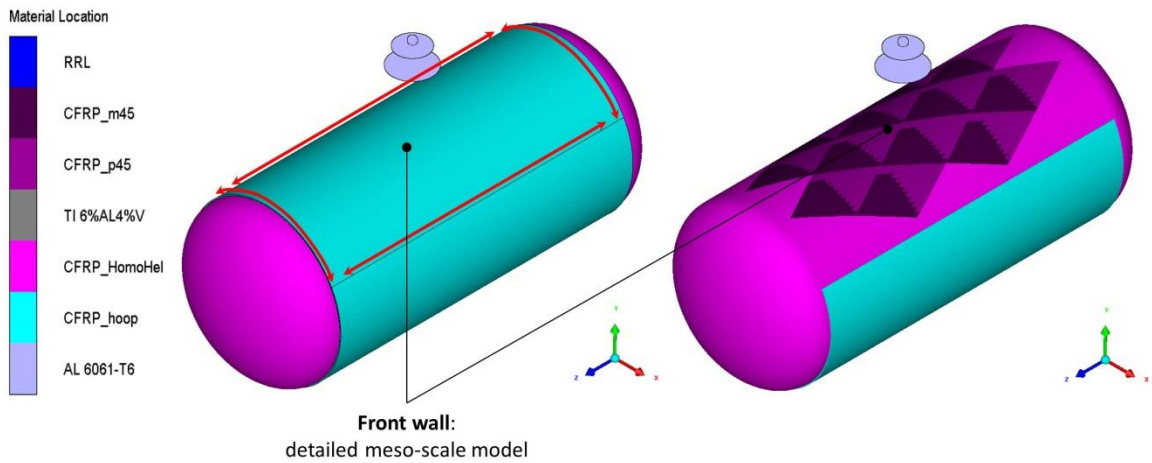
Figure 82 – Modeling of the COPV
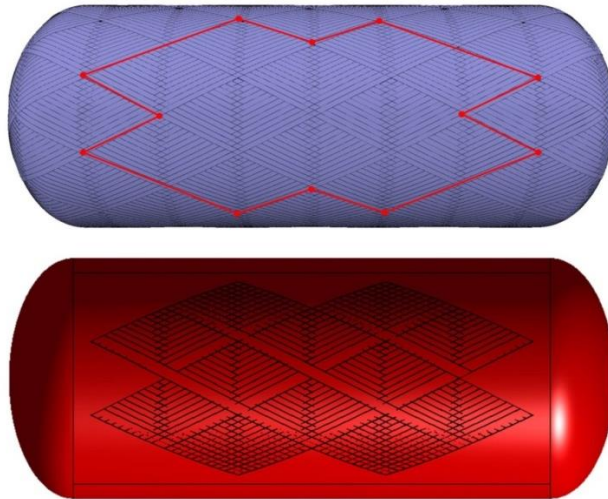
Figure 83 – Representation of the helical layer: model from the manufacturing software (top); geometrical model for HVI simulations (bottom)

Representation of the helical layer for the meso-scale numerical model is shown in Fig. 83 in comparison with the model of the same layer obtained using the filament winding software (ComposiCAD). It can be deduced from the figure that the numerical model precisely represents the chosen filament winding pattern in the front wall region.

Complete damping out of the shock wave shortly after its reflection from the rear wall allows for further simplification of the numerical model. This is due to lack of the need to apply the boundary conditions imitating the action of the reflected pressure pulse on the front wall. The action of the gas on the composite shell is, therefore, can be represented by the static inflation pressure only. The latter was simply taken into account by applying the "pressure" boundary condition to the inner side of the liner and setting it to 20 MPa.

The two interactions resulting in the perforation of the external shield and the complete perforation of the vessel's front wall are shown in Fig. 84. The SPH particles were deactivated at the later time in order to avoid their interaction with the rear wall, which physically do not occur due to ablation of the tertiary debris cloud.

Resulting damage of the hoop, helical and titanium layers is represented in Fig. 85 − 87. The damage of the composite is represented in terms of the 6 damage coefficients described in *Section 4.4.3*. Damage to the titanium liner corresponds to the Johnson-Cook failure model (*Section 2.3.2.1*).
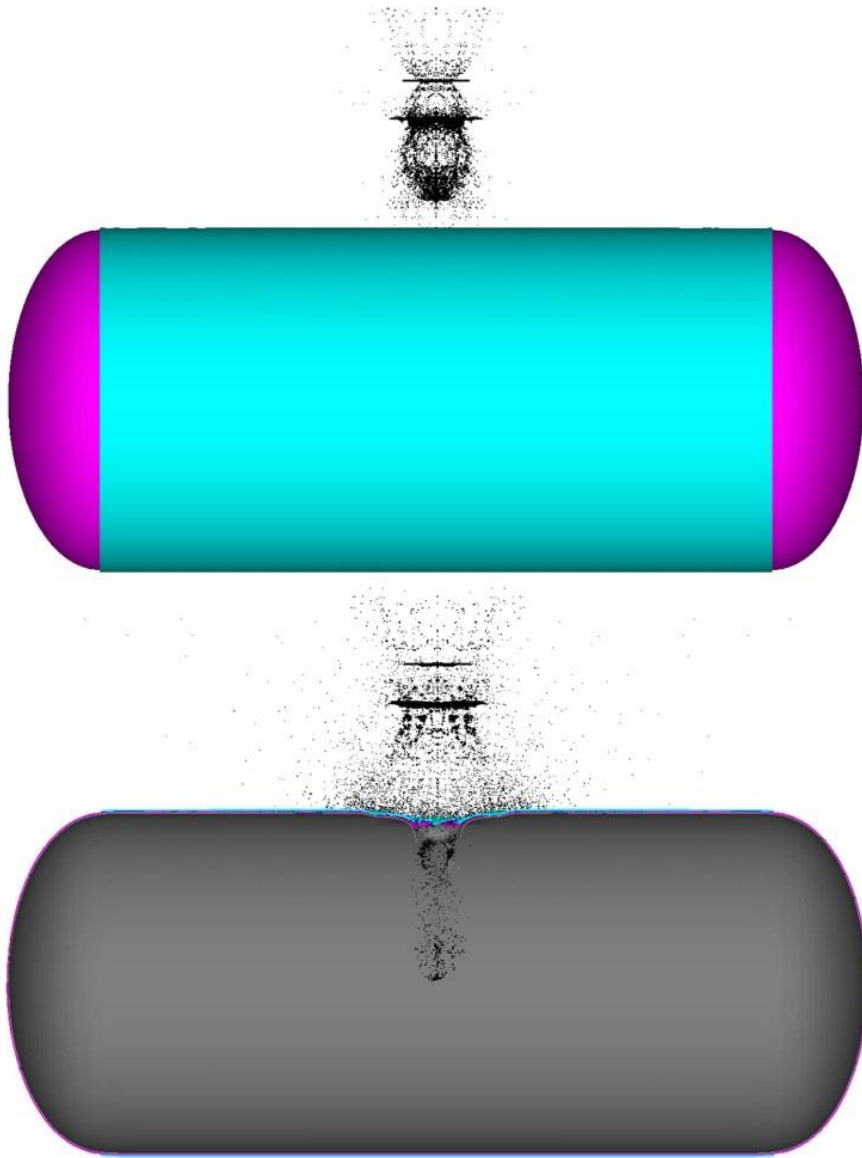
Figure 84 – Interaction of the secondary debris cloud with the composite pressure wall:

before perforation (top) and after perforation (bottom; cross-section)
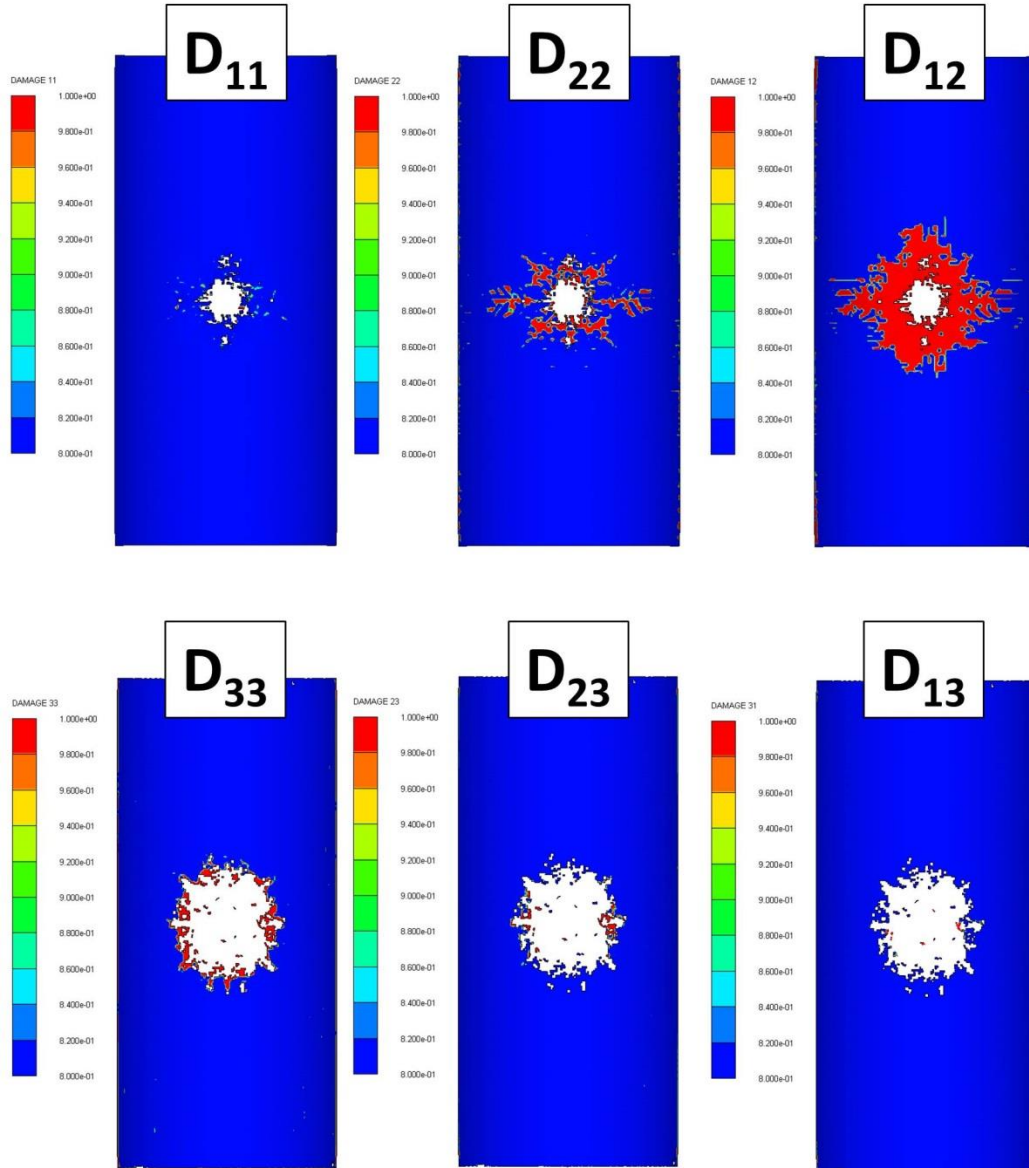
Figure 85 – Damage of the hoop layer (top) and interlaminar damage between the hoop

and the helical layers (bottom)
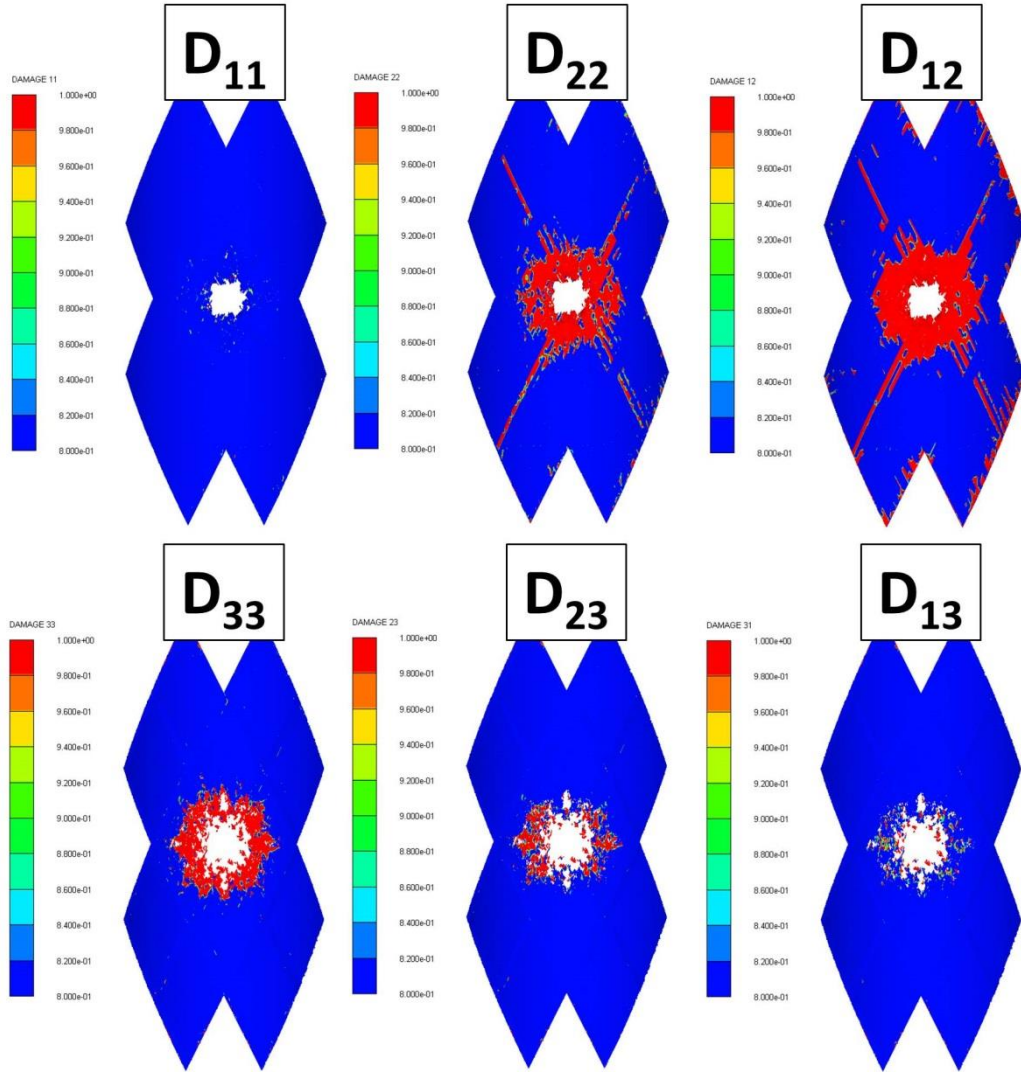
Figure 86 – Damage of the helical layer (top) and interlaminar damage between the

helical layers (bottom)
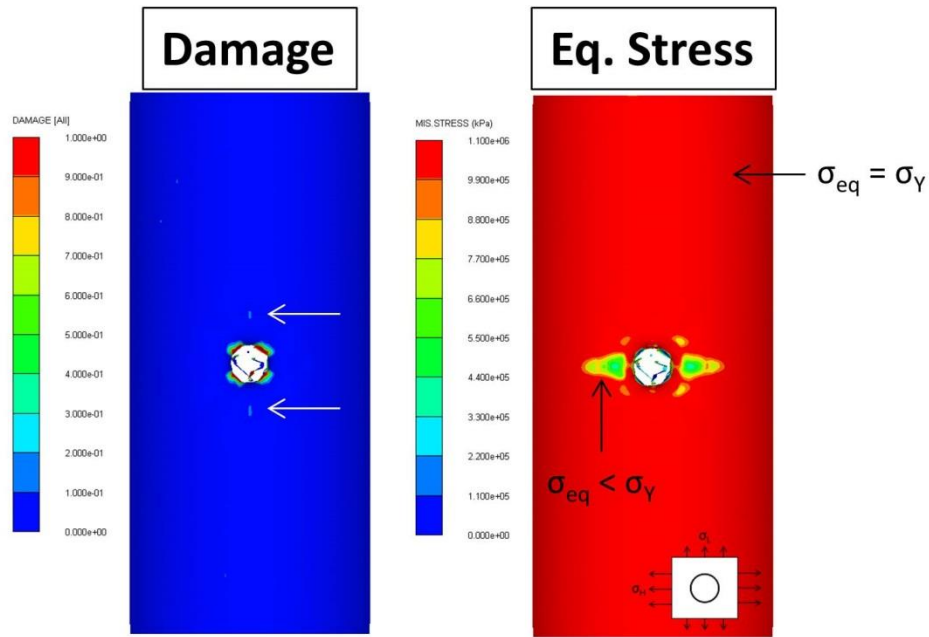
Figure 87 – Damage and stresses in the titanium liner

As it can be deduced from the figures, the main damage mechanism for the carbon fiber reinforced layers is the propagation of cracks in the composite matrix along fibers (represented by the damage coefficients D_{22} and D_{12}). These cracks originate in the regions damaged by the secondary debris cloud and are propelled further by the action of the vessel's internal pressure. Presenting in both the hoop and helical layer, the matrix cracks may physically result in only local redistribution of the load between the adjacent fibers.

At the same time, no fiber breakage (D_{11}) away from the perforation region was detected in any of the composite layers, providing that the available margin of safety is sufficient to efficiently redistribute the loads between the fibers adjacent to the perforated hole and resist disintegration of the composite. The established criterion for fragmentation (fiber breakage across the hoop layer) is therefore not satisfied and the vessel's catastrophic failure under given conditions is unlikely to happen.

Although regions of damage initiation are also detected in titanium liner (marked by the white arrows in Fig. 87), the energy supplied by the vessel's internal pressure is not enough for fracture (D < 1).

4.8 Summary

This chapter introduces the *two-step procedure* suitable for modeling of the behavior of shielded composite overwrapped vessels subjected to perforating impacts by orbital debris. The analysis according to this procedure consists of the following steps: 1) a preliminary and simplified 2-dimensional simulation estimating parameters of the pressure impulse produced by the reflected shock wave on the perforated front wall of a COPV; and 2) a 3-dimensional analysis of HVI on the shielded COPV with the meso-scale representation of the composite and implicit representation of the action of the pressurized gas on the composite shell through a set of boundary conditions. The implicit modeling of the gas allows for dramatic reduction of the computational time, while the meso-scale representation of the composite makes it possible to simulate the post-impact damage progression in the filament-wound material, including its helical layers.

Experimental study presented in this chapter revealed that damage of a filament-wound composite is significantly dependent on the filament winding pattern used in its fabrication. Patterns with the higher degree of interweaving of the filament bands demonstrated the ability to better impede propagation of HVI-induced damage, even in the presence of pre-loading. Pre-loading by itself was found to result in significant increase of the area affected by impact damage. On the contrary, increase of impactor energy may be a reason for the change of the dominating energy absorption mechanism in the composite panel and result in a reduction of the area damaged by the impact.

The presence of the winding pattern dependence observed experimentally requires utilization of relatively high level of detail in representing a filament-wound composite. For that, the *meso-scale modeling approach* was introduced for the use at the step 2 of the two-step modeling procedure. The approach is based on the explicit representation of the fiber-reinforced filament bands and resin-rich regions between them, and was found to be capable of predicting the main experimentally observed features of HVI damage in composites with different filament winding patterns. Due to its generality, the meso-scale approach can also be used in HVI simulations with the standard laminated composites and was preliminarily validated for this class of materials using experimental data available from the literature. Good correlation with experiments has been revealed in terms of predicted delamination area and qualitative representation of external damage.

The chapter ends with the example of the application of the developed two-step modeling procedure to the investigation of a typical lightly shielded COPV fragmentation hazard. In this example, estimation of the shock wave parameters conducted using the 2D axisymmetric simulation indicated that it will most likely dissipate long before returning to the front wall of the shielded COPV filled by gas, even when it is impacted by a relatively large (up to 10 mm) hypervelocity projectile. This observation allowed for further simplification of the modeling procedure. The conducted 3-dimensional analysis predicted that the shielded COPV pressurized up to MEOP will unlikely to fail catastrophically in the case of the perforating impact by 7 mm hypervelocity projectile.

5. CONCLUSIONS AND FUTURE WORK

5.1 Conclusions

For convenience, the main results of the study are briefly listed in Fig. 88. The more detailed description of the results and conclusions of the current research project is provided below.
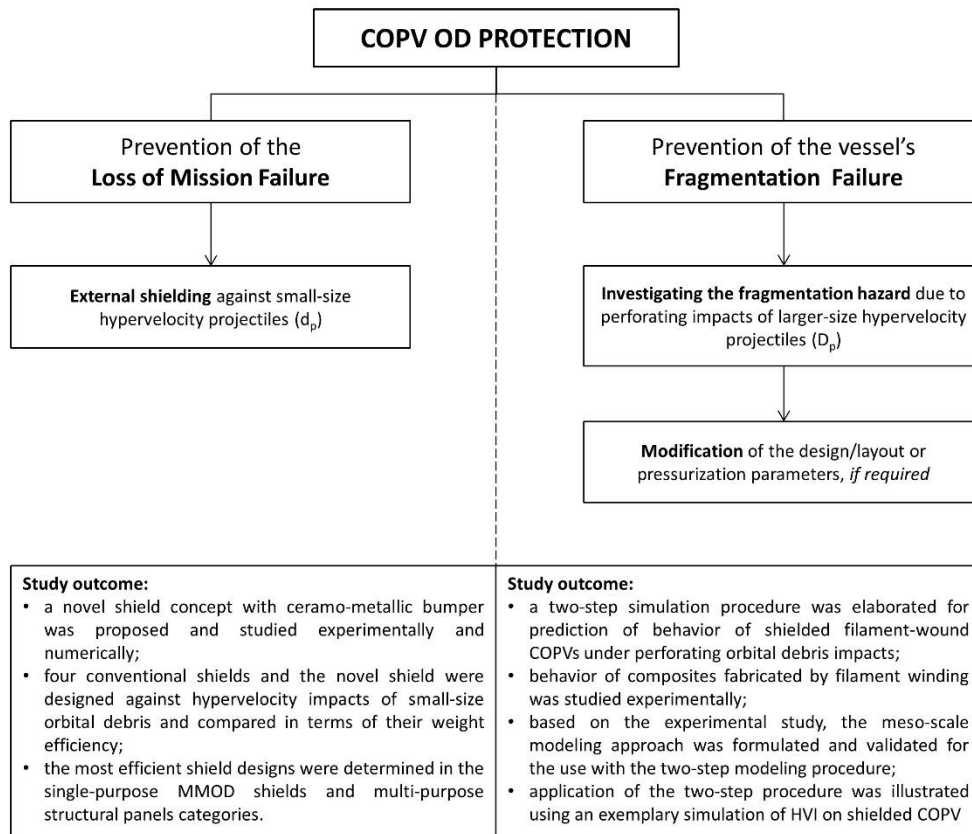
Figure 88 – Main outcomes of the research project

1. A novel shield concept with the aluminum bumper coated with the high impedance ceramic material (silicon carbide) was proposed. The performance of the ceramo-metallic shield was studied by means of the physical and numerical experiments. These studies indicate a superiority of the novel shield as compared with the all-aluminum

Whipple shield. This can be attributed to better disruption of the projectile, formation of debris cloud with finer fragments and spall suppression provided by the ceramo-metallic bumper of the novel shield.

2. The novel shield and four conventional shields, including the Whipple shield, stuffed Whipple shield, and shields using honeycomb and foam-core sandwich panels, were designed to protect a spacecraft pressure vessels against small-size hypervelocity projectiles (up to 1 mm) in such a way to provide no scratch of the vessel's surface and have the minimal possible weight in their class. The design employed the ballistic limit equations for preliminary sizing of the shields and numerical modeling in order to support the BLE predictions (e.g., WS) or obtain parameters of the shields when the BLEs were inapplicable (e.g., SWS in ESA configuration and FCSP) or provided inconsistent predictions (as in the case of HCSP).

3. The introduced modeling approach employed a combination of SPH and FE solvers in order to facilitate modeling of fragmentation and reduce the effects associated with the SPH tensile instability. The experimentally-based procedure for identification of the required erosion strain was proposed for the use with this modeling approach.

4. The original meso-scale approach to modeling of FCSP in hypervelocity impact simulations was introduced and verified by means of the physical experiment.

5. The obtained shielding designs were compared in terms of their structural weight in two separate categories, namely the "Single-purpose MMOD shields" and "Multi-purpose structural panels". Based on this comparison, it was concluded that in the former category the ceramo-metallic and all-aluminum Whipple shields are the preferable choices over the stuffed Whipple shield, which is typically thought of as

more advanced configuration when protection is being designed against large-size hypervelocity projectiles. The novel ceramo-metallic shield has up to 11% lower weight as compared with the equivalent all-aluminum Whipple shield and up to 31% lower weight as compared with the stuffed Whipple shield (non-ballistic weight included). In the "Multi-purpose structural panels" category, the foam-core sandwich panel can have less than half the weight as compared to a honeycomb-core panel with the similar ballistic performance, even in the presence of the minimal bending stiffness constraint limiting further reduction of facesheets' thickness of the foam-core panel. The results of this analysis can be used to direct the designer's choice toward the shielding configurations that were found most efficient in their categories.

6. The two-step modeling procedure was proposed for simulating behavior of shielded COPVs subjected to perforating impacts by orbital debris. In this procedure, instead of the full coupling between the gas and pressurized composite shell requiring time-consuming 3-dimensional analysis, the modeling of the shock wave evolution in the gas was uncoupled from the rest of interactions. As a result, the computationally expensive 3D analysis was substituted by a set of 2D axisymmetric analysis and 3D analysis with the representation of the action of the gas on pressurized shell through the boundary conditions, omitting this way explicit modeling of the gas and dramatically reducing the number of degrees of freedom in the analysis.

7. Additional means of simplifying the modeling were identified for the gas-filled pressure vessels. It was found in the computational experiment that for the typical lightly shielded COPV impacted by a large-size hypervelocity projectile (up to 10 mm), the generated shock wave tends to dissipate completely shortly after its reflection from

the rear wall of the vessel. This observation allows skipping the 2D axisymmetric simulation. It should be mentioned that this will not be the case for liquid-filled vessels, for which the 2-dimensional shock wave evolution modeling would still be required.

8. Due to the lack of data on HVI behavior of composites fabricated by filament winding, the experimental study was carried out. As a result of this study, it was found that HVI damage of such composites exhibits significant dependence on the filament winding pattern used in their manufacturing. The patterns with a higher degree of the interweaving of filament bands demonstrated the ability to better impede propagation of HVI-induced damage. The explicit representation of the winding pattern, therefore, is required for the adequate representation of the physics of COPV damage in numerical modeling.

9. In order to incorporate the detailed representation of the winding patterns into numerical simulations, the meso-scale modeling approach was proposed. In this approach, the fiber-reinforced filament bands and resin-rich regions between them are represented explicitly. By doing that, it becomes possible to uncouple the description of the behavior of these two physically different components of the filament-wound composite and employ more suitable material models for each of them, and to represent virtually any winding pattern. The use of this approach allowed predicting the main experimentally observed features of HVI damage in composites with different filament winding patterns.

5.2 Contribution to Knowledge

The following findings and results of the research are believed to be unique and contribute to the body of knowledge:

- the proposed design of the orbital debris shield with the outer bumper consisting of an aluminum substrate coated from both sides by the high impedance ceramic material (silicon carbide);

- quantification of the weight efficiency of the five shielding systems having the same ballistic performance and designed against small-size hypervelocity projectiles;

- the simulation approach employing SPH method for modeling of fragmentation of external bumper(s) and FEM for modeling of rear walls of the shields, combined with the experimentally-based erosion strain identification procedure;

- the meso-scale model of the foam-core sandwich panel for hypervelocity impact simulations;

- the two-step modeling procedure for simulating shielded COPV behavior when subjected to perforating impacts by large-size hypervelocity projectiles, allowing to dramatically reduce the number of degrees of freedom in the numerical computation;

- theoretically predicted dissipation of the shock wave inside the typical lightly shielded gas-filled COPV when it was generated by a perforating impact of a large-size (up to 10 mm) hypervelocity projectile and the corresponding means of simplifying the modeling procedure;

- experimentally discovered dependence of the HVI damage in composites fabricated by filament winding on the winding pattern used in manufacturing;

- the meso-scale modeling approach for simulating HVI-induced damage of composite materials fabricated by filament winding.

5.3 Future Work

The essence of numerical modeling is a simplification of a physical system while retaining its most important details. The simplification often requires making assumptions. Some of the important assumptions made in this work are related to describing the behavior of materials subjected to hypervelocity impact loading. In particular, the behavior of all materials in this study was described using Mie-Gruneisen equation of state. The well-known limitation of this EOS is that it does not permit phase transformations, i.e. the change of material state from solid to liquid and/or vapor. The assumption of no phase transformations is suitable for velocities up to 7 km/s, when only relatively small fraction of material in debris cloud undergoes a transition from solid to liquid phase. However, these effects are much more pronounced at higher velocities. For instance, materials are subject to complete vaporization in the case of Al-Al impacts at 24 km/s [94]. Although equations of state permitting phase transformations have been formulated and this was done quite long ago (e.g., [95 – 98]), their use is still limited by lack of required constant values for many structural materials. A great deal of experimental work is therefore required in order to provide the means of extending the capabilities of numerical modeling to velocities well above 7 km/s.

The similar conclusion applies to experimental studies of the behavior of composites subjected to HVI. In particular, it was suggested in this work that the knowledge of dynamic fracture toughness of carbon-fiber reinforced plastics may be required for accurate

predictions of composite damage in numerical modeling. Results on this topic presented by different experimentalists do not permit making definitive conclusions and rather conflicting. The predictions, for example, are ranging from defining dynamic fracture toughness as being almost the same as the static value even for the thermoplastic composites [99], to its dramatic reduction [80, 81], or even increase with the increase of strain rates [100]. In all cases, the observations were made at strain rates significantly lower than those corresponding to hypervelocity impacts and additional studies on this topic seem to be imperative.
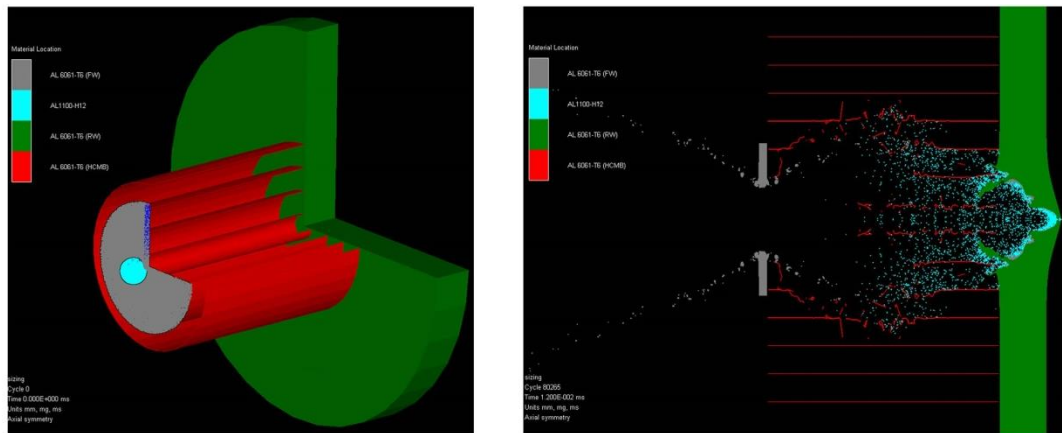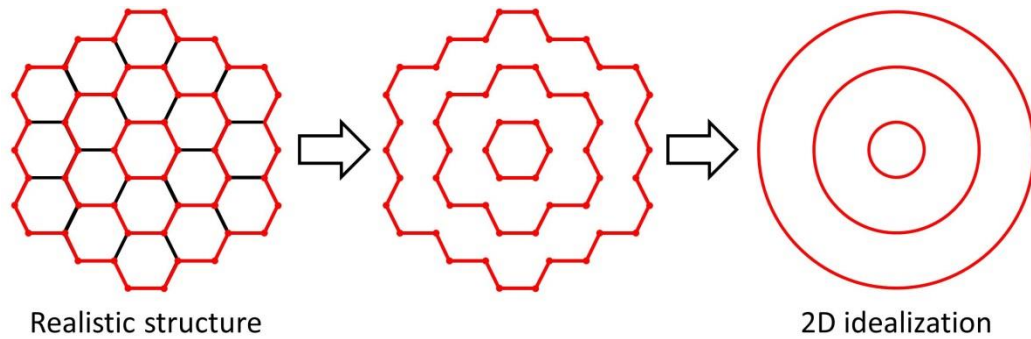
Figure 89 – 2D simplification of the HCSP model

Another important direction for the future work can be a search for more computationally efficient numerical schemes, providing the capability of obtaining reasonable estimations

of OD shields ballistic performance and not requiring long-duration numerical simulations. This is especially the case for the multipurpose sandwich panels considered in this study. In the Author's modeling, the intermediate layers of these panels (honeycomb and foam) were represented on the meso-scale level, which required performing computationally demanding 3D analyses. The attractive alternative to this could be a 2D idealization of the panel's geometry, such that it would still represent its main features required for HVI analysis. An example of such idealization is provided in Fig. 85 for the honeycomb-core sandwich panel. The idealization is based on the fact that the main effect of the honeycomb in the case of normal impact is the channeling of the debris cloud. The constraining of the debris cloud due to channeling can be represented through substituting the honeycomb core by a set of concentric circles, as it is shown in Fig. 89. With such simplification, the model will be suitable for 2D axisymmetric analysis. Although seeming to be quite promising in terms of reduction of computational time, this approach requires future evaluation by means of comparing its predictions with experimental data.

Modeling of HVI on liquid-filled COPVs is also of interest for the future studies. Although the formulated two-step modeling procedure is suitable for these vessels, at certain conditions shock wave in the liquid formed by the perforating impact can be strong enough to produce damage on the rear wall. Numerical modeling of the liquid-filled COPVs might, therefore, require the meso-scale representation of the larger fraction of the composite shell.

PRELIMINARY STUDIES OF OTHER SHIELDING CONCEPTS

This section presents results of theoretical evaluation of shielding performance of two additional concepts, different from those considered in *Chapter 3*. These concepts are represented by shields with combined mesh/plate bumpers and shields made of foam-core sandwich panels filled with a lightweight material.

A.1 Shields with Combined Mesh/Plate Bumpers

A.1.1 Concept description

In its "conventional" design, the bumper of a Whipple shield is monolithic and made of an isotropic material, typically aluminum, known for its ability to efficiently break up medium-density projectiles. Other possible designs of the shielding systems are continuously being sought with the ultimate purpose of increasing their structural weight efficiency. In this regard, application of *metallic meshes* was found to be beneficial due to their low areal density. Fragmentation of hypervelocity projectiles on stand-alone metallic meshes was experimentally studied [21, 22]. The meshes demonstrated the ability to significantly decelerate the projectiles [21] and break them up by forming jets of material that "squeezed" through the mesh apertures [22].

Experimental studies conducted by NASA [101, 102] showed that so-called mesh double-bumper shield (Fig. A.1), consisting of *spaced* discrete (mesh), continuous (aluminum plates) and flexible (fabrics) layers, may have lower ballistic weight as compared with the conventional Whipple shield with the continuous bumper. However, shielding systems

with multiple *spaced* layers are typically required higher non-ballistic parasitic weight for fasteners, spacers etc. [67]
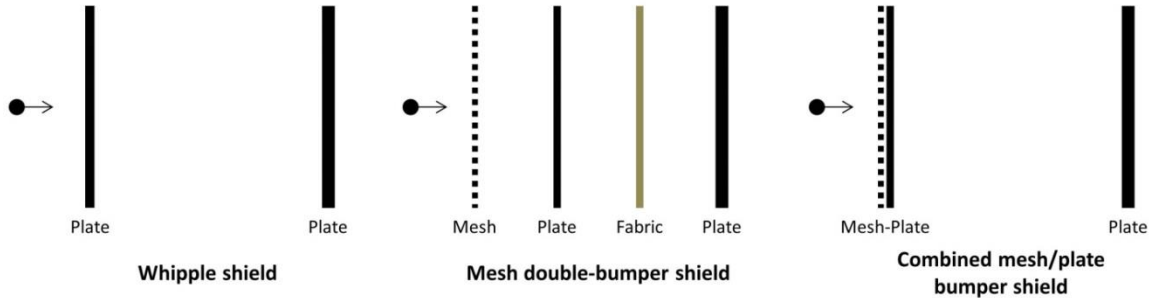
Figure A.1 – Design of a Whipple shield, mesh double-bumper shield and combined mesh/plate bumper shield

In this preliminary study, we evaluate another possibility of enhancing the performance of the standard Whipple shield using metallic meshes. Instead of considering multiple spaced bumpers, we investigate the ballistic performance of a combined mesh/plate bumper (Fig. A.1) where an external layer of fine woven mesh is *directly* applied on a surface of the aluminum plate. As compared with the standard continuous aluminum shield, such combination of discrete and continuous layers may be favorable as it provides either increase of the total thickness of a bumper (in case of aluminum mesh) while maintaining the same weight/areal density, or better initial breakup of a projectile due to its interaction with material of higher shock impedance than aluminum (in case of using steel mesh). In addition, the non-ballistic weight of a shield with such bumper is expected to be similar as for the Whipple shield.

All investigations in this study were conducted by means of numerical modeling using SPH solver of ANSYS AUTODYN hydrocode for the case of 1 mm aluminum projectile impacting the shields at a speed of 7 km/s.

Schematic representation of the layout of numerical experiments is exemplified in Fig. A.2. Here the combined mesh/plate bumper consists of a layer of metallic mesh backed by an aluminum plate. First discrete layer (mesh) provides an initial breakup of a projectile, which is followed by propagation of the formed smaller fragments (size smaller than mesh aperture) through the continuous medium (e.g. aluminum plate) resulting in their further disruption and deceleration.
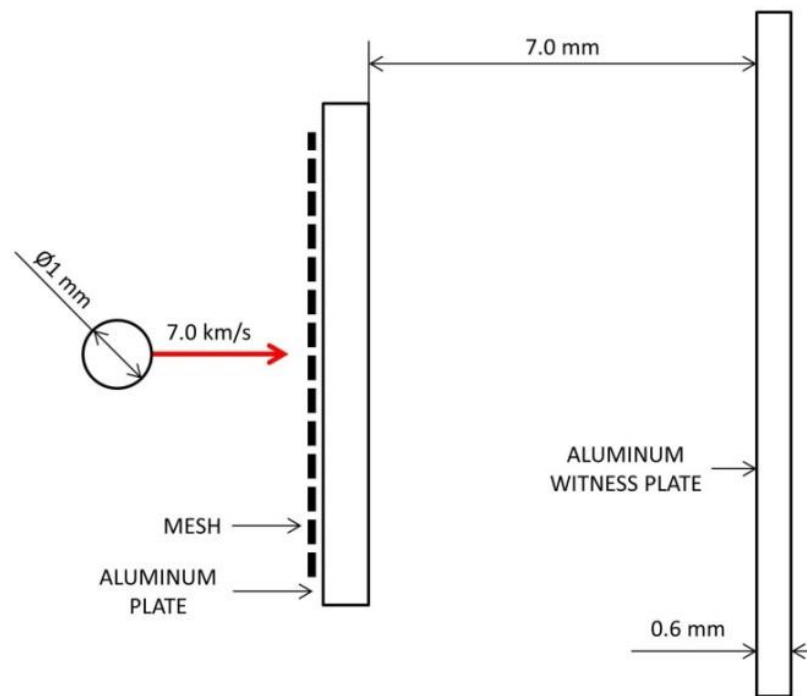
Figure A.2 – Initial setup for numerical experiments on combined mesh/plate bumpers

Weight and areal density of all mesh/plate bumper configurations were equivalent to those of 1 mm-thick aluminum plate bumper. The latter was considered as a reference configuration to compare with. In order to evaluate shielding performance of all configurations, a 0.6 mm-thick aluminum witness plate was placed at a standoff of 7 mm from each bumper.

185

Two types of meshes have been explored in this study: mesh made of Al6061-T6 aluminum alloy and a steel mesh. Steel meshes are typically made of stainless steel. However, due to lack of the full set of material constants specific to stainless steel, 4340 steel properties have been used for modeling of steel mesh assuming an adequate level of similarity in behavior of these materials under shock loading. 1 mm-diameter projectile was modeled as it had been made of unalloyed aluminum Al1100-H12 and had a velocity of 7 km/s. The behavior of aluminum and steel parts was represented in the modeling by a combination of Mie-Gruneisen equation of state and Johnson-Cook strength and failure models. Corresponding material properties employed in the simulations are provided in Appendix B.

It is known that mesh efficiency as a bumper depends on its geometrical parameters [101], which are the wire diameter d_w and the size of the aperture L_a (see Fig. A.3 (a)). From this perspective, the simplest choice would be using a mesh with the smallest possible aperture. However, typical meshes of <u>sub-millimeter</u> aperture along with the reduction of L_a exhibit:

a) reduction of a wire diameter, which reduces their efficiency as an impact protective element;

b) reduction of an aperture-to-wire diameter ratio $\left(\dfrac{L_a}{d_w}\right)$ and, consequently, increase of the areal density. This, in turn, reduces the advantage of a mesh over a continuous material bumper.

On the other hand, the use of coarse meshes with $L_a \geq d_p$ (projectile diameter) obviously would not make much sense either, as projectile may get through a mesh aperture without

being damaged. Having these considerations in mind, a mesh with the following geometrical parameters has been chosen: aperture size $L_a = 0.39$ mm and wire diameter $d_w = 0.18$ mm, which makes projectile diameter-to-aperture size ratio $\frac{d_p}{L_a} = 2.56$ and aperture-to-wire diameter ratio $\frac{L_a}{d_w} = 2.17$.
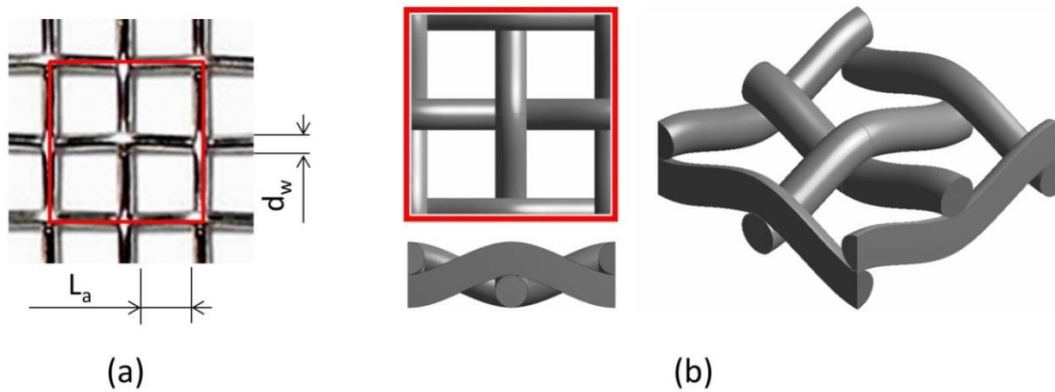
Figure A.3 – Geometric modeling of a woven metallic mesh: a) metallic mesh; b) geometric model of a unit cell

Due to the three-dimensional structure of the woven mesh, the mesoscale approach to the representation of its geometry has been utilized. Geometrical model of a unit cell (translation unit) of the metallic mesh is shown in Fig. A.3 (b). It can be seen in the figure that the mesoscale approach enables realistic representation of the winding pattern of a mesh in numerical modeling.

Table A.1 – Thicknesses of aluminum plates for different bumper configurations

Type of bumper	Thickness of aluminum plate
All-aluminum (no mesh)	1.000 mm
Al mesh + Al plate	0.905 mm
Steel mesh + Al plate	0.723 mm

As it has been mentioned, another element of a combined bumper configuration is an aluminum plate. In order to obtain comparable results, weight and areal density of all combined bumpers were equivalent to those of 1 mm-thick aluminum plate bumper. This was achieved by varying thicknesses of the aluminum plates, whereas mesh parameters (wire diameter and aperture size) were the same for both aluminum and steel meshes. Corresponding thicknesses of the aluminum plates in the mesh/plate bumper layouts are given in Table A.1. It can be noticed that use of a steel mesh significantly reduces the thickness of an aluminum plate of the combined bumper due to the high density of steel.

A.1.2. Numerical modeling

SPH method (Smooth particles hydrodynamics) has been used for all simulations performed in this study. It is a mesh-free Lagrangian method that uses "particles" representing continuum as interpolation points to estimate values of functions and their spatial derivatives [42].

Due to the symmetry of the problem, only quarter of the each configuration has been modeled, whereas the rest part has been represented using corresponding symmetry constraints. This technique allows a significant reduction of the computational time.
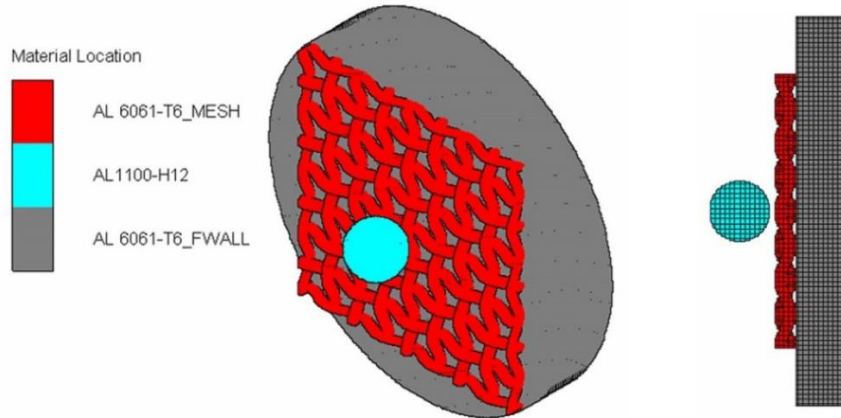
Figure A.4 – SPH model with mesoscale representation of a mesh bumper

SPH model of a combined mesh-plate bumper and a projectile is shown in Fig. A.4 (symmetric parts are shown using "mirror reflection" of the quarter-model). The main parameter of SPH particles is a smoothing length, which to some extent is equivalent to the element size in finite element calculations. In this study, the smoothing length was constant throughout the simulations and equal to 0.02 mm. This resulted in 50 particles along the projectile diameter and approximately 16,400 particles representing the quarter of a 1 mm projectile. A number of SPH particles used to represent mesh/plate bumpers varied depending on configuration (steel or aluminum mesh), but in all cases was over a million.
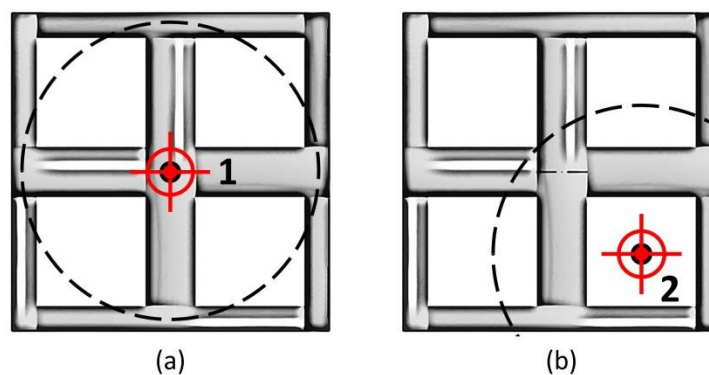
Figure A.5 – Positioning of the center of impact in numerical experiments: a) projectile aligned with crossover point; b) projectile aligned with the center of aperture

Due to the irregular tree-dimensional structure of the metallic mesh, the impact of a projectile at different locations may have different consequences in terms of damage to the witness plate. In this study we considered two different cases: impact of a projectile at the crossover point (wires' intersection; see Fig. A.5 (a)) and impact of a projectile in the center of aperture (Fig. A.5 (b)). The former case was considered as the most optimistic, as wires' intersection provided a significant increase in the overall bumper thickness. The latter case was considered as the worst scenario. It is believed, that all other cases are somewhere between those two in terms of damage to the witness plate.

The domain size in calculations with the 1-mm projectiles was determined by diameters of the representative elements of bumpers and rear walls, which in all cases were equal to 5 and 12 mm, correspondingly. The far-field boundary condition applied only to the far edge of the rear wall and corresponded to the "zero velocity" constraint in AUTODYN. Energy conservation was ensured for all analyzes described in the following sections.

A.1.3 Results of numerical modeling

This section presents results of HVI simulations for the reference configuration with the all-aluminum bumper and the mesh/plate bumper configurations. Fig. A.6 – A.11 illustrate the evolution of shapes of debris clouds prior to impact on the witness plates in the case of different bumper configurations and mesh/projectile alignments. Comparing Fig. A.6 and Fig. A.7, one can see that impact of the projectile on the mesh/plate bumper in the case when the projectile is aligned with a crossover point, leads to the "branching" of the debris cloud with additional "branches" inclined to the initial direction of impact. This effect itself may be considered as positive, resulting in better distribution of momentum over the area

of the witness plate. However, the size of the leading fragment in Fig. A.7 (c), mainly consisting of material of the aluminum plate, is considerably larger. Moreover, comparison of Fig. A.11 (a) and (b) shows that most of the material in the case of the reference configuration is distributed over the surface of debris cloud, whereas there is a significant concentration of large fragments close to the axis of debris cloud in the case of the combined mesh/plate bumper.

Alignment of the projectile with the center of aperture (Fig A.8) leads to the formation of a relatively large central fragment mainly consisting of the projectile material (see Fig A.8 (b)). Expansion of debris cloud in this case is noticeably lower than in the case of impact on the reference configuration (compare Fig. A.8 (c) with Fig A.6 (c)), which results in a wedge-like shape of the cloud. The velocity of the central fragment is quite high, as it reaches the witness plate at $t \approx 2.00$ μs (about 9% earlier than in the case of reference configuration). Aforementioned restraint of the cloud expansion seems to be imposed by initial "squeezing" of the projectile through the aperture of the mesh.

Using of a steel mesh and crossover point alignment of the projectile leads to a large expansion of debris cloud prior to its impact on the witness plate (see Fig. A.9 (c)). Analogous to the case of aluminum mesh combined bumper, these impact conditions produce a concentration of significant amount of material close to the axis of the cloud (see Fig. A.11 (d)). This material mainly originates from the aluminum plate of the mesh/plate bumper.

In the case of a steel mesh and projectile aligned with the center of the aperture, shape of debris cloud is quite different from the one observed in analogous conditions for aluminum

mesh combined bumper (compare Fig. A.8 (c) and Fig. A.10 (c)). Another difference is the concentration of projectile material along the axis of debris cloud (see Fig A.10 (c) and Fig. A.11 (e)), instead of its spreading over the front surface of the cloud (as in Fig. A. 11 (c)). It can be explained as a result of the interaction of the projectile with the steel mesh, which is much denser than projectile material. Due to low thickness of the aluminum plate (see Table A.1), this configuration provides the lowest deceleration of the debris cloud, which reaches the witness plate at $t = 1.65$ µs (25% earlier than in the case of the reference configuration).
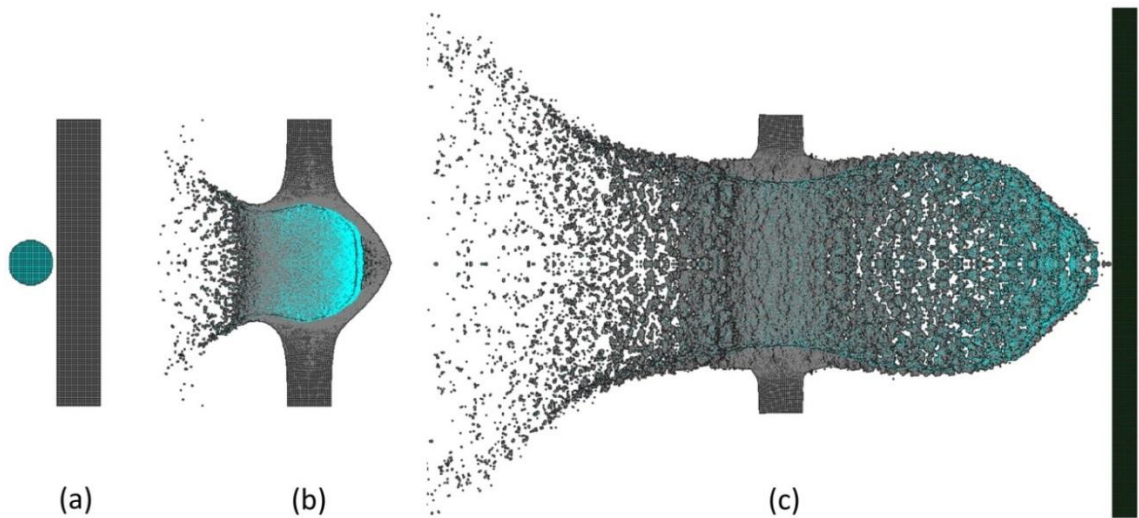
Figure A.6 – Impact of aluminum projectile on aluminum bumper: a) $t = 0$; b) $t = 0.55$ µs; c) $t = 2.20$ µs
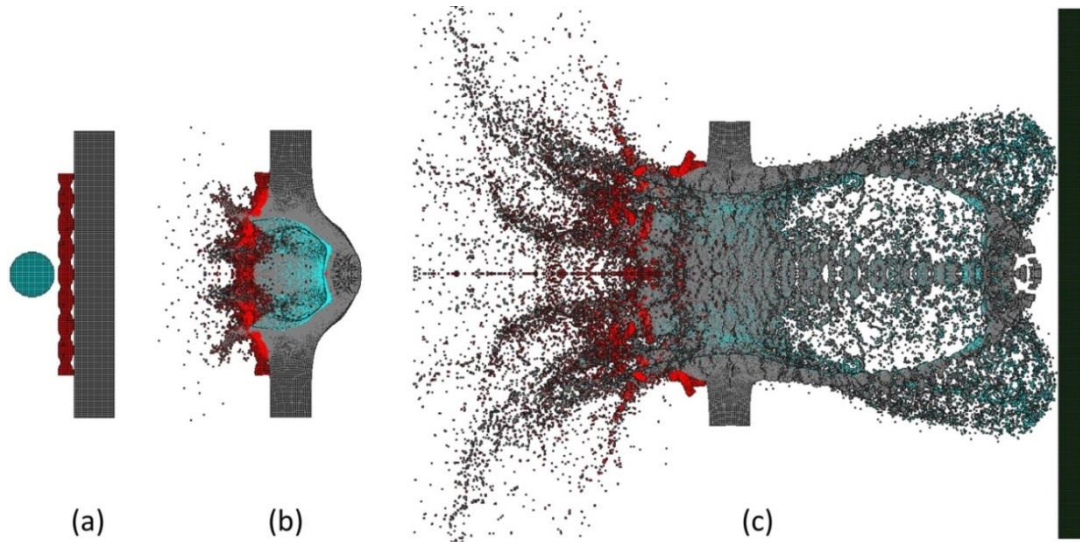
Figure A.7 – Impact of aluminum projectile on combined aluminum mesh-aluminum plate bumper (proj. aligned with crossover point): a) t = 0; b) t = 0.59 μs; c) t = 2.57 μs*

*impact of the central fragment on the rear wall takes place about 0.13 μs later (~2.7 μs)
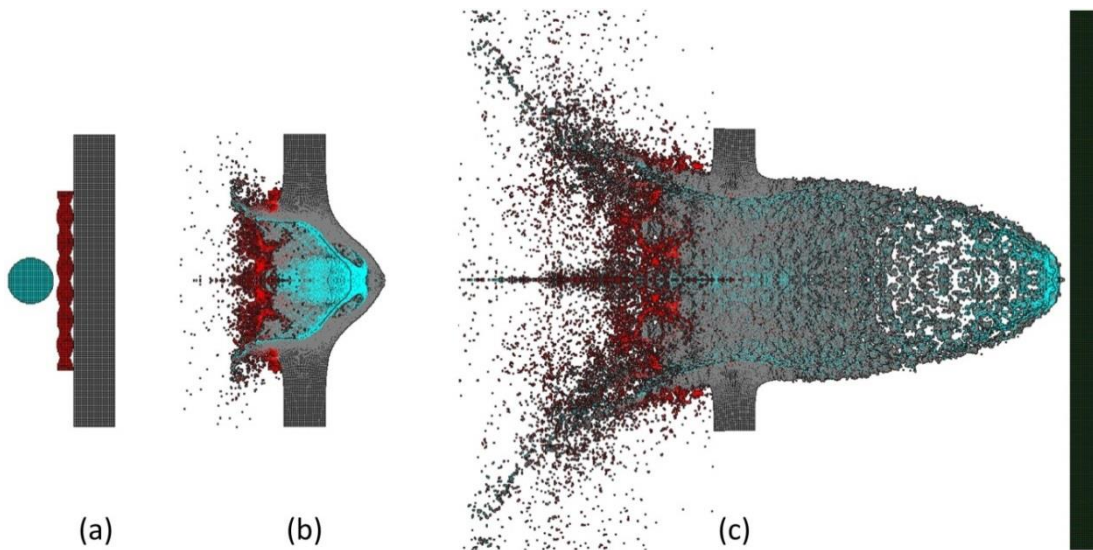
Figure A.8 – Impact of aluminum projectile on combined aluminum mesh-aluminum plate bumper (projectile aligned with aperture): a) t = 0; b) t = 0.55 μs; c) t = 2.01 μs
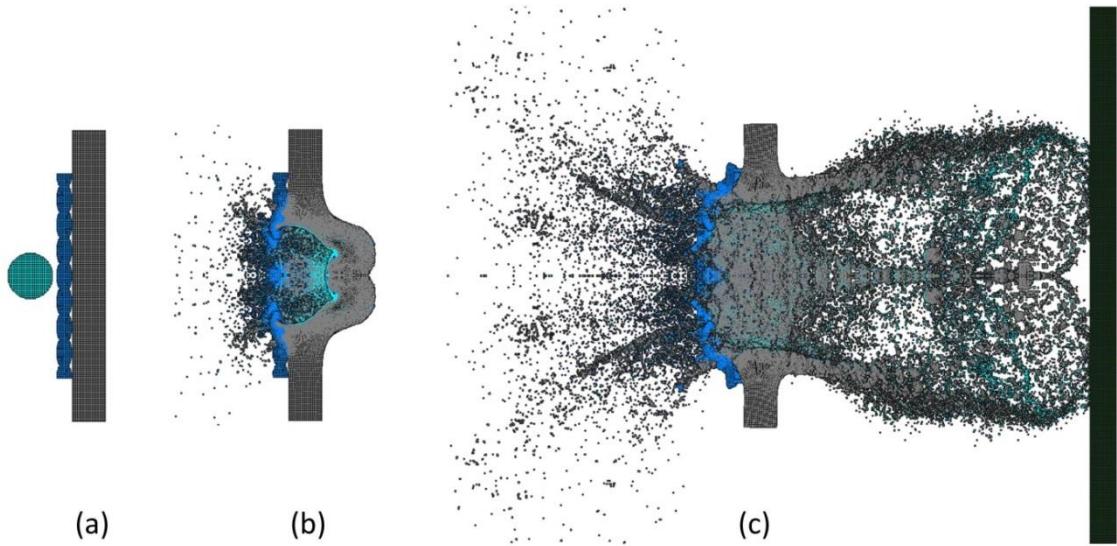
Figure A.9 – Impact of aluminum projectile on combined steel mesh-aluminum plate
bumper (projectile aligned with crossover point): a) t = 0; b) t = 0.55 μs; c) t = 2.20 μs
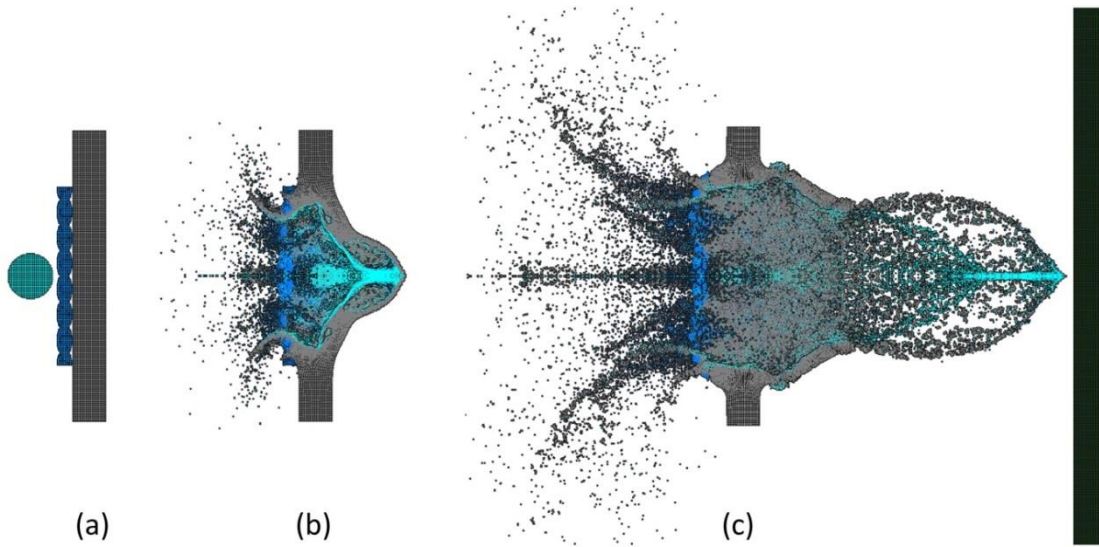
Figure A.10 – Impact of aluminum projectile on combined steel mesh-aluminum plate
bumper (projectile aligned with aperture): a) t = 0; b) t = 0.55 μs; c) t = 1.65 μs
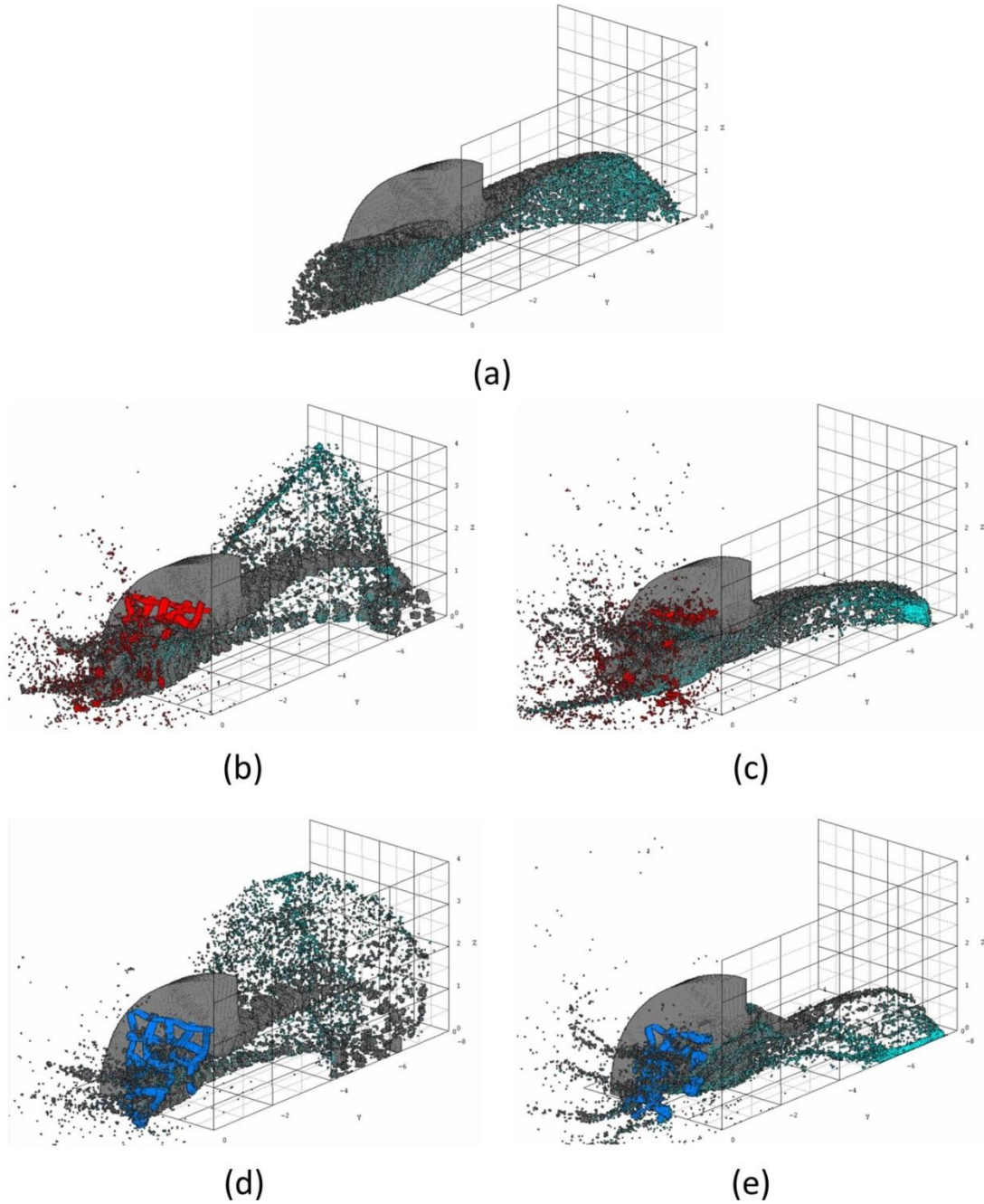
Figure A.11 – Structure of debris clouds prior to impact on the witness plates

Fig. A.12 – A.16 illustrate material location at t = 5.5 µs after impact and damage of the witness plates expressed in terms of effective strain. For the reference configuration, given impact conditions lead to bulging of the witness plate without its perforation (see Fig.

A.12). In the case of aluminum mesh combined bumper and crossover point alignment of the projectile, the same impact conditions lead to the formation of a relatively small perforation hole in the center of the witness plate (Fig. A. 13 (a)). Deformations of the witness plate are highly non-uniform (Fig. A.13 (b)) due to "branching" of the debris cloud. Alignment of the projectile with the center of aperture results in the formation of a large central hole in the witness plate (Fig. A.14).

In the case of the steel mesh combined bumper and crossover point alignment of the projectile, given impact conditions lead to the formation of a series of perforation holes in the witness plate (Fig. A.15). Alignment of the projectile with the center of aperture results in the formation of a large perforation hole by the highly accelerated central fragment of debris cloud (Fig. A.16).

(a) (b)
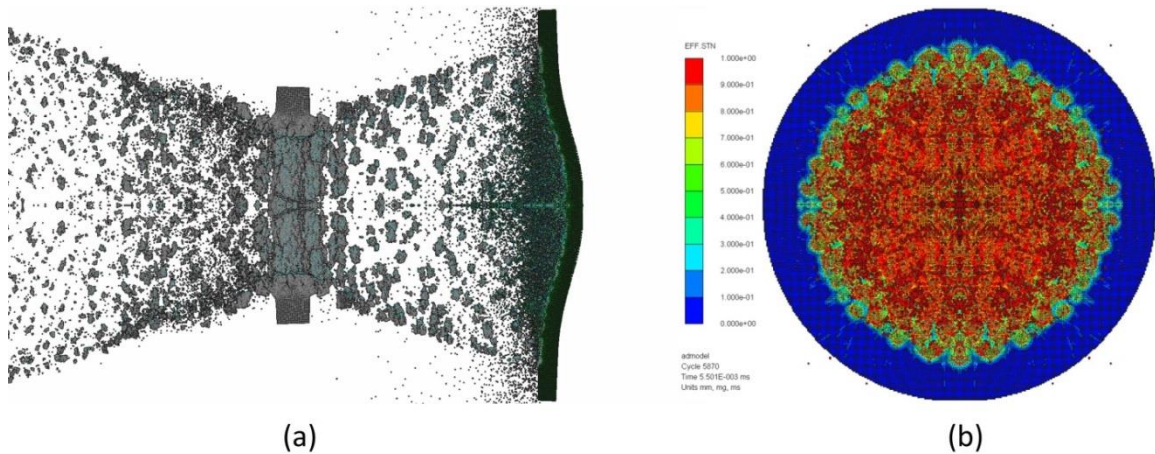
Figure A.12 – Impact of aluminum projectile on aluminum bumper at t = 5.5 μs: a) material location; b) deformation of the witness plate
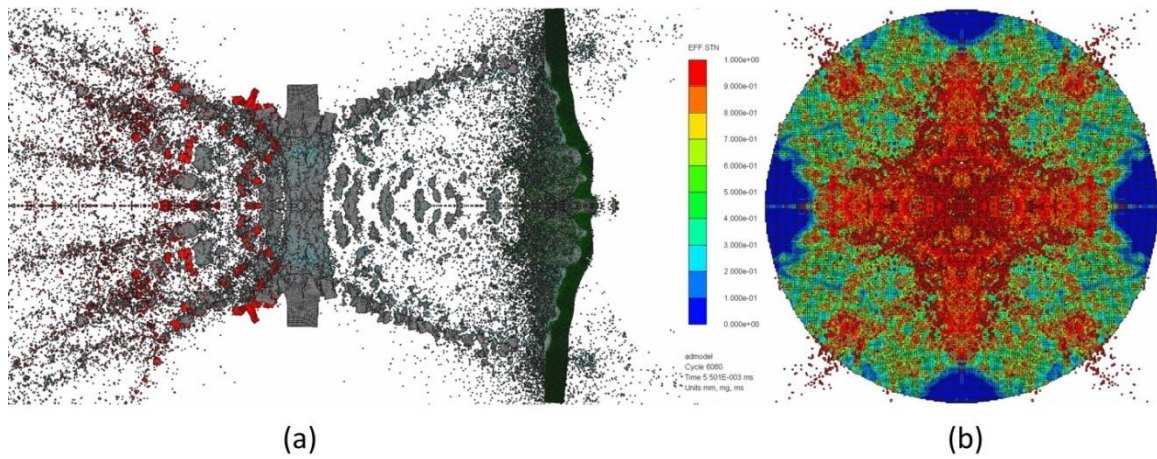
Figure A.13 – Impact of aluminum projectile on combined aluminum mesh-aluminum plate bumper (projectile aligned with crossover point) at t = 5.5 μs: a) material location; b) deformation of the witness plate
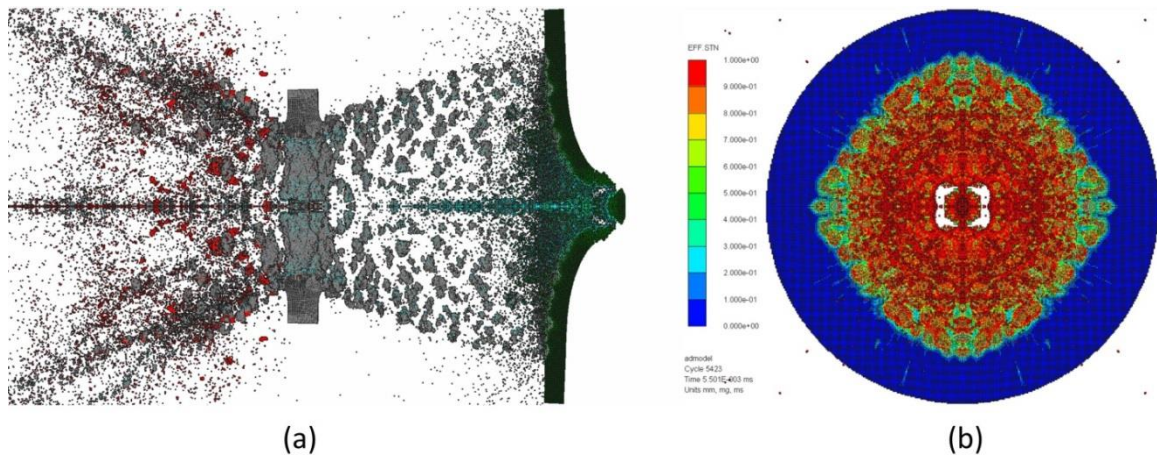
Figure A.14 – Impact of aluminum projectile on combined aluminum mesh-aluminum plate bumper (projectile aligned with aperture) at t = 5.5 μs: a) material location; b) deformation of the witness plate
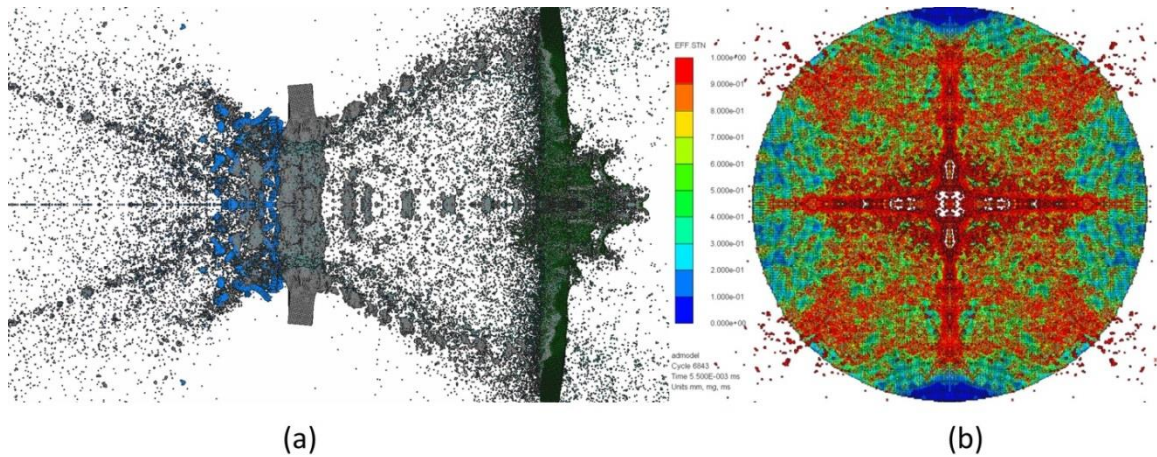
Figure A.15 – Impact of aluminum projectile on combined steel mesh-aluminum plate bumper (projectile aligned with crossover point) at t = 5.5 μs: a) material location; b) deformation of the witness plate
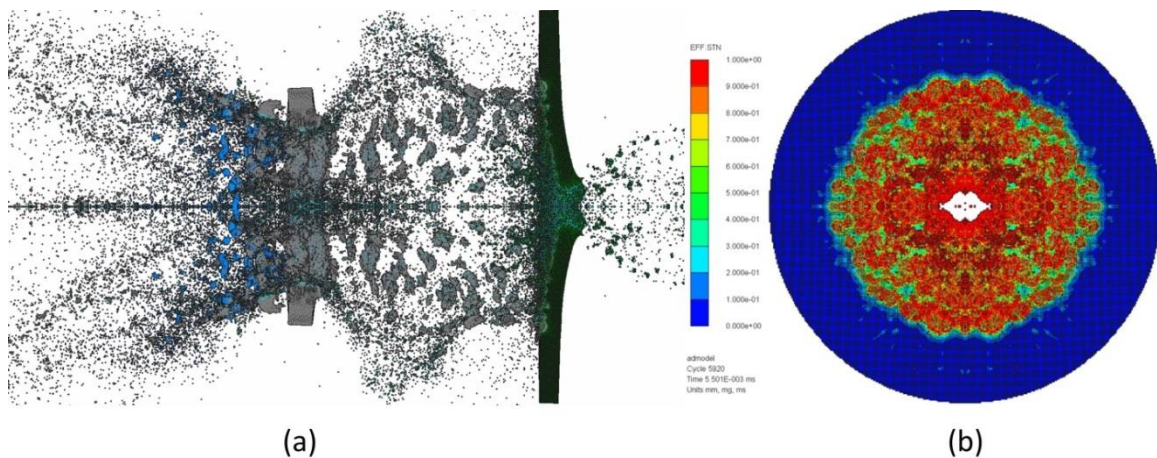
Figure A.16 – Impact of aluminum projectile on combined steel mesh-aluminum plate bumper (projectile aligned with aperture) at t = 5.5 μs: a) material location; b) deformation of the witness plate

Dimensional parameters of the witness plate perforation holes are given in Table A.2. Here areas of perforations were determined from Fig. A.13 – A.16 using Adobe Photoshop tools.

The equivalent diameter of perforation was calculated as the diameter of a circle having

the same area as the total area of perforation, i.e. $D_{eff} = \sqrt{\dfrac{4A_{tot}}{\pi}}$.

Table A.2 – Dimensions of the witness plate perforation holes

Parameter	Dimensionality	AL	ALM-1	ALM-2	STM-1	STM-2
Area of central perforation hole (A_{cent})	mm^2	N/A	0.093	2.179	1.737	0.871
Total perforation area (A_{tot})	mm^2	N/A	0.093	2.179	2.592	0.871
Equivalent diameter of perforation (D_{eff})	mm	N/A	0.344	1.666	1.817	1.053

Here and below: AL – aluminum bumper; ALM / STM – aluminum mesh or steel mesh combined bumper, correspondingly; 1 or 2 – impact at the crossover point or the center of aperture
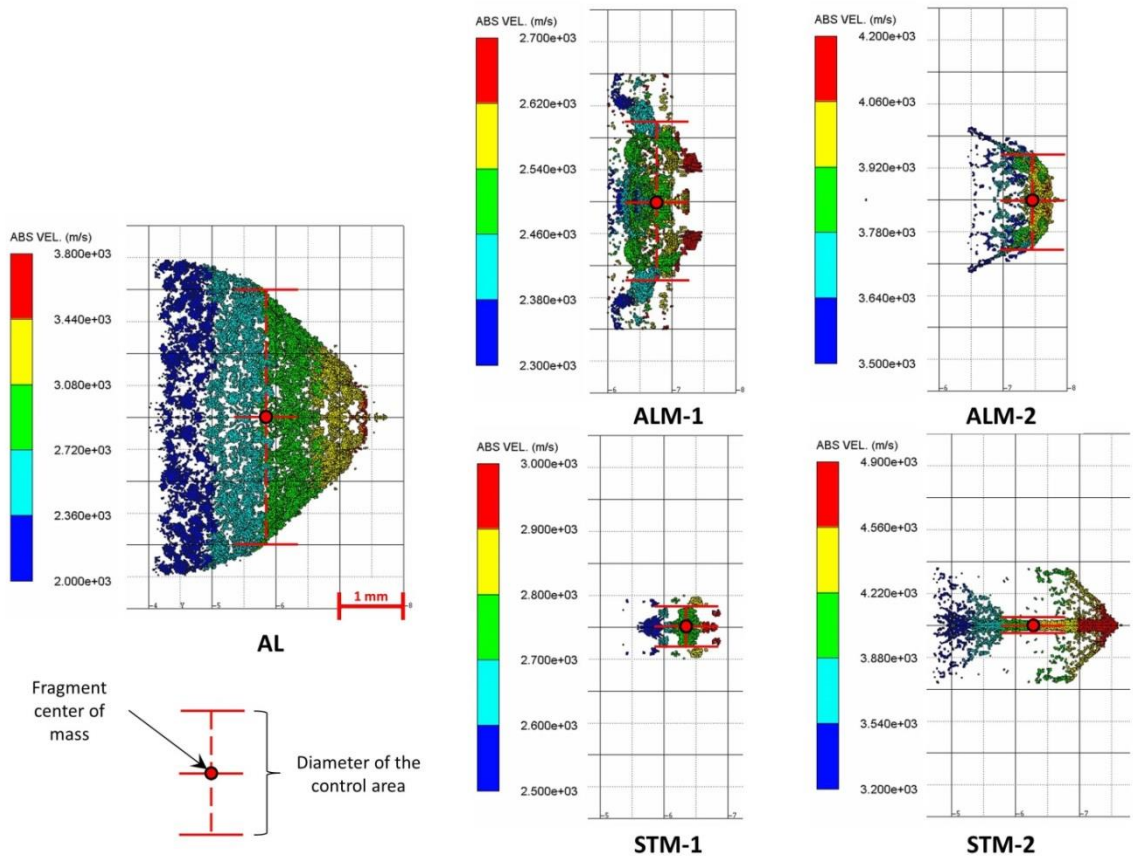
Figure A.17 – Central fragments of debris clouds

According to Table A.2, central fragments most of all contribute to the damage of the witness plates. Parameters of the largest central fragment for each shielding configuration just before impact on the witness plate were obtained using "Output Fragment Analysis" function of AUTODYN and were summarized in Table A.3. Here "Characteristic dimension" (L_{char}) represents the length of the diagonal of the bounding box that contains the fragment completely. It should be noted that due to smooth distribution of material over the contour of debris cloud in the case of all-aluminum bumper (see Fig. A.6 (c) and Fig. A.11 (a)), large fraction of debris cloud is considered by AUTODYN as a single fragment, which therefore, has a large characteristic dimension and comprises 124,132 SPH particles. Considered central fragments are shown in Fig. A.17.

Table A.3 – Parameters of the central fragment

Parameter	Dimensionality	AL	ALM-1	ALM-2	STM-1	STM-2
Characteristic dimension	mm	7.3	5.41	3.43	1.16	3.82
Volume	mm^3	1.0370	0.4673	0.2223	0.0573	0.1646
Mass	mg	2.69	1.23	0.575	0.153	0.421
Average Speed	m/s	2635	2415	3803	2752	4154

The damaging potential of the central fragments depends on the spatial distribution of their material relatively to the witness plate and fragments' momentum and/or kinetic energy. In order to account for the spatial distribution of material, fragments' energy and momentum were averaged over the control area. The latter is the area of a circle with diameter equal to the diameter of the fragment's cross-section parallel to the witness plate and drawn through the fragment's center of mass, as it is shown in Fig. A.17. Damaging potentials of the central fragments in terms of both kinetic energy per unit area and

momentum per unit area are summarized in Fig. A.18 for each shielding/impact configuration.

	AL	ALM-1	ALM-2	STM-1	STM-2
■ Momentum, g/mm*ms	0.29	0.31	0.63	0.65	8.57
■ Kin. Energy, J/mm2	0.41	0.38	1.20	0.90	19.03
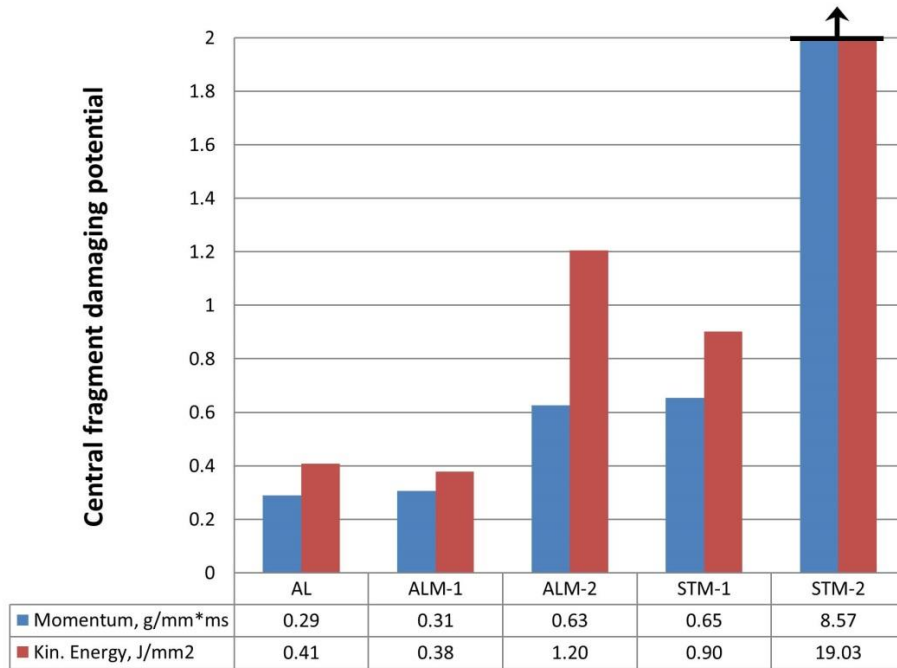
Figure A.18 – Damaging potential of the central fragments

As it is clearly seen from Fig. A.18, damaging potentials of the central fragments created as a result of the impact on aluminum mesh/plate bumper (impact at the center of aperture) and steel mesh/plate bumper (both impact configurations) are much greater than that in the case of impact on the all-aluminum bumper. This analysis explains more severe damage patterns (i.e. perforation) of the witness plates observed in the corresponding numerical experiments as compared with the impact on the all-aluminum bumper. The highest damaging potential is associated with the central fragment formed after impact at the center of the aperture on steel mesh/plate bumper. This results from its shape elongated in the direction of impact (see Fig. A.17), which makes this fragment more effective penetrator than the other considered fragments having much larger control areas associated with them.

According to Fig. A.18, central fragments resulting from impacts on all-aluminum bumper and aluminum mesh/plate bumper in the case of projectile centered at the crossover point, have very similar damaging potentials, and yet there is a small central perforation of the witness plate in the latter case. This can be explained by the fact that, in addition to the largest central fragment for which damaging potential was calculated, the configuration with the mesh/plate bumper has additional smaller fragments at the center of debris cloud (see Fig. A.11 (b)) contributing to the overall witness plate damage. At the same time, there are no such fragments in the case of the all-aluminum bumper (Fig. A.11 (a)).

The same reasoning applies to the case of steel mesh/plate bumper when the projectile is aligned with crossover point. These conditions lead to the formation of multiple central fragments (see Fig. A.11 (d)), only largest of which was considered in damaging potential calculations. Altogether, these fragments are responsible for the largest overall perforation area, as given in Table A.2.

A.2 Filled Foam-core Sandwich Panels

A.2.1 Concept description

In addition to the FCSP ballistic performance of which was investigated in Section 3.5.2.2, two supplementary configurations have been studied in this section. Those configurations are based on the concept of aluminum foam filled with a light-weight material behaving like a liquid when subjected to impact loading. The combination of multishock action of aluminum foam with the effectiveness of fluids in absorption of the kinetic energy of debris cloud may be advantageous for the shielding system.

Paraffin was considered in this study as the filler material. Being one of the lightest solids (ρ=0.918 g/cm^3, which is less than the density of water), it behaves similarly to fluid revealing no strength under high strain rate loading. From the manufacturing point of view, it would be easy to fill aluminum foam by immersion of a piece of foam into a tank with molten paraffin, then cooling it down to T<T$_{melt}$ and removing the filled piece of foam.

(a)   (b)
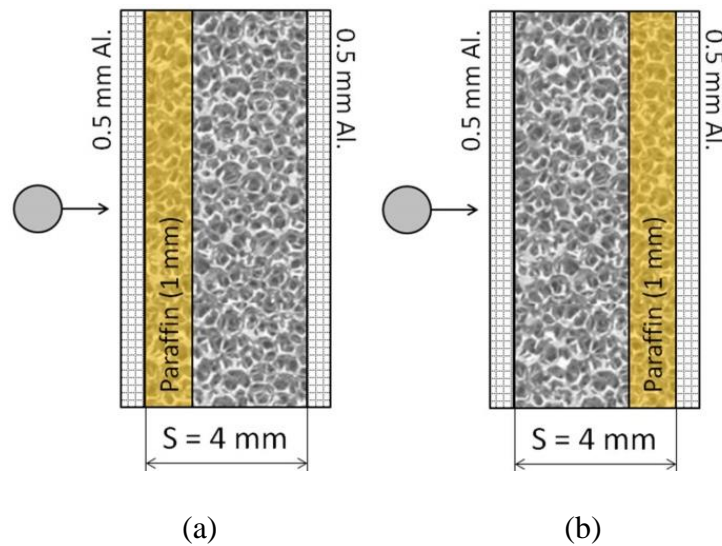
Figure A.19 – Aluminum foam panels

Due to relatively large difference between the densities of aluminum foam and paraffin ($\frac{\rho_{paraff}}{\rho_{foam}} = 11.3$), it is not possible to obtain a weight-efficient design filling the entire space between facesheets with paraffin. Therefore, only partial filling of the foam was considered. This can be quantified by a filling coefficient β, which represents a fraction of aluminum foam filled by paraffin. Thickness of partially filled foam layer having the same weight as non-filled foam can be calculated as

$$L_{FP} = \frac{L_F}{1 + \beta \cdot \dfrac{1-\alpha}{\alpha} \cdot \dfrac{\rho_{paraff}}{\rho_{AL}}}, \tag{A.1}$$

where L_F is the thickness of non-filled foam to compare with; α is the relative density of aluminum foam; ρ_{AL} is the density of aluminum. Having $L_F = S = 16$ mm (standoff between facesheets of the non-filled panel), $\alpha = 0.03$ (3% aluminum foam) and $\beta = 0.25$ (25% of foam thickness will be filled with paraffin), one can get the thickness of the foam layer $L_{FP} = 4$ mm and thickness of the paraffin-filled part of the foam layer as $L_P = \beta \cdot L_{FP} = 1$ mm. Therefore, adding 1 mm-thick layer of paraffin requires fourfold reduction of foam thickness in order to obtain a panel of the same weight/areal density as the non-filled one.

Two configurations with partially filled aluminum foam have been studied: one with the filled part adjacent to the front facesheet, and another with paraffin-filled part adjacent to the rear facesheet. They are schematically shown in Fig. A.19.

A.2.2. Numerical modeling

Properties of Al6061-T6 and Al1100-H12 and material models used to represent their behavior in numerical simulations are described in Appendix B. The behavior of paraffin has been represented in terms of shock equation of state only, as the material does not reveal strength effects under high strain rate loading. Properties of paraffin are presented in Appendix B and correspond to material model from the standard material library of AUTODYN.
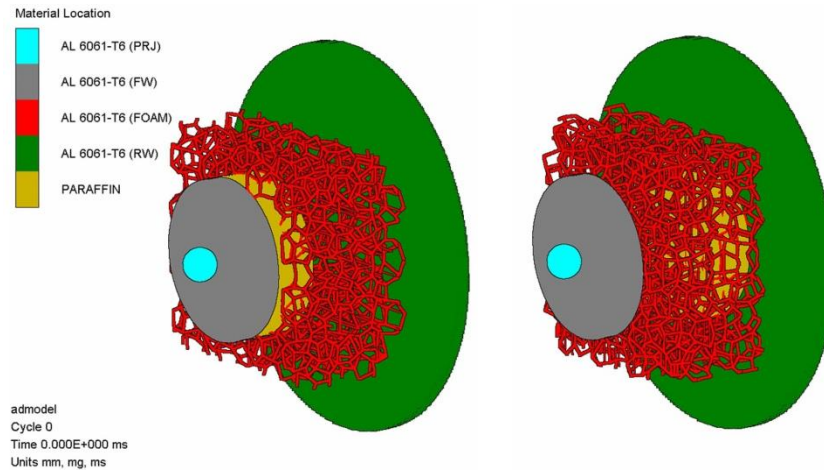
Figure A.20 – Numerical models of the studied foam core sandwich panels

SPH models of the foam core sandwich panels are exemplified in Fig. A.20. Each of them consisted of approximately 2 million SPH particles. In order to represent thin ligaments of aluminum foam with satisfactory accuracy, the smoothing length of 0.015 mm has been used. All models exploited the idea of the quarter-symmetry. Although aluminum foam has a random structure and is not exactly symmetric relatively to any cutting plane, isotropy of its effective properties allows for such assumption. To prevent «mixing» of foam and filler materials at the initiation of numerical analysis, we created a set of channels within paraffin object surrounding ligaments and preventing their initial "numerical" contact with the filler.

A.2.3 Results of numerical modeling

Results of simulations for the filled-foam core panels are exemplified in Fig. A.21 – A.22. Comparison of the figures shows that having paraffin-filled part of the core closer to the rear wall is more advantageous, as it initially provides multishocking of the debris cloud and then absorbing the kinetic energy of the dispersed fragments, although neither configuration prevents the perforation.

205
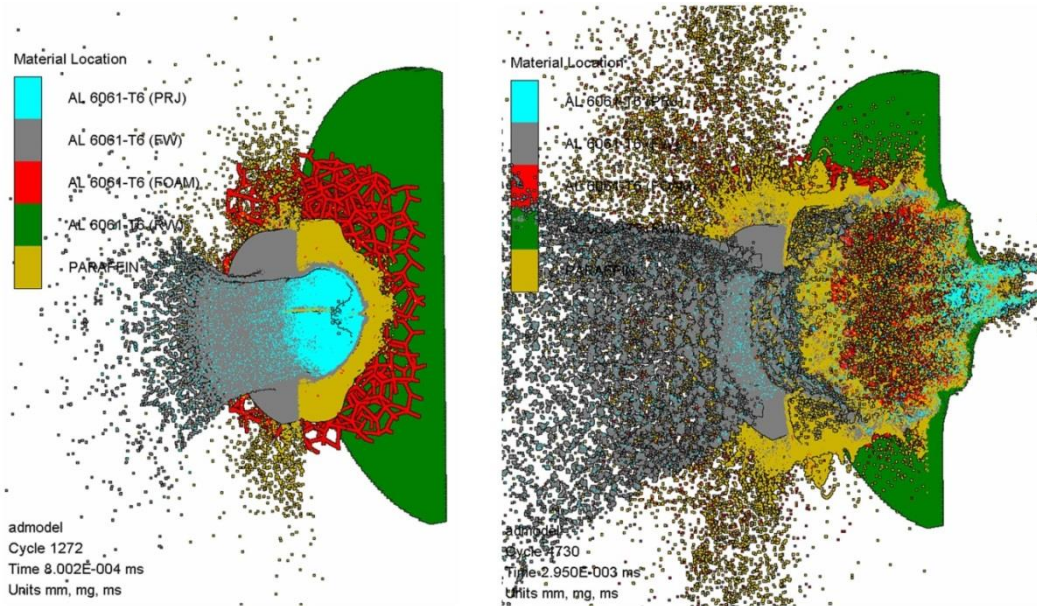
Figure A.21 – Results for filled foam core sandwich panel (paraffin at the front wall)
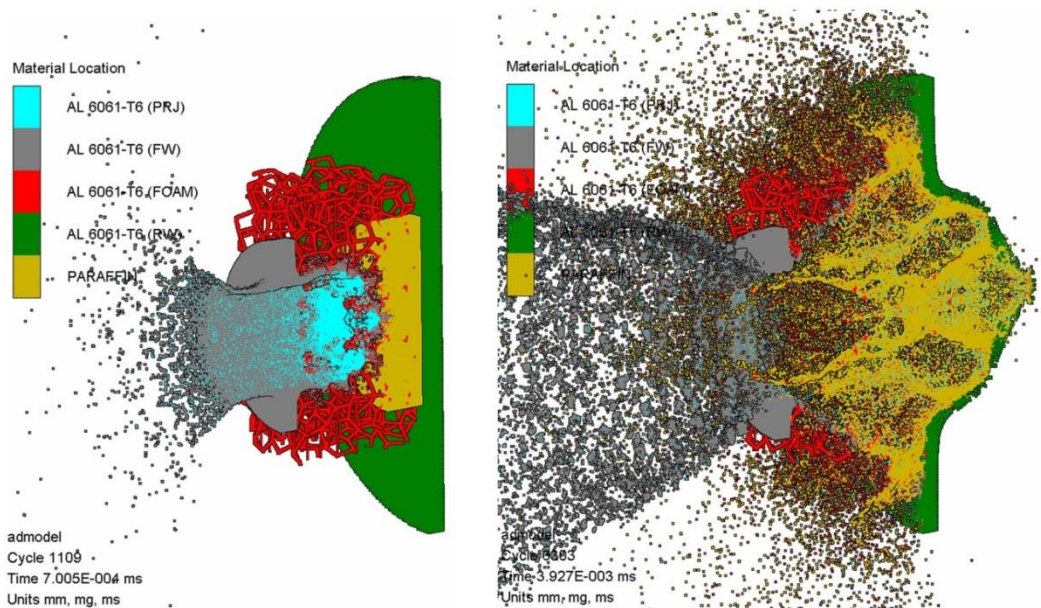
Figure A.22 – Results for filled foam core sandwich panel (paraffin at the rear wall)

A.3 Conclusions

In general, our simulations show that use of the mesh/plate combined bumpers in

considered configurations for protection against small-size (~1 mm) orbital debris impacts

do not provide a tangible advantage over a standard aluminum-plate bumper. In all cases considered in this study, witness plates were perforated if shielded by a mesh/plate bumper, while at the same impact conditions (mass and speed of the projectile) there was no perforation of the witness plate shielded by the reference aluminum bumper.

In comparison with the steel mesh combined bumper, a combination of aluminum mesh and aluminum plate demonstrated better efficiency while having the same weight/areal density. This can mainly be attributed to the fact that initial interaction of the projectile with the steel mesh did not provide a strong enough effect to compensate the reduction of the thickness of the backing aluminum plate.

As only one combination of dimensional mesh/projectile parameters has been considered in this preliminary study, our results do not exclude the existence of other combinations or impact conditions when combined mesh/plate bumpers may be more efficient.

For the future studies, it can be suggested to consider the mesh-plate bumpers with two layers of aluminum mesh. These mesh layers should be superposed in a way so that the center of the aperture in the first layer of mesh would be at the same relative position as crossover point in the second layer. This combination might improve initial fragmentation of a projectile and prevent the formation of a large central fragment that was observed in this study in the case of impacts aligned with the center of the aperture.

The evaluated filled-foam configurations revealed quite different behavior under hypervelocity impact loading. However, they both did not prevent perforation of the rear wall and, therefore, were found to be not weight-efficient for protection against 1 mm orbital debris particle. The reason for such result is the dramatic reduction of the foam

thickness when filling it with paraffin as compared with the non-filled foam panel due to the large difference between densities of paraffin and foam (~11.3, as it has been calculated in Section A.2.1). It should be noted, however, that the filled-foam configuration may be more efficient in shielding systems that use aluminum foam of higher density. This would be the case when shielding system is being designed against larger-size projectiles (e.g., 5 - 10 mm).

MATERIAL PROPERTIES USED IN NUMERICAL SIMULATIONS

Table B.1 − Material properties of all metals used in numerical simulations

Component of material model	Property	Dimensionality	Al1100-H12	Al6061-T6	Al2024-T4	4340 Steel	Ti6Al4V
Mie-Gruneisen Equation of state	Reference density	g/cm^3	2.707	2.703	2.796	7.860	4.419
	Gruneisen gamma	–	1.970	1.970	2.000	1.670	1.230
	C$_0$	m/s	5386	5240	5328	4578	5130
	S		1.339	1.400	1.338	1.330	1.028
	Ref. temperature	K	293	293	300	293	295
	Specific heat	J/kgK	884	885	875	477	525
Johnson-Cook Strength model	Shear modulus	MPa	24722	26000	27600	77000	41900
	Yield stress	MPa	148	324	265	792	1098
	Hardening constant	MPa	345	114	426	510	1092
	Hardening exponent	–	0.183	0.420	0.340	0.260	0.930
	Strain rate constant	–	0.001	0.002	0.015	0.014	0.014
	Thermal softening exponent	–	0.859	1.340	1.000	1.030	1.100
	Melting temperature	K	893	925	775	1793	2110
	Reference strain rate	/s	1.000	1.000	1.000	1.000	1.000
Johnson-Cook Failure model	Damage constant, D$_1$	–	0.071	-0.770	0.112	0.050	-0.090
	Damage constant, D$_2$	–	1.248	1.450	0.123	3.440	0.270
	Damage constant, D$_3$	–	-1.142	-0.470	1.500	-2.120	0.480
	Damage constant, D$_4$	–	0.147	0.000	0.007	0.002	0.014
	Damage constant, D$_5$	–	1.000	1.600	0.000	0.610	3.870
Reference documents			[103]	[104]	[106]	[55, 105]	[106]

Table B.2 – Material properties of Kevlar-Epoxy composite [57]

Property	Units	Value
EOS		Orthotropic
Reference density	g/cm^3	1.65
Stiffness Matrix Coefficients:		
C11	kPa	3.425x10^6
C22	kPa	1.35x10^7
C33	kPa	1.35x10^7
C12	kPa	1.14x10^6
C23	kPa	1.20x10^6
C 31	kPa	1.14x10^6
Material Axes Option		X-Y Space
Rotation Angle	deg.	0
X-origin (mm)	mm	0
Y-origin (mm)	mm	0
Reference Temperature (K)	K	300
Specific Heat Capacity ()	J/kgK	1420
Volumetric Response		Polynomial
Polynomial EOS Parameters		
A1	kPa	4.15389 x10^6
A2	kPa	4 x10^7
A3	kPa	0.0
B0	none	0.0
B1	none	0.0
T1	kPa	4.15389 x10^6
T2	kPa	0.0
Strength		Elastic
Shear Modulus	kPa	1.0x10^6
Failure: Material Stress/Strain		1.0x10^{20}
Tensile Failure Stress 11	kPa	1.0x10^{20}
Tensile Failure Stress 22	kPa	1.0x10^{20}
Tensile Failure Stress 33	kPa	1.0x10^{20}
Tensile Failure Stress 12	kPa	1.0x10^{20}
Tensile Failure Strain 11	mm/mm	0.01
Tensile Failure Strain 22	mm/mm	0.08
Tensile Failure Strain 33	mm/mm	0.08
Tensile Failure Strain 12	mm/mm	1.0x10^{20}
Epoxy Melting Temperature	K	1.0x10^{20}
Kevlar Decomposition Temperature	K	400

Table B.3 – Material properties of Nextel fabric [57]

Property	Units	Value
Reference density	g/cm^3	2.6
Solid sound speed	m/s	2500
Porous sound speed	m/s	100
Density #1	g/cm^3	0.898
Density #2	g/cm^3	1.300
Density #3	g/cm^3	2.000

Density #4	g/cm^3	2.500
Density #5	g/cm^3	2.900
Pressure #1	kPa	0.0
Pressure #2	kPa	2.0×10^3
Pressure #3	kPa	3.5×10^4
Pressure #4	kPa	1.0×10^5
Pressure #5	kPa	2.0×10^5
Crush density	g/cm^3	2.3
Strength model		Elastic
Shear modulus	kPa	0.0

Table B.4 – Material properties of paraffin [105]

Component of material model	Property	Units	Value
Equation of state	Reference density	g/cm^3	0.918
	Gruneisen gamma	–	1.180
	C$_0$	m/s	2908
	S	–	1.560
	Ref. temperature	K	0.000
	Specific heat	J/kgK	0.000

Table B.5 – Summary of the proposed meso-scale material model for CFRP

FILAMENT BANDS	RESIN-RICH LAYERS
Equation of state (EOS)	Equation of state (EOS)
Type: Orthotropic with polynomial volumetric response $$p = p(\varepsilon_{vol}) - \frac{1}{3}[C_{11} + C_{21} + C_{31}] \cdot \varepsilon_{11}^d - $$ $$ - \frac{1}{3}[C_{12} + C_{22} + C_{32}] \cdot \varepsilon_{22}^d - \frac{1}{3}[C_{13} + C_{23} + C_{33}] \cdot \varepsilon_{33}^d$$ where C_{ij} are the orthotropic material stiffness matrix coefficients and $p(\varepsilon_{vol})$ is the pressure contribution from volumetric strain: $$p = K'\varepsilon_{vol} + A_2(\varepsilon_{vol})^2 + A_3(\varepsilon_{vol})^3 + (B_0 + B_1\varepsilon_{vol}).$$ Here A_i and B_i are material constants; ρ_0 is the initial density; e is internal energy per unit mass; and K' is an "effective" bulk modulus of orthotropic material: $$K' = -\frac{1}{9}[(C_{11} + C_{22} + C_{33} + 2(C_{12} + C_{23} + C_{31}))]$$	*Type*: Mie-Gruneisen with shock Hugoniot $$p = p_H + \Gamma\rho \cdot (e - e_H),$$ where Γ is Gruneisen gamma; p_H and e_H are the reference pressure and specific energy determined from material's shock Hugoniot defined via linear relationship between shock velocity (U_s) and particle velocity (U_p) $$U_s = C_0 + S \cdot U_p.$$ Here C_0 is the bulk acoustic sound speed and S is the slope of the $U_s - U_p$ relationship.
	Failure model
	Failure initiation: $$e^2 = \left(\frac{\sigma_{33}}{Z_T}\right)^2 + \left(\frac{\sigma_{23}}{S_{ILSS}}\right)^2 + \left(\frac{\sigma_{13}}{S_{ILSS}}\right)^2 \geq 1,$$ where Z_T is through-the-thickness tensile strength and S_{ILSS} is interlaminar shear strength of composite.
Failure model	
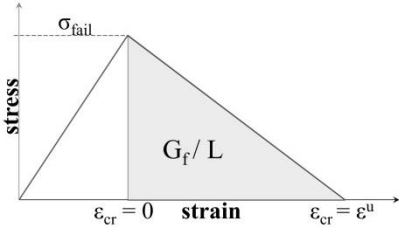
Failure initiation:

$$e^2 = \left(\frac{\sigma_{11}}{X_T}\right)^2 + \left(\frac{\sigma_{12}}{S}\right)^2 + \left(\frac{\sigma_{13}}{S}\right)^2 \geq 1$$

for the fiber failure, and

$$e^2 = \left(\frac{\sigma_{22}}{Y_T}\right)^2 + \left(\frac{\sigma_{12}}{S}\right)^2 \geq 1$$

for the transverse matrix cracking.

Here X_T and Y_T are the longitudinal and in-plane transverse strength of a composite, correspondingly; S is the in-plane shear strength

Failure propagation: failure is instantaneous. Damage tensor coefficients, corresponding to intra-band stresses (i.e. D_{11}, D_{22} and D_{12}), take on their maximum value ($D_{ij} = 1$) immediately upon satisfaction of the corresponding failure criterion.

Failure propagation: microcracking represented by linear softening

Here G_f is fracture energy, L is a characteristic cell dimension in the direction of failure; ε^u is the ultimate strain before microcracks form a macrocrack:

$$\varepsilon^u = 2G_f / \sigma_{fail}L \cdot$$

Between $\varepsilon_{cr} = 0$ and $\varepsilon_{cr} = \varepsilon^u$ softening is defined by damage parameter $D_{ij} = \varepsilon_{cr} / \varepsilon^u$, such that failure surface in the course of failure progression can be updated according to the following rule:

$$e_{33}^2 = \left(\frac{\sigma_{33}}{Z_T(1-D_{33})}\right)^2 + \left(\frac{\sigma_{23}}{S_{ILSS}(1-D_{23})}\right)^2 + \left(\frac{\sigma_{31}}{S_{ILSS}(1-D_{31})}\right)^2 \geq 1$$

Table B.6 – Mechanical properties of AS4/APC-2 thermoplastic composite ($V_f = 60\%$)

Material property	Dimensionality	Value
Density, ρ	g/cm^3	1.60
Longitudinal Young's modulus, E_1	GPa	138
Transverse Young's modulus, E_2	GPa	10.3
In-plane shear modulus, G_{12}	GPa	5.7
In-plane Poisson's ratio, v_{12}	–	0.30
Longitudinal tensile strength, X_T	MPa	2070
Transverse tensile strength, Y_T	MPa	86
In-plane shear strength, S	MPa	186
Flexural Strength	MPa	2000

Table B.7 – Mechanical properties of APC-2 PEEK thermoplastic resin

Material property	Dimensionality	Value
Density, ρ	g/cm^3	1.32
Young's modulus, E	GPa	3.6
Tensile strength, at break	MPa	100
Tensile strength, at yield	MPa	95
Failure strain, %	–	70
Yield strain, %	–	5

Table B.8 – Properties of constituents of the unidirectional T700SC-24K-50C/UF3376-100

Property	Dimensionality	Value	Source of data
T700S carbon fibers			
Reference density	g/cm3	1.80000E+00	Manufacturer data
Young's Modulus 11 $\left(E_{11}^f\right)$	kPa	2.30000E+08	Manufacturer data
Young's Modulus 22 $\left(E_{22}^f\right)$	kPa	1.40000E+07	Data for AS4 fibers (close analog of T700S) adopted from [87]
Shear Modulus 12 $\left(G_{12}^f\right)$	kPa	1.40000E+07	
Shear Modulus 23 $\left(G_{23}^f\right)$	kPa	7.00000E+06	
Tensile Failure Stress 11 $\left(\sigma_{11}^f\right)$	kPa	4.90000E+06	Manufacturer data
UF3376-100 epoxy resin			
Reference density	g/cm3	1.18000E+00	Manufacturer data
Young's Modulus $\left(E_m\right)$	kPa	3.10000E+06	Manufacturer data
Tensile Failure Stress $\left(Y_m\right)$	kPa	9.65000E+04	Manufacturer data
Poisson's Ratio	none	3.00000E-01	A typical value

Table B.9 – Properties of unidirectional filament band of T700SC-24K-50C/UF3376-100

Property	Dimensionality	Value	Source of data/Estimation technique
Equation of state: Ortho			
Reference density	g/cm3	1.49000E+00	Experiment
Stiffness		Engineering constants	
Young's Modulus 11	kPa	1.22000E+08	Rule of mixtures [115]: $E_{11} = \upsilon_f \cdot E_{11}^f + \upsilon_m \cdot E_m \approx \upsilon_f \cdot E_{11}^f$
Young's Modulus 22	kPa	8.17200E+06	Modified rule of mixtures [115]: $\dfrac{1}{E_{22}} = \dfrac{1}{\upsilon_f + \eta\upsilon_f}\left[\dfrac{\upsilon_f}{E_{22}^f} + \dfrac{\upsilon_m}{E_m}\right]$, where $\eta \approx 0.5$
Young's Modulus 33	kPa	8.17200E+06	$E_{22} = E_{33}$ due to transverse isotropy
Poisson's Ratio 12	none	2.70000E-01	A typical value for CFRPs
Poisson's Ratio 23	none	4.20000E-01	A typical value for CFRPs
Poisson's Ratio 31	none	1.80856E-02	Classical lamination theory: $v_{31} = v_{13}E_{33}/E_{11}$, where $v_{13} = v_{12}$
Shear Modulus 12	kPa	3.67600E+06	Hashin-Rosen self-similar model [116]: $G_{12} = G_m\left[\dfrac{\left(1+\upsilon_f\right)\cdot G_{12}^f + \left(1-\upsilon_f\right)\cdot G_m}{\left(1-\upsilon_f\right)\cdot G_{12}^f + \left(1+\upsilon_f\right)\cdot G_m}\right]$

			where $G_m = \dfrac{E_m}{2 \cdot (1 + \nu_m)}$
Shear Modulus 23	kPa	2.87700E+06	$G_{23} = \dfrac{E_{22}}{2 \cdot (1 + \nu_{23})}$ due to transverse isotropy
Shear Modulus 13	kPa	3.67600E+06	$G_{13} = G_{12}$
Volumetric response		Polynomial	
Bulk Modulus A1 = K'	kPa	1.86921E+07	See expression for K' in Table 3
Parameter A2	kPa	0.00000E+00	Assumed based on experimental data from [83]
Parameter A3	kPa	0.00000E+00	
Parameter B0	none	2.50000E+00	Calculated using a method proposed in [83], which is based on experimentally established similarity of the normalized shock response of different CFRP systems
Parameter B1	none	2.50000E+00	

Failure Model: Orthotropic softening			
Tensile Failure Stress 11	kPa	2.31200E+06	Rule of mixtures: $X = \upsilon_f \cdot \sigma_{11}^f + \upsilon_m \cdot \sigma_m \approx \upsilon_f \cdot \sigma_{11}^f$
Tensile Failure Stress 22	kPa	4.20000E+04	Chamis's micromechanical equations [87]: $Y = \left[1 - \left(\sqrt{\upsilon_f} - \upsilon_f \right) \cdot \left(1 - \dfrac{E_m}{E_{22}^f} \right) \right] \cdot Y_m^*,$ where $Y_m^* = \beta \cdot Y_m$ and $\beta = \left[1 - \sqrt{\dfrac{4 \cdot \upsilon_v}{(1 - \upsilon_f) \cdot \pi}} \right]$ - correlation factor taking into account presence of voids
Maximum Shear Stress 12	kPa	2.20000E+04	Chamis's micromechanical equations [87]: $S = \left[1 - \left(\sqrt{\upsilon_f} - \upsilon_f \right) \cdot \left(1 - \dfrac{G_m}{G_{12}^f} \right) \right] \cdot S_m^*,$ where $S_m^* = \beta \cdot S_m$ and $S_m = Y_m / \sqrt{3}$
Fracture Energy 11	J/m2	0.00000E+00	Assumption of brittleness of intra-ply failure (see Table B.5)
Fracture Energy 22	J/m2	0.00000E+00	
Fracture Energy 12	J/m2	0.00000E+00	
Damage Coupling Coefficient	none	2.00000E-01	Standard value recommended in Autodyn [60]
Erosion: Geometric strain			
Erosion Strain	none	0.20	
Type of Geometric Strain		Instantaneous	

Table B.10 – Properties of the resin-rich regions of T700SC-24K-50C/UF3376-100

Property	Dimensionality	Value	Source of data/Estimation technique
Equation of state			
Reference density	g/cm3	1.18000E+00	As of the epoxy resin (see Table B.8)
Stiffness		Engineering constants	
Young's Modulus	kPa	3.10000E+06	As of the epoxy resin (see Table B.8)
Poisson's Ratio	none	3.00000E-01	As of the epoxy resin (see Table B.8)
Volumetric response		Shock	
Gruneisen coefficient	none	1.13000E+00	Data for epoxy resin of the same
Parameter C1	m/s	1.47962E+03	density as UF3376 from Autodyn
Parameter S1	none	1.49000E+00	materials library
Failure Model: Orthotropic softening			
Tensile Failure Stress 33	kPa	4.20000E+04	Same as Tensile Failure Stress 22 from Table B.9
Maximum Shear Stress 23	kPa	2.20000E+04	Chamis's micromechanical equations [87]: $$S = \left[\frac{1 - \sqrt{\upsilon_f} \cdot \left(1 - G_m / G_{23}^f\right)}{1 - \upsilon_f \cdot \left(1 - G_m / G_{23}^f\right)} \right] \cdot S_m^*,$$ where $S_m^* = \beta \cdot S_m$ and $S_m = Y_m / \sqrt{3}$
Maximum Shear Stress 31	kPa	2.20000E+04	Same as Max. Shear Stress 12 from Table B.9
Fracture Energy 33 (G_{Ic})	J/m2	9.50000E+01	Experiment (see Section 4.6.2)
Fracture Energy 31 (G_{IIc})	J/m2	1.40000E+02	Experiment (see Section 4.6.2)
Fracture Energy 23 (G_{IIIc})	J/m2	1.40000E+02	Same as G_{IIc} (see Section 4.6.2)
Damage Coupling Coefficient	none	2.00000E-01	Standard value recommended in Autodyn [60]
Erosion: Geometric strain			
Erosion Strain	none	1.20000E+00	
Type of Geometric Strain		Instantaneous	

APDL SCRIPTS FOR GENERATING THE OPEN-CELL FOAM MODEL

C.1 APDL Script Performing Generation of RVE of Aluminum Foam

```
NOTE: prior to running the script, frame model of

translation unit of Wearie-Phelan packing should be

imported in ANSYS Mechanical APDL environment.


! SXRVE - RVE size in X direction in METERS

SXRVE = 20e-3

! SYRVE - RVE size in Y direction in METERS

SYRVE = 20e-3

! SZRVE - RVE size in Z direction in METERS

SZRVE = 40e-3


/PREP7


! Merge all coincident lines and keypoints. TOLER = 1e-3,

GTOLER = 2e-3

NUMMRG, ALL, 0.25e-3, 0.5e-3

! Compress numbering of keypoints and lines

NUMCMP, KP

NUMCMP, LINE
```

```
! Find number of lines

*GET,N,LINE,0,COUNT


! --------- X DIRECTION ----------

! Determine number of repetitions in X direction

XNREP = (SXRVE/5e-3) - 1

*DO, I, 1, XNREP, 1

! Define a local CS

CLOCAL,100+I,0,I*5e-3

! Activate global CS

CSYS, 0

! Translate lines

LTRAN,I+100,1,N,1,0,1,0

! Merge all coincident nodes and keypoints

NUMMRG,ALL,0.25e-3,0.5e-3

*ENDDO

! Compress numbering of keypoints and lines

NUMCMP, KP

NUMCMP, LINE

! --------- END OF X DIRECTION ----------


! --------- Y DIRECTION ----------

! Find number of lines

*GET,NY,LINE,0,COUNT
```

```
! Determine number of repetitions in Y direction

YNREP = (SYRVE/5e-3) - 1

*DO,J,1,YNREP,1

! Define a local CS

CLOCAL,1000+J,0,0,J*5e-3

! Activate global CS

CSYS, 0

! Translate lines

LTRAN,J+1000,1,NY,1,0,1,0

! Merge all coincident nodes and keypoints

NUMMRG,ALL,0.25e-3,0.5e-3

*ENDDO

! Compress numbering of keypoints and lines

NUMCMP, KP

NUMCMP, LINE

! --------- END OF Y DIRECTION ----------


! --------- Z DIRECTION ----------

! Find number of lines

*GET,NZ,LINE,0,COUNT

! Determine number of repetitions in Z direction

ZNREP = (SZRVE/5e-3) - 1

*DO,Q,1,ZNREP,1

! Define a local CS
```

```
CLOCAL,10000+Q,0,0,0,Q*5e-3

! Activate global CS

CSYS, 0

! Translate lines

LTRAN,Q+10000,1,NZ,1,0,1,0

! Merge all coincident nodes and keypoints

NUMMRG,ALL,0.25e-3,0.5e-3

*ENDDO

! Compress numbering of keypoints and lines

NUMCMP, KP

NUMCMP, LINE

! --------- END OF Z DIRECTION ----------


! Find number of lines

*GET,NN,LINE,0,COUNT

! Find coordinates of the Bounding box

LSEL, ALL

*GET, MINX, KP, 0, MNLOC, X

*GET, MAXX, KP, 0, MXLOC, X

*GET, MINY, KP, 0, MNLOC, Y

*GET, MAXY, KP, 0, MXLOC, Y

*GET, MINZ, KP, 0, MNLOC, Z

*GET, MAXZ, KP, 0, MXLOC, Z

LX = MAXX - MINX
```

```
XCEN = (LX/2) + MINX

LY = MAXY - MINY

YCEN = (LY/2) + MINY

! Define a local CS

CLOCAL,100000,0,XCEN,YCEN,0

LTRAN,0,1,NN,1,0,1,1

CSYS, 0

*GET, MINNX, KP, 0, MNLOC, X

*GET, MAXXX, KP, 0, MXLOC, X

*GET, MINNY, KP, 0, MNLOC, Y

*GET, MAXXY, KP, 0, MXLOC, Y

*GET, MINNZ, KP, 0, MNLOC, Z

*GET, MAXXZ, KP, 0, MXLOC, Z


PARSAV,,C:\Users\ ... folder path ... \Parameters,txt
```

C.2 APDL Script Performing Foam Randomization

```
!---- PARAMETERS ----

! RAD1 - radius of a foam ligament in METERS

RAD1 = 0.14625e-3

! Boundaries of RVE
```

```
! NOTE: X and Y boundary are [-XBOUND; +XBOUND] and [-
YBOUND; +YBOUND], correspondingly

! NOTE: Z boundary is [0; +ZBOUND]

XBOUND = 0.108e-1

YBOUND = 0.108e-1

ZBOUND = 0.417e-1

!Characteristic dimension of foam

LCHAR = 0.366e-3

!---- END of PARAMETERS ----


/PREP7


! Merge all coincident lines and keypoints. TOLER = 1e-3,
GTOLER = 2e-3

NUMMRG,ALL,0.25e-3,0.5e-3

! Compress numbering of keypoints and lines

NUMCMP, KP

NUMCMP, LINE

! Find number of keypoints

*GET,NKP,KP,0,COUNT

*DO,J,1,NKP,1

!Find coordinates of a keypoint

*GET,XKP,KP,J,LOC,X

*GET,YKP,KP,J,LOC,Y
```

```
*GET,ZKP,KP,J,LOC,Z


!Check if keypoint is on a boundary of RVE

*IF, XKP, GT, XBOUND, THEN

CH1 = 1

*ELSE

CH1 = 0

*ENDIF

*IF, XKP, LT, -1*XBOUND, THEN

CH2 = 1

*ELSE

CH2 = 0

*ENDIF

*IF, YKP, GT, YBOUND, THEN

CH3 = 1

*ELSE

CH3 = 0

*ENDIF

*IF, YKP, LT, -1*YBOUND, THEN

CH4 = 1

*ELSE

CH4 = 0

*ENDIF

*IF, ZKP, GT, ZBOUND, THEN
```

```
CH5 = 1

*ELSE

CH5 = 0

*ENDIF

*IF, ZKP, LT, 0, THEN

CH6 = 1

*ELSE

CH6 = 0

*ENDIF

CH = CH1+CH2+CH3+CH4+CH5+CH6

*IF, CH, GT, 0, THEN

AAA = 1

*ELSE

XNEW = XKP + RAND(-1,1)*LCHAR

YNEW = YKP + RAND(-1,1)*LCHAR

ZNEW = ZKP + RAND(-1,1)*LCHAR

KMODIF, J, XNEW, YNEW, ZNEW

*ENDIF

*ENDDO


! Merge all coincident lines and keypoints. TOLER = 1e-3,

GTOLER = 2e-3

NUMMRG,ALL,0.15e-3,0.25e-3

! Compress numbering of keypoints and lines
```

```
NUMCMP, KP

NUMCMP, LINE

! Find number of lines

*GET,N,LINE,0,COUNT

*DO,I,1,N,1

! Define the working plane normal to a location of the line

No. "I"

LWPLAN,-1,I

! Determine length ("depth") of a line

*GET,DEPTH,LINE,I,LENG

! Create a cylindrical volume of radius RAD1 and length

DEPTH on the working plane

CYL4,0,0,RAD1,,,, DEPTH

*ENDDO
```

EXPERIMENTAL RESULTS FOR HVI DAMAGE OF SANDWICH PANELS

AND WHIPPLE SHIELD CONFIGURATIONS

Test #	UM-I-0.4(A)-16FC-0.4	Test date	Nov 02, 2015

Projectile diameter, mm 1.00

Projectile speed, km/s 6.965

Front facesheet, mm 0.4

Rear facesheet, mm 0.4

Core thickness, mm 16

Bumper	Core

Rear wall	Witness plate
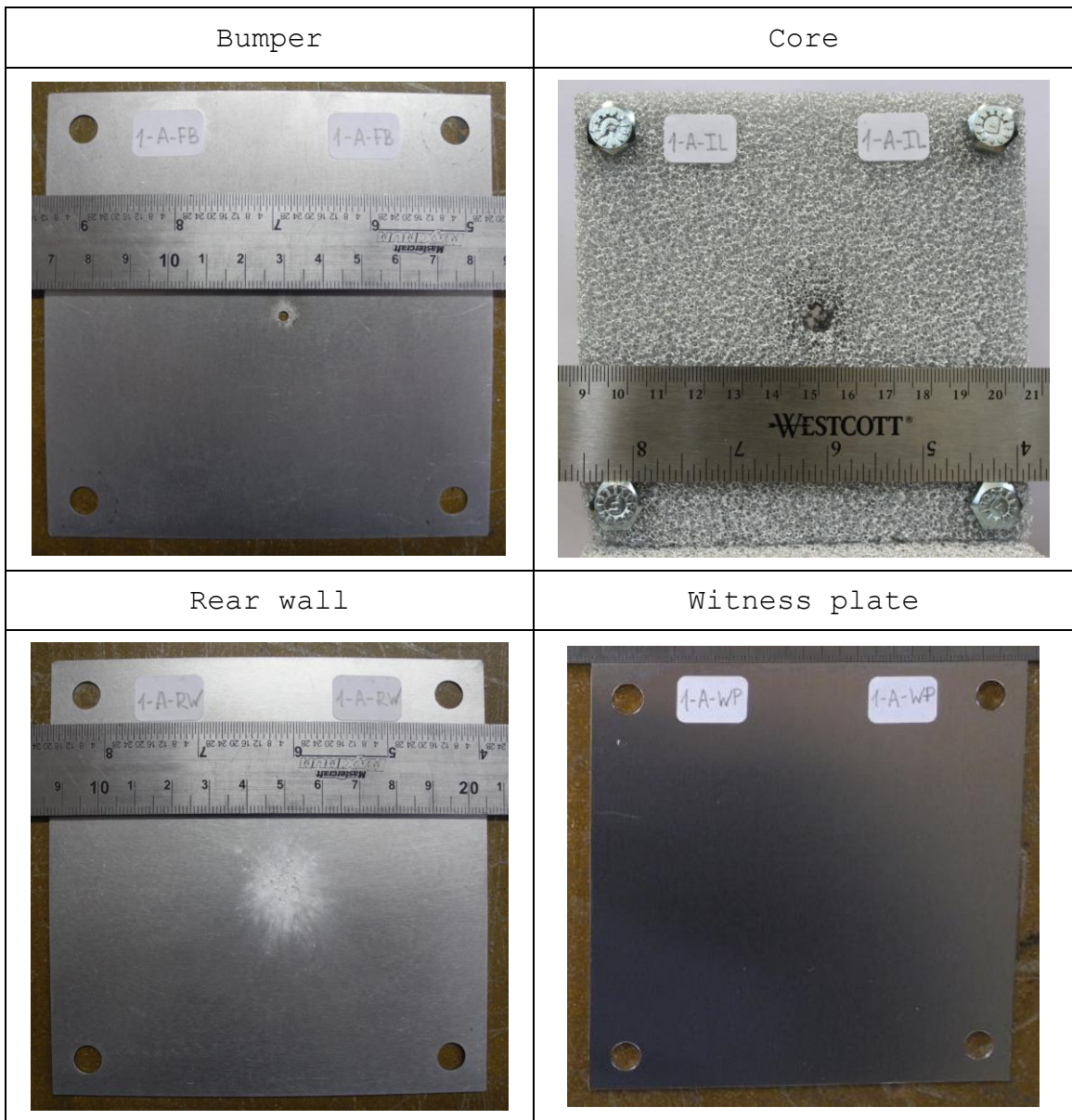
Test #	UM-I-0.4(A)-16FC-0.4	CONTINUED

Description of the damage:

No perforation of the rear wall; momentum bulge on the rear wall is barely visible; damage of the rear wall is mainly represented by discoloration.

Framing camera imagery:
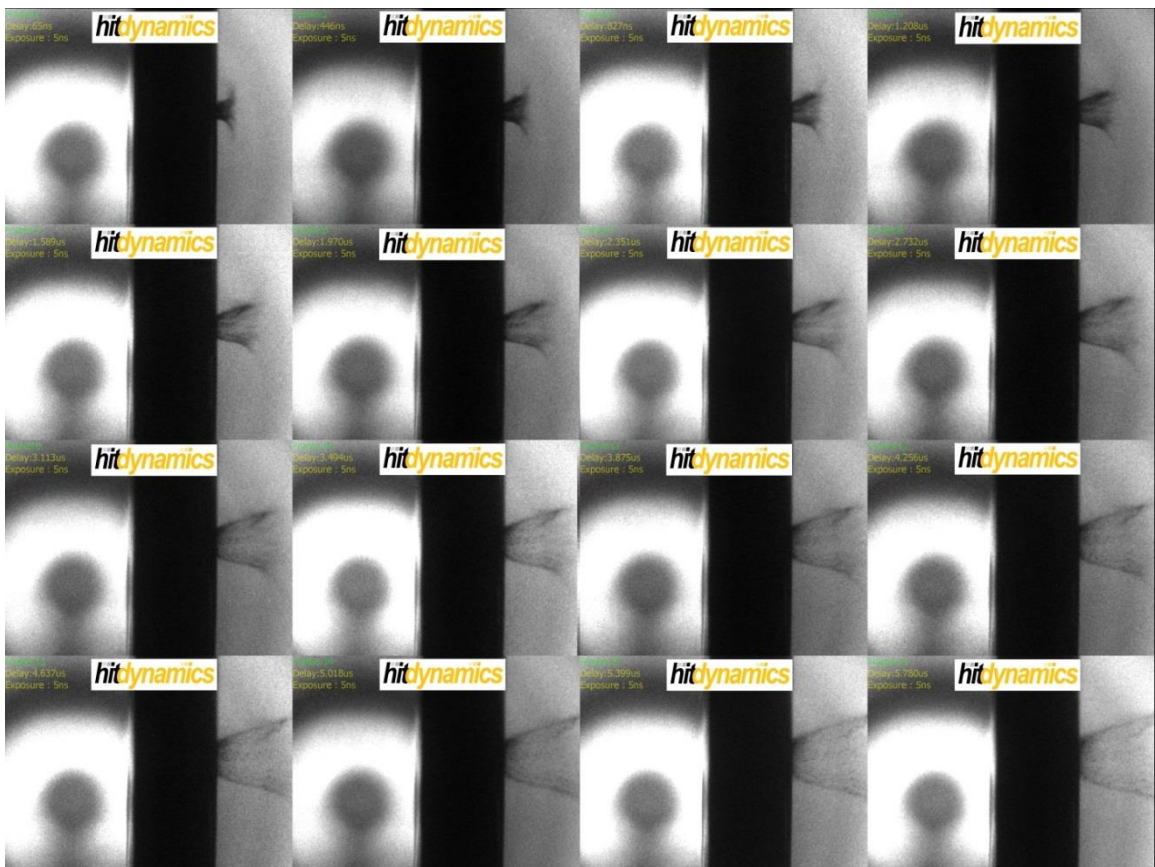
Test #	UM-IV-0.4(A)--0.4	**Test date**	Nov 03, 2015

Projectile diameter, mm   1.00

Projectile speed, km/s   7.102

Bumper, mm   0.4

Rear wall, mm   0.4

Standoff, mm   16

Bumper	Rear wall (front)
Rear wall (back)	Witness plate
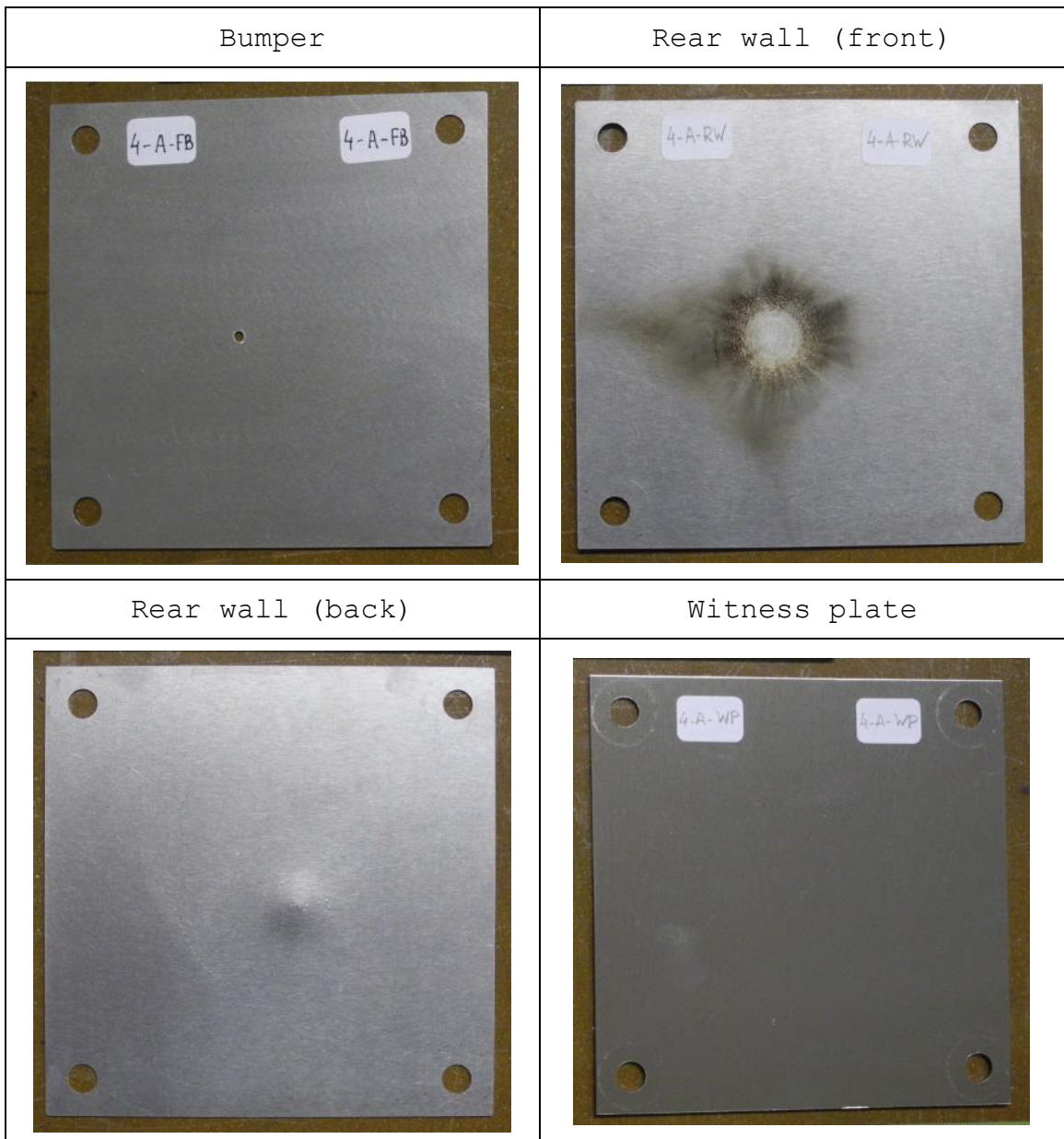
Test #	UM-IV-0.4(A)--0.4	CONTINUED

Description of the damage:

Momentum bulge on the rear wall; no perforations of the rear wall visible by the naked eye; multiple submillimeter bulges on the back of the rear wall; "burned" regions surrounding damaged area on the front of the rear wall.

Framing camera imagery:

Test #	UM-V-0.4(B)--0.4	**Test date**	Nov 03, 2015

Projectile diameter, mm   1.00

Projectile speed, km/s   7.063

Bumper, mm   0.05(SiC) + 0.4 + 0.05(SiC)

Rear wall, mm   0.4

Standoff, mm   16

Bumper	Rear wall (front)
Rear wall (back)	**Witness plate**

Test #	UM-V-0.4(B)--0.4	CONTINUED

<u>Description of the damage</u>:

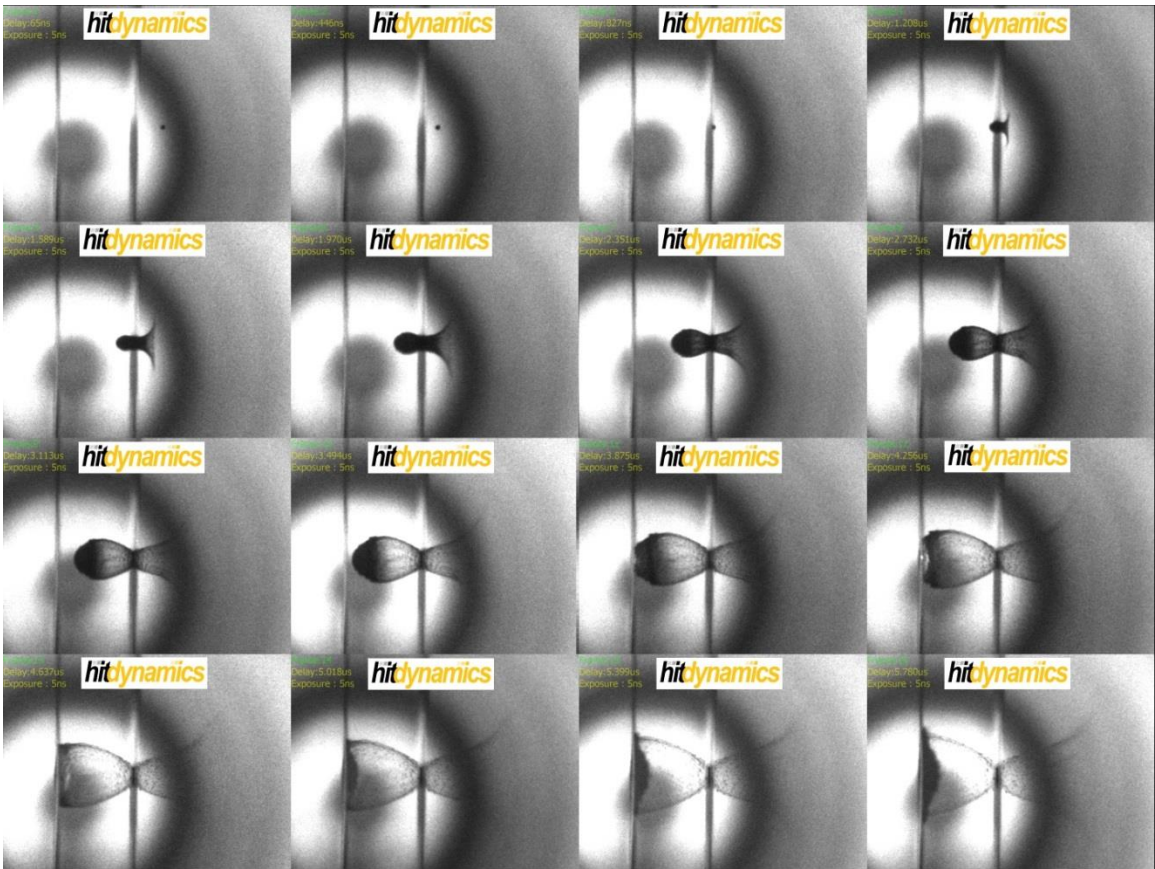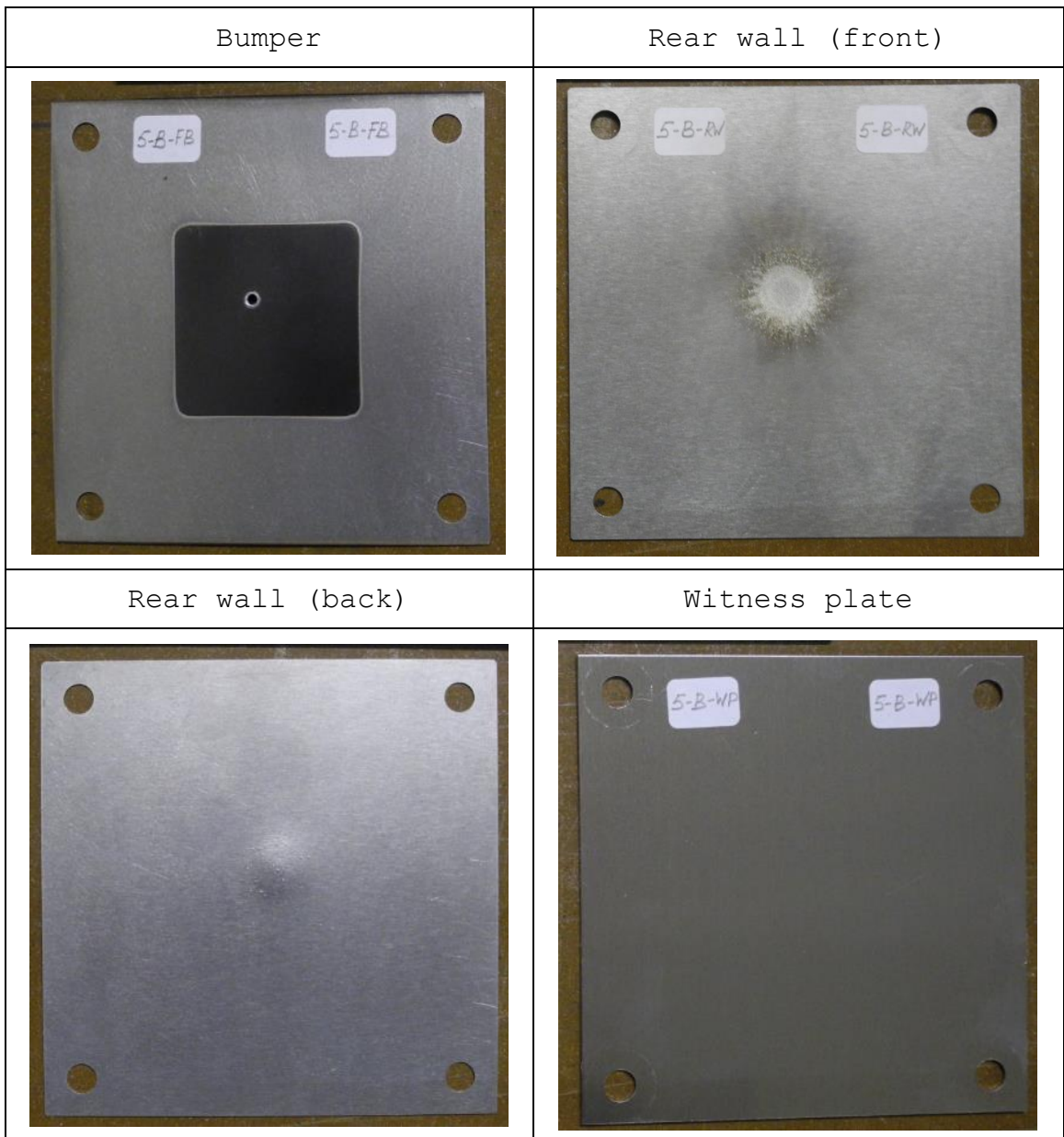Momentum bulge on the rear wall; no perforations of the rear wall visible by the naked eye; multiple submillimeter bulges on the back of the rear wall.
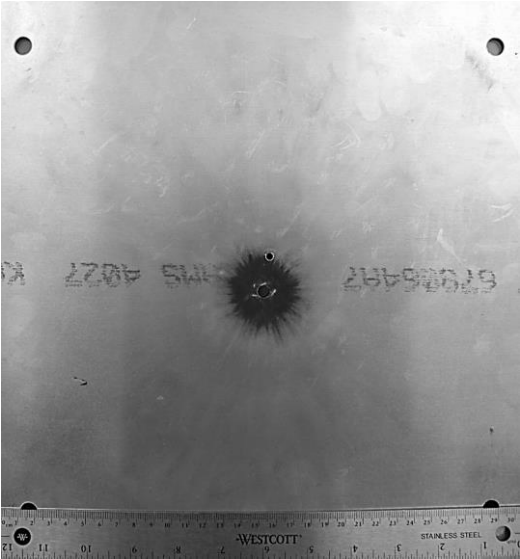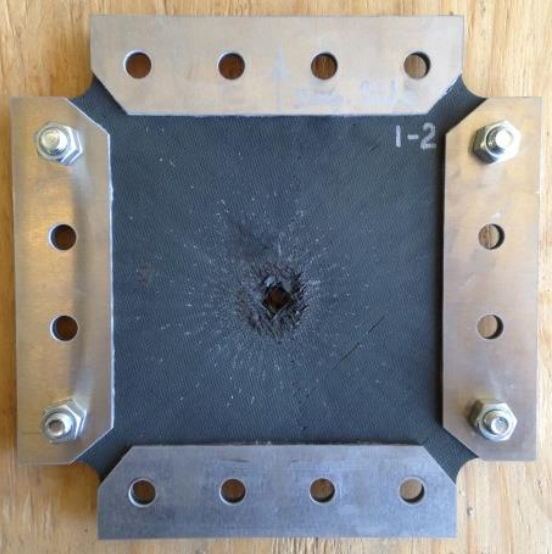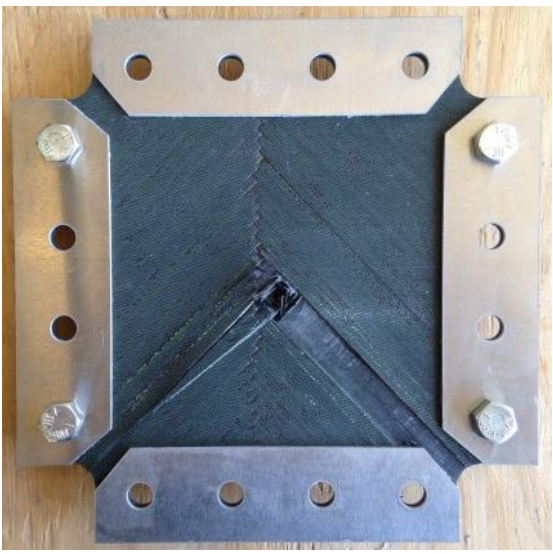
<u>Framing camera imagery</u>:
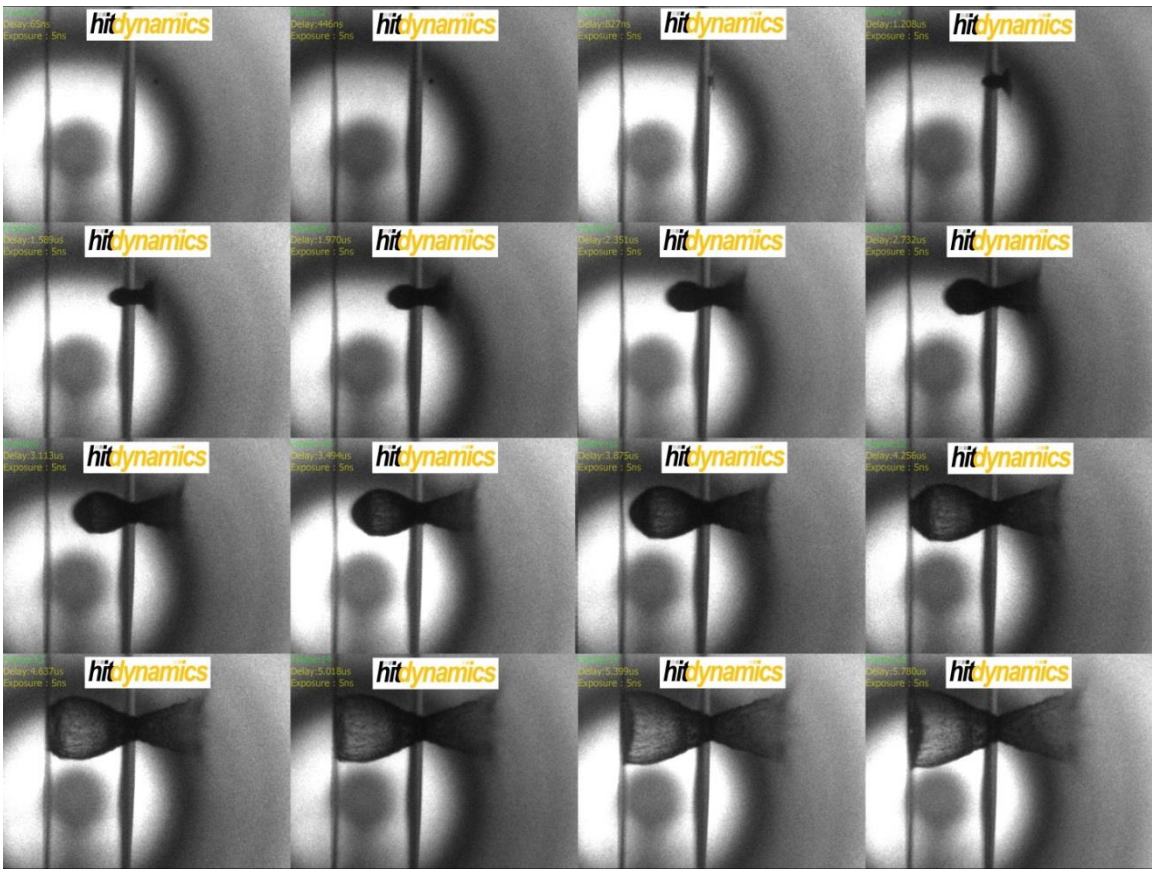
EXPERIMENTAL RESULTS FOR HVI DAMAGE OF THE FILAMENT-WOUND SPECIMENS

Test #	1-2	**Test date**	May …, 2015

Weaving: LDI

Projectile diameter, mm   3.125

Projectile speed, km/s   6.822

Pre-loading (strain)   N/A

Bumper (back)	Witness plate
Composite specimen: front	Composite specimen: back

233

Test #	2-1	Test date	May …, 2015

Weaving: LDI

Projectile diameter, mm 3.125

Projectile speed, km/s 6.828

Pre-loading (strain) 0.00483

Bumper (back)	Witness plate
Composite specimen: front	Composite specimen: back
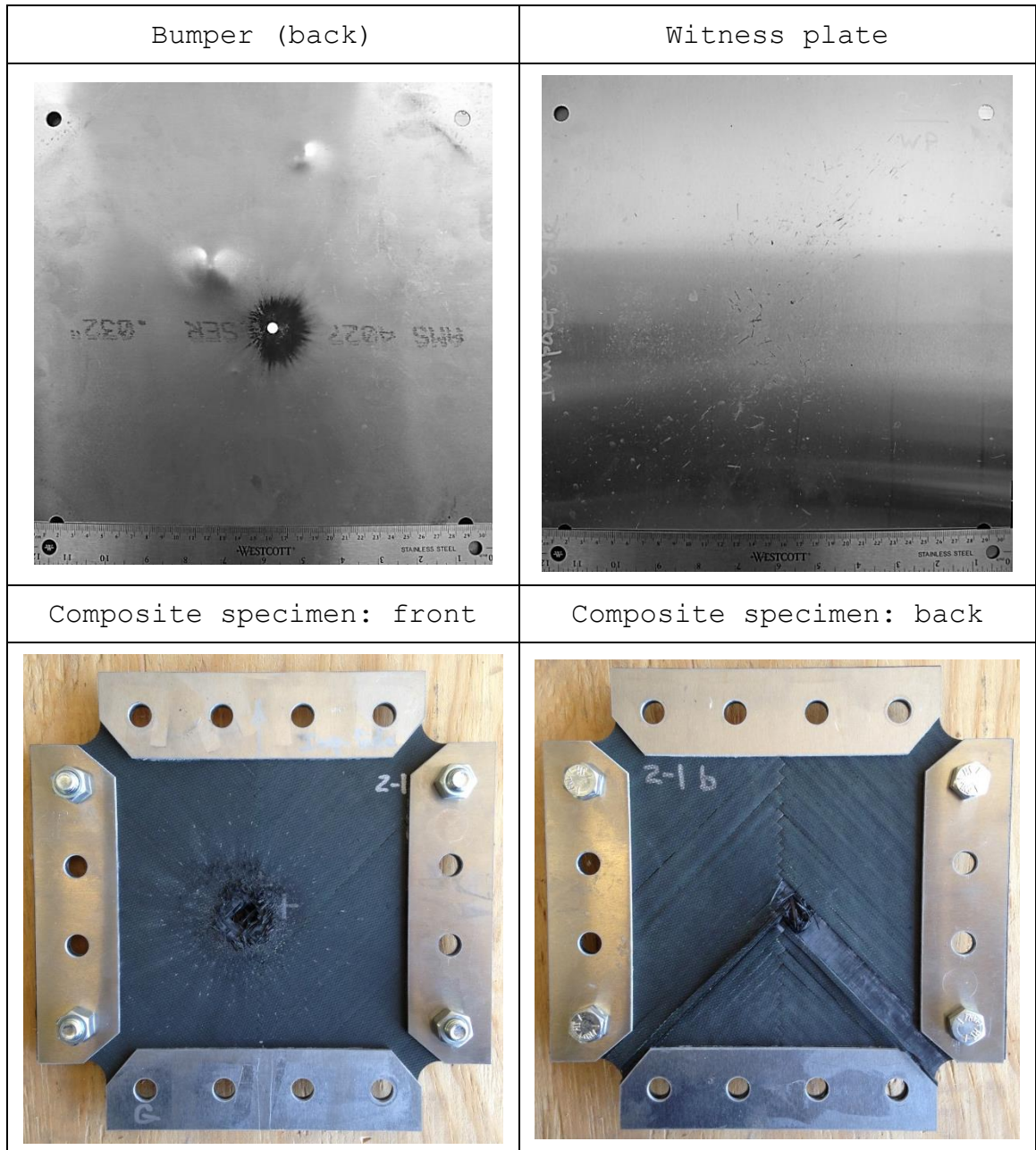
Test #	3-2	**Test date**	May …, 2015

Weaving: HDI

Projectile diameter, mm 3.125

Projectile speed, km/s 6.847

Pre-loading (strain) N/A

Bumper (back)	Witness plate
Composite specimen: front	Composite specimen: back

Test #	4-2	**Test date**	May …, 2015

Weaving: HDI

Projectile diameter, mm   3.125

Projectile speed, km/s   6.878

Pre-loading (strain)   0.00483

Bumper (back)	Witness plate
Composite specimen: front	Composite specimen: back

236

Test #	1-3	**Test date**	May …, 2015

Weaving: LDI

Projectile diameter, mm   4.763

Projectile speed, km/s   6.786

Pre-loading (strain)   N/A

Bumper (back)	Witness plate
Composite specimen: front	Composite specimen: back

Test #	2-3	Test date	May …, 2015

Weaving: LDI

Projectile diameter, mm 4.763

Projectile speed, km/s 6.786

Pre-loading (strain) 0.00540

Bumper (back)	Witness plate
Composite specimen: front	Composite specimen: back

Test #	4-3	**Test date**	May …, 2015

Weaving: HDI

Projectile diameter, mm   4.763

Projectile speed, km/s   6.922

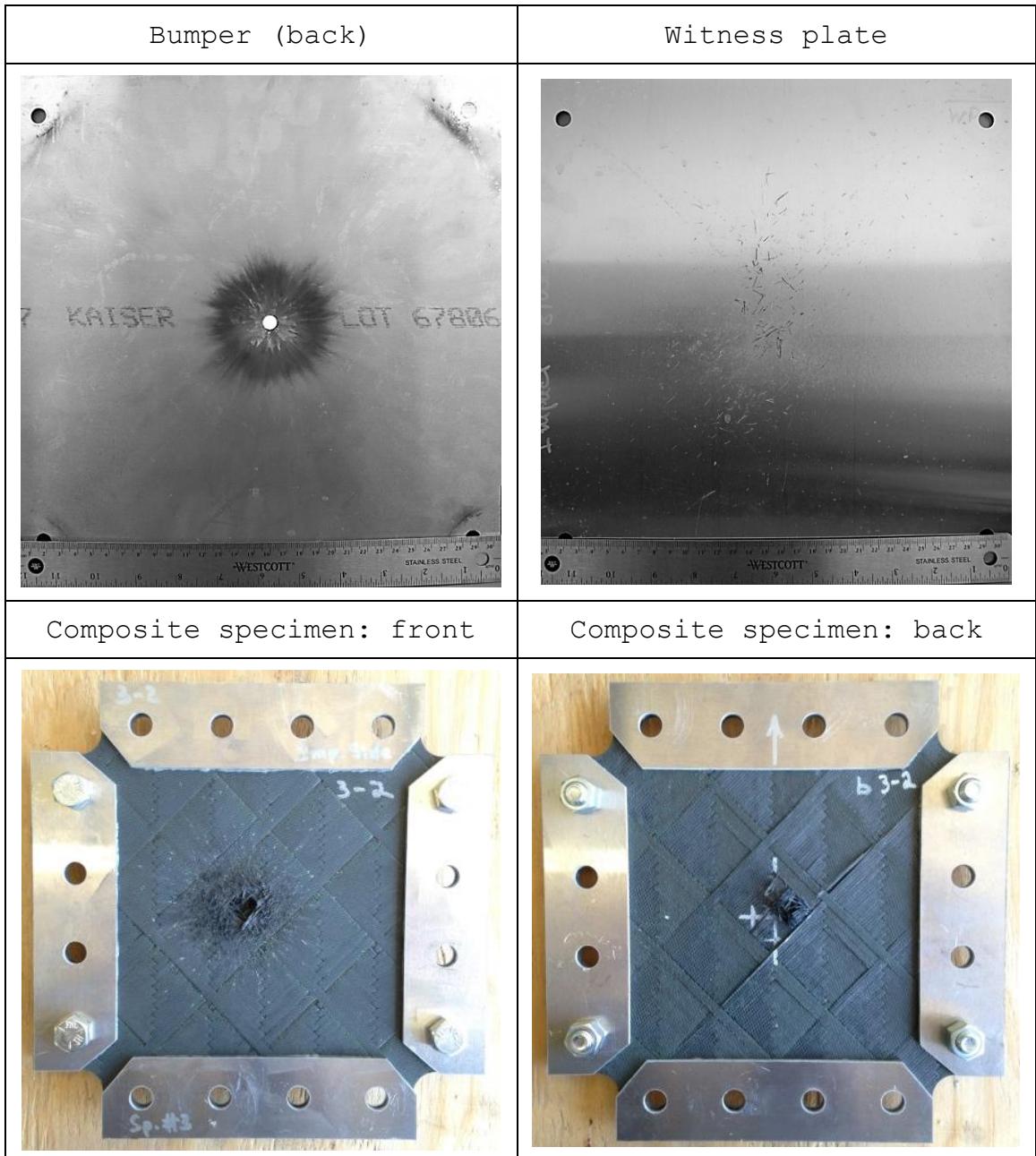Pre-loading (strain)   N/A

Bumper (back)	Witness plate
Composite specimen: front	Composite specimen: back

239

Test #	3-3	**Test date**	May …, 2015

Weaving: HDI

Projectile diameter, mm 4.763

Projectile speed, km/s 6.781
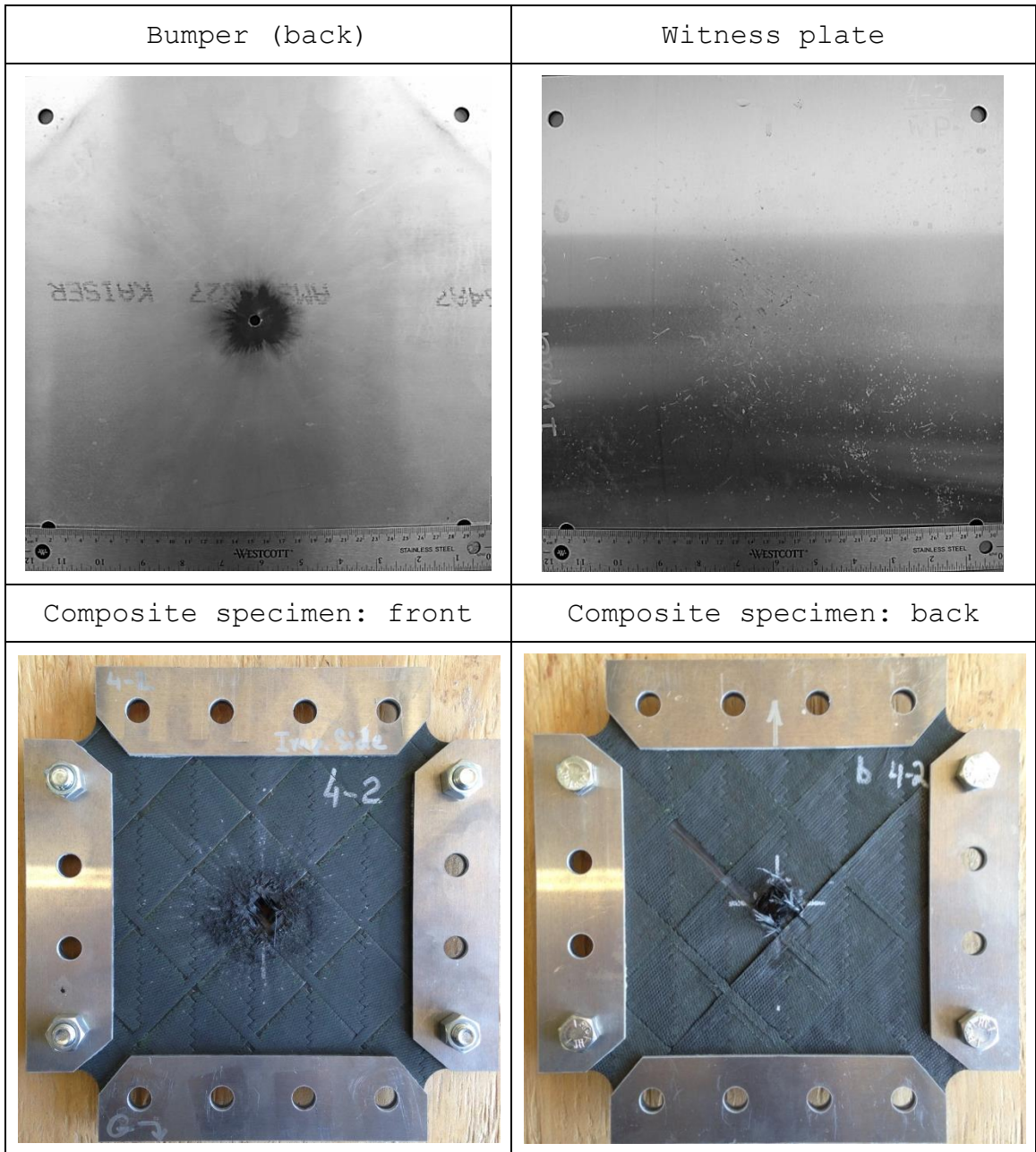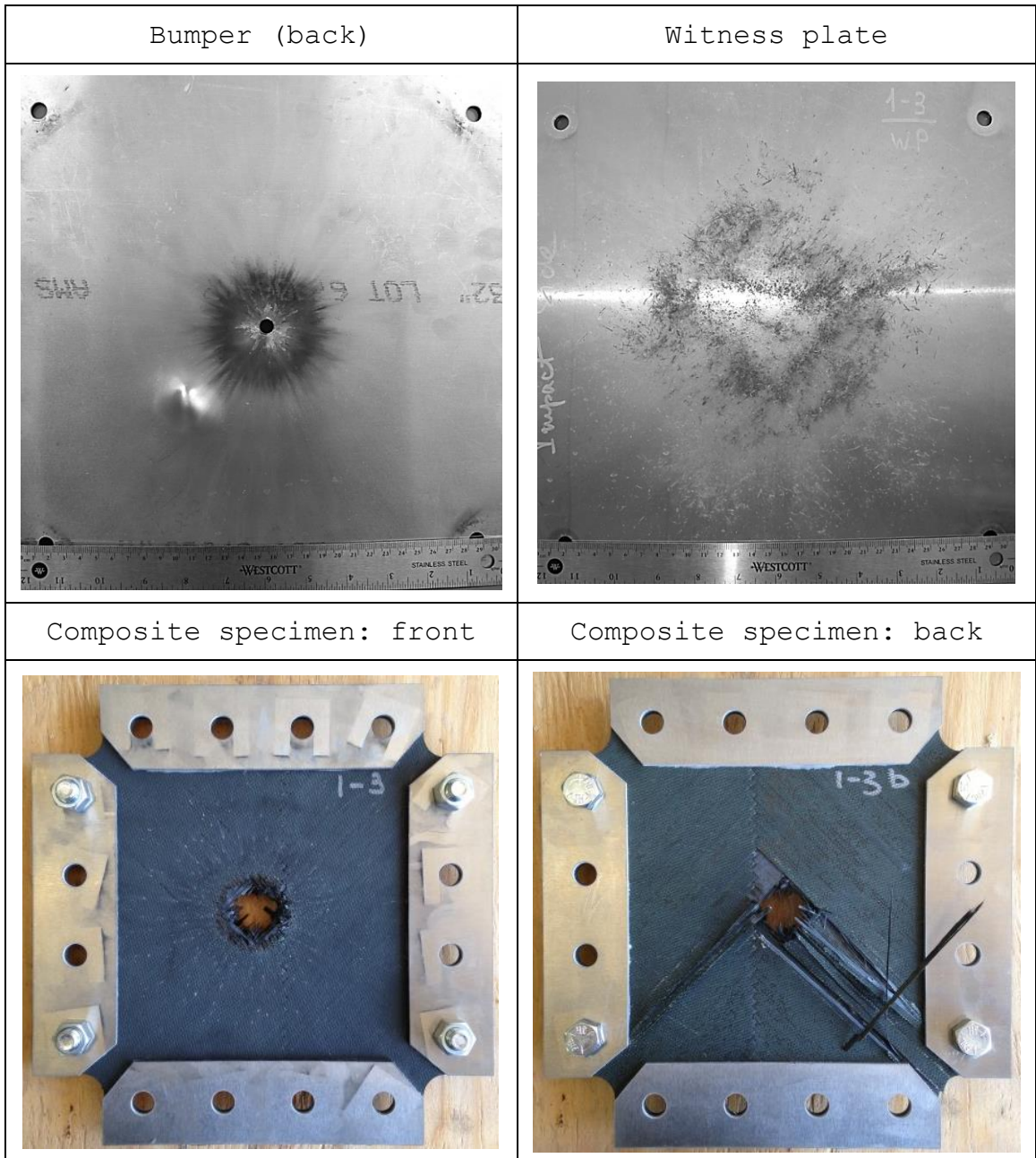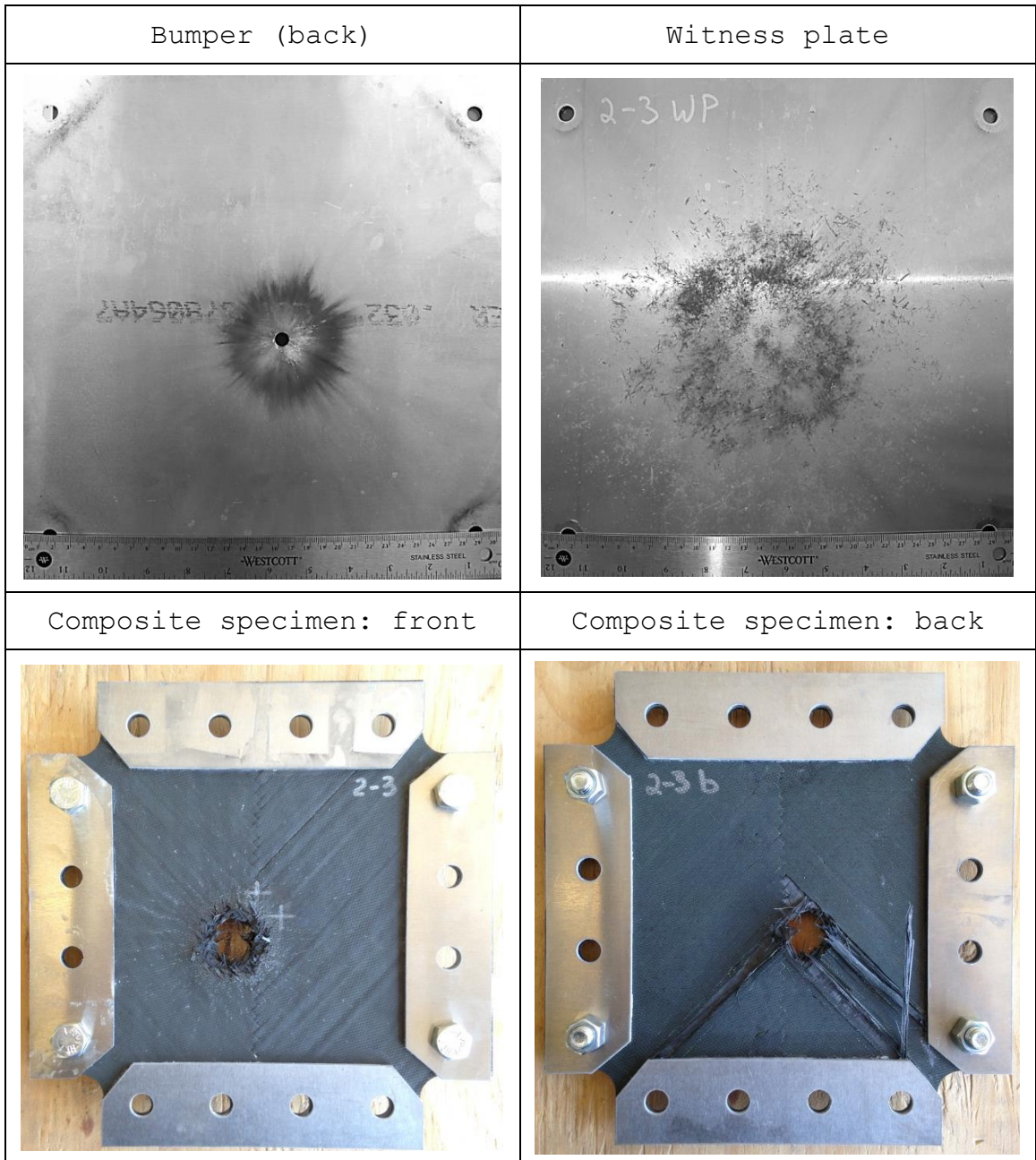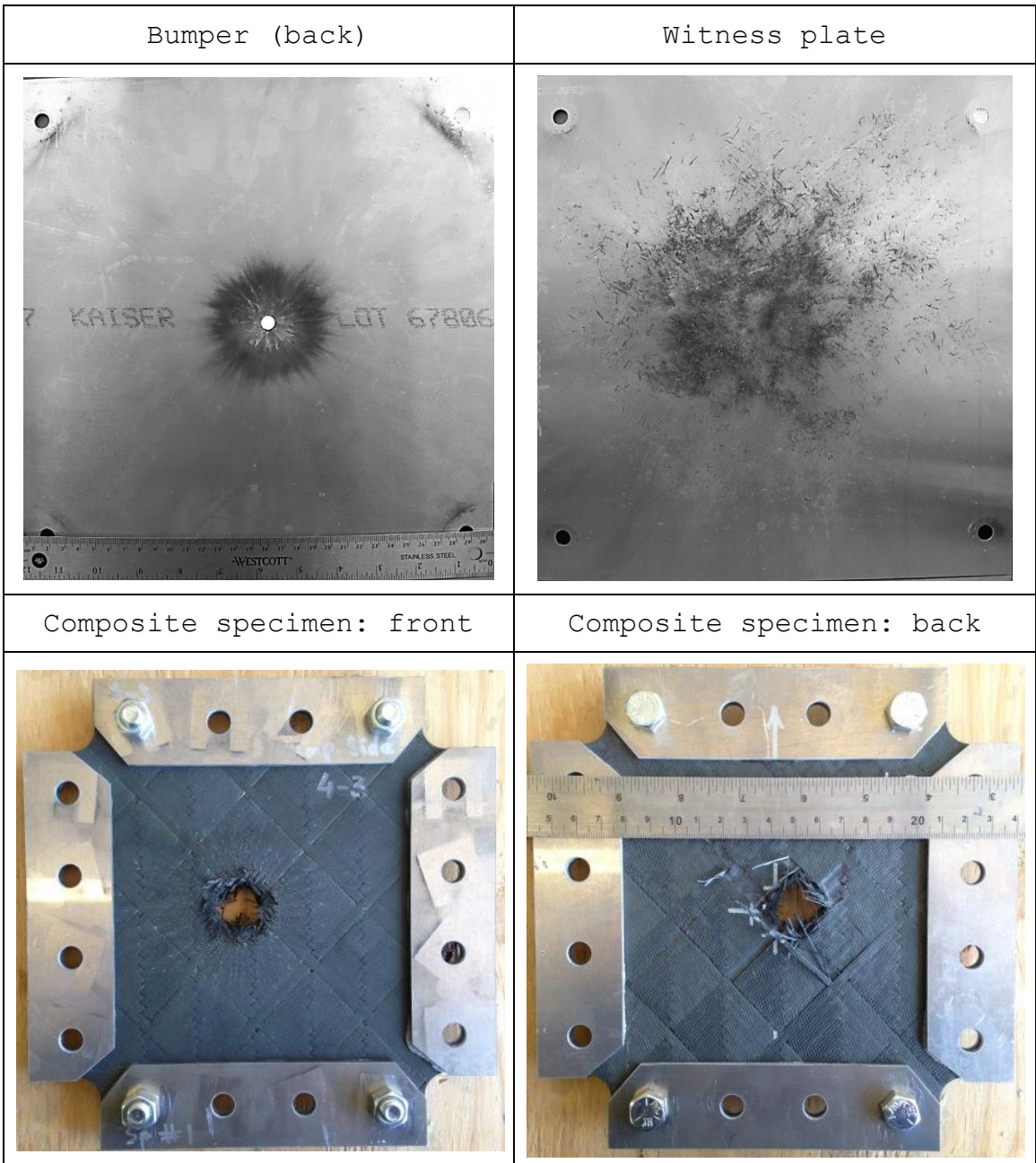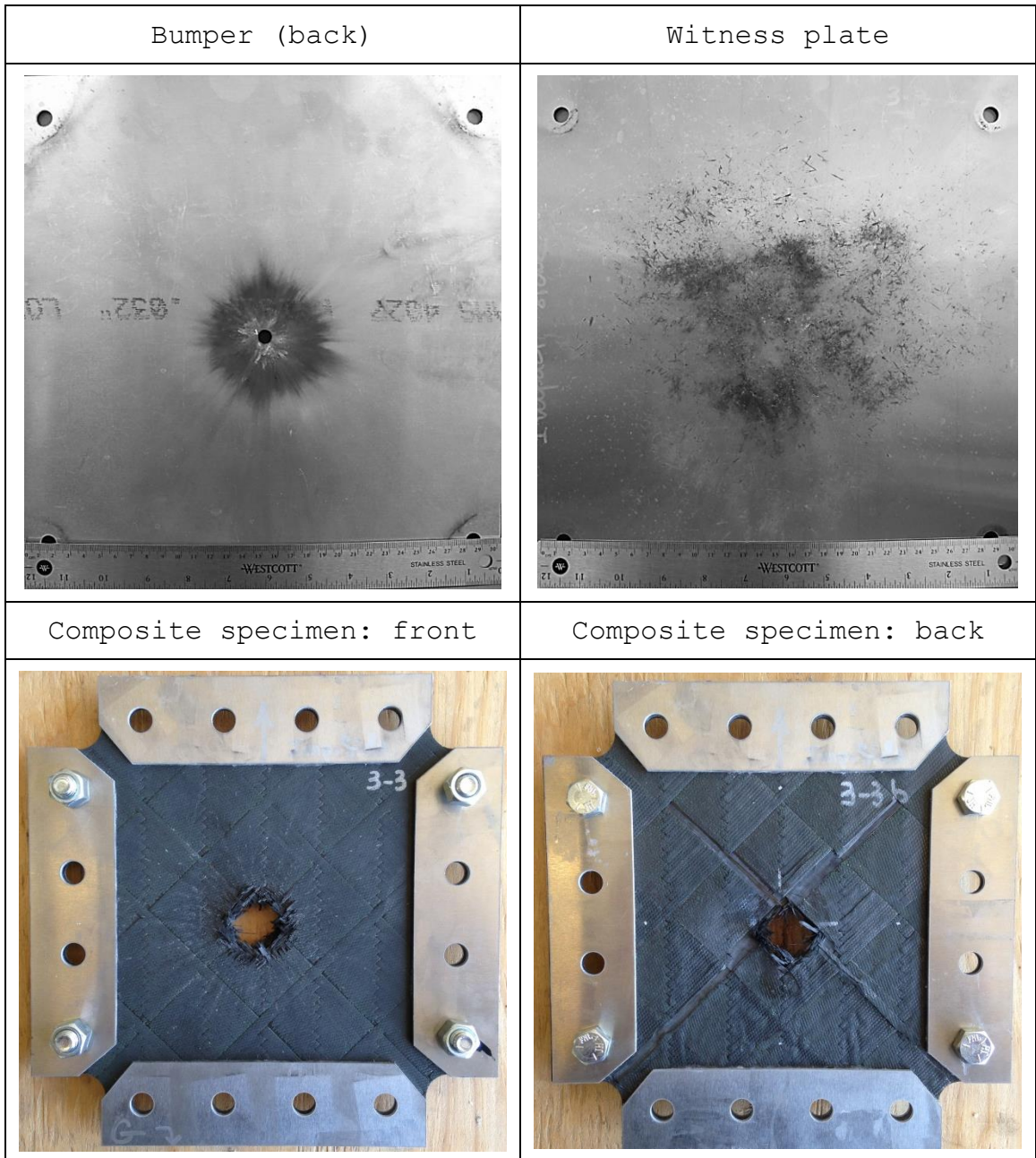
Pre-loading (strain) 0.00548

Bumper (back)	Witness plate
Composite specimen: front	Composite specimen: back

REFERENCES

1. http://orbitaldebris.jsc.nasa.gov/faqs.html

2. Krisko P.H. The New NASA Orbital Debris Engineering Model ORDEM 3.0. In: Proceedings of AIAA/AAS Astrodynamics Specialist Conference, 4-7 Aug. 2014, San Diego, CA, United States.

3. Christiansen E.L. et al., "Handbook for Designing MMOD Protection" NASA Johnson Space Center, NASA/TM-2009-214785 (2009).

4. IADC protection manual. IADS-04-03, ver. 4.0 (2011)

5. ESA Space Debris Mitigation Handbook. ESA Contract 14471/00/D/HK (2000, as updated in 2002)

6. Whipple F. Meteorites and Space Travels, Astronomical Journal, 1161, p. 131 (1947)

7. Stansbery E.G. et al. NASA Orbital Debris Engineering Model ORDEM 3.0 - User's Guide. Orbital Debris Program Office. NASA/TP-2014-217370 (2014)

8. MASTER-2009. Software user manual. European Space Agency (2011)

9. Process for Limiting Orbital Debris. NASA technical standard. NASA-STD-8719.14A (2012)

10. United Nations. General assembly. UN A/AC.105/697 (1998)

11. McLaughan P.B., Forth S.C., Grimes-Ledesma L.R. Composite Overwrapped Pressure Vessels, A Primer NASA/SP–2011–573 (2011)

12. Schaefer F., Schneider E, Lambert M. An experimental study to investigate hypervelocity impacts on pressure vessels. Proceedings of the second European conference on space debris, ESDC, Darmstadt, Germany, March 1997

13. Generic technologies. Solicitation No.9F063-130093/A. Public Works and Government Services Canada on behalf of Canadian Space Agency (2013)

14. Peters S.T. Composite filament winding. ASM International, Materials Park (2011)

15. Maveyraud, C., Vila, J.P., Sornette, D., Le Floc'h, C., Dupillier, J.M., Salome, R. Numerical modeling of the behavior of high pressure vessel under hypervelocity impact. Mech. Ind. 2, 57 – 62 (2001)

16. Hayhurst, C.J., Hiermaier, S.J., Clegg, R.A., Riedel, W., Lambert, M. Development of material models for Nextel and Kevlar-epoxy for high pressures and strain rates. Int. J. Impact Eng. 23, 365-376 (1999)

17. White, D.M., Taylor, E.A., Clegg, R.A. Numerical Simulation and Experimental Characterization of Direct Hypervelocity Impact on a Spacecraft Hybrid Carbon Fibre/Kevlar Composite Structure. Int. J. Impact Eng. 29, 779-790 (2003)

18. Piekutowski A J. Formation and Description of Debris Clouds Produced by Hypervelocity Impacts, NASA CR 4706 (1997).

19. Crews J.L., Christiansen E.L., Williamsen J.E., Robinson J.R., Nolen A.M. Enhanced whipple shield. Patent US5610363 A (1997)

20. Destefanis R., Faraud M., Trucci M. Columbus debris shielding experiments and ballistic limit curves, Int. J. Impact Eng., 23, pp. 181 – 192 (1999)

21. Higashide M., Tanaka M., Akahoshi Y, Harada S., Tohyama F. Hypervelocity impact tests against metallic meshes. Int. J. Impact Eng., 33, pp. 335-342 (2006)

22. Myagkov N.N., Shumikhin T.A., Bezrukov L.N. Experimental and numerical study of peculiarities at high-velocity interaction between a projectile and discrete bumpers. Int. J. Impact Eng., 37 (9), pp. 980-994 (2010)

23. Rudolph M., Shaefer F., Destefanis R. Faraud M., Lambert M. Fragmentation of hypervelocity aluminum projectiles on fabrics. Acta Astonautica, 76, pp. 42-50 (2012)

24. https://directory.eoportal.org/web/eoportal/satellite-missions/c-missions/cassiope

25. Thoma K, et al, Status And Perspectives in Protective Design, Space Debris 2, 201–224, 2000.

26. Ryan S., Hedman T., Christiansen E.L., Honeycomb vs. foam: Evaluating potential upgrades to ISS module shielding, Acta Astronautica, 67, 2010, 818–825.

27. Ryan S, Christiansen EL. Hypervelocity impact testing of advanced materials and structures for micrometeoroid and orbital debris shielding, Acta Astronautica 83 (2013) 216–231

28. Beeson H.D., Davis D.D., Ross W.L., Tapphorn R.M. Composite Overwrapped Pressure Vessels. NASA/TP – 2002 – 210769.

29. Rucker R.A. Demonstration of hazardous hypervelocity test capability. NASA JSC TR 692-001 (1991)

30. Christiansen E.L., Kerr J.H., Whitney J.P. Debris cloud ablation in gas-filled pressure vessels. Int. J. Impact Engng, Vol. 20, pp. 173 – 184 (1997)

31. Schaefer F., Schneider E, Lambert M., Mayseless M. Propagation of hypervelocity impact fragment clouds in pressure gas. Int. J. Impact Engng, Vol. 20, pp. 697 – 710 (1997)

32. Schaefer F., Schneider E, Lambert M. Impact fragment cloud propagating in a pressure vessel. Acta Astronautica, Vol. 39, No. 1, pp. 31 – 40 (1997)

33. Schaefer F., Schneider E, Lambert M. An experimental study to investigate hypervelocity impacts on pressure vessels. Proceedings of the second European conference on space debris, ESDC, Darmstadt, Germany, March 1997 (ESA SP-393, May 1997)

34. Lambert M., Schneider E. Hypervelocity impacts on gas-filled pressure vessels. Int. J. Impact Engng, Vol. 20, pp. 491 – 498 (1997)

35. Telitchev I.Ye., Schaefer F.K., Schneider E.E. and Lambert M. Analysis of the fracture of gas-filled pressure vessels under hypervelocity impact. Int. J. Impact Engng, Vol. 23, pp. 905 – 919 (1999)

36. Telitchev I.Ye., Eskin D. Engineering model for simulation of debris cloud propagation inside gas-filled pressure vessels. Int. J. Impact Engng, Vol. 29, pp. 703 – 712 (2003)

37. Schaefer F., Schneider E, Lambert M. Impact damage on shielded gas-filled vessels. Proceedings of the second European conference on space debris, European Space Operations Centre, Darmstadt, Germany, 21 March 2001 (Vol.2).

38. Olsen G.D., Nolen A.M. Hypervelocity impact testing of pressure vessels to simulate spacecraft failure. Int. J. Impact Engng, Vol. 26, pp. 555 – 566 (2001)

39. Telitchev I.Ye.. Analysis of burst conditions of shielded pressure vessels subjected to space debris impact. J. Press Vess Technol – Trans ASME; 127:179 – 83 (2005)

40. Guan G., Pang B. and Ha Y. Investigation into damage of aluminum gas-filled pressure vessels under hypervelocity impact. Key Engineering Materials, Vols. 348 – 349, pp. 785 – 788 (2007)

41. Hayhurst, C.J., Ranson, J.H., Gardner, D.J. and Birnbaum, N.K., Modelling of microparticle hypervelocity oblique impacts on thick targets, International Journal of Impact Engineering, Vol. 17, pp. 375-386 (1995)

42. Monaghan, J.J. Smooth particle hydrodynamics. Ann. Rev. Astron. Astrophys. 30, 543 – 574 (1992)

43. Shintate K., Sekine H. Numerical simulation of hypervelocity impacts of a projectile on laminated composite plate targets by means of improved SPH method. Composites: Part A, 35, 683–692 (2004)

44. Xu F., Zhao Y., Li Y., Kikuchi M. Study of numerical and physical fracture with SPH method. Acta Mechanica Solida Sinica, Vol. 23 (2010)

45. Pezzica, G., Destefanis, R., Faraud, M. Numerical simulation of orbital debris impact on Spacecraft. In: International Conference on Structures under Shock and Impact, SUSI. 275-284 (1996)

46. Hayhurst, C.J., Clegg, R. Cylindrically symmetric SPH simulations of hypervelocity impacts on thin plates. Int. J. Impact Eng. 20, 337 – 348 (1997).

47. Hayhurst, C.J., Livingstone, I.H., Clegg, R., Fairlie, G.E., Hiermaier, S.J., Lambert, M. Numerical simulation of hypervelocity impacts on aluminum and Nextel/Kevlar Whipple shields. In: Proceedings of Hypervelocity Shielding Workshop, 8 - 11 March 1998, Galveston, Texas.

48. Michel, Y., Chevalier, J.-M., Durin, C., Espinosa, C., Malaise, F., Barrau, J.-J. Hypervelocity impacts on thin brittle targets: Experimental data and SPH simulations. Int. J. Impact Eng. 33, 441 – 451 (2006)

49. Clegg, R.A., White, D.M., Riedel, W., Harwick, W. Hypervelocity impact damage predictions in composites: Part I - material model and characterization. Int. J. Impact Eng. 33, 190 – 200 (2006)

50. Palmeri, D., Schaefer, F., Hiermaier, S., Lambert, M. Numerical simulation of non-perforating impacts on shielded gas-filled pressure vessels. Int. J. Impact Eng. 26, 591 – 602 (2001)

51. Salome R., Albouys V., Le Floc'h C., Sornette D., Vila J.P. (2001) High pressure composite tank behavior under an hypervelocity impact. Proceedings of the second European conference on space debris, European Space Operations Centre, Darmstadt, Germany, 19 – 21 March 2001.

52. Meyers M.A. Dynamic behavior of materials. John Wiley and Sons, Inc. (1994)

53. Zukas J. A. Introduction to hydrocodes. Elsevier (2004)

54. Steinberg D. Equation of state and strength properties of selected materials. Livermore, CA: Lawrence Livermore National Laboratory (1996)

55. Johnson G.R., Cook W.H. Fracture characteristics of three metals subjected to various strains, strain rates, temperatures and pressures. Engineering Fracture Mechanics, 21 (1), pp. 31-48 (1985)

56. Holmquist T.J., Johnson G.R. Response of silicon carbide to high velocity impact, J. Appl. Phys., 91 (9), 5858–5866 (2002).

57. Advanced Material Models for Hypervelocity Impact Simulations - AMMHIS, Final Report to ESA Contract No. 12400/97NL/PA(SC), EMI Report No. E 43/99, Freiburg, Germany, July 30, 1999.

58. Chen, J.K., Allahdadi, F.A., Sun, C.T. A quadratic yield function for fiber-reinforced composites. J. Compos. Mat. 31, 788 – 811 (1997)

59. Sun, C.T., Chen, J.L. A Simple Flow Rule for Characterizing Nonlinear Behavior of Fiber Composites. J. Compos. Mat. 23, 1009 – 1020 (1989)

60. AUTODYN® Composite Modelling. Revision 1.3. Release 14.0, 2011.

61. Elfer N.C. Structural damage prediction and analysis for hypervelocity impacts - Handbook. NASA Contractor report 4706 (1996)

62. Ryan S., Christiansen E. Micrometeoroid and Orbital Debris (MMOD) Shield Ballistic Limit Analysis Program. NASA/TM–2009–214789 (2010).

63. Ryan S.J., Christiansen E.L., Lear D.M. Development of the Next Generation of Meteoroid and Orbital Debris Shields. In: AIP Conference Proceedings, 28 Dec 2009, 1195 (1).

64. Ryan, S., Thaler, S. Artificial Neural Networks for Characterizing Whipple Shield Performance, Procedia Engineering 58, 31 – 38 (2013).

65. http://www.3m.com/market/industrial/ceramics/pdfs/fabric_styles_properties_3.pdf

66. Christiansen E.L. Enhanced meteoroid and orbital debris shielding, Int. J. Impact Eng. 17, 217-228 (1995).

67. Destefanis R, Schaefer F, Lambert M. Faraud M. Schneider E. Enhanced space debris shields for manned spacecraft, Int. J. Impact Eng., 29, pp. 215-226 (2003)

68. Shaefer F. Hypervelocity impact testing, impacts on pressure vessels. Final report to ESA Contract 10556/93, EMI E 14/01, Erns-Mach-Institut, Freiburg, Germany (2001)

69. Yew CH, Rodney BK. A study of damage in composite panels produced by hypervelocity impact. Int J Impact Eng 1987; 5:729-38.

70. Schonberg WP. Hypervelocity impact response of spaced composite material structures. Int J Impact Eng 1990; 10:509-23.

71. Christiansen EL. Investigation of hypervelocity impact damage to space station truss tubes. Int J Impact Eng 1990; 10(1):125-33.

72. Silvestrov VV, Plastinin AV, Gorshkov NN. Hypervelocity impact on laminate composite panels. Int J Impact Eng 1995; 17(1):751-62.

73. Schonberg WP. Protecting spacecraft against orbital debris impact damage using composite materials. Compos A; 31(1):869-78 (2000)

74. Tennyson RC, Lamontagne C. Hypervelocity impact damage to composites. Compos A; 31(1): 785-94 (2000)

75. Wicklein M, Ryan S, White DM, Clegg RA. Hypervelocity impact on CFRP: testing, material modelling, and numerical simulation. Int J Impact Eng; 35(1):1861-9 (2008)

76. Cherniaev A, Telichev I. Numerical simulation of impact damage induced by orbital debris on shielded wall of composite overwrapped pressure vessel. Appl Compos Mat; 21(6):861-884 (2014)

77. Bradley WL. Relationship of matrix toughness to interlaminar fracture toughness. In: Friedrich K, editor. Application of Fracture Mechanics to Composite Materials. Amsterdam: Elsevier, p.159-187 (1989)

78. Lamontagne CG, Manuelpillai GN, Taylor EA, Tennyson RC. Normal and oblique hypervelocity impacts on carbon fibre/PEEK composites. Int. J. Impact Engng; 23(1):519-532 (1999)

79. http://www.cemselectorguide.com/pdf/APC-2_PEEK_031912.pdf

80. Smiley AJ, Pipes RB. Rate effects on mode I interlaminar fracture toughness in composite materials. J Comp Mats 1987; 21: 670-687.

81. Smiley AJ, Pipes RB. Rate sensitivity of mode II interlaminar fracture toughness in graphite/epoxy and graphite/PEEK composite materials. Comp Sci Tech 1987; 29: 1-15.

82. Hartwig G. Fiber composites in cryogenic applications. In: Proceedings of ECCM-8 Conference. Naples, June, 1998. p. 197-206.

83. Ryan S, Wicklein M, Mouritz A, Riedel W, Shafer F, Thoma K. Theoretical prediction of dynamic composite material properties for hypervelocity impact simulations. Int. J. Impact Eng. 36: 899–912 (2009)

84. Baluch AH, Park Y, Kim CG. Hypervelocity impact on carbon/epoxy composites in low Earth orbit environment. Composite Structures 2013; 96(1): 554-560

85. Hayes BM, Gammon LM. Optical microscopy of fiber-reinforced composites. ASM International, 2010.

86. http://www.toraycfa.com/pdfs/T700SDataSheet.pdf

87. Chamis CC. Simplified composite micromechanics equations for strength, fracture toughness, impact resistance and environmental effects. NASA TM – 83696 (1984)

88. http://www.tcrcomposites.com/pdfs/resindata/resin_select_v12_1110.pdf

89. Sun C.T., Han C. A method for testing interlaminar dynamic fracture toughness of polymeric composites, Compos B; 35(6–8): 647-655 (2004)

90. Tsai JL, Guo C, Sun CT. Dynamic delamination fracture toughness in unidirectional polymeric composites, Composites Science and Technology; 61(1): 87-94 (2001)

91. ASTM D5528-01. Standard Test Method for Mode I Interlaminar Fracture Toughness of Unidirectional Fiber-Reinforced Polymer Matrix Composite, Annual Book of ASTM Standard. ASTM (2001)

92. Adams DF, Carlsson LA, Pipes RB. Experimental characterization of advanced composite materials. Third edition. CRC Press (2003)

93. AUTODYN® User's Manual. Release 14.0, 2011.

94. Christiansen E.L. Meteoroid/Debris shielding. NASA TP-2--3-210788 (2011)

95. Tillotson, J. H. "Metallic Equations of State for Hypervelocity Impact",GA-3216, General Atomic, San Diego, CA, July 1962

96. Allen, R. T. Equation of State of Rocks and Minerals, General Atomic, San Diego, CA, Report GAMD-7834 (1967)

97. Brodie & Hormuth. "The PUFF-66 Computer Program", AFWL-TR-66-48, Air Force Weapons Laboratory, Albuquerque, NM, May 1966

98. Bakken L. H., Anderson, P.D. "An Equation of State Handbook (Conversion Relations between the WONDY/TOODY and the PUFF/KO/HEMP Classes of Shock Wave Propagation Computer Codes)", Sandia Rep. SCI-DR-68-123, Sandia Laboratory, Albuquerque, NM, January 1969

99. Beguelin P., Barbezat M., Kausch H.H. Mechanical characterization of polymers and composites with a servohydraulic high-speed tensile tester. J Phys III, 1, 1867-1880 (1991)

100. You H., Youm Y.J. Loading rate effect on mode I interlaminar fracture of carbon/epoxy composite. J Reinforced Plastics Composites, 16, 537-549 (1997)

101. Christiansen E.L., Kerr J.H. Mesh double-bumper shield: a low-weight alternative for spacecraft meteoroid and orbital debris protection. Int. J. Impact Eng., 14, pp.169–180 (1993)

102. Horz F., Cintala M., See T., Bernhard R., Cardenas F., Davidson W., Haynes J. Comparison of continuous and discontinuous collisional bumpers: dimensionally scaled impact experiments into single wire meshes. NASA technical memorandum no. 104749 (1992)

103. Gupta N.K., Iqbal M.A., Sekhon G.S. Experimental and numerical studies on the behavior of thin aluminum plates subjected to impact by blunt- and hemispherical-nosed projectiles, Int. J. Impact Eng., 32, pp. 1921-1944 (2006)

104. Corbett B.M. Numerical simulations of target hole diameters for hypervelocity impacts into elevated and room temperature bumpers. Int. J. Impact Eng., 33, pp. 431-440 (2006).

105. Johnson G.R., Cook W.H. Selected Hugoniots: EOS, 7th Int. Symp. Ballistics (1969)

106. Kay G. Failure Modeling of Titanium 6Al-4V and Aluminum 2024-T3 with the Johnson-Cook Material Model. DOT/FAA/AR-03/57 (2003)

107. Nazarenko A. I. Space debris modeling. (Series "Mechanics, Control and Informatics") M.: IKI RAN. 216 p. (2013)

108. Weaire D, Phelan R. A counter-example to Kelvin's conjecture on minimal surfaces, Phil. Mag. Lett. 69: 107–110 (1994)

109. Taylor E.A., Herbert M.K., Vaughan B.A., McDonnell J.A. Hypervelocity Impact on Carbon Fibre Reinforced Plastic / Aluminum Honeycomb: Comparison with Whipple Bumper Shields. Int. J. Impact Eng., 23 (1), pp. 883-893 (1999).

110. Yasensky J., Christiansen E. Hypervelocity Impact Evaluation of Metal Foam Core Sandwich Structures. JSC63945 (2007).

111. Destefanis R., Schäfer F., Lambert M., Faraud M. Selecting enhanced space debris shields for manned spacecraft. Int. J. Impact Eng., 33, pp. 219-230 (2006).

112. Stellingwerf R.F., Wingate C.A., Impact modeling with smooth particle hydrodynamics, Int. J. Impact Eng., 14 (1), pp. 707-718 (1993).

113. Allahdadi F.A., Carney T.C., Hipp J.R., Libersky L.D., Petschek A.G. High strain lagrangian hydrodynamics: a three-dimensional SPH code for dynamic material response, Phillips Laboratory, PL-TR-92-1054 (1992).

114. Musante R.E., Morrow J.D., Active spall suppression armor. Patent number 4934245 (1990)

115. Gibson R.F. Principles of Composite Material Mechanics, Second Edition, 2007.

116. Hashin Z, Rosen B.V. The elastic moduli of fiber reinforced materials. J. Applied Mech. (1964).